Numerical Analysis of the Multi-Section Nature of the Regional Blended Wing Body Aircraft at Low Speed

by

Oliverio Esteban VELAZQUEZ SALAZAR

THESIS PRESENTED TO ÉCOLE DE TECHNOLOGIE SUPÉRIEURE IN
PARTIAL FULFILLMENT OF THE REQUIREMENTS FOR THE DEGREE
OF DOCTOR IN PHILOSOPHY
PH.D.

MONTREAL, DECEMBER 4TH, 2020

ÉCOLE DE TECHNOLOGIE SUPÉRIEURE
UNIVERSITÉ DU QUÉBEC

BOARD OF EXAMINERS

THIS THESIS HAS BEEN EVALUATED

BY THE FOLLOWING BOARD OF EXAMINERS

Professor François Morency, Thesis Supervisor
Département de génie mécanique at École de technologie supérieure

Professor Julien Weiss, Thesis Co-supervisor
Département de génie mécanique at École de technologie supérieure

Professor James Lapalme, President of the Board of Examiners
Département de génie de la production automatisée at École de technologie supérieure

Professor François Garnier, Member of the jury
Département de genie mécanique at École de Technologie Supériéure

Professor Eric Laurendeau, External Evaluator
Département de genie mécanique at École Polytechnique de Montréal

THIS THESIS WAS PRENSENTED AND DEFENDED

IN THE PRESENCE OF A BOARD OF EXAMINERS AND PUBLIC

ON NOVEMBER 20$^{\text{TH}}$, 2020

AT ÉCOLE DE TECHNOLOGIE SUPÉRIEURE

ACKNOWLEDGMENT

Thank you Grace for showing me patience and meditation, and trying to make my life a little healthier. Thank you, Armando, for always finding ways to communicate your ever-present support. I love you all.

There is a special place in this section for Kristy, my girlfriend/partner, who has shared this path with me. In a certain way, she nurtured this thesis with me. Thank you for always believing in me and never giving up. Thank you for being there in the good times and the bad ones. Thank you for giving me the time to finish this project so that we can start the next one together. I love you.

There is a particular space here too for Rory Wheeler, without whom this project would have never seen the light of day. Thank you, Rory, for your unwavering support. I hope I can repay the favor one day.

Next, I must thank Professor Alain Ehrlacher. Since the first day we met, you've always been a constant source of enlightenment to show me what I could… should become, and how much I can accomplish. Still, to this day, I believe the seeds for my PhD were planted at your office, 9 years ago. Thank you for being a great Mentor, and a great example of what a great engineer should be.

Next, I'd like to thank Mohammed Chouak, for his constant feedback on my work; it was always on point. Thank you for the tips and advice; you were most objective, and your advice allowed me to value my accomplishments more fairly.

I'd like to thank my friends from the BRECI, in particular Liliana and Gino. It was a pleasure working with both of you as an ÉTS ambassador. Through our mutual experiences I managed to learn more about university than I did at my desk. Thank you for your time and support.

Next, I would like to thank professors Garnier and Seers for their constant visits to the lab and their always cheerful attitude. I'd also like to thank all the people that were, in one way or

Analyse numérique basse vitesse de la nature multi-section de l'avion à fuselage intégré

Oliverio Esteban VELAZQUEZ SALAZAR

RÉSUMÉ

L'avion a fuselage intégré ou BWB pour ses initiales en anglais est un concept innovant qui assemble tous les éléments d'un avion à l'intérieur d'une unique enveloppe. Cette configuration propose des gains en consommation de carburant ainsi qu'un impact environnemental plus faible. Des nombreux travaux scientifiques utilisent ou développent cette configuration, particulièrement dans le cadre de transport des passagers et dans le cadre de conception de drones. Dans sa modalité de transport de passagers, les travaux aérodynamiques existants se basent prioritairement sur des versions long-courrier en conditions de croisière. Toutefois, les études de marché actuelles montrent une tendance croissante sur la demande d'aéronefs de moyenne portée pour 100-150 passagers. Par ailleurs, la géométrie de cet avion incorpore plusieurs profils aérodynamiques, cordes, angles de flèche et de vrillage distribués sur l'envergure de l'avion. Dans le cas du BWB, ces distributions ne sont pas nécessairement constantes ou même régulières au sens mathématique; ceci donne lieu à différents comportements aérodynamiques en fonction des différentes sections de l'aéronef. Cette nature multi-section prévoit l'existence de fortes interactions entre le corps central et l'aile extérieure de l'avion. Ces interactions – uniques au BWB – seraient particulièrement importantes lors des manœuvres basse vitesse comme le décollage et l'atterrissage. Ce comportement unique pourrait être exploité pour générer plus de portance naturelle à basse vitesse avant même d'envisager des dispositifs hypersustentateurs. L'objectif de cette thèse est de développer des outils de conception spécifiques au BWB basés sur l'hypothèse d'une interaction unique entre le corps central et l'aile extérieure concernant le décalage du décrochage et l'augmentation naturelle de la portance à basse vitesse pour ce type d'avion. Cette étude original permettrait d'exploiter ces interactions lors des phases de design conceptuel des BWB.

La méthodologie adoptée propose l'analyse numérique d'un BWB régional à basse vitesse. D'abord, un modèle géométrique du BWB régional est construit en utilisant des méthodes de design conceptuel couplées aux contraintes géométriques de l'avion. Ensuite le comportement à basse vitesse d'un BWB est comparé à celui d'un avion conventionnel. Le comportement aérodynamique de chaque avion est simulé grâce à des méthodes de volumes finis couplées aux équations RANS appliquées sur une enveloppe d'angles d'attaque centrés autour de l'angle de décrochage. Une fois les différences de comportement ciblées, il est possible de proposer des méthodes pour identifier l'interaction basse vitesse entre le corps central et l'aile extérieure. Dans le cas présent, une analyse de l'influence du vrillage sur la portance maximale est proposée. Des méthodes RANS permettent de simuler le comportement basse vitesse du BWB autour du décrochage avec différents vrillages. Les résultats démontrent bel et bien l'existence d'un couplage exploitable entre le corps central et l'aile extérieure à basse vitesse. Ces résultats sont utilisés pour calibrer un modèle original de calcul de portance maximale pour un BWB à basse vitesse.

X

Cette thèse revoit plusieurs résultats connus de la littérature comme l'intérêt de concevoir le décrochage de l'aile le plus près possible de l'encrage ainsi que l'effet retardateur du vrillage d'une aile sur le décrochage de celle-ci. Quant aux résultats originaux, on retrouve une géométrie de BWB régional utilisée comme point de départ d'autres travaux scientifiques. De plus, un modèle basse fidélité de calcul de portance maximale du BWB est proposé. Par ailleurs, l'analyse comparative à basse vitesse entre un avion conventionnel et un BWB montre que le corps central du BWB apporte une résistance au décrochage inexistante dans l'avion conventionnel. L'analyse du vrillage montre qu'il est possible de coupler le comportement aérodynamique du corps central avec celui de l'aile extérieure afin d'augmenter la génération de portance naturelle. En particulier, il a été démontré qu'une augmentation du vrillage était aussi accompagnée, dans le cas du BWB, par une augmentation de la portance maximale. Les résultats numériques sont utilisés pour calibrer le modèle de portance maximale proposé. Ce modèle est un apport à la communauté scientifique intéressée dans le développement d'ailes complexes et d'avions comme le BWB.

En tout, cette thèse aura mis en relief la caractéristique unique des BWB de pouvoir coupler le comportement du corps central avec celui de l'aile extérieure pour maximiser la portance maximale de l'avion et optimiser son point de décrochage global. Les travaux futurs devront se centrer sur l'utilisation de méthodes de simulation numérique plus exactes, pour autant que les ressources numériques le permettent, ainsi que l'exploration de plus de géométries BWB afin de générer un modèle de portance maximale plus robuste. Cela dit, les résultats généraux sont satisfaisants et démontrent des nouveaux avantages du BWB par rapport aux avions conventionnels, cette fois-ci, sous conditions de basse vitesse.

Mots-clés : aéronautique, aérodynamique, BWB, CFD, RANS, portance maximale, basse vitesse, design d'aéronefs

Numerical analysis of the multi-section nature of the blended wing body aircraft at low speed

Oliverio Esteban VELAZQUEZ SALAZAR

ABSTRACT

The blended wing body aircraft, or BWB for short, is an innovative concept that gathers all of the elements of an aircraft inside a unique wing envelope. This configuration promises a lower environmental footprint coupled with sizable fuel savings. Numerous scientific papers already either use or are expanding on this configuration; particularly for passenger transport and UAV applications. Concerning the passenger transport, the existing aerodynamic works on the BWB focus mainly on large-capacity, long-range designs under cruise conditions. However, current market forecasts show an expected increase in demand for regional, medium capacity aircrafts for 100-150 passengers. Moreover, this aircraft`s unique geometry incorporates multiple airfoil, chord, sweep and twist distributions along the wingspan. For the BWB, these distributions are not necessarily constant or mathematically smooth; giving raise to different aerodynamic behaviour depending on which section of the aircraft is analysed. This multi-section nature of the BWB hints at the hypothesis that the BWB designer may have the ability to consciously align the aerodynamic behaviour of the centerbody with that of the outer wing to obtain predictable low speed behaviour, in particular, to generate a stronger natural lift at low speeds. The objective of this thesis is to develop BWB-specific design tools, based on the hypothesis of the existence of a unique interaction between the centerbody and the outer wing, with respect to natural lift at low speeds for this aircraft configuration. This original work would allow designers to incorporate said predictive coupling in the conceptual design phases of future BWBs.

The proposed methodology is based on the numerical analysis of a regional BWB at low speed. First, a geometrical model of the baseline regional BWB was generated by applying classic aircraft design methods coupled with BWB-specific constraints. This was followed by the comparison of the low speed behaviour between a conventional aircraft and a BWB. The aerodynamic behaviour of each aircraft was simulated via RANS simulations applied over a series of angles of attack spread around the stall angle. Based on the behavioural differences, a coupling between the centerbody and the outer wing is proposed. Specifically, a study of the impact of twist distribution on maximum lift is carried out. Once again, RANS simulations at low speed are applied, this time, over three BWB geometries with different twist distributions. The results validate the hypothesis of a strong coupling between centerbody and outer wing at low speeds. Furthermore, these original results are used to calibrate a low-fidelity model of the maximum lift coefficient of a BWB at low speeds.

This thesis brings forth some known results from classic wing theory like the importance of stalling close to the wing root and the stall delay effect introduced by the twist. On the original side, a baseline regional BWB geometry is proposed for use in future works. This geometry has already been used in other theses and scientific works. Furthermore, a mathematical low-

fidelity model of the maximum lift coefficient of a BWB has been developed. Moreover, analysis of the behavioural differences between a conventional aircraft and a BWB show that the centerbody of a BWB generates a stall-resistance phenomenon which is non-existent in conventional aircrafts. Analysis of the twist distribution on the BWB shows that it is possible to couple the aerodynamic characteristics of the outer wing with those of the centerbody to amplify natural lift generation. In particular, it was found that, on top of delaying stall, increased twist can also lead to increased maximum lift in the case of a BWB aircraft. The numerical results are used to calibrate the proposed maximum lift coefficient model. This model is a contribution to the scientific community interested in the development of complex wings and all-wing aircrafts like the BWB.

In conclusion, this thesis shows the unique characteristic of the BWB to allow the designer to couple the outer wing and the centerbody behaviours to increase maximum lift and optimize its stall behaviour at low speed. Future work should focus on the use of more accurate simulation methods as well as the exploration of a larger BWB model database so as to enhance the robustness of the maximum lift prediction model. Nevertheless, the general results of this thesis are satisfactory and unveil previously undocumented advantages of the BWB with respect to conventional aircrafts at low speed.

Keywords: aeronautics, aerodynamics, aircraft design, BWB, CFD, RANS, maximum lift, low speed.

TABLE OF CONTENTS

LIST OF TABLES

LIST OF FIGURES

Page

LIST OF ABREVIATIONS

AIAA	American Institute of Aeronautics and Astronautics
AOA	Angle of Attack
BWB	Blended Wing Body [aircraft]
CAD	Computer Aided Design
CB	Centerbody
CG	Center of Gravity
CFD	Computational Fluid Dynamics
CFL	Courant-Friedrichs-Lewy [number]
CONACYT	Consejo Nacional de Ciencia y Tecnología
CRM	Common Research Model
CV	Control Volume
DPW5	Drag Prediction Workshop 5
EPNL	Estimated Perceived Noise Levels
ERA	Environmentally Responsible Aviation
ÉTS	École de Technologie Supérieure
FV	Finite Volumes [Method]
HPC	High-Performance Computing
IATA	International Air Transport Association
ICAO	International Civil Aviation Organisation
JST	Jameson-Schmidt-Turkel [scheme]
LE	Leading Edge

LLT	Lifting Line Theory
MDO	Multi Disciplinary Optimization
NASA	National Aeronautics and Space Administration
NTF	National Transonic Facility
OOM	Orders of Magnitude
OW	Outer Wing
PAX	Passengers
RANS	Reynolds-Averaged Navier-Stokes [equations]
SA	Spalart-Allmaras [turbulence model]
SU2	Stanford University Unstructured [software]
TAW	Tube and Wing [aircraft]
TE	Trailing Edge
TOL	Take-off and Landing
TW	Transition Wing
UAV	Unmanned Aerial Vehicle
VLM	Vortex-Lattice Method

LIST OF SYMBOLS

AR Aspect ratio

a_{sound} Speed of sound $[m/s]$

a_0 Local lift slope $[rad^{-1}]$

b Wingspan $[m]$

C_D Global drag coefficient (3D) [-]

C_{D0} Zero-lift drag coefficient (3D) [-]

C_d Local drag coefficient (2D) [-]

C_L Global lift coefficient (3D) [-]

C_{Lmax} Maximum global lift coefficient (3D) [-]

$C_{L,\alpha}$ Global lift slope $[rad^{-1}]$

C_l Local lift coefficient (2D) [-]

C_{lmax} Maximum local lift coefficient for a section/profile (2D) [-]

C_{lstall} Stall lift coefficient of the spanwise section with the maximum local lift coefficient (2D) [-]

C_M Global pitch moment coefficient (3D) [-]

C_m Local pitch moment coefficient (2D) [-]

C_{TSFC} Thrust-specific fuel consumption $[kg/N.s]$

c Local chord $[m]$

$\bar{c}$ Mean aerodynamic chord $[m]$

c_f Skin friction coefficient [-]

c_p Pressure coefficient [-]

D Drag force $[N]$

d   Local drag force per unit span $[N/m]$

E Endurance $[s]$

e Specific internal energy $[J/kg]$

e_k Specific kinetic energy $[J/kg]$

e_0 Total specific kinetic energy $[J/kg]$

$f(\Lambda)$ Sweep correction function [-]

H_{cr} Cruise altitude $[m]$

k Specific turbulent kinetic energy $[J/kg]$

L Lift force $[N]$

l Local lift force per unit span $[N/m]$

L/D Lift to drag ratio [-]

M Mach number [-]

M_{cr} Critical Mach number [-]

M_∞ Freestream Mach number [-]

N_{CFL} CFL number [-]

n_{LLT} Calibration parameter for the compound wing model [-]

Pr Prandtl number

p Pressure $[N/m^2]$

q_∞ Dynamic pressure $[N/m^2]$

$\boldsymbol{q}$ Heat flux vector $[W/m^2]$

$\vec{R}$ (Chapter 2) Aerodynamic force vector $[N]$

R (Chapter 3) Range [m]

Re Reynolds number [-]

XXVIII

r_α Stall ratio [-]

S_{ref} Reference surface $[m^2]$

s_f Structure factor

s_{run} Runway length $[m]$

T (Chapter 2) Temperature $[K]$

T (Chapter 3) Thrust force $[N]$

T/W Thrust-to-weight ratio $[N/N]$

V Velocity $[m/s]$

V_a Approach speed $[m/s]$

V_{eff} Effective speed seen by the airfoil section $[m/s]$

V_∞ Freestream velocity $[m/s]$

$\boldsymbol{v}$ Velocity vector $[m/s]$

W_{crew} Crew mass $[kg]$

W_e Empty mass of the aircraft $[kg]$

W_f Fuel mass $[kg]$

$W_{payload}$ Payload mass $[kg]$

W_{TO} Design Takeoff mass $[kg]$

W/S Wing loading $[kg/m^2]$

y wingspan coordinate $[m]$

α Angle of attack $[°\ or\ rad]$

α_{3D} Global angle of attack (disambiguation) $[°\ or\ rad]$

α_{L0} Local zero-lift angle of attack $[°\ or\ rad]$

α_{eff} Effective angle of attack $[°\ or\ rad]$

α_i Induced angle of attack $[°\ or\ rad]$

α_s Stall angle

Γ Circulation $[m^2/s]$

$\delta_{L\Lambda}$ Lift correction factor for the global lift (compound wing model) [-]

δ_α^{CL} Base lift correction factor for the compound wing model [-]

δ_Ω^{CL} Twist lift correction factor for the compound wing model [-]

$\delta_n^{\alpha_i}$ n-th correction factor for the induced angle of attack [-]

XXX

η Normalized wingspan section [-]

$\kappa_{L\Lambda}$ Sweep correction factor [-]

κ_{LS} Stall correction factor [-]

$\kappa_{L\Omega}$ Twist correction factor [-]

Λ Sweep angle $[° \; or \; rad]$

$\Lambda_{0.25c}$ Sweep angle at the quarter chord position $[° \; or \; rad]$

Λ_{LE} Sweep angle at the leading edge $[° \; or \; rad]$

λ (Chapter 2) Thermal conductivity $[W/K.m]$

λ (Chapter 3) Wing tapper ratio $[-]$

μ Viscosity $[kg/m.s]$

μ_{dyn} Dynamic viscosity $[kg/m.s]$

μ_{tur} Turbulent viscosity $[kg/m.s]$

ρ Air density $[kg/m^3]$

ρ_∞ Freestream air density $[kg/m^3]$

τ_w skin shear stress $[N/m^2]$

$\boldsymbol{\underline{\tau}}$ **S**hear stress tensor $[N/m^2]$

$\boldsymbol{\underline{\tau}_{tot}}$ Total stress tensor $[N/m^2]$

$\boldsymbol{\underline{\tau}_{dyn}}$ Dynamic stress tensor $[N/m^2]$

$\boldsymbol{\underline{\tau}_{rey}}$ Reynolds stress tensor $[N/m^2]$

ϕ Twist angle/distribution $[° \ or \ rad]$

Ω Total twist $[rad^{-1}]$

ω Normalized twist distribution [-]

INTRODUCTION

According to the 2018 International Civil Aviation Organization Annual Report (ICAO, 2018), civil transportation went from 4500 million passenger-km in 2009 to over 8200 million passenger-km, which represent more than a 80% increase in 10 years. The constant increase in demand of airline transportation raises questions concerning the increasing fuel costs and the ecological impact of the aeronautical industry. NASA's N+, Europe's Vision 2020 and Europe's Flightpath 2050 were three programs created to address these problems. These programs focused on developing technologies to reduce fuel consumption, air pollution (CO_2, NO_x) and noise propagation. While numbers and deadlines differ between programs, reductions of up to 50% in combustion, noise emissions and fuel consumption were proposed with respect to its reference values for year 2000 (IATA, 2013).

The Blended Wing Body (BWB) was created in an attempt to meet the increasing design constraints brought forth by these goals (Liebeck, 2004). This aircraft concept inspired by the flying wings family is characterized by better lift-to-drag (L/D) ratio, fuel consumption and noise shielding for large passenger aircrafts with respect to conventional tube and wings (TAW) aircrafts. Multiple research groups have proposed initial design solutions ranging from conceptual design propositions (Diedrich, Hileman, Tan, Willcox, & Spakovszky, 2006; Mohr, Paulus, Baier, & Hornung, 2012) to structural solutions for this geometry (Geuskens, Bergsma, Koussios, & Beukers, 2009).

Among the multiple design challenges introduced by the BWB, the existing literature suggests a strong interest in the study of the aerodynamic behaviour of this aircraft; namely the evolution of its local and global aerodynamic coefficients like the pressure and the wall friction coefficients (c_p, c_f) as well as the lift, drag and/or moment coefficients (C_L, C_D, C_M) with respect to different input conditions.. The vast majority of prior BWB aerodynamic research focuses on the prediction and optimisation of the aerodynamic coefficients at cruise conditions (Liebeck, 2004; N. Qin et al., 2004; Reist & Zingg, 2013). As the knowledge on cruise behaviour increases, the BWB community has started to shift its interest towards alternative,

yet critical, flight phases. Yet, few research works exist on the low-speed near-stall conditions seen during take-off and landing (Park, Chang, & Ko, 2017). The behaviour during these critical phases has been open to interpretation, where some authors hypothesize a classic behaviour requiring conventional high lift devices (Paulus, Wirth, & Hornung, 2013) while some others hypothesise an enhanced natural lift requiring simpler high-lift devices (Hileman, Reynolds, De La Rosa Blanco, Law, & Thomas, 2007). Given these differences, a better understanding of the low speed behaviour of this particular aircraft is required. In turn, this would allow future designers to incorporate accurate low-speed behaviour in their own BWB designs.

Furthermore, the particular geometry of this aircraft combines varying airfoil, chords, sweep and twist distributions along the wingspan. Furthermore, these variations can be radical from one section to the next and are not necessarily smooth. This is defined in this thesis as a compound wing due to the fact that some sections of this aircraft present different geometric characteristics than its neighbours. This term is derived from the discrete compound wing concept described by Jamei, Maimun, Mansor, Azwadi, and Priyanto (2016), with the difference that our concept of compound wing is continuous instead of discrete. Based on this compound nature, the author hypothesizes that the centerbody (CB) and the outer wing (OW) can be coupled together to obtain a predictable low speed behaviour resulting from a blending of the aerodynamic behaviour of each zone. This coupling could be modeled and exploited during the design phases of the aircraft. In this thesis, this hypothesized coupling is also referred to as a CB/OW interaction.

Historically, the majority of the aerodynamic research on the BWB has been based on numerical methods applying multiple fidelity models. These methods present a varying degree of accuracy but are mostly widely accepted for general aerodynamic analysis. Considering the successful application of numerical methods on prior simulations of large aircraft geometries, it is reasonable to adopt numerical simulations to characterize the aerodynamic behaviour of the BWB as proposed by Blessing, Pham, and Marshall (2009).

Additionally, recent forecasts consider that 70% of new aircrafts between 2010 and 2029 will be regional and inter-regional aircrafts with the capacity for between 70 and 200 passengers (Deloitte, 2010; ICAO, 2018). This means that the development of BWB technology is highly desirable for the regional market in order to keep up with the expected market demands. Accordingly, some regional BWB concepts have been developed for cruise conditions (Kanazaki et al., 2013; Nara & Kanazaki, 2010; Reist & Zingg, 2013).

In light of this knowledge, this doctoral project is focused around the low speed aerodynamics of the regional BWB. The project is based on the hypothesis that, for the BWB, the interaction between the CB and the OW can be manipulated to attain a strong impact in the lift capabilities near stall of the aircraft – during takeoff and landing phases. The objective of this project is to identify and exploit a BWB-specific interaction between the CB and the OW that could be used to increase natural lift capabilities at low speeds for this aircraft configuration. This objective is attained through the development of a BWB regional model, a numerical comparison between BWB and TAW aircrafts near stall and a study of the CB/OW interaction.

Each subobjective is part of the methodology used to attain the thesis objective. The BWB model is generated based on classic aircraft design methodologies (Raymer, 2006; Roskam, 1985) coupled with BWB-specific design (Bradley, 2004), with the use of low-fidelity models and for aerodynamic prediction (Deperrois, 2009b; Drela, 1989). NASA's Common Research Model is then used as a tube and wing (TAW) representative of conventional aircrafts (Vassberg, Dehaan, Rivers, & Wahls, 2008). Numerical simulations of both BWB and TAW are carried out with SU2's RANS model (Palacios et al., 2014). After a CB/OW interaction has been identified, a CFD parametric study is carried out to exploit this interaction for low fidelity prediction.

The first chapter introduces the literature review around the BWB subject. This first chapter presents the reasoning behind the industrial problematic that led to the BWB. Further interest is given to the presentation and current achievements on the BWB, with a particular focus on the low speed aerodynamics and the numerical approaches used in prior research works.

Finally, the literature review ends with the proposition of a research problem and the specific objectives proposed to solve it.

The second chapter presents the main models and methods used in this thesis to predict the airflow behaviour around an aircraft. The conservation equations in their original form are presented. The chosen CFD RANS approach is then validated with a NACA 0012 test case. Finally, a generalized compound wing LLT model for maximum lift coefficient prediction is introduced. The specifics of the CFD RANS model chosen are left in the APPENDIX I and II.

The third chapter focuses on the generation of the regional BWB geometry and the verification of the numerical approach. The specific constraints introduced by the regional nature of the aircraft are resolved into the conceptual design of the regional BWB. This is followed by the validation of the RANS model for near stall analysis and the validation of the mesh strategy.

The fourth chapter presents the TAW configuration under low speed conditions and compares its stall development to that of a BWB. The comparison starts with a qualitative analysis focused on determining average tendencies. This is followed by a global quantification of the performance of both aircrafts based on the CFD results. Some conclusions on the low speed aerodynamic performance of the baseline regional BWB are achieved at this point; in particular, the chapter's results point towards the pertinency of the CB/OW interaction hypothesis.

The fifth chapter focuses on the CB/OW interaction stated earlier. To validate this hypothesis, multiple twist distributions for the regional BWB are compared against each other via a RANS approach. These results are further used to calibrate the generalized compound wing LLT maximum-lift-coefficient prediction model which is proposed for future conceptual design studies on similar geometries.

CHAPTER 1

LITERATURE REVIEW, RESEARCH PROBLEM AND OBJECTIVES

1.1   Introduction

In the context of increased technical constraints on the aeronautical design, the focus has shifted towards new configurations like the BWB (Liebeck, 2004). This project was developed as a contribution to the BWB development effort. Specifically, this project focuses around the low speed aerodynamics of the BWB. This results from the identification of knowledge gaps in the existing literature that could be exploited to develop more comprehensive BWB-specific design tools for future aircraft designers. This chapter presents the relevant literature review concerning the BWB that led to the proposal of this project. Particular focus is given to experimental and numerical works, low speed aerodynamics, stall and BWB design. As a result of this review, the chapter concludes with the presentation of the research problem and the thesis objective.

1.2   Market Forecast and Technology Roadmap

Aeronautical market forecasts show a faster growth than any other transport method at an average annual growth rate of 5% since 1990. This trend is expected to continue until, at least, 2030 (Bombardier, 2017). Particularly, demand for the 100-200 passenger aircrafts will represent 50% of the estimated growth due to the emergence of regional markets and the increased demand of point-to-point transport (Kanazaki et al., 2013). This indicates a need to develop regional solutions for the regional markets.

Following this sustained growth, technical constraints concerning economical and environmental factors have steadily increased over the years as part of the new aeronautical development programs for all sizes of aircraft. As an example, NASA's N+ program's main goals aimed to reduce noise, emissions and required fuel by more than 50% relative to 2005 reference levels (Suder, 2012). Consequently, the BWB novel configuration was developed as

a solution to face these constraints (Greener by Design, 2003; Maier, 2011). The literature shows ever increasing interest in the development of this configuration as a candidate to substitute the ageing global aircraft fleet, in particular for mid and long-range missions. Considering the expected growth of the future regional markets it is necessary to also consider the development of regional scale, 100 passenger BWBs for the future generation regional aircrafts.

1.3   The BWB: a new aircraft concept

The BWB is the result of modern investigation into the development of flying-wing-like aircrafts in the face of the evolving industrial constraints previously introduced. Originally presented by Liebeck (2004), the BWB integrates all the mechanisms needed for flight within a unique lifting surface - a smooth blending between the aircraft's main body and the outer wing -. This differs from classic Tube and Wing (TAW) configurations comprised of a defined fuselage, a wing and a control tail. The BWB's extended working surfaces, promise a higher fuel efficiency and lower noise impact with respect to conventional aircrafts, but also present the drawbacks of more complex and highly interdependent systems (Liebeck, 2004; Maier, 2011). To give an idea of the generic differences between both configurations, Figure 1-1 presents a scheme of a generic BWB planform view with respect to a comparable TAW configuration.

It must be noted that, while the BWB is comprised of a unique wing, the centerbody's (CB) main purpose is to house the cabin while the outer wing (OW) is optimized for mission performance. This requires radically different airfoils between the CB and the OW, as well as different sweep angles, different twist distributions and different local dimensions. This is defined by the author as the BWB's compound wing nature, where different sections of the aircraft result in substantially different local behaviors of the aerodynamic coefficients (different stall angles, different maximum lift coefficients, different drag, etc.).
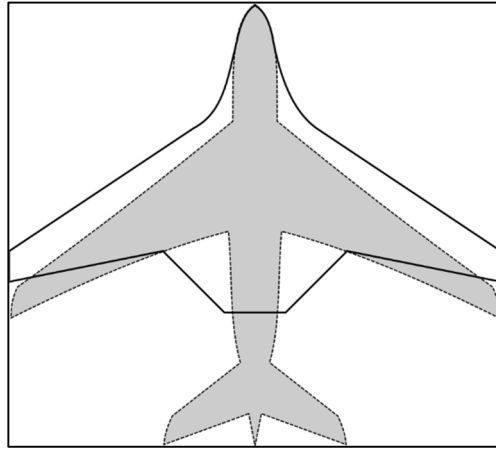
Figure 1-1:   Representation of a
BWB planform (transparent) over a
classical TAW planform (grey).

1.3.1   BWB Advantages

The BWB's first advantage is comprised by its aerodynamics. As a reference, current expected *L/D* ratio in transport aviation ranges between 15 and 20 (Torenbeek, 2013b). By comparison, with values ranging between 15 and 25 for optimized BWB (Velazquez, Weiss, & Morency, 2015), the BWB promises, on average, a better lift-to-drag ratio (*L/D*) than classic configurations.

This better aerodynamics reduce both the fuel consumption and the fuel weight of the aircraft. This reduction is derived from the diminished drag caused by the airframe shape. It is estimated between 20% and 30% per passenger-distance with respect to early 2000 values (Bolsunovsky et al., 2001; Liebeck, 2004; N. Qin et al., 2004). In turn, less fuel consumption translates into less combustion gases ejected into the atmosphere, as well as less operating costs for the operators.

Furthermore, the BWB's unique lifting surface provides the ability to achieve smoother loads and pressure distributions over the whole airframe (Liebeck, 2004; Ning Qin, Vavalle, & Moigne, 2005). In turn, this reduces the typical mechanical stress concentration around the

wing root seen in classical TAW. This results in a lighter structural weight in that zone. Moreover, this same unique surface allows for a semi-elliptic lift distribution along the wingspan (Ning Qin et al., 2005), resulting in increased drag reduction when compared to TAW designs. A conceptual scheme of these mechanical loads distribution is presented in Figure 1-2, adapted from (Liebeck, 2004).
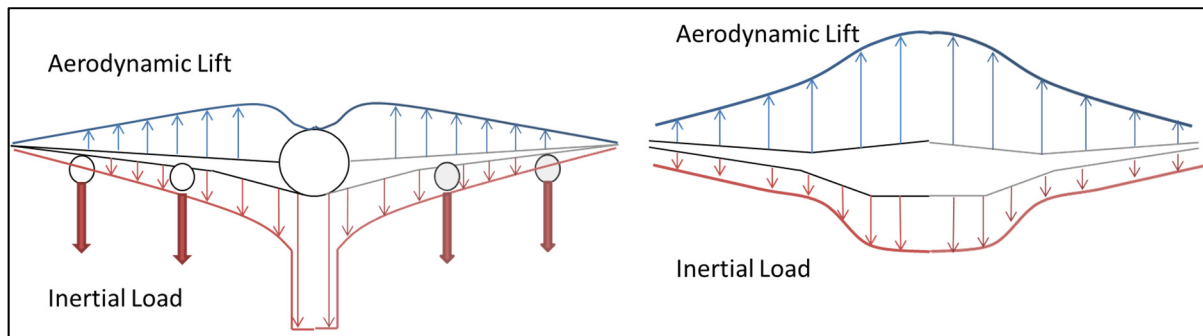
Figure 1-2:   Schematic load distribution for the TAW (left) and the BWB (right). Adapted from (Liebeck, 2004)

Finally, the estimated perceived noise levels (EPNL) promise a lower value than TAW aircrafts. According to Dobrzynski (2010), the main sources for airframe noise are: landing gears, slotted slats, flap and slat side-edges, flap and slat tracks and spoilers. The addition of slats and flaps, when deployed, drastically modify the flow conditions behind the wing, resulting in a higher noise impact during approach for complex high-lift devices. For this reason, the developers of the UK's silent aircraft initiative (The Cambridge-MIT Institute, 2003), proposed the BWB's manta ray-like shape to provide natural noise shielding to the ground user. Further investigation led to the development of the SAX-40 aircraft (Hileman, Spakovszky, Drela, & Sargeant, 2007), capable of attaining under 62dBA at the airport perimeter comparable to background noise in a well populated area.

Along with EPNL, fuel consumption is one of the main issues of future aircraft designs. It is therefore unsurprising that the BWB has been chosen as the flagship concept on multiple design projects focused around the reduction of EPNL, combustion emissions and fuel consumption. Examples of this are the Environmentally Responsible Aviation (ERA) project

(Collier et al., 2010), the SAX-40 project (Hileman, Spakovszky, et al., 2007) and the ACFA2020 project (Maier, 2011) related to NASA's N+ program, ACARE's Vision 2020 and Flightpath 2050 programs (IATA, 2013).

1.3.2 BWB Challenges

In contrast to its promising advantages, the BWB comes with its own set of challenges. These challenges are linked to the uniqueness of its lifting surface, the complexity of interdependent system interactions and the lack of BWB-specific know-how on structures, aerodynamics, safety and design among others. Some of these points are explored in the following paragraphs.

First, the BWB does not come with a cylindrical fuselage like the TAW. Thus, there is no cylindrical pressure distribution around the cabin. This creates bending moments on the skin of the cabin of the BWB (Mukhopadhyay, Sobieszczanski-Sobieski, Kosaka, Quinn, & Vanderpaats, 2004). To address this issue, the structure of the cabin needs to be reinforced by adequate materials and geometries, resulting in a weight increase of the cabin. New configurations like the multi-bubble cabin (van der Voet, Geuskens, Ahmed, van Eyben, & Beukers, 2012) and new materials like the PRSEUS panels (Velicki & Thrash, 2010) compete as viable solutions for the cabin problem of the BWB.

Moreover, the lack of a dedicated empennage raises the problem of stability and control. While possible to achieve, the handling of this aircraft demands a different approach to commands since the same surfaces must be used for different control commands like roll and pitch for example (Bolsunovsky et al., 2001). Also, since the relative distance between the Center of Gravity (CG) and the trailing surfaces is inferior to TAW aircrafts, the pitch moment generated by the control surfaces is weaker. As a consequence, more complex active control systems are needed to handle the aircraft (Nangia & Palmer, 2002). A comprehensive control study was carried out for the ACFA 2020 project. It concluded that while proper control and stability is attainable, the fuel mass plays a major role for trim conditions. However, this also makes the

fuel system safety critical since it must be operational to keep the aircraft CG within acceptable range (Maier, 2011).

Public acceptance is still a source of debate given the amount of new technologies incorporated into the aircraft – distributed propulsion, next generation engines, boundary layer ingestion nacelles, new composite materials among others -. It is still unclear if a new set of safety regulations and certifications specific to the BWB will be required. Finally it will be necessary to analyse the possible psychological effects of flying with limited windows available for the passengers (Liebeck, 2004).

1.3.3   BWB conceptual design

Conceptual aircraft design is a tool developed by multiple aircraft designers around the world (Anderson, 1999; Raymer, 2006; Torenbeek, 2013a). These general methods are used in the first stages of aircraft development to try out new configurations. The general conceptual design approach for most aircrafts can be summarized by the scheme presented in Figure 1-3: (1) The client's demands are translated into mission requirements. (2) Initial proposed values for the aircraft's expected performance allow for the definition of the design takeoff weight W_{TO}. (3) Critical performance parameters are selected based on the mission segments that the designer wants to prioritize. (4) Complementary design parameters are defined and the aircraft geometric layout is proposed. (5) A detailed weight estimation of the aircraft is carried out and compared against W_{TO}. Any margin found is added as extra fuel. (6) Performance validation is carried out: aerodynamic prediction is used to verify the actual aerodynamic parameters of the proposed geometry, while runway distances, maximum range, stability, power requirements, service ceiling and load factor for the current geometry are calculated. If the performance prediction is non-compliant with mission requirements, the new data is sent back to step (3) and iterated upon until mission compliance is reached. (7) Once the mission requirements have been attained, geometric modifications are proposed so as to obtain a more refined conceptual aircraft for the mission.
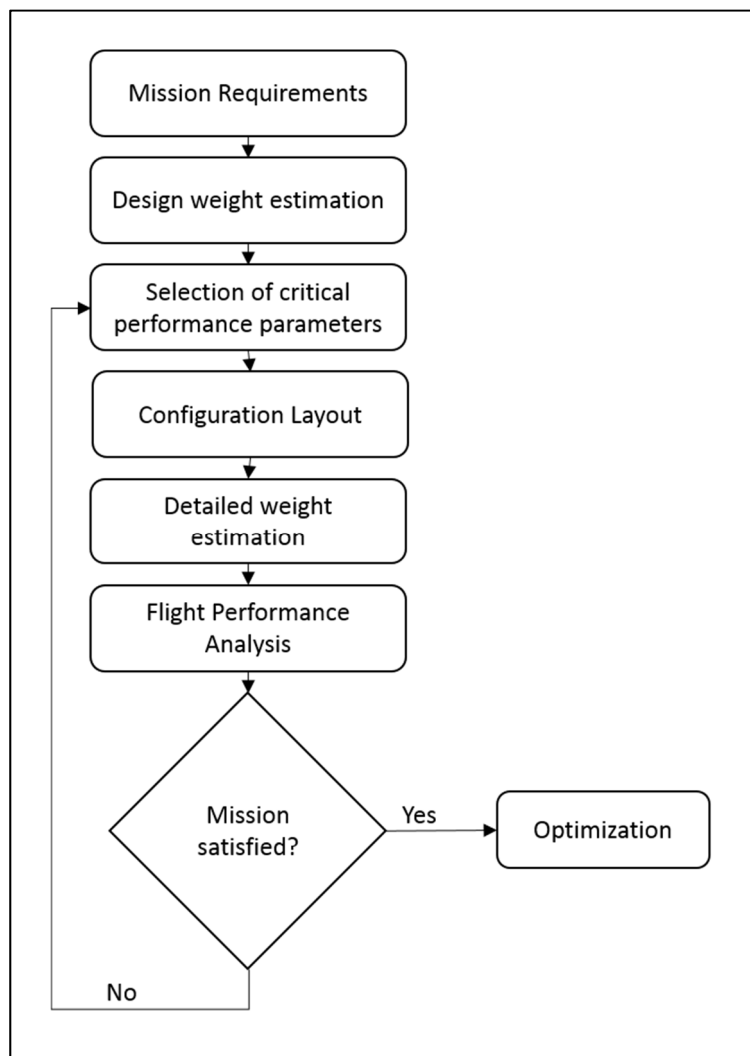
Figure 1-3:   The 7 steps of the conceptual design
approach.

The initial BWB concepts were proposed based on this general approach (Liebeck, 2004; N. Qin et al., 2004). However, the specific methods of each step used for classic TAW do not directly translate to BWB aircrafts. To work around this, BWB-specific configuration layout (Bradley, 2004) and airframe weight estimation (Howe, 2001) methods were developed. In turn, these methods were incorporated into multi disciplinary optimization (MDO) techniques for 250+ passengers BWBs (Osterheld, Heinze, & Horst, 2001; Vos & Van Dommelen, 2012).

These MDO techniques are in-house developments and focus on either large transport BWBs or UAV sized BWBs. These works don't account for 100-passenger sized BWBs.

Due to height requirements, only a percentage of the BWB length is usable for cabin space (Bradley, 2004). As a consequence, these constraints are specially punishing for the regional BWB whose volume efficiency is smaller than the 250+ passenger BWB (Nickol, 2012). Thus, Reist and Zingg (2013) propose the addition of cabin height constraints into the conceptual design of the regional BWB.

1.3.4   Experimental characterisation of the BWB

Prior to the beginning of this project, access to empirical data on this configuration was rather scarce. Available experimental data was limited mainly to research on unmanned aerial vehicles and scaled-down wind tunnel tests similar to the ones carried out by Wisnoe, Nasir, Kuntjoro, and Mamat (2009). Some experimental data was however generated by large aeronautical institutions like NASA (Carter, Vicroy, & Patel, 2009; Vicroy, 2009) and the US Air Force (Gebbie, Reeder, Tyler, Fonov, & Crafton, 2007). NASA's ERA project provided a series of wind tunnel and flight tests for its scaled down X-48 prototype (Regan, 2008).

Of particular interest are the tests carried out by Vicroy (2009) on the X-48B geometry. These low-speed tests aimed to analyze the static and dynamic stability of the X-48B BWB. Figure 1-4 show the lift coefficient C_L and the pitch moment coefficient C_M for the X-48B BWB with respect to the angle of attack α, as depicted by Vicroy (2009). The figure shows results for both "slats retracted" and "slats open" configurations. The "slats retracted" configuration is comparable to a BWB without high-lift devices. For this configuration, the C_L increases up to an initial stall angle – characterized by an unstable pitch break where C_M stops decreasing –. C_L decreases during the pitch break and then increases again. This pitch break doesn't happen with slats open, where C_M simply crashes after the stall angle is attained.

Compared to a classic behaviour presented later in Figure 1-5, the BWB low speed behaviour seems atypical. This is consistent with similar results on $C_L - \alpha$ curves obtained by (Gebbie et al., 2007) on a different BWB geometry. Both BWB geometries – without high lift devices - show an increase in lift after the initial stall. Finally, the "slats-extended" geometry show a unique extended stall somewhere between 20° and 30°. The addition of slats improves maximum lift coefficient and delays stall, as expected of high-lift devices. However, no explanation is given for the existence of an extended stall going from $\alpha \approx 20°$ to $\alpha \approx 30°$. Conclusions on the source of this deviation from conventional TAW are not further developed in these reference works. Our interpretation of these results suggests that there might be a particular interaction between the CB and the OW capable of delaying stall and enhancing the maximum lift coefficient depending on the CB/OW positioning. In particular, it is hypothesized that, with the right positioning between the CB and the OW, the CB might contribute with a non-negligible stall resistance of its own. The capacity to naturally generate this stall-resistance phenomenon is considered unique to the BWB. In the prior phrase, natural lift generation refers to the ability of the airframe to passively generate lift without addition of other geometries like high-lift devices.
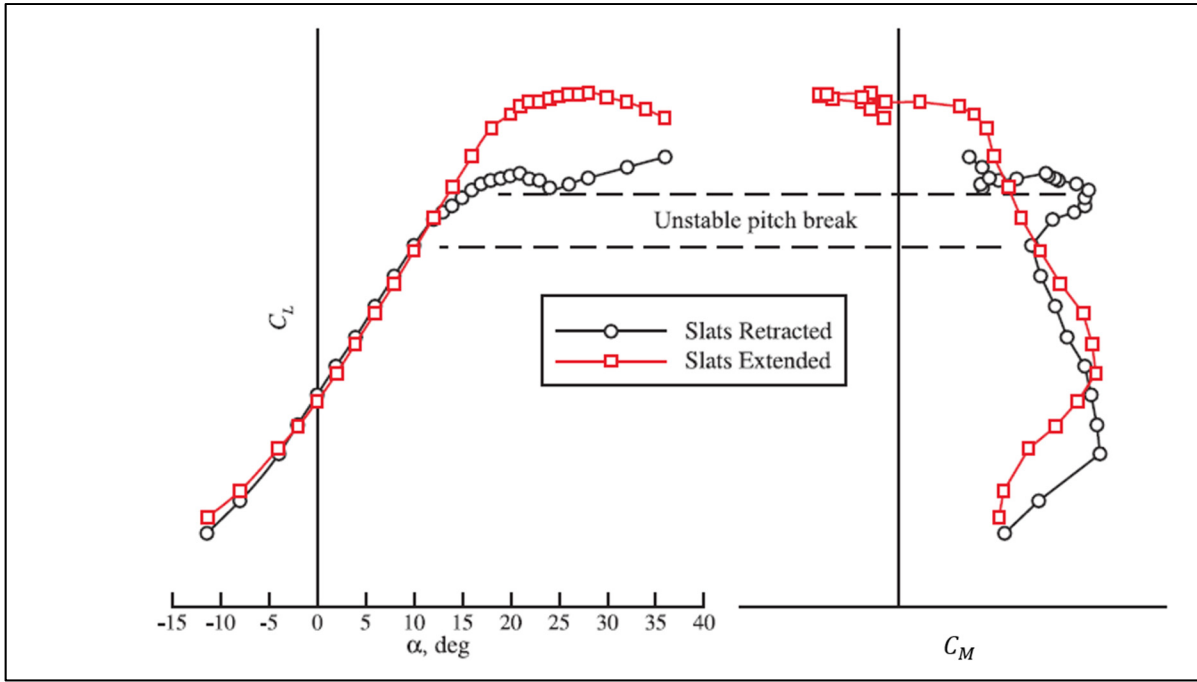
Figure 1-4:   Lift and pitching moment of slat extended and retracted X-48 configurations. Reproduced with the permission of (Vicroy, 2009).

In the previous paragraph, the term "CB/OW interaction" refers to a coupling between the CB and the OW that could be modeled with a design rule. This follows the idea that the CB properties and the OW properties could be combined to attain better performance for a given aerodynamic variable. For this to be true, the corresponding aerodynamic variable would have to be sensitive to small modifications to the CB, the OW and/or the relative position between CB and OW. At this point, any change in reference airfoil shapes or reference surfaces is to be avoided. In the present case, we hypothesize the existence of a CB/OW interaction capable of resisting stall.

1.3.5   Numerical characterisation of the BWB

Analysis of the BWB aerodynamic behaviour has primarily been done through numerical methods. Initial simulations concern Euler and RANS models on Finite Volume Methods (FV) (Liebeck, 2004; N. Qin et al., 2004). Simpler Vortex-Lattice Methods have been used in the

initial conceptual design phases (Diedrich et al., 2006), as well as in MDO analysis (van Dommelen & Vos, 2014), while surrogate models have been progressively developed by independent researchers (Wan & Chen, 2014).

A dedicated analysis on numerical capabilities needed for a classic FV RANS approach on baseline BWBs was proposed by Blessing et al. (2009). This study analyses two BWB geometries at an angle of attack $\alpha = 0°$ at both cruise and low-speed conditions. The research proposes the adoption of a CFD RANS methodology coupled with the Spalart-Allmaras (SA) turbulence model to predict aerodynamic behaviour of the BWB geometries. Results show that mesh independence for this case was found for 20+ million nodes.

Flight conditions across studies concern mainly cruise phases, with limited studies on gust (Cai, Wu, & Liang, 2014), and low-speed phases (Blessing et al., 2009; Paulus et al., 2013) prior to this project. Increased interest on low-speed has appeared in recent years (Panagiotou, Fotiadis-Karras, & Yakinthos, 2018; Park et al., 2017) concerning UAV aircrafts.

1.4   Low-speed aerodynamics

In the context of a flight mission, an aircraft has to takeoff, climb, cruise, do specific maneuvers, descent and land (Anderson, 1999). Most of these flight phases occur around cruise speed which is usually around Mach 0.85 (roughly $900 km/h$ at 12 500 m of altitude). Naturally, most prior aerodynamic works on the BWB configuration were developed under cruise conditions. From Liebeck's initial BWB proposition (Liebeck, 2004) to Reist's regional BWB optimisation method (Reist & Zingg, 2015), the majority of the BWB research consider cruise conditions. Takeoff and landing however happen at comparatively low speeds, usually below Mach 0.2, hence the "low-speed" classification. While characterized by a short length with respect to the total flight time, these low-speed regimes are crucial for the safe completion of the flight mission. This section presents low-speed works relevant to this project both for the BWB and TAW geometries.

1.4.1   Stall and low-speed introduction

The low speed regime is particularly constrained by the maximum lift provided by the aircraft at these speeds. Consider the classic equation of the total lift force L with respect to the air density ρ_∞, the aircraft speed V_∞^2, the reference surface S_{ref} and the global lift coefficient C_L (1.1). This clearly states that the lift force decreases with the square of the flight speed. In order to ensure safe completion of the mission at these low speeds, it is usually necessary to compensate the loss of lift force due to a decreasing speed by increasing the lift coefficient until the maximum lift coefficient C_{Lmax} is attained.

$$L = \frac{1}{2}\rho_\infty V_\infty^2 S_{ref} C_L \qquad (1.1)$$

As a result, the low-speed regime is controlled by the aerodynamic conditions linked to C_{Lmax}. Figure 1-5 presents a classical $C_L - \alpha$ curve where α represents the angle of attack. This curve is characterized by a linear zone at low angles of attack and a non-linear "stall zone", characterized by the maximum lift coefficient C_{Lmax} attained at a stall angle of attack α_{stall}. After this point is reached, any further increase in α results only in a loss of lift coefficient. This is known as stall. Stall can be progressive as depicted in Figure 1-5 or semi-instantaneous. Stall can be defined for both 2D geometries like airfoils and 3D geometries like wings and aircrafts. In the present work, global stall alludes to the point of maximum global lift coefficient C_{Lmax} of a 3D body while local stall is associated to the point of maximum local lift coefficient C_{lmax} of a section airfoil of that body.
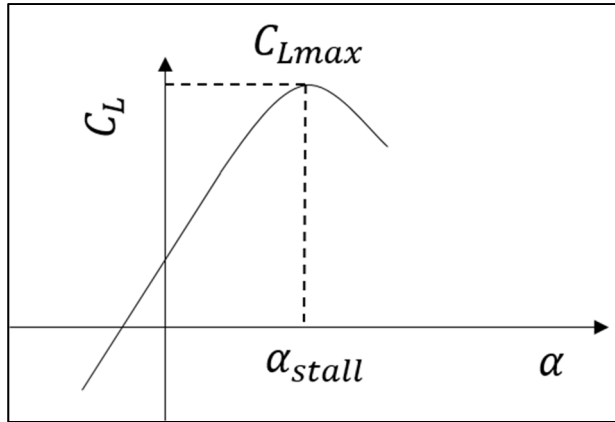
Figure 1-5:   Classic $C_L - \alpha$ curve

Note that, in the literature, low-speed is usually synonym of high-lift. However, the term "high-lift" is usually reserved to the specific analysis of geometries with high-lift devices like flaps and slats whereas low-speed is a broader term for take-off and landing conditions as a whole.

Accurate prediction of aerodynamic coefficients at the conceptual design stage is necessary in order to give a proper sizing of the final geometry. In particular, the estimation of C_{Lmax} is used to define whether or not high lift devices are required and, given the case, its nature, configuration and dimensions. For this reason, multiple models and methods on the estimation of C_{Lmax} exist in the literature. Some of the most relevant ones are presented in the following sub-sections.

1.4.2   RANS methods for low speed prediction

One of the most widely used method for aerodynamic flow prediction consist on the application of the Reynolds-Averaged Navier-Stokes (RANS) equations on a discretized grid with finite volume schemes. Presenting good accuracy in the linear lift zone, its accuracy in the stall zone is still source of debate. That being said, different authors have successfully used RANS approaches coupled with turbulent models to estimate maximum lift coefficients (C_{Lmax}) for simple geometries. Particularly, Philips et al. (Alley et al., 2007) used a RANS approach with the Spalart-Allmaras (SA) turbulence model to estimate maximum lift coefficients for

trapezoidal wings, while Grosvenor (Grosvenor, 2007) uses a similar approach for near-stall prediction of rotor blades. Both studies show acceptable accuracy: within 1° for the stall angle of attack and with no perceivable error for the value of maximum lift coefficient C_{Lmax}. Furthermore, Geissler and Haselmeyer (2006) also use a RANS-SA approach in their study of dynamic stall onset on infinite wings with "good agreement" between measured and calculated pressure distributions.

RANS methods applied to low-speed aerodynamics have seen increased interest from the TAW community, particularly in the context of AIAA's High-Lift Prediction Workshops (Rumsey & Slotnick, 2014; Rumsey, Slotnick, Long, Stuever, & Wayman, 2011; Rumsey, Slotnick, & Sclafani, 2018). These workshops aim to assess the current capacity of available numerical methods - like RANS - to accurately predict high-lift behaviour. They are based on a common TAW geometry containing integrated high-lift devices. Results show different levels of accuracy depending on the implementation of the RANS method (Rumsey et al., 2018).

The common geometry used in these workshops is known as the Common Research Model (CRM) and was specifically designed by NASA (Vassberg et al., 2008) to provide a common geometric reference for both High-Lift Prediction Workshops and Drag Prediction Workshops.(Levy et al., 2014; Vassberg et al., 2010). This geometry, representing a TAW, is available in multiple configurations with and without tails/nacelles/high lift devices and multiple wind tunnel tests are available to the public. In particular, the wing-body geometry used in DPW5 (Levy et al., 2014) is representative of a TAW without tail or high lift devices (Figure 1-6).
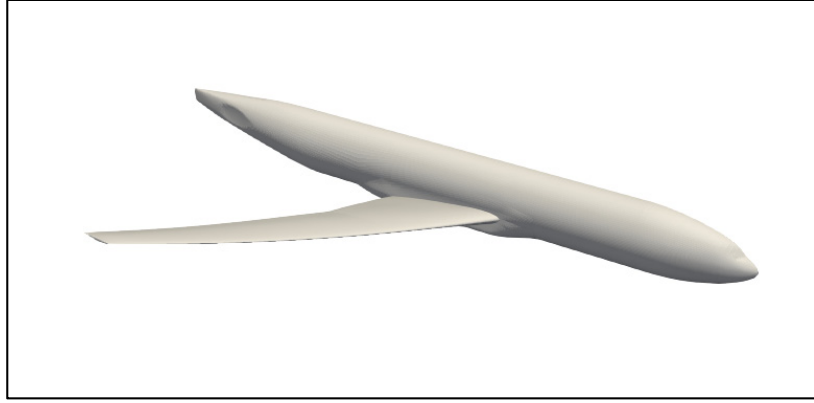
Figure 1-6:   CRM WB geometry

In particular, the SU2 implementation of the RANS method with a Spalart-Allmaras turbulence model (Palacios et al., 2013) has been successfully used recently to predict C_{lmax} on the 2D NACA 0012 airfoil (Tagawa, Morency, & Beaugendre, 2018). According to the paper, the results are less than 1% afar from other numerical codes (CFL3, OVERFLOW). The experimental data on the NACA 0012 geometry is proposed by Abbott and Von Doenhoff (1959) and Ladson, Hill, and Johnson Jr (1987).

Finally, concerning the BWB, Paulus et al. (2013) presented a study on high-lift and control surface optimization of the ACFA2020 BWB. This work is based on the design of high-lift devices for the BWB. After a 2D analysis on the positioning of high-lift devices with respect to the wing, a 3D CFD RANS approach is used to calculate the different 3D lift contributions for each separate component (clean BWB, slats, flaps). Each contribution is then added up to estimate the flow behaviour around the aircraft during approach. The difficulty experienced in incorporating high-lift devices into a unique 3D mesh of the aircraft and carrying a single RANS simulation (instead of adding separated calculations) limited the accuracy of the results, but it still yielded design tendencies as to how to choose the geometric positioning of the multiple elements in the high lift device system for the BWB. Note that, according to Hileman, Reynolds, et al. (2007) and Torenbeek (2013a), complex high-lift devices might not even be needed on the BWB.

1.4.3   Low-fidelity models and methods for low speed prediction

Use of high-fidelity models like RANS has been proven to be time and resource intensive with solving times ranging between a few days and a few weeks in the case of an aircraft. On top of this, resources required far surpass the capabilities of single workstations (Jameson & Fatica, 2006; Witherden & Jameson, 2017). For this reason, low fidelity models are better suited for initial design explorations. Low-fidelity models and methods are characterized by relatively cheap computational resources requiring no specific hardware to be applied, with relatively fast implementation and solving times and with accuracies ranging, on average, between 5% and 20%.

With respect to swept wings within the linear lift zone, initial works by Cheng, Chow, and Melnik (1981) and Guermond (1990) propose the extension of the LLT by applying a Matched Asymptotic Expansion method on the potential flow partial differential equations on the lifting surface and on its wake. Their works yield interesting results acceptable for high aspect ratio wings. It is worth noting the presence of the cosine of the sweep angle as a factor in the final solution with respect to an unswept wing. A more modern approach was recently proposed by Reid and Hunsaker , where the whole LLT was reestablished from zero by generating a concave lifting curve consisting of a locus of representative aerodynamic centers and the concept of jointed trailing vortexes which are both perpendicular to the lifting curve along a distance δ and parallel to the freestream direction afterwards. Results show better agreement than previous LLT extensions within the linear lift zone.

In the case of C_{Lmax} a few methods for classic wings are available in the literature. The simplest model for C_{Lmax} is proposed as a rule of thumb (Corke, 2003) presented in equation (1.2), where the maximum global lift coefficient of a trapezoidal wing C_{Lmax} is given as a fraction of the wing airfoils' local maximum lift coefficient C_{lmax} and depends on the quarter chord sweep angle $\Lambda_{0.25c}$.

$$C_{Lmax} = 0.9 \cos(\Lambda_{0.25c}) \, C_{lmax} \qquad (1.2)$$

However, this rule of thumb however is too broad to be applied to complex wings. At this point, particular attention is given to the works of Phillips (Alley et al., 2007; Phillips, 2004; Phillips & Alley, 2007; Phillips & Hunsaker, 2019; Phillips, Hunsaker, & Joo, 2019; Phillips & Snyder, 2000) who proposed a direct non-iterative C_{Lmax} prediction model for linearly swept, linearly twisted, trapezoidal wings. This model was validated against high-fidelity predictions with a surprising accuracy of up 1% on C_{Lmax}. Due to its wide applicability for 3D wings, Phillips' work has seen active and successful use in the literature as a key element for preliminary tube and wing (TAW) aircraft design and for developing richer models like the unsteady non-linear LLT model proposed by Sugar-Gabor (2018) and the Hodson et al. LLT model for generalized geometries (Hodson, Hunsaker, & Spall, 2017), which is a direct iterative application of the works of Phillips and Snyder (2000). Hodson et al.'s iterative model is meant for lift and drag prediction on the linear lift zone and does not consider the maximum lift coefficient C_{Lmax} at stall. Furthermore, it must be noted the existence of an iterative LLT C_{Lmax} prediction model developed for elliptic wings (Gallay & Laurendeau, 2015) based on the α-methods for viscous coupling.

On the method side for 2D airfoils, Drela's XFOIL panel method (Drela, 1989) has seen wide application in the research community. Drela's work couples a panel method with boundary layer equations in order to estimate the full aerodynamic spectrum of the airfoil consisting of aerodynamic coefficients evolution, maximum lift coefficient, L/D and pressure distributions. This method has been known to achieve, in some cases, even better results than high-fidelity RANS models for single element geometries (Morgado, Vizinho, Silvestre, & Páscoa, 2016). Due to its versatility, XFOIL has been adapted into XFLR: a widely spread pseudo 3D panel method proposed by (Deperrois, 2009a).

On the 3D wing side, Laurendeau has worked on multiple low-fidelity C_{Lmax} prediction methods. Gallay and Laurendeau (2015) proposed an LLT-based iterative method for estimating pre and post stall flows on generalized elliptic wings. On the same line of thought, Parenteau, Sermeus, and Laurendeau (2018) propose a viscous database-coupled VLM

approach for maximum lift estimation of a trapezoidal wing. These methods are iterative and haven't been validated for BWB-like geometries.

Most of these models work either on classic trapezoidal wings or on elliptic wings. However these geometries don't quite represent a BWB. Figure 1-7 presents a conventional BWB planform with radically different airfoils between the CB and the OW and different sweep and twist distributions for the CB and the OW. We consider these two airfoils as radically different since their camber distribution is different one being single cambered and the other being double cambered. This results in an aircraft where the airframe geometry must be defined locally and cannot simply be expressed with general global parameters like would be the case for a trapezoidal wing. Lyu and Martins (2013) propose the use of at least 4 different parameters at each wingspan section y to define the BWB airframe shape: local twist (ϕ), local sweep (Λ), local section airfoil and local section chord (c). This kind of multiple local parameter variation is referred to as a compound wing due to its closeness to the original compound wing concept (Jamei et al., 2016). Note that a multi-section wing presents non-smooth variations on top of being a compound wing. There is one previous implementation of Phillips and Snyder (2000) original model applied to compound-wings proposed by Hodson et al. (2017). This implementation is based upon numerical iterations of the Phillips and Snyder model. It is meant for lift and drag prediction on the linear lift zone and does not consider the maximum lift coefficient C_{Lmax} at stall.
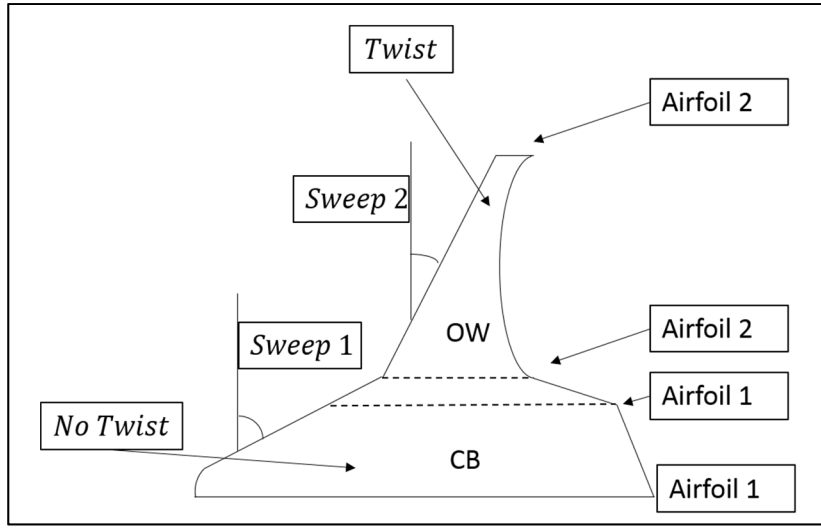
Figure 1-7:   BWB simplified planform with local parameters

1.5   Synthesis of the literature review and presentation of the research problem

The analysis of prior work on the BWB shows the importance of the regional BWB as a frontrunner for next-generation aircraft configurations. While there is a limited amount of experimental data, the development of Computational Fluid Dynamics (CFD) and High-Performance Computing (HPC) have opened the road to more extensive studies ranging from complex surfaces implementation (Carter, Campbell, Pendergraft Jr, Friedman, & Serrano, 2006) to surface optimization (Reist & Zingg, 2016). Yet, while sufficient work has been done on the aerodynamics at cruise conditions, we will see that there are significantly less works and still pending questions concerning low speed aerodynamics for the BWB.

On that regard, early works on the low speed aerodynamics of the BWB follow different assumptions: some assume that high-lift devices are required for complementary lift generation (Paulus et al., 2013) and some consider that complementary lift generation is not required (Hileman, Reynolds, et al., 2007). To further this issue, available wind tunnel data on other BWB geometries show that there might be a CB/OW interaction at low speeds that has a high impact on the trigger of stall for the BWB. The following hypothesis is made: the CB and OW aerodynamic characteristics could be combined to delay stall and generate higher natural lift.

If validated, this CB/OW interaction could be used in substitution of complex high-lift devices to sustain lift at low speeds.

The question on whether or not a BWB is capable of generating sustained lift at low speeds without high lift devices is raised. If so, in the context of current market forecasts, the regional BWB would become more attractive than the TAW, since it would not need to implement complex high-lift systems into the design, all the while reducing fuel consumption and noise pollution.

1.6   Thesis objective and research plan

Taking into account the aforementioned literature review, the upcoming research tendencies on the BWB and the knowledge gaps previously exposed, the scientific objective of this thesis is to develop BWB-specific design tools, based on the hypothesis of a stall-delaying CB/OW interaction, that could be used to better predict and design natural lift at low speeds for this aircraft configuration. We remind here that the term interaction refers to an hypothesized predictable coupling between the CB and the OW aerodynamic behaviour at low speed.

This objective is carried out through three sub-objectives:

1. To propose a conceptual design of the regional BWB and verify the applicability of the RANS method close to stall.
2. To simulate the CRM and the regional BWB configuration at low speeds through the use of the verified RANS method and to compare the lift and drag coefficients evolution leading to stall for each case so as to extract differences between both configurations near stall, focusing on eventual fuselage/wing and CB/OW interactions.
3. To verify the existence of the CB/OW interaction at low speeds through twist parametrization using RANS and to use these results to propose design guidelines and calibrate a general C_{Lmax} prediction model for BWB geometries.

Each one of these sub-objectives is the main focus of chapters 3, 4 and 5 respectively. Chapter 3 presents the flight mission and critical parameters characterizing the regional BWB, as well as the CFD numerical domain, mesh and verification of the RANS model. Chapter 4 focuses on the local and global aerodynamic coefficients differences between CRM and BWB at different angles of attack leading to stall. Finally, Chapter 5 focuses on the CB/OW interaction via the analysis of twist angle on the lift coefficient of the aircraft, in particular C_{Lmax}. This chapter provides a general model for predicting C_{Lmax} on BWB-like geometries.

<div align="center">

CHAPTER 2

MATHEMATICAL AND NUMERICAL MODELS

</div>

2.1   Introduction

The previous chapter introduced the objective of this thesis. The objective of this chapter is to introduce the aerodynamic variables, the physical models and the numerical methods used to attain the research objective. First, a quick reminder of the aerodynamic variables associated with flight mechanics is proposed. This is followed by the governing equations of fluid flows and the introduction of the RANS-SA model. Following this, the finite volume method employed is introduced. The chapter finishes with the mathematical development of the compound-wing low fidelity model for C_{Lmax} prediction used later on chapter 5. This model constitutes one of the original contributions of this thesis.

2.2   Flight Mechanics

This section formally introduces the multiple aerodynamic coefficients used across this thesis. It presents both the aerodynamic forces and its non-dimensional counterparts used for experimental and numerical analysis. For further details, the reader may refer to the works of (Anderson, 1999, 2001, 2005) from which this sub-section is inspired.

2.2.1   The aerodynamic force

Figure 2-1 presents a scheme of the microscopic forces applied by the fluid in motion on the airframe of an aircraft. These microscopic forces are represented by the pressure p and the skin shear stress τ_w. The pressure represents the local stress perpendicular to the wall while the shear stress represents the local stress tangent to the wall. The total aerodynamic force $\vec{R}$ is the macroscopic representation of both p and τ_w on the surface of the aircraft. This relation is defined in equation (2.1).
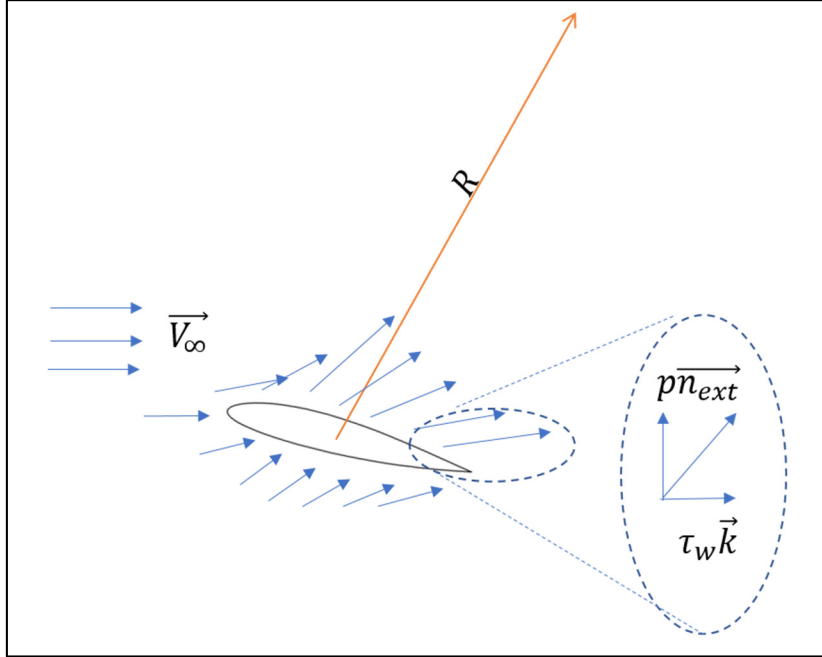
Figure 2-1:   Aerodynamic force and local constraints.

$$\vec{R} = \iint_{Airframe} -p\overrightarrow{n_{ext}}dS + \iint_{Airframe} \tau_w\vec{k}dS \qquad (2.1)$$

For comparison purposes, these variables are usually replaced by their non-dimensional counterparts. Let p_∞ be the freestream pressure, ρ_∞ the freestream density, V_∞ the freestream velocity and S_{ref} a given reference surface. The pressure coefficient c_p represents the local pressure difference with the freestream conditions normalized by the dynamic pressure q_∞ while the skin friction coefficient c_f represents the skin shear stress normalized by the dynamic pressure q_∞:

$$q_\infty = \frac{1}{2}\rho_\infty V_\infty^2 \qquad (2.2)$$

$$c_p = \frac{p - p_\infty}{q_\infty} \qquad (2.3)$$

$$c_f = \frac{\tau_w}{q_\infty} \tag{2.4}$$

These coefficients are commonly used in aircraft analysis to study the local flow of a given airfoil or surface. Note that for some 3D applications, some CFD solvers like SU2 (Palacios et al., 2013) use a vector form of the skin friction coefficient in the canonical base of the $\mathbb{R}^3$ space, thus giving not only value but also direction to the skin friction. This will be useful in chapter 4's qualitative analysis of the aircraft geometries.

$$\vec{c_f} = \frac{1}{q_\infty}\left(\tau_{wx}\vec{\imath} + \tau_{wy}\vec{\jmath} + \tau_{wz}\vec{k}\right) = \overrightarrow{c_{fx}} + \overrightarrow{c_{fy}} + \overrightarrow{c_{fz}} \tag{2.5}$$

2.2.2   Lift, drag and moment coefficients

While the pressure and skin friction coefficients (c_p, c_f) are used to analyze the local behaviour on any given point of the airframe, the analysis of the global behaviour of the aircraft is done through the lift $(\vec{L})$, drag $(\vec{D})$ and lateral $(\vec{Q})$ forces. These forces are simply another representation of the aerodynamic force $\vec{R}$ in the base $(\vec{\imath}, \vec{\jmath}, \vec{k})$.

$$\vec{R} = \vec{L} + \vec{D} + \vec{Q} = D\vec{\imath} + Q\vec{\jmath} + L\vec{k} \tag{2.6}$$

In this new base decomposition, $\vec{\imath}$ is the unit vector parallel to the freestream velocity vector $\overrightarrow{V_\infty}$, $\vec{\jmath}$ is the canonical unit vector in the wingspan direction of the aircraft, and $\vec{k}$ is the orthogonal complement of $(\vec{\imath}, \vec{\jmath})$ in $\mathbb{R}^3$. Due to the existence of a plane symmetry in the models and inputs of this research, the global lateral force Q is assumed non-existent throughout the rest of this paper. For simplicity, in these expressions, the force vectors are swapped for its magnitudes: $L = \|\vec{L}\|, D = \|\vec{D}\|$ and $Q = \|\vec{Q}\|$.

Thus, for practical purposes, the aerodynamic force is divided in lift L and drag D, where L is responsible for pulling the aircraft above the freestream horizon while D is responsible for

resisting the movement of the aircraft trough the airflow along the freestream direction. Figure 2-2 shows a simple representation of these forces at a given angle of attack α.
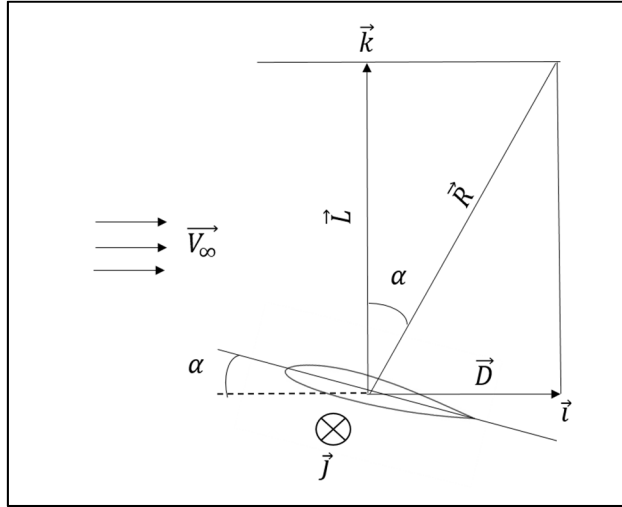
Figure 2-2:   Lift and drag forces on an object.

Similarly to c_p and c_f, the non-dimensional aerodynamic coefficients (C_L, C_D) are preferred to their dimensional counterparts. Let S_{ref} denote a reference surface, then:

$$C_L = \frac{L}{q_\infty S_{ref}}; \ C_D = \frac{D}{q_\infty S_{ref}} \tag{2.7}$$

Note that these coefficients have a 2-dimmensional variant (C_l, C_d) in such a way that (C_L, C_D) represent their weighted integral along the wingspan b. Let (l, d) be the local lift and drag forces "per unit length" and let c be the local chord. Then (C_l, C_d) represent the planar non-dimensional lift and drag forces for $y \in \left[-\frac{b}{2}; \frac{b}{2}\right]$:

$$C_l = \frac{l}{q_\infty c}; \ C_d = \frac{d}{q_\infty c} \tag{2.8}$$

$$C_L = \frac{1}{S_{ref}} \int_{-\frac{b}{2}}^{\frac{b}{2}} C_l(y) \, c(y) \, dy; \quad C_D = \frac{1}{S_{ref}} \int_{-\frac{b}{2}}^{\frac{b}{2}} C_d(y) \, c(y) \, dy \tag{2.9}$$

2.3   Governing equations

This section presents the conservation equations used to model the airflow around the aircraft. These equations contain a continuity equation (2.11), a momentum equation (2.12) also known as the Navier-Stokes equations and an energy equation (2.13). A few hypotheses are required before introducing these equations. This section is inspired on the works by Currie (2002), Ferziger and Peric (2012) and Palacios et al. (2014).

The first hypothesis concerns the flow compressibility. The non-dimensional velocity of an airflow can be represented by its Mach number M defined as the ratio between the flow velocity and the speed of sound a_{sound}

$$M = \frac{V}{a_{sound}} \tag{2.10}$$

If $M < 0.3$, the flow can be considered as incompressible, and compressible otherwise. The freestream Mach number for our low speed is calculated as $M_\infty \approx 0.2$. This value remains under the incompressibility limit of 0.3. However, the actual local Mach number at a local point on the upper surface is unknown. The hypothesis is made to consider the airflow as compressible. Posteriori analysis shows local Mach numbers as high as 0.6, thus validating this choice.

The second consideration concerns the source terms. Source terms are not accounted for in any equation: there are no heat sources considered and body forces are assumed negligible with respect to inertial forces in this framework

The instantaneous conservative equations for homogeneous, compressible flow without heat sources are presented in equations (2.11) to (2.13):

$$\frac{\partial \rho}{\partial t} + div(\rho \boldsymbol{v}) = 0 \tag{2.11}$$

$$\frac{\partial}{\partial t}(\rho \boldsymbol{v}) + \boldsymbol{div}(\rho \boldsymbol{v} \otimes \boldsymbol{v} + p\underline{\boldsymbol{I}}) - \boldsymbol{div}(\underline{\boldsymbol{\tau}}) = \boldsymbol{0} \tag{2.12}$$

$$\frac{\partial}{\partial t}\left[\rho\left(e + \frac{1}{2}\boldsymbol{v}.\boldsymbol{v}\right)\right] + div\left(\rho \boldsymbol{v}\left(e + \frac{1}{2}\boldsymbol{v}.\boldsymbol{v} + \frac{p}{\rho}\right)\right) - div(\underline{\boldsymbol{\tau}}.\boldsymbol{v} - \boldsymbol{q}) = 0 \tag{2.13}$$

where ρ is the air density, $\boldsymbol{v}$ is the velocity vector, p is the pressure, $\underline{\boldsymbol{I}}$ is the 4th order identity tensor, $\underline{\boldsymbol{\tau}}$ is the shear stress tensor, e is the specific internal energy, $e_k = \frac{1}{2}\boldsymbol{v}.\boldsymbol{v}$ is the specific kinetic energy, and $\boldsymbol{q}$ is the heat flux vector. Furthermore, under the assumption of an ideal gas, p and e can be estimated as follows:

$$p = \rho R T \tag{2.14}$$

$$e = c_v T = \frac{R}{\gamma - 1}T \tag{2.15}$$

where $R = 287.058 \, J/K. kg$ is the specific gas constant of the air, $\gamma = 1.4$ is the heat capacity ratio and T is the temperature. The shear stress tensor for a Newtonian fluid is then given as

$$\underline{\boldsymbol{\tau}} = \mu\left(\boldsymbol{grad}(\boldsymbol{v}) + \boldsymbol{grad}(\boldsymbol{v})^T - \frac{2}{3}div(\boldsymbol{v})\underline{\boldsymbol{I}}\right) \tag{2.16}$$

where μ represents the dynamic viscosity. Finally, the heat flux is modelled following Fourrier's heat law by using the air's thermal conductivity λ:

$$\boldsymbol{q} = -\lambda \, \boldsymbol{grad}(T) \tag{2.17}$$

The terms μ and λ represent actual physical properties of the air. They are modeled, in this case, by the Sutherland law:

$$\mu_{dyn} = \mu_0 \left(\frac{T}{T_0}\right)^{3/2} \frac{T_0 + S}{T + S} \tag{2.18}$$

$$\lambda_{dyn} = \frac{\mu_{dyn} c_p}{Pr_{dyn}} \tag{2.19}$$

where μ_{dyn} is the dynamic viscosity, $\mu_0 = 1.716 \times 10^{-5} \ kg/m.s$, $T_0 = 273.15 \ K$ and $S = 110.4 \ K$ are reference constants, $c_p = \frac{\gamma R}{\gamma - 1}$ is the specific heat capacity at constant pressure and $Pr_{dyn} = 0.72$ is the Prandtl number associated to the dynamic viscosity.

At this point, the problem proposed by the governing equations is mathematically closed. However, further simplifications are needed in order to numerically solve these equations. Note the introduction of index "dyn" in equations (2.18) and (2.19). The simplification of the governing equations will introduce new terms which are usually represented by the turbulent viscosity μ_{tur}, and the turbulent energy k. The particular representations of these terms specific to the Reynolds-Averaged Navier-Stokes equations are introduced in the next section.

2.4   CFD RANS numerical approach

Section 2.3 presented the general equations characterizing the airflow around the aircraft. However, solving these equations directly through current numerical methods requires numerical resources beyond those available to the author. Indeed, according to Jameson and Fatica (2006), the amount of calculation points necessary to properly solve all the turbulent scales in 3 dimensions is proportional to $Re^{9/4}$, where Re is the Reynolds number. For an average aircraft this represents about 10 quadrillions (10^{16}) (Jameson & Fatica, 2006). For this project, which is focused around aeronautical design, dedicated characterisation of the turbulence is not needed past an acceptable representation of the global behaviour of the aircraft. Within this framework, the literature review shows that Reynolds-Averaged Navier-

Stokes (RANS) approaches coupled with turbulence models are widely used in the context of aircraft design. In particular, the literature review shows that RANS methods near stall conditions have been successfully used to predict boundary layer development and separation in previous works (Geissler & Haselmeyer, 2006; Grosvenor, 2007). Their computer cost, their maturity and their previous relative success would explain the frequent application of RANS approaches in current state-of-the-art research on high-lift workshops for complex geometries (Rumsey et al., 2018). Accounting for the aeronautical design approach, the amount of specific calculations to be done, the available resources and the available numerical tools, as well as the level of fidelity needed for design purposes, a *RANS* approach was considered necessary and sufficient to attain the objectives of this thesis. In particular, the RANS model developed in SU2 v5.0.0 (Palacios et al., 2013) was used during this thesis. A description of this *RANS* approach along with the Finite Volume Method is presented in APPENDIX I and APPENDIX II. These sections are based on the works of (Blazek, 2015), (Ferziger & Peric, 2012), Pope (2000) and Palacios et al. (2013).

2.5 Compound wing LLT model

The last two sections introduced the numerical methods proposed for a high-fidelity simulation of the airflow field around the BWB. In this section however, a lifting line theory (LLT) method for predicting the maximum lift coefficient C_{Lmax} for compound wings is proposed. This model is justified and calibrated at Chapter 5. Furthermore, it constitutes a contribution to the research community in the context of maximum lift prediction. This model is based on previous works by Phillips and Alley (2007).

2.5.1 Context

Prandtl's lifting line theory has become a classic prediction tool for early design phases in aircraft design. While powerful, this theory is based on potential flow and is usually limited to non-viscous phenomena and straight wing geometries. Nevertheless, based on this theory,

Phillips and Alley managed to create a model to estimate C_{Lmax} for linearly swept, linearly twisted wings with an estimated error of $\pm 1\%$ (Phillips & Alley, 2007).

Consider the fundamental equation of the lifting line theory as proposed by Phillips and Alley (2007) and used in most LLT models.

$$\alpha_{3D} - \phi(y) - \alpha_{L0}(y) = \frac{2\Gamma(y)}{a_0(y)V_\infty c(y)} + \frac{1}{4\pi V_\infty} \int_{-\frac{b}{2}}^{\frac{b}{2}} \frac{\left(\frac{d\Gamma}{dy}\right) d\psi}{y - \psi} \qquad (2.20)$$

Based on Prandtl's lifting line theory, equation (2.20) considers the circulation $\Gamma(y)$ about any section of the wing where y is the wingspan coordinate measured from the centerline, the global angle of attack α_{3D}, the effective angle of attack $\alpha_{eff}(y)$, the local geometric twist at each section $\phi(y)$ – ϕ is considered positive when it decreases the local angle of attack and negative otherwise -, the local zero-lift angle of attack $\alpha_{L0}(y)$ of the local airfoil, the local lift slope $a_0(y) = \frac{dC_l}{d\alpha}$, and the local chord $c(y)$, the freestream speed V_∞ and the half wingspan $(b/2)$. The reader may find the majority of these parameters presented in Figure 2-3. This figure is divided into a top view of the trapezoidal wing (a), a cut from the local section y presenting the local section airfoil and the local twist (b), and the lift curve of the local airfoil presenting the zero-lift angle of attack α_{L0} for the local section and the local lift slope a_0 (c). Consider that the airfoil-specific data like α_{L0} and a_0 must be extracted from a viscous database.
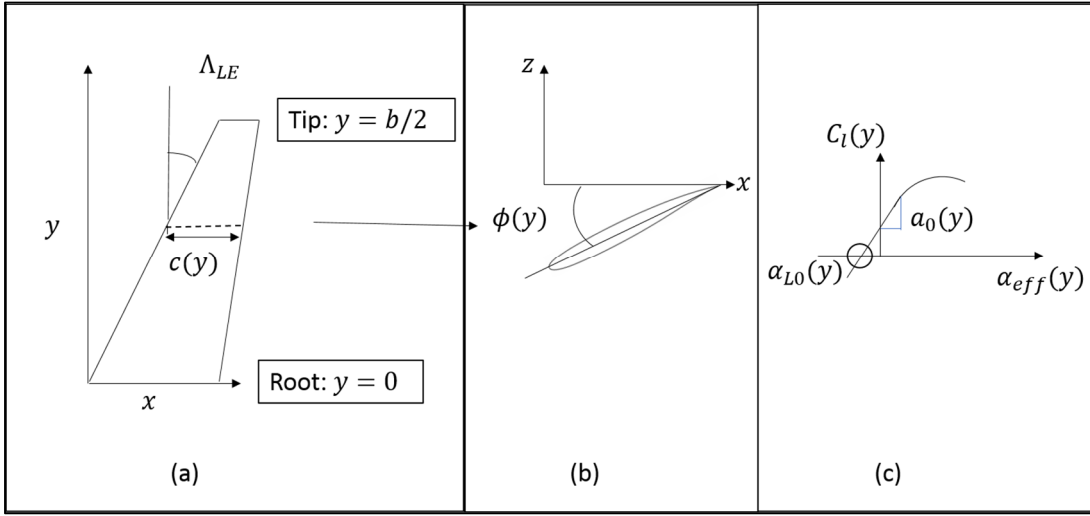
Figure 2-3:   Scheme of local parameters. Trapezoidal wing with local sweep and local chord (a). Section cut presenting local airfoil and local twist (b). Local lift curve of the local airfoil (c)

In order to solve equation (2.20), Phillips and Alley (2007) propose to separate the left-hand side of the equation into two: a twist dependent term and a twist independent term. To do so, they introduce the concept of total twist Ω in equation (2.21) and the normalized twist distribution $\omega(y)$ in equation (2.22). Ω is simply the difference between the left-hand side evaluated at the root and the left-hand side evaluated at a reference section like the tip.

$$\Omega = (\alpha_{3D} - \phi - \alpha_{L0})_{root} - (\alpha_{3D} - \phi - \alpha_{L0})_{ref} \qquad (2.21)$$

$$\omega(y) = \frac{(\alpha_{3D} - \phi - \alpha_{L0})_{root} - (\alpha_{3D} - \phi - \alpha_{L0})_{(y)}}{\Omega} \qquad (2.22)$$

With this in mind, the left-hand side of equation (2.20) can be rewritten as:

$$\alpha_{3D} - \phi(y) - \alpha_{L0}(y) = (\alpha_{3D} - \phi - \alpha_{L0})_{root} - \Omega\omega(y) \qquad (2.23)$$

Now, the term $(\alpha_{3D} - \phi - \alpha_{L0})_{root}$ is independent of the wingspan coordinate while the second term $\Omega\omega(y)$ is dependent on the total twist and the wingspan coordinate. The linearity

of equation (2.20) allows for its decomposition in a system of 2 equations (2.24) and (2.25), where the total circulation is given as $\Gamma = \Gamma_1 + \Gamma_2$.

$$\frac{2\Gamma_1(y)}{a_0(y)V_\infty c(y)} + \frac{1}{4\pi V_\infty}\int_{-\frac{b}{2}}^{\frac{b}{2}} \frac{\left(\frac{d\Gamma_1}{dy}\right)d\psi}{y - \psi} = (\alpha_{3D} - \phi - \alpha_{L0})_{root} \tag{2.24}$$

$$\frac{2\Gamma_2(y)}{a_0(y)V_\infty c(y)} + \frac{1}{4\pi V_\infty}\int_{-\frac{b}{2}}^{\frac{b}{2}} \frac{\left(\frac{d\Gamma_2}{dy}\right)d\psi}{y - \psi} = -\Omega\omega(y) \tag{2.25}$$

At this point, a Fourier decomposition is introduced where the change of variable $y = \frac{b}{2}\cos(\theta)$ has been applied.

$$\Gamma(\theta) = 2bV_\infty \sum_{n=1}^{\infty} A_n \sin(n\theta) \tag{2.26}$$

For ease of notation, y and θ are interchanged in the equations (ie. $\Gamma(y) \equiv \Gamma(\theta)$), even though, strictly speaking, there is a variable change in place (ie. $\Gamma(y) = \Gamma\left(\frac{b}{2}\cos(\theta)\right)$). By separating Γ into 2 terms, the $(A_n)_{n\in\mathbb{N}}$ sequence is rewritten as

$$A_n = a_n(\alpha_{3D} - \phi - \alpha_{L0})_{root} - \Omega b_n \tag{2.27}$$

Phillips and Alley show that the new sequences $(a_n)_{n\in\mathbb{N}}$ and $(b_n)_{n\in\mathbb{N}}$ are defined by equations (2.28) and (2.29).

$$\sum_{n=1}^{\infty}\left(a_n\left(\frac{4b}{a_0 c(\theta)} + \frac{n}{\sin(\theta)}\right)\sin(n\theta)\right) = 1 \tag{2.28}$$

$$\sum_{n=1}^{\infty}\left(a_n\left(\frac{4b}{a_0 c(\theta)} + \frac{n}{\sin(\theta)}\right)\sin(n\theta)\right) = 1 \tag{2.29}$$

Equations (2.28) and (2.29) are solved by defining N different reference sections $(\theta_i)_{i \in [1,N]}$ and inversing the resulting matrix, which is the same for both sequences. Following this, Phillips and Alley use the sequences a_n and b_n to define multiple coefficients which eventually lead to the following expression of the maximum lift coefficient C_{Lmax}

$$C_{Lmax} = \left(\frac{C_L}{C_{lmax}}\right)_{\Omega=0} \kappa_{L\Lambda}\kappa_{Ls}\left(C_{lstall} - \kappa_{L\Omega} \, C_{L,\alpha}\Omega\right) \tag{2.30}$$

In this equation, the parameter $\left(\frac{C_L}{C_{lmax}}\right)_{\Omega=0}$ corresponds to the ratio between the global lift coefficient C_L and the maximum local lift coefficient C_{lmax} when there is no twist. $\kappa_{L\Lambda}$ corresponds to a sweep correction factor used to account for sweep; Phillips and Alley (2007) propose reference data for evaluation of $\kappa_{L\Lambda}$. κ_{Ls} is the stall correction factor introduced by the non-linearities near stall; again, Phillips and Alley (2007) propose reference evaluation methods. C_{lstall} corresponds to the stall lift coefficient of the section with the maximum local lift coefficient. $\kappa_{L\Omega}$ corresponds to a twist correction factor that must be calculated for each geometry. $C_{L,\alpha}$ corresponds to the global lift slope. Parameters $\left(\frac{C_L}{C_{lmax}}\right)_{\Omega=0}$, $C_{L,\alpha}$ and $\kappa_{L\Omega}$ depend on a_n and b_n. While parameters $\kappa_{L\Lambda}$ and κ_{Ls} are evaluated based on Phillips and Alley (2007).

Phillips and Alley's model has been successfully validated against trapezoidal wings (Alley et al., 2007). However, the BWB doesn't comply with the original hypotheses on which this model was built. In particular the non linear variation of local properties for compound wings, like sweep, twist, chord or airfoil shape distributions, is not part of those original hypotheses. In order to adapt this model to compound-wing geometries, a local sweep correction is introduced at the circulation level. The introduction of this correction is aimed to extract a new stall correction factor in the expression of C_{Lmax} that could compensate the local variations of the aircraft geometry. However, in order to do so, all of the terms must be re-evaluated accounting for this local correction. The following subsections present the specific modifications and derivations incurred by the compound wing model. For more details on the

original LLT model or the Phillips LLT model, the reader is referred to (Anderson, 2001) and (Phillips & Alley, 2007) respectively.

2.5.2   Multi-Sweep correction

The idea behind the compound wing model is to introduce a multi-sweep correction factor in the circulation Γ that is local to each section as presented in the following equation:

$$\Gamma(\theta) = 2bV_\infty f(\Lambda) \sum_{n=1}^{\infty} A_n \sin(n\theta) \tag{2.31}$$

In this equation, $f(\Lambda)$ is a sweep correction function dependent on the local LE sweep angle $\Lambda = \Lambda_{\text{LE}} = \Lambda(\theta)$. This function must have the following properties: (1) f is defined in the interval $I = \left[-\frac{\pi}{2}; \frac{\pi}{2}\right]$, (2) $f(0) = 1$, (3) $0 \leq f(\Lambda)_{|\Lambda \in I} \leq 1$, (4) f is of class C^1 in I and (6) f is monotonically decreasing in I. A convenient choice for this correction is $\cos(\Lambda)$, as this particular term defines the effective speed seen by the local airfoil ($V_{eff} = V_\infty \cos(\Lambda)$) and is present multiple times in early works on swept wing extensions of the LLT model (Guermond, 1990).

As a consequence of this correction, the previous sequence A_n defined in equation (2.26) and the new sequence A_n defined in equation (2.31) do not share the same values. At this point the compound wing model revolves around solving the fundamental equation of the LLT (2.20) with this new circulation.

2.5.3   Derivative of the circulation Γ

To solve equation (2.20), it is first necessary to determine the derivative of the corrected Γ function. If we consider an uncorrected circulation $\hat{\Gamma}$

$$\hat{\Gamma}(\theta) = 2bV_\infty \sum_{n=1}^{\infty} A_n \sin(n\theta) \tag{2.32}$$

then the total circulation is given as $\Gamma(\theta) = f(\Lambda)\hat{\Gamma}(\theta)$. Then the first derivative of the circulation is given as

$$\frac{d\Gamma}{dy} = \frac{df(\Lambda)}{d\Lambda}\frac{d\Lambda}{dy}\hat{\Gamma}(\theta) + f(\Lambda)\frac{d\hat{\Gamma}(\theta)}{dy} \tag{2.33}$$

Due to the characteristics of $f(\Lambda)$, we know that $\forall \Lambda \in \mathbb{R}, |f(\Lambda)| < 1$. Since f is monotonically decreasing and bounded, and f is continuous and differentiable, then $\frac{df}{d\Lambda}$ is continuous and bounded. Furthermore, for most aircrafts, the sweep can be considered almost constant along the wingspan, only changing at a discrete finite number of sections:

$$\Lambda = \begin{cases} \Lambda_0 \ for \ 0 < y < y_1 \\ \Lambda_1 \ for \ y_1 < y < y_2 \\ \quad\quad ... \\ \Lambda_N \ for \ y_N < y < y_{N+1} = b/2 \end{cases} \tag{2.34}$$

As such, $\forall y \notin \{y_0, y_1, ..., y_N\}, \frac{d\Lambda}{dy} = 0$.

In the case of a complex distribution, the same approach can be used. The wingspan can be discretized into a very large number of intervals, with Λ changing only between different intervals, but staying constant within the same interval. Do note that while $\frac{d\Lambda}{dy} \equiv 0$ within an interval, Λ itself is not quite constant as it changes between different intervals. For this reason f also changes between different intervals.

We also note that, $\hat{\Gamma}(\theta)$ is also bounded since $\lim_{n\to\infty}|A_n| \to 0$. Thus, we can safely assume that, within each interval, $\left|\frac{df(\Lambda)}{d\Lambda}\frac{d\Lambda}{dy}\hat{\Gamma}(\theta)\right| \ll f(\Lambda)\frac{d\hat{\Gamma}(\theta)}{dy}$. We conclude that $f(\Lambda)$ can be considered constant for the purposes of calculating the derivative of Γ.

$$\frac{d\Gamma}{dy} \approx f(\Lambda)\frac{d\hat{\Gamma}(\theta)}{dy} \tag{2.35}$$

2.5.4   Derivation of the induced angle of attack α_i

With the derivative of Γ known, it is now necessary to evaluate the induced angle of attack α_i after the introduction of the sweep correction factor. An initial expression of α_i is given as

$$\alpha_i(y_0) = \frac{1}{4\pi V_\infty}\int_{-\frac{b}{2}}^{\frac{b}{2}} \frac{\left(\frac{d\Gamma}{dy}\right)dy}{y_0 - y} \tag{2.36}$$

Swapping y for θ and introducing the Fourier decomposition results in the following expression of α_i with respect to $f(\Lambda)$

$$\alpha_i = \frac{1}{\pi}\sum_{n=1}^{N}\left(nA_n\int_{\theta=0}^{\theta=\pi} f(\Lambda(\theta))\frac{\cos(n\theta)\,d\theta}{\cos(\theta)-\cos(\theta_0)}\right) \tag{2.37}$$

It is now necessary to calculate each integral J_n defined as

$$J_n = \int_{\theta=0}^{\theta=\pi} f(\Lambda(\theta))\frac{\cos(n\theta)\,d\theta}{\cos(\theta)-\cos(\theta_0)} \tag{2.38}$$

In order to calculate J_n, the interval $[0,\pi]$ is divided in M sub intervals of same length: $[\theta_j;\theta_{j+1}]$ where $0=\theta_0 < \theta_1 < \cdots < \theta_{M-1} < \theta_M = \pi$ and $\theta_{j+1} = \theta_j + \frac{\pi}{M}$. If Λ is assumed

constant inside each separate sub-interval $[\theta_j; \theta_{j+1}]$, then $\forall \theta \in [\theta_j; \theta_{j+1}], \Lambda(\theta) = \Lambda_j$. As a consequence, the constant local correction factor f_j can be defined as

$$\forall \theta \in [\theta_j; \theta_{j+1}], \qquad f_j = f(\Lambda_j) \tag{2.39}$$

and a new expression of J_n is found where f_j is outside of the integral:

$$J_n = \sum_{j=0}^{M-1} f_j \int_{\theta=\theta_j}^{\theta=\theta_{j+1}} \frac{\cos(n\theta)}{\cos(\theta) - \cos(\theta_0)} d\theta \tag{2.40}$$

Now, we introduce the integral K_n and the weight factor q_{nj} as follows:

$$K_n = \int_{\theta=0}^{\theta=\pi} \frac{\cos(n\theta)\, d\theta}{\cos(\theta) - \cos(\theta_0)} = \frac{\pi \sin(n\theta_0)}{\sin(\theta_0)} \tag{2.41}$$

$$q_{nj} = \frac{1}{K_n} \int_{\theta=\theta_j}^{\theta=\theta_{j+1}} \frac{\cos(n\theta)}{\cos(\theta) - \cos(\theta_0)} d\theta \tag{2.42}$$

Then, the J_n sequence becomes

$$J_n = K_n \delta_n^{\alpha_i} \tag{2.43}$$

Where $\delta_n^{\alpha_i}$ is the n-th correction factor for the induced angle of attack

$$\delta_n^{\alpha_i} = \sum_{j=0}^{M-1} f_j q_{nj} \tag{2.44}$$

Finally, the induced angle is given by the following expression:

$$\alpha_i(\theta_0) = \frac{1}{\pi} \sum_{n=1}^{N} n A_n \delta_n^{\alpha_i} \frac{\sin(n\theta_0)}{\sin(\theta_0)} \tag{2.45}$$

Particular attention must be brought to the q_{nj} terms. The analytical calculation of the integral in the numerator of q_{nj} is not straightforward. For simplicity, this expression is evaluated by using numerical integration. In this case a midpoint integration is applied:

$$q_{nj}^{num} = \frac{1}{K_n} \left(\frac{\cos(n\theta_{j+1/2})}{\cos(\theta_{j+1/2}) - \cos(\theta_0)} \right) \left(\frac{2\pi}{M} \right) \tag{2.46}$$

At this point, a numerical correction must be added so that we respect the theoretical value $\sum_{j=0}^{M-1} q_{nj} = 1$. To do so, the local segment $[\theta_{j0}, \theta_{j0+1}]$, containing the singularity $\theta = \theta_0$, is found and substituted by a new term $q_{nj0}^{num,new}$:

$$q_{nj0}^{num,new} = q_{nj0}^{num} - \left(\left(\sum_{j=0}^{M-1} q_{nj}^{num} \right) - 1 \right) \tag{2.47}$$

Thus resulting in the effective expression:

$$\sum_{j=0}^{M-1} q_{nj}^{num} = 1 \tag{2.48}$$

2.5.5 Introducing the total twist Ω

The previous sub-section introduced an expression for the induced angle of attack. Let us now define the absolute local angle $\Delta\alpha$ as the left-hand side of equation (2.20):

$$\Delta\alpha(\alpha_{3D}, y) = \alpha_{3D} - \phi(y) - \alpha_{L0}(y) \tag{2.49}$$

By construction, $\Delta\alpha$ depends on the global angle of attack α_{3D} and the spanwise location y. Let us now define $\Delta\alpha_{rmax}$ and $\Delta\alpha_{rmin}$ as the maximum and minimum absolute angle for a given α_{3D}.

$$\Delta\alpha_{rmax}(\alpha_{3D}) = max(\Delta\alpha(\alpha_{3D}, y)) \qquad (2.50)$$

$$\Delta\alpha_{rmax}(\alpha_{3D}) = min(\Delta\alpha(\alpha_{3D}, y)) \qquad (2.51)$$

These maximum and minimum happen at the reference sections y_{rmax} and y_{rmin}:

$$\Delta\alpha(0, y_{rmax}) = \max_{y\in[0;b/2]} \Delta\alpha(0, y) \qquad (2.52)$$

$$\Delta\alpha(0, y_{rmin}) = \min_{y\in[0;b/2]} \Delta\alpha(0, y) \qquad (2.53)$$

A slightly different version of the total twist Ω is now introduced, based on the new maximum and minimum reference positions instead of the root and the tip:

$$\Omega = \Delta\alpha_{rmax} - \Delta\alpha_{rmin} \qquad (2.54)$$

Finally, the normalized twist distribution ω is defined with the new Ω:

$$\omega(\theta) = \frac{\Delta\alpha_{rmax}(\alpha_{3D}) - \Delta\alpha(\alpha_{3D}, \theta)}{\Omega} \qquad (2.55)$$

These changes are necessary to ensure that ω varies between 0 and 1. By construction, Ω and ω are independent of α_{3D}. Finally, we find the previous expression of the absolute angle of attack with respect to the new global twist:

$$\Delta\alpha(\alpha_{3D}, \theta) = \Delta\alpha_{rmax}(\alpha_{3D}) - \Omega\omega(\theta) \tag{2.56}$$

2.5.6   Solving the fundamental equation

By using the corrected circulation Γ proposed in equation (2.31), the induced angle of attack proposed in equation (2.45) and the absolute angle of attack proposed in equation (2.56), a new expression of the fundamental equation of the LLT is found:

$$\Delta\alpha_{rmax}(\alpha_{3D}) - \Omega\omega(\theta) = \sum_{n=1}^{N} \left(A_n \left(f(\Lambda(\theta)) \frac{4b}{a_0(\theta)c(\theta)} + \delta_n^{\alpha_i}(\theta) \frac{n}{\sin(\theta)} \right) \sin(n\theta) \right) \tag{2.57}$$

As proposed by Phillips and Alley (2007), the sequence of Fourier coefficients (A_n) is separated into two: the sequence (a_n) linked to α_{3D}, and the sequence (b_n) linked to Ω:

$$A_n = \Delta\alpha_{rmax}a_n - \Omega b_n \tag{2.58}$$

Following Phillips and Alley approach, equation (2.57) is separated into two new discretized equations accounting, this time, for multi-sweep corrections:

$$\sum_{n=1}^{\infty} \left(a_n \left(f(\Lambda(\theta)) \frac{4b}{a_0 c(\theta)} + \delta_n^{\alpha_i} n \frac{1}{\sin(\theta)} \right) \sin(n\theta) \right) = 1 \tag{2.59}$$

$$\sum_{n=1}^{\infty} \left(b_n \left(f(\Lambda(\theta)) \frac{4b}{a_0 c(\theta)} + \delta_n^{\alpha_i} n \frac{1}{\sin(\theta)} \right) \sin(n\theta) \right) = \omega(\theta) \tag{2.60}$$

These equations are different from the original equations (2.28) and (2.29) proposed by Phillips and Alley. In order to find a_n and b_n, classical LLT resolution approaches are applied (Anderson, 2001). A_n is found by applying equation (2.58). With this equation in place, it is now possible to derive an expression of the global lift coefficient.

2.5.7   Global lift coefficient C_L

The global lift coefficient C_L in the linear zone is calculated as a function of A_n and (a_n, b_n). Let us introduce the aspect ratio as $AR = b^2/S_{ref}$. Then, after some change of variables and simplifications, we obtain the following expression

$$C_L = \frac{L}{\frac{1}{2}\rho_\infty V_\infty^2 S_{ref}} = AR \sum_{n=1}^{N} \left(A_n \times 2 \int_0^\pi f(\Lambda) \sin(n\theta) \sin(\theta)\, d\theta \right) \tag{2.61}$$

Let us, again, divide the interval $[0; \pi]$ in M sub intervals $[\theta_j; \theta_{j+1}]_{j\in[\![0,M-1]\!]}$ following the method proposed in section 2.5.4. Let us, again, define Λ_j, and thus f_j in the same way. Then C_L can be expressed as a sum of intermediary integrals:

$$C_L = AR \sum_{n=1}^{N} A_n \left(2 \sum_{j=0}^{M-1} f_j \int_{\theta_j}^{\theta_{j+1}} \sin(n\theta) \sin(\theta)\, d\theta \right) \tag{2.62}$$

Now, δ_n^{CL} is introduced as the weighted sweep correction carried by a given interval $[\theta_j; \theta_{j+1}]$

$$\delta_n^{CL} = \frac{1}{\pi/2} \sum_{j=0}^{M-1} f_j \int_{\theta_j}^{\theta_{j+1}} \sin(n\theta) \sin(\theta)\, d\theta \tag{2.63}$$

This simplifies C_L as a sum of the $A_n \delta_n^{CL}$ series:

$$C_L = \pi AR \sum_{n=1}^{N} A_n \delta_n^{CL} \tag{2.64}$$

From a global perspective, this expression can be further simplified by introducing the lift correction factor $\delta_{L\Lambda}$

$$\delta_{L\Lambda} = \delta_1^{CL}\left(1 + \sum_{n=2}^{N} \frac{A_n \delta_n^{CL}}{A_1 \delta_1^{CL}}\right) \tag{2.65}$$

Resulting in a final expression for C_L with respect to A_1 and $\delta_{L\Lambda}$:

$$C_L = \pi AR A_1 \delta_{L\Lambda} \tag{2.66}$$

In order to calculate $\delta_{L\Lambda}$, it is necessary to calculate the integral inside each δ_n^{CL}. Said integral can be calculated by using basic trigonometric formulas. Their analytical expression is given as follows:

$$if\ n = 1, \quad \int_{\theta_j}^{\theta_{j+1}} \sin^2(\theta)\, d\theta \ = \left[\frac{\theta}{2} - \frac{1}{4}\sin(2\theta)\right]_{\theta_j}^{\theta_{j+1}}{}_L \tag{2.67}$$

$$if\ n > 1, \quad \int_{\theta_j}^{\theta_{j+1}} \sin(n\theta)\sin(\theta)\, d\theta \tag{2.68}$$

$$= \frac{1}{n^2 - 1}\left[\sin(n\theta)\cos(\theta) - n\sin(\theta)\cos(n\theta)\right]_{\theta_j}^{\theta_{j+1}}{}_L$$

Now, $\delta_{L\Lambda}$ is a correction factor applied to the global C_L and used later in the model. However, we also need an expression of C_L directly as a function of (a_n, b_n). To do so, we inject equation (2.58) into equation (2.66). This results in the following expression

$$C_L = \pi AR\left(\Delta\alpha_{rmax}\delta_\alpha^{CL} - \Omega\delta_\Omega^{CL}\right) \tag{2.69}$$

where δ_α^{CL} represents the base lift correction and δ_Ω^{CL} represents the twist lift correction as follows:

$$\delta_\alpha^{CL} = \sum_{n=1}^{N} a_n \delta_n^{CL} \tag{2.70}$$

$$\delta_\Omega^{CL} = \sum_{n=1}^{N} b_n \delta_n^{CL} \tag{2.71}$$

Finally, the expression of the global lift slope is directly found as a function of δ_α^{CL}:

$$C_{L,\alpha} = \pi AR \delta_\alpha^{CL} \tag{2.72}$$

2.5.8   Ratio C_L/C_l

To find an expression similar to equation (2.30) as given by Phillips & Alley, an expression of the ratio C_L/C_l is required. This is achieved by first analyzing the ratio C_l/C_L. First, we derive an expression of C_l with respect to A_n:

$$C_l = \frac{\rho_\infty V_\infty \Gamma}{\frac{1}{2}\rho_\infty V_\infty^2 c} = f(\Lambda)\frac{4b}{c}\sum_{n=1}^{\infty} A_n \sin(n\theta) \tag{2.73}$$

Now, an expression of $\Delta\alpha_{rmax}$ is found by isolating this term in equation (2.69).

$$\Delta\alpha_{rmax} = \frac{1}{\pi AR \delta_\alpha^{CL}} C_L + \frac{\delta_\Omega^{CL}}{\delta_\alpha^{CL}}\Omega \tag{2.74}$$

By injecting this expression of $\Delta\alpha_{rmax}$ into equation (2.58), we obtain an expression of A_n with respect to C_L, δ_α^{CL}, δ_Ω^{CL}, $C_{L,\alpha}$, Ω, a_n and b_n:

$$A_n = \frac{C_L}{C_{L,\alpha}} \left(a_n + \frac{C_{L,\alpha}\Omega}{C_L} \left(a_n \frac{\delta_\Omega^{CL}}{\delta_\alpha^{CL}} - b_n \right) \right) \tag{2.75}$$

Substituting this expression of A_n into equation (2.73), results in a twist-dependent expression of C_l:

$$C_l = f(\Lambda) \frac{4b}{c} \frac{1}{C_{L,\alpha}} C_L \sum_{n=1}^{\infty} \left(a_n + \frac{C_{L,\alpha}\Omega}{C_L} \left(a_n \frac{\delta_\Omega^{CL}}{\delta_\alpha^{CL}} - b_n \right) \right) \sin(n\theta) \tag{2.76}$$

For ease of notation, we now introduce the function K:

$$K(\theta) = \frac{C_{L,}}{f(\Lambda)} \frac{c(\theta)}{4b} \tag{2.77}$$

This yields the following expression of C_l/C_L:

$$\frac{C_l}{C_L} = \frac{1}{K} \sum_{n=1}^{\infty} a_n \sin(n\theta) + \left(\frac{C_{L,\alpha}\Omega}{C_L} \right) \sum_{n=1}^{\infty} \frac{1}{K} \left(\left(a_n \frac{\delta_\Omega^{CL}}{\delta_\alpha^{CL}} - b_n \right) \right) \sin(n\theta) \tag{2.78}$$

Let us now define the term $\left(\frac{C_L}{C_l} \right)_{\Omega=0}$ as the lift coefficient ratio in the absence of twist and the term $\kappa_{L\Omega}$ as the twist correction factor:

$$\left(\frac{C_L}{C_l} \right)_{\Omega=0} = \frac{K}{\sum_{n=1}^{\infty} a_n \sin(n\theta)} \tag{2.79}$$

$$\kappa_{L\Omega} = \frac{1}{K} \sum_{n=1}^{\infty} \left(a_n \frac{\delta_\Omega^{CL}}{\delta_\alpha^{CL}} - b_n \right) \sin(n\theta) \tag{2.80}$$

Then, equation (2.78) can be readily rearranged into the following expression:

$$\frac{C_L}{C_l} = \left(\frac{C_L}{C_l}\right)_{\Omega=0} \left(1 - \left(\frac{C_{L,\alpha}\Omega}{C_l}\right)\kappa_{L\Omega}\right) \tag{2.81}$$

This expression is similar to the one proposed by Phillips et al. (Phillips & Alley, 2007). Note that equation (2.81) is valid at all sections θ in the linear lift zone. We must now limit the analysis on a specific section linked to the maximum lift coefficient.

2.5.9   Definition of the reference section

We have now obtained an analytical expression of C_L/C_l. However, this expression is valid for all sections $\theta \in [0; \pi]$ so long as α_{3D} is within the linear lift zone. The idea now is to choose a reference section θ_{ref} that would represent the aircraft at stall conditions.

In this case, our reference condition is different than the one proposed by Phillips et al. Our new reference condition is based on the closeness to stall of each section. Let α_{eff} be the effective local angle of attack in radians:

$$\alpha_{eff} = \alpha_{3D} - \phi - \alpha_i = \alpha_{L0} + \frac{2\Gamma}{a_0 V_\infty c} \tag{2.82}$$

Now let $\alpha_{2Dstall}$ be the stall angle of the 2D airfoil at section θ in radians. This stall angle is assumed to be imported from a viscous airfoil database. Then, we introduce the stall ratio r_α as the ratio between α_{eff} and $\alpha_{2Dstall}$:

$$r_\alpha(\alpha_{3D}, \theta) = \frac{\alpha_{eff}(\alpha_{3D}, \theta)}{\alpha_{2Dstall}(\theta)} \tag{2.83}$$

The stall ratio is a useful variable to determine whether or not a section has stalled locally. If $r_\alpha < 1$ then the section hasn't attained stall conditions, whereas if $r_\alpha > 1$, the section has already stalled. The reference condition is simply defined as the section with maximum stall ratio. This condition ensures that the reference section corresponds to the section with maximum, if any, stall conditions. Its mathematical expression is given as follows:

$$\theta_{ref} = \left\{ \theta \in \left[0, \frac{\pi}{2}\right] \mid r_\alpha \text{ is } maximum \right\} \tag{2.84}$$

By construction, θ_{ref} depends on α_{3D} and varies with it: the reference section changes with angle of attack. The previous expression can be developed further by finding the roots of the derivative of r_α. This implies the derivation of both α_{eff} and $\alpha_{2Dstall}$. By developing equation (2.84), it is found that the reference section is also the solution of the following equation:

$$\frac{dr_\alpha}{d\theta} = \left(\frac{2\frac{d\Gamma}{d\theta} a_0 V_\infty c - 2\Gamma V_\infty (\frac{da_0}{d\theta} c + a_0 \frac{dc}{d\theta})}{(a_0 V_\infty c)^2} + \frac{d\alpha_{L0}}{d\theta} \right) \alpha_{2Dstall}(\theta) \tag{2.85}$$

$$- \left(\frac{2\Gamma}{a_0 V_\infty c} + \alpha_{L0} \right) \frac{d\alpha_{2Dstall}}{d\theta} = 0$$

Note that in the case of a trapezoidal wing with unique airfoil, this reference condition is equivalent to the reference condition proposed by Phillips and Alley (2007).

From this moment onwards, we use the ref index to indicate the functions evaluated at the reference section, which varies with the angle of attack. For example, $f_{ref} = f\left(\Lambda(\theta_{ref})\right)$. This allows us to analyze C_L/C_l at the reference section:

$$\left(\frac{C_L}{C_l}\right)_{ref} = \left(\frac{C_L}{C_l}\right)_{0,\theta_{ref}} \left(1 - \left(\frac{C_{L,\alpha}\Omega}{C_{lref}}\right) \kappa_{L\Omega,ref}\right) \tag{2.86}$$

According to equation (2.84), the reference section is particularly dependent on Γ and $d\Gamma/d\theta$, which are both dependent on A_n. Since A_n is dependent on $\xi = \left(\frac{C_{L,\alpha}\Omega}{C_L}\right)$, then Γ, $d\Gamma/d\theta$ and θ_{ref} are also dependent on ξ. From here, $\kappa_{L\Omega,ref}$ also becomes dependent on ξ. Thus making $\left(\frac{C_L}{C_l}\right)_{ref}$ depend twice on ξ, first via θ_{ref}, and then also via $\chi = \xi\left(\frac{C_L}{C_l}\right) = \left(\frac{C_{L,\alpha}\Omega}{C_l}\right)$. For this reason, equation (2.80) cannot be used straightforwardly to calculate $\kappa_{L\Omega,ref}$ with respect to a given χ. To work around this problem, $\kappa_{L\Omega}$ can be calculated backwards based on the procedure proposed by Phillips and Alley (2007):

1. For a given angle α_{3D}, define $\xi = \left(\frac{C_{L,\alpha}\Omega}{C_L}\right)$ as the independent variable.

2. Based on this value, calculate $\theta_{ref}(\xi)$.

3. Use this reference section to evaluate $\left(\frac{C_L}{C_l}\right)_{ref}$ and $\left(\frac{C_L}{C_l}\right)_{0,ref}$ based on equations (2.78) and (2.79).

4. Calculate $\chi_{ref} = \left(\frac{C_L}{C_l}\right)_{ref}\xi$.

5. The corresponding $\kappa_{L\Omega,ref}$ for the initial ξ is found by rearranging equation (2.81):

$$\kappa_{L\Omega,ref} = \frac{1}{\chi_{ref}}\left(1 - \frac{\left(\frac{C_L}{C_l}\right)_{ref}}{\left(\frac{C_L}{C_l}\right)_{0,\theta_{ref}}}\right) \qquad (2.87)$$

6. Repeat steps 1-6 for multiple angles of attack.

7. Use the different values of $(\chi_{ref}, \kappa_{L\Omega,ref})$ obtained at each angle to define $\kappa_{L\Omega,ref}$ with respect to χ_{ref}.

2.5.10   Reference section stall

Now that the reference section has been introduced, and that $\kappa_{L\Omega,\text{ref}}$ has been defined, they can be used to evaluate the ratio C_{Lmax}/C_{lstall}, where C_{lstall} is the maximum lift coefficient of the reference section airfoil as given by the viscous airfoil database. The main idea is to estimate the reference section θ_{ref} at a given angle of attack α_{3D}, and then use this section to calculate $(C_L/C_l)_{0,ref}$. Furthermore, $C_{lstall}(\theta_{ref})$ is used to define $\chi_{stall} = \left(\frac{C_{L,\alpha}\Omega}{C_{lstall}}\right)$, and the resulting value of χ_{stall} is used to obtain $\kappa_{L\Omega,\text{ref}}^{stall} = \kappa_{L\Omega,\text{ref}}(\chi_{stall})$. This makes it possible to determine an initial value of C_L when the reference section stalls:

$$C_L = \left(\frac{C_L}{C_l}\right)_{0,\theta_{ref}} \left(C_{lstall} - (C_{L,\alpha}\Omega)\kappa_{L\Omega,\text{ref}}^{stall}\right) \tag{2.88}$$

This expression however, is not yet complete, and it must be further corrected to account for non-linear phenomena that appear near stall.

2.5.11   Determining C_{Lmax}

Equation (2.78) returns the C_L that the linear LLT model would attain when the selected reference section stalls. Three correction factors are now introduced in the calculation of C_{Lmax}. First, there is an average sweep correction factor $\kappa_{L\Lambda}^{phill}$ which conveys the simple presence of sweep. Then, there is the multi-sweep correction factor for stall $\kappa_{L\Lambda}^{multi}$ which conveys the variation of sweep. Finally, there is the non-linear stall correction factor that would otherwise be present in a regular trapezoidal wing κ_{Ls}.

$\kappa_{L\Lambda}^{phill}$ is calculated over the mean aerodynamic quarter chord angle $\bar{\Lambda}$, and retakes the correction proposed by Phillips and Alley (2007) for swept wings, where the coefficients $\kappa_{\Lambda 1}$ and $\kappa_{\Lambda 2}$ are extracted from that publication.

$$\overline{\Lambda} = \frac{1}{S} \int_{-b/2}^{b/2} \Lambda_{0.25c}(y)c(y)dy \tag{2.89}$$

$$\kappa_{L\Lambda}^{phill} = 1 + \kappa_{\Lambda 1}\overline{\Lambda} - \kappa_{\Lambda 2}\overline{\Lambda}^2 \tag{2.90}$$

The second correction factor $\kappa_{L\Lambda}^{multi}$ is given as

$$\kappa_{L\Lambda}^{multi} = \left(\frac{f(\Lambda_{ref})}{\delta_{L\Lambda}}\right)^{n_{LLT}} \tag{2.91}$$

Where f is the sweep correction function and $\delta_{L\Lambda}$ is the global C_L correction. The parameter n_{LLT} is a calibration parameter.

Finally, the third correction factor κ_{Ls} directly corresponds to the stall correction factor as proposed by Phillips and Alley (2007).

$$\kappa_{Ls} = \kappa_{Ls}^{Phill} = 1 + (0.0042AR - 0.068)(1 + 2.3\chi_{stall}) \tag{2.92}$$

This results in the following expression of the global lift C_L with respect to the reference stall lift C_{lstall}

$$C_L(C_{lstall}) = \left(\frac{C_L}{C_l}\right)_{0,ref} \kappa_{L\Lambda}^{phill}\kappa_{L\Lambda}^{multi}\kappa_{Ls}\left(C_{lstall} - (C_{L,\alpha}\Omega)\kappa_{L\Omega,ref}\right) \tag{2.93}$$

Note that this expression predicts the global C_L when the reference section at angle α_{3D} stalls. This means that $C_L(C_{lstall})$ is dependent on α_{3D}. As a result, it is necessary to identify the moment when the aircraft stalls in order to find C_{Lmax}. To do so, we look for the angle whose reference section yields a stall ratio r_α closest to 1:

$$\alpha_{3Dstall} = \left\{ \alpha_{3D} \in \mathbb{R} \text{ so that } \left| r_\alpha \left(\theta_{ref}(\alpha_{3D}) \right) - 1 \right| \text{ is minimum} \right\} \tag{2.94}$$

Finally, the maximum lift coefficient is given as

$$C_{Lmax} = C_L(C_{lstall})_{(\alpha_{3D}=\alpha_{3Dstall})} \tag{2.95}$$

To sum it up, the local circulation Γ is penalized by a function $f(\Lambda)$ (Eq. (2.31)). This penalty is integrated into the fundamental equation of the LLT to yield the corrected Fourier coefficients a_n and b_n (Eqs. (2.59) and (2.60)). These coefficients are used to define multiple parameters, resulting in an expression of C_L/C_l. This expression is evaluated at a reference section θ_{ref} (Eq. (2.84)). Following this, the ratio C_L/C_{lref} is evaluated at local stall (Eq. (2.88)) and corrected (Eq. (2.93)) to yield an expression of $C_L(C_{lstall})$ for multiple angles of attack α_{3D}. Finally, C_{Lmax} is found by choosing the first angle α_{3D} whose reference section presents local stall (Eqs. (2.94) and (2.95)).

2.6   Chapter summary

This chapter's objective was to introduce the different physical, numerical and mathematical tools used or developed during this research. This comprises the RANS model implemented in the SU2 open source code as well as the compound wing LLT prediction model for C_{Lmax}.

First, the introduction of the aerodynamic coefficients in section 2.2 introduce the aeronautical framework of this research. This introduction familiarises the reader with the variables of interest of this research. This is important since investigating the link between the design parameters and the evolution of C_{Lmax} at low speed is, ultimately, one of the goals of this research.

Section 2.3 introduce the general governing equations for fluid flows. General hypotheses are made based on the physical conditions of the problem. The airflow, is assumed to be compressible, homogeneous, Newtonian, without sources and without body forces.

Assessment of current numerical capabilities and available resources concluded in the choice of a RANS-SA approach which, according to the literature review, yields time-average results with acceptable accuracy for our purposes.

Section 2.4 introduces the CFD RANS approach, which is further developed in APPENDIX I and APPENDIX II. The unsteady term is solved with a 1st order euler implicit scheme. The JST discretization scheme was introduced for the diffusive-convective term. The viscous term uses a Green-Gauss approach. Also, a brief presentation of the boundary conditions is laid out to close the problem.

Finally, section 2.5 introduces the compound wing prediction model for C_{Lmax}. This model was developed as a generalized low-fidelity design tool for maximum lift prediction. This model constitutes an original contribution to the BWB development efforts. Only the theoretical approach is presented in this chapter while the justification, implementation and calibration are left for Chapter 5.

With the presentation of the theoretical tools done, the following chapter will focus on the development and validation of the conceptual aircraft design of the regional BWB and the verification of the RANS-SA approach for low speed RANS simulations.

CHAPTER 3

REGIONAL BWB FOR LOW SPEED APPROACH: MODEL GENERATION AND VALIDATION

3.1   Introduction

With the definition of the physical models and numerical methods done, it is now necessary to generate a regional BWB geometry on which to analyse the low speed phenomena. This chapter focuses on the construction of the baseline regional BWB used to carry out the low-speed predictions. It has one objective: to establish the geometrical and numerical framework used to study the low speed phenomena for the BWB. This is accomplished by (1) proposing a regional BWB geometry and (2) validating the use of the chosen numerical method for low speed conditions. First, a conceptual aircraft design model of the regional BWB is generated by introducing modifications to the classic conceptual design approach. Afterwards, a validation of the suitability of the RANS-SA model and the numerical settings and implementation chosen is carried out based on previous existing data on the NACA 0012 and the CRM geometries. This results in a mission-compliant regional BWB geometry and a validated numerical approach to study low speed phenomena.

3.2   BWB configuration

This section introduces the regional BWB from a conceptual design perspective. The current regional BWB design is based on previous design methodologies by Corke (2003), Raymer (2006), Anderson (1999), Bradley (2004) and Roskam (1985). For conciseness, only an overview of the design methodology is presented in this section.

Consider a classic conceptual aircraft design approach as proposed by Anderson (1999) and Raymer (2006). Figure A III-1 from Annex I, synthetises such an approach in detail. Due to new BWB- specific constraints, the general approach for conceptual aircraft design was modified to prioritize OW surface repartition. This is a consequence of both the definition of

the reference surface for a BWB and the cabin size constraints required for a regional BWB. On top of this, the proposed BWB geometry contemplates the absence of high-lift devices. For these reasons, a few concessions were added to the classic conceptual aircraft approach so as to attain a compliant geometry.

Figure 3-1 presents the modified approach for the regional BWB where blocks in black represent the modifications done to the classical approach: first the mission requirements are assessed (range R, endurance E, runway length s_{run}, passengers (PAX), cruise Mach speed M_{cruise}). Then an initial value for the maximum lift-to-drag ratio $(L/D)^0_{max}$, the thrust specific fuel consumption C^0_{TSFC}, the structure factor s^0_f – ratio of the empty weight W_e to the takeoff weight W_{TO} – and the cruise altitude H^0_{cr} is proposed from historic data. Usually H^0_{cr} is fixed by mission requirements. For academic purposes and reasons explained further down, this parameter is left flexible and is allowed to change during the design. Following this, weight fractions for each phase of the aircraft are either proposed from historic data or calculated; this results in the calculation of the design takeoff weight W_{TO}.

Note the appearance of a new parameter S_{ref} which is the planform reference surface. The conventional approach would require us to fix the wing loading W/S, and to use this wing loading to find an adequate reference surface as $S_{ref} = W_{TO} \cdot \frac{1}{W/S}$. This is exactly what is done in the first iteration loop. For ulterior loops, S_{ref} is introduced as a fixed parameter – in black in the figure -. This stems from the fact that, in the case of the BWB, S_{ref} corresponds to the whole projected area on the z plane– CB included -. This introduces a new problem since the CB is defined by a minimum surface which cannot be reduced due to cabin size constraints. In turn, this greatly reduces the surface of the outer wing. As an example, consider an hypothetical regional BWB with a design takeoff weight of $W_{TO} \approx 50\,000\ kg$ and a wing loading of $W/S = 200\ kg/m^2$. This would result in a reference surface of $S_{ref} \approx 250\ m^2$. Note that reference values for W/S for a BWB oscillate between $200\ kg/m^2$ and $350\ kg/m^2$ (Velazquez et al., 2015), thus this value of S_{ref} would be close to a best case scenario. Now considering the cabin size constraints, a CB planform surface for 100 passengers would require

values of $S_{CB}^{planform} \approx 200 \, m^2$, this barely leaves $50 m^2$ for the OW planform surface, representing roughly 20% of the lifting surface. While these are not the exact values, the order of magnitude is the same as that of the final aircraft. In an effort to maintain outer wings with which to interact, it was thus decided to fix S_{ref} after the initial iteration, and instead derive the wing loading as $W/S = W_{TO}/S_{ref}$, where W_{TO} has already been fixed as explained in the previous paragraph. Due to this change, it will be necessary to verify that the wing loading works for different flight phases. Most flight phases depend on other parameters which can be chosen to match the mission requirements later in the design loop. However, for the cruise phase, it is necessary to release the altitude as a variable and to calculate it by cruise-matching the given wing loading.

The final critical parameters T/W (thrust-to weight ratio) and C_{Lmax} (maximum lift coefficient) are chosen based on historical data and early analysis of requirements for mission performance. These critical parameters are used to define a geometry layout based on aspect ratio AR, wing sweep Λ, wing taper λ and, of course S_{ref} as chosen by the aircraft designer. At this point, airfoil geometries are chosen for the CB and for the OW.

Once the initial geometry has been proposed, aerodynamic prediction is done to verify the actual aerodynamic parameters offered by the geometry $\left((L/D)_{max}, C_{D0}, C_{Lmax}, C_{L,cruise}, K \right)$. At this point, the aerodynamic prediction is carried out using the low fidelity viscous vortex-lattice method presented in APPENDIX IV II and developed as an extension of the works of Drela and Youngren (2008).

Parallel to this, a detailed weight estimation is done to give a better estimation of the actual weight of the structure. Detailed weight estimation is divided in 2 parts: the airframe weight estimation according to BWB methodologies (D Howe, 1996) and the rest of the aircraft weight according to classic weight estimation by Raymer (2006) and Roskam (1985). With this new estimation, a new structure factor s_f is calculated along with the required fuel weight W_f for this airframe. At this point of the design loop, any difference between W_{TO} and W_f is added as

extra fuel in order to obtain the same proposed takeoff weight W_{TO} for which the critical parameters where proposed.

The updated aerodynamic and weight parameters are used to verify if the proposed geometry, with the updated choices, answers to the mission requirements. These tests are comprised on runway length estimations (s_{run}) for takeoff and landing (TOL), thrust to speed graph analysis to estimate minimum and optimum cruise speeds, flight ceiling estimation, maximum range estimation, $V - n$ load diagrams and stability. If the mission is not satisfied, the updated data is used as a starting point to generate a new proposal starting from the critical parameters.

The aircraft is redesigned in an inner loop until the resulting predictions from the low fidelity models satisfy the mission requirements. Afterwards, if the mission is satisfied, an outer-loop modifies the initial structure factor based on previous estimations of the structural weight, thus closing the gap between design takeoff weight and final takeoff weight. Inner loops are then run to verify mission compliance at all times and modify the design as necessary. Once the final geometry has been fixed, RANS simulations are used to predict the final aerodynamic characteristics and the final performance of the aircraft. Note that, contrary to classic aircraft design, the final baseline geometry proposed here might not necessarily be the most optimum possible geometry. This is a result from (1) the limited accuracy of the predicting models applied, (2) the inherent limitations from a preliminary design algorithm and (3) the author's decision to modify some constraints of the design loop in order to obtain a workable geometry relevant to this research project. This being said, this geometry can, within the limits of the preliminary design and low fidelity prediction models used, comply with the mission requirements while lending itself to a CB/OW analysis.

Figure 3-1 is proposed here as a summary of the modifications applied to obtain a regional BWB geometry. For conciseness, the symbols used in this figure are introduced in the next relevant subsections of the BWB configuration section of this chapter. In particular, the following subsection introduces the flight mission and the mission requirements on which the baseline regional BWB was built.
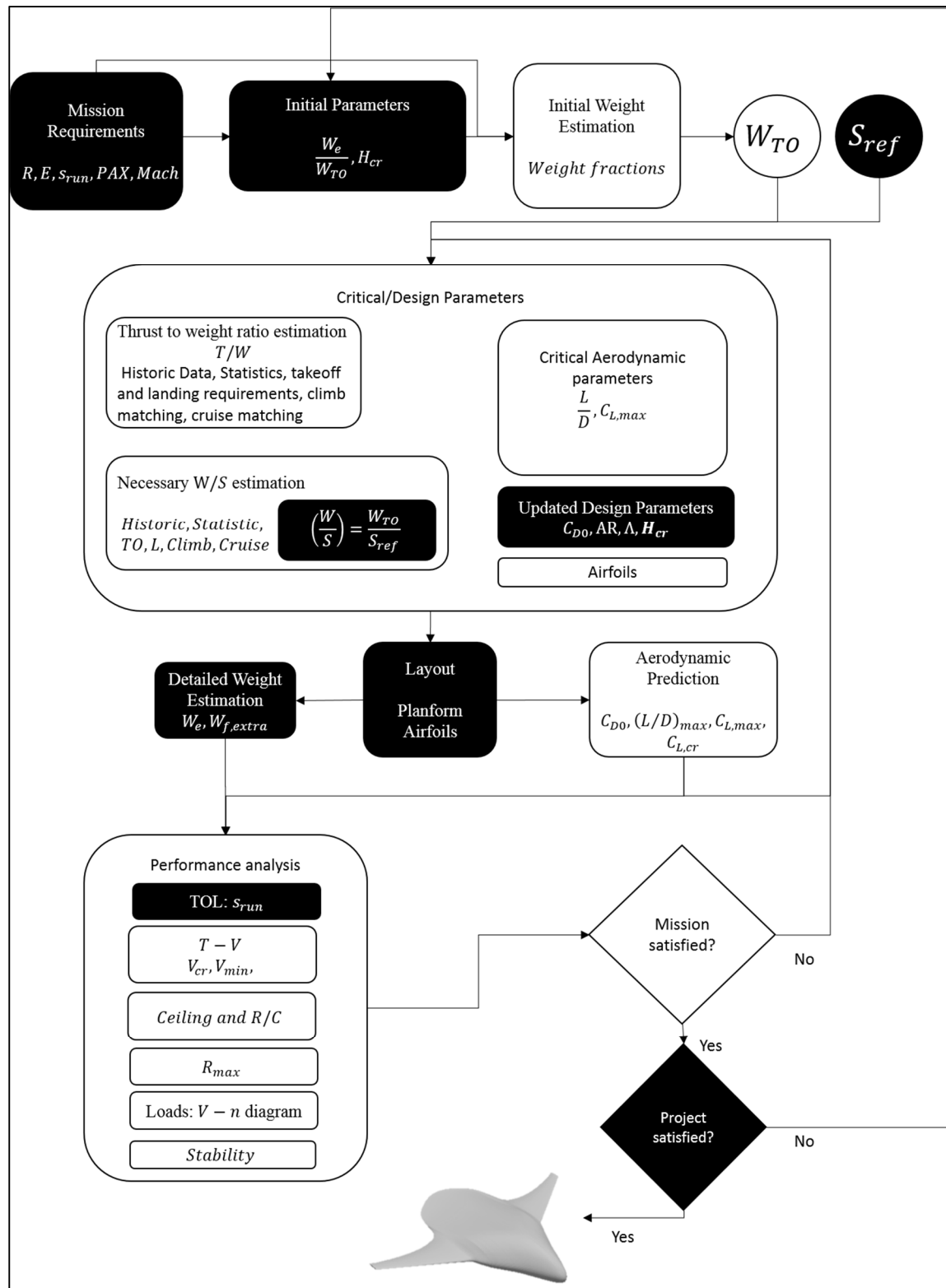
Figure 3-1:   Conceptual design for the regional BWB without high-lift devices.

3.2.1   Regional Mission

A visual representation of an academic transport mission (Raymer, 2006) is proposed in Figure 3-2. The mission is defined by a take-off phase (0 → 1), a climb phase (1 → 2), a cruise phase (2 → 3), a loiter phase (3 → 4) and a landing phase (4 → 5). Note that, following Raymer's recommendations, descent is implicitly assimilated into the cruise.
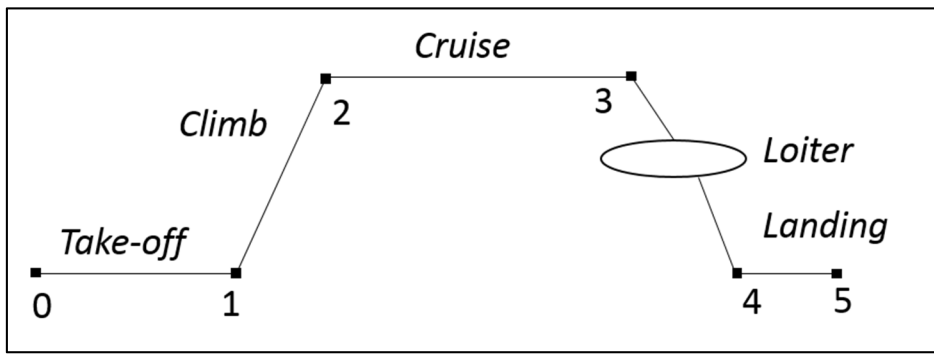
Figure 3-2:   Mission segments

The mission's requirements are based on current values for the Bombardier CRJ1000 (Bombardier, 2015) and the Embraer E-190 (Frawley, 2003), representative of regional jets. This mission requires an aircraft designed to carry 100 passengers (PAX, 11 640 kg) and 5 crew members (582 kg) along 2500 km at Mach 0.78. The maximum acceptable field length is set at 2000 m, which is comparable to that of current CRJ1000 and E190. The loiter time is set to a conventional 45 minutes. Table 3-1 summarizes these constraints.

Table 3-1:   Mission parameters

Mission parameter	Symbol	Value
Passengers	PAX	100
Payload	$W_{payload}$	11640 kg
Crew	W_{crew}	582 kg
Range	R	2500 km
Cruise Mach speed	M_{cr}	Mach 0.78
Field Length (takeoff and landing)	s_{run}	2000 m
Loiter time	E	45 min

3.2.2   Critical and Design Parameters

The final critical parameters are presented in Table 3-2. The L/D ratio is estimated from RANS numerical simulations using the low speed parameters: $M = 0.2$ and a Reynolds number of $Re = 74 \times 10^6$ for a mean aerodynamic chord of $\bar{c} = 16.9\ m$ at sea level. This choice is made in order to work within the limitations of the low fidelity models which are designed for low speed analysis. According to Anderson (1999) the lift coefficient increases slightly with M up to transonic speeds while the zero-lift drag coefficient C_{D0} is almost constant with respect to M up to the critical Mach number M_{cr}, which is usually higher than 0.8. As for the Reynolds number, it stays roughly in the same order of magnitude since the decreased speed of $M = 0.2$ is compensated by the increased air density and viscosity at sea level with respect to cruise conditions. This is true so long as the conditions stay below the critical Mach number. Coincidentally, $M_{cruise} = 0.78$. The resulting L/D value is comparable with that of similar regional BWBs (Reist & Zingg, 2015).

As previously stated, the wing loading W/S is obtained based on $S_{ref} = 316m^2$, where S_{ref} contains all the lifting planform surfaces and not just the outer wing surface. T/W and C_{TSFC} are based on the CF34-8C engines (General Electric, 2015) used in current regional jets. Three CF34-8C5 engines (General Electric, 2015) were used to match the thrust requirements at cruise for a final total maximum thrust at sea level of $T_{max,SL} = 193.5kN$. The maximum lift

coefficient $C_{L,max}$ is estimated via RANS simulations at a value of $C_{L,max} = 0.67$ for the baseline BWB without high-lift devices. While this number seems low when compared to conventional aircrafts, it must be noted that the BWBs' reference surface is larger than that of a conventional aircraft. As a reference, the CRJ1000 has a net wing surface of $77.4m^2$ (Bombardier, 2015); accounting for the wingbox hidden surface, this translates to a reference surface of $S_{ref}^{TAW} \approx 100m^2$. The BWBs' reference surface is roughly three times as much. In other words, the BWBs' lower $C_{L,max}$ would be equivalent to a value of ~ 2 for a conventional aircraft.

Table 3-2:   Regional BWB critical parameters

Critical Parameters	Value
L/D	16.6
W/S	140 $kg/m2$
T/W	0.441
$TSFC$	0.680 $lb/lb - h$
C_{Lmax}	0.67

3.2.3   Layout configuration

The BWB is divided in three sections. The first section is the CB, housing the passenger cabin and the cargo hold. The second section is the transition wing (TW) connecting the CB to the OW. Logically, the last section is the OW. The following subsections present the definition of the cabin and the exterior layout respectively.

3.2.3.1   Cabin/hold layout

The CB contains both the passenger cabin and the cargo hold. The cabin of the BWB includes the cockpit and the passenger cabin. It is sized according to Bradley (2004). The design proposes the 4x3 row configuration presented in Figure 3-3. The sweep angle of the bay (60°) defines the maximum number of seats per row ranging from 6 to 12.
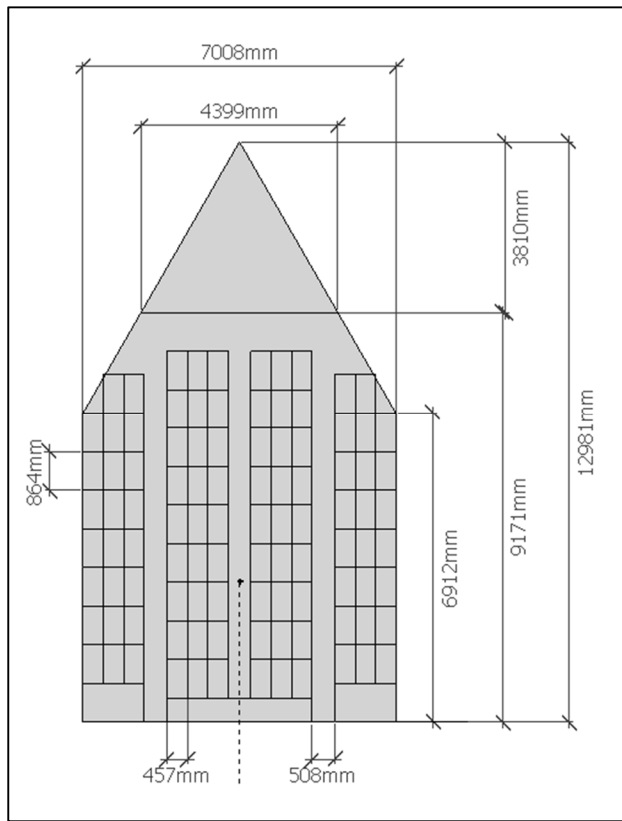
Figure 3-3:   Cabin Layout

The hold contains four LD3-equivalent containers ($1.62m \times 2.00m \times 1.53m$) for a maximum cargo volume capacity of $20m^3$. These LD3 containers are located left and right of the passenger cabin, adding $2 \times 1.53\ m$ to the span of the CB.

Moreover, the CB geometrical constraints concern a minimum height of $1.89m$ for the cabin and $1.62m$ for the cargo hold. On top of this, the cabin requires a minimum floor space to

house the passengers and the LD3 containers. For a given airfoil around the CB, only a limited percentage of the chord has the necessary thickness to house the cabin and the hold. For higher payload BWBs, this percentage is estimated to 70% of the chord (Bradley, 2004; Liebeck, 2004); however for the regional BWB, this percentage varies between 20% and 55% depending on the cabin/hold local chord, height requirements and local airfoil choice.

The regional BWB uses a LA2573A airfoil (Liebeck, 1989) for the CB based on BWB propositions by Liebeck (2004). This airfoil is fitted around the cabin geometry so that the latter is comprised inside the CB's aerodynamic shape. Figure 3-4 shows how the airfoil is positioned around the cabin trying to maximise the usable space all the while minimising airfoil chord length all throughout the wingspan of the centerbody. Finally, the planform surface of the centerbody is calculated at $S_{CB} = 205m^2$.
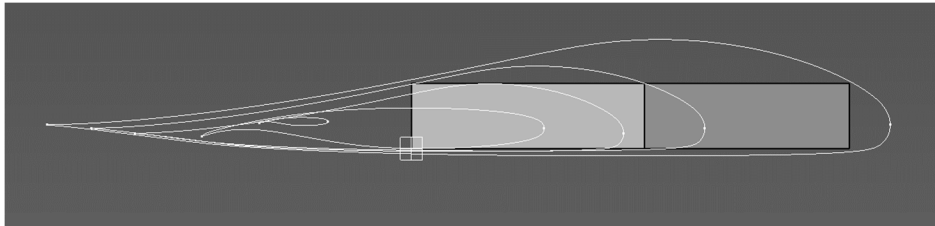
Figure 3-4:   Airfoil positioning around the cabin

3.2.3.2   Exterior layout

Figure 3-5 presents a planform view of the aircraft decomposed into CB, TW and OW. The x axis represents the chordwise abscise measure from the LE of the centerline. The y axis represents the half-wingspan ordinate. Furthermore, the principal two leading edge sweep angles are also present. The CB is characterized by a LA2573A airfoil at its ends ($y = 0m$ and $y = 5m$) while the OW is characterized by an SC(2)-0712 airfoil at its ends ($y = 6.5m$ and $y = 17.2m$). The transition wing is self explanatory. Due to reasons already explained, the reference surface S_{ref} is set to $S_{ref} = 316\ m^2$. This results in a 65%-35% surface distribution

between the CB and the rest of the wing $(S_{CB} = 0.65S_{ref}, S_{OW+TW} = 0.35S_{ref})$. This distribution is in line with the 2/3-1/3 distribution proposed earlier.
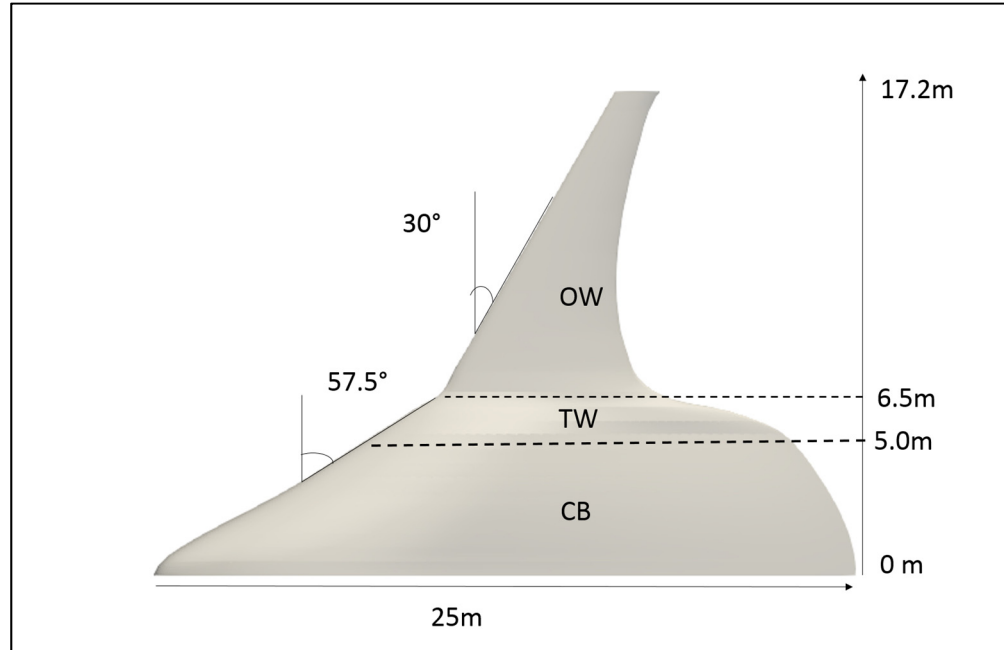
Figure 3-5:   Final BWB sections

Note that this Figure doesn't include engines or control surfaces. While these subsystems were set during the preliminary design process, the choice was made to deliberately not include engine, control and landing gear surfaces. This allowed to simplify the already complex BWB geometry. Figures 3-5 and 3-6 present the baseline geometry used for low-fidelity and high-fidelity aerodynamic prediction. Furthermore, Figure 3-6 presents a 3D view of the aircraft with its main dimensions. The passenger cabin is added in blue to this 3D view to give a perspective of the size of the cabin compared to the size of the BWB.
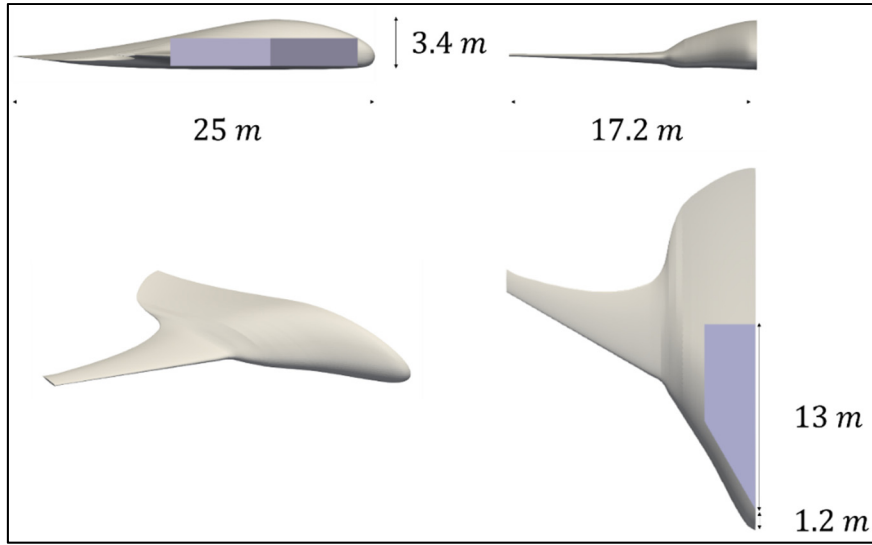
Figure 3-6:   Multiview drawing of the final BWB configuration

The 3D CAD model is generated based on sections 1, 8, 11, 14 and 29 of Table 3-3. Table 3-3 also presents all the reference section airfoils used on chapter 5 to represent the BWB for the compound wing model. All the PosX airfoils are obtained by cutting the 3D CAD model at the y_{LE} wingspan coordinate and are either a slightly modified LA2573A, a slightly modified SC(2)-0712 or a mix between the 2 reference airfoils. Furthermore, this table also shows the position of each airfoil's LE with respect to the centerline's LE as well as the local chord (c) and leading edge sweep angle (Λ_{LE}).

Table 3-3: BWB airfoils layout

	Airfoil	ID	x_{LE} [m]	y_{LE} [m]	z_{LE} [m]	c [m]	Λ_{LE} [°]
CENTERBODY	LA 2573A	1	0.000	0.000	0.000	25.0	0.0
	Pos50	2	0.285	0.500	-0.026	24.7	29.7
	Pos100	3	0.945	1.00	-0.027	23.9	52.9
	Pos150	4	1.80	1.50	-0.030	22.9	59.7
	Pos200	5	2.75	2.00	-0.039	21.8	62.2
	Pos250	6	3.72	2.50	-0.055	20.6	62.7
	Pos300	7	4.65	3.00	-0.081	19.4	61.8
	LA 2573A	8	5.50	3.50	-0.10	18.2	59.3
	Pos400	9	6.28	4.00	-0.17	17.1	57.5
	Pos450	10	7.06	4.50	-0.22	15.9	57.5
	LA 2573A	11	7.91	5.04	-0.25	14.5	57.5
TW	Pos550	12	8.63	5.50	-0.22	12.9	57.5
	Pos600	13	9.42	6.00	-0.17	10.4	57.5
	SC(2)-0712	14	10.3	6.54	-0.10	7.60	57.5
OUTER WING	Pos700	15	10.7	7.25	-0.10	6.44	30.0
	Pos750	16	11.1	7.96	-0.085	5.76	30.0
	Pos800	17	11.5	8.68	-0.072	5.14	30.0
	Pos850	18	11.9	9.39	-0.058	4.62	30.0
	Pos900	19	12.3	10.1	-0.044	4.15	30.0
	Pos950	20	12.7	10.8	-0.029	3.75	30.0
	Pos1000	21	13.1	11.5	-0.015	3.37	30.0
	Pos1050	22	13.6	12.2	0.000	3.06	30.0
	Pos1100	23	14.0	13.0	0.014	2.74	30.0
	Pos1150	24	14.4	13.7	0.028	2.49	30.0
	Pos1200	25	14.8	14.4	0.043	2.22	30.0
	Pos1250	26	15.2	15.1	0.057	2.01	30.0
	Pos1300	27	15.6	15.8	0.072	1.78	30.0
	Pos1350	28	16.0	16.5	0.086	1.60	30.0
	SC(2)-0712	29	16.4	17.2	0.10	1.60	30.0

3.2.4 Aircraft performance summary

This subsection summarises the characteristics of the final regional BWB geometry resulting from the conceptual aircraft design. These values were obtained through iterative application of the method described in Figure 3-1. First, The geometric characteristics like wingspan (b),

planform reference surface (S_{ref}), aspect ratio (AR), wing sweep (Λ), root chord (c_{root}), mean aerodynamic chord ($\bar{c}$), twist (ϕ) and taper (λ) are presented in Table 3-4.

Table 3-4:   Regional BWB geometric parameters

b	S_{ref}	AR	$\Lambda_{LE,CB}$	$\Lambda_{LE,OW}$	$c_{root,CB}$	$c_{root,OW}$	$\bar{c}$	ϕ	λ_{OW}
$34.4m$	$316m^2$	3.76	57.5°	30°	$25m$	$7.6m$	$16.9m$	0°	0.20

Following that, Table 3-5 shows the aerodynamic parameters resulting from high-fidelity analysis of the geometry. This considers the zero-lift drag coefficient C_{D0}, the estimated cruise lift coefficient $C_{L,cruise}$, the maximum lift coefficient C_{Lmax}, and the estimated maximum and cruise L/D. The validation of the RANS-SA models for low speed prediction is carried out in section 3.3. It must be noted that the Oswald factor of this aircraft, with the given parameters, attains a value of $1.10 > 1$. This shouldn't be possible, and while the exact reason is still unclear, it might be a symptom of unexpected CFD RANS limitations. At this point however, the geometry is accepted as-is for the purposes of analysing mainly the lift distribution.

Table 3-5:   Aerodynamic values

C_{D0}	$C_{L,cruise}$	$C_{L,max}$	$(L/D)_{max}$	$(L/D)_{cr}$
0.0118	0.230	0.670	16.6	15.3

Table 3-6 presents the weight distribution for the regional BWB along with the lengthwise position x of the element's center of gravity (CG), starting from the leading edge of the central chord. The structural weights are found by coupling BWB-specific airframe weight prediction methods (D. Howe, 2001) with classic equipment weight estimations based on linear regressions of the values proportioned by Roskam (1985) with respect to W_{TO}. These values result in a global CG located between $x_{CG} = 11.14$ at W_{TO} and $x_{CG} = 11.49$ at zero fuel; this assumes that the fuel on the wings is consumed first.

Table 3-6:   Detailed weight of the BWB and CG position along the length of the aircraft at maximum weight.

Item	Mass (kg)	$x\ (m)$
Airframe: Centerbody	6442	13,8
Airframe: Wing	2575	14,7
Landing Gear Main	382	14,7
Landing Gear Front	2167	0,9
Propulsion system	4667	20,0
Fixed Equipment	6592	7,9
Structure	22825	12,3
Fuel CB	4838	5,0
Fuel Wing	4838	14,7
Fuel	9677	9,9
Crew	467	3,8
PAX	9340	9,9
Luggage	2415	11,9
Transport Load	12222	10,0
Total	44724	11,1

Table 3-7 presents the estimated cruise altitude H_{cr}, cruise thrust $T_{max,H_{cr}}$ – varying linearly with air density $\frac{\rho_{air,H}}{\rho_{air,SL}}$ -, the estimated minimum and cruise speeds and the maximum range R_{max}.

Table 3-7:   Power and cruise performance

$T_{max,H_{cr}}$	H_{cruise}	$V_{cr,min}$	V_{cr}	R_{max}
34.3 kN	14.3 km	115 m/s	230 m/s	2500 km

Table 3-8 focuses on the low-speed performance values, namely the maximum thrust at sea level $T_{max,SL}$, the low speed altitude H_{TOL}, the estimated stall and approach speeds

corresponding to H_{TOL}, and the maximum runway length required which corresponds to the takeoff runway. For these calculations, a drag increase due to the landing gear was added with a value of $\Delta C_{D0,LG} = 6.89 \times 10^{-3}$ for landing, based on relations proposed by Anderson (1999).

Table 3-8: Power and landing performance for a 2500 km range mission at $H_{TOL} = 0m$

$T_{max,SL}$	H_{TOL}	V_{stall}	$V_{approach}$	S_{run}
$193\ kN$	$0\ m$	$52\ m/s$	$68\ m/s$	$1.41 km$

Based on these tables, and according to the mission requirements presented at the beginning of this chapter, the conceptual design proposed here is capable of accomplishing the regional mission proposed.

3.3 High-fidelity prediction model

The previous section introduced the BWB geometry obtained by adapting existing conceptual aircraft design methodologies to the geometric constraints of the regional BWB. In order to analyse the low speed aerodynamics of the aircraft, the research sub-objectives contemplate to use the RANS-SA model implemented in SU2 (Palacios et al., 2013). This more computationally intensive approach, has been at the centre of recent high-lift prediction workshops for aircraft-size applications (Rumsey & Slotnick, 2014). While results remain widespread, successful prediction of stall conditions has been achieved during these workshops depending on mesh and settings chosen. This subsection presents a verification of the RANS-SA approach with the chosen numerical settings for low speed analysis; it is divided in 2 parts: (1) validation of the numerical method and (2) analysis of the mesh size dependence.

3.3.1 RANS model validation

The finite volume numerical method presented in APPENDIX II was proposed based on current practices for aeronautical simulations. As previously stated, this model is commonly used for aircraft-size high-lift configurations. However, the specific schemes, turbulent model, gradient calculation and linear solver used together in this work and implemented by SU2 required verifications for our application. A 2D validation of the NACA0012 airfoil at stall conditions is performed. Further validations on the boundary layer detachment at high speeds are presented in APPENDIX V based on NASA's Fifth CFD Drag Prediction Workshop (Levy et al., 2014).

3.3.1.1 Convergence criterion for 3D aircraft simulations

Common convergence criteria used in the literature are based on residual values or, better yet, on the number of orders of magnitude (OOM) that a given residual has decreased since the beginning of the simulation (Ferziger & Peric, 2012). For this work, simulations with a reduction of at least 3 OOM where considered converged so long as all of the following conditions apply:

- The simulation presents at least 3 OOMs reduction on the residual of the density R_ρ.
- Within the last 10 000 iterations either the absolute difference between maximum and minimum values of C_L is less than 10^{-3} (eq. (3.1)), or the relative error ϵ_{C_L} with respect to the final iteration is less than 1% (eq. (3.2)).
- Within the last 10 000 iterations either the absolute difference between the maximum and the minimum value of C_D is less than 10^{-4} (eq. (3.3)), or the relative error ϵ_{C_D} with respect to the final iteration is less than 1% (eq. (3.4)).

$$\left| C_L^{(max)} - C_L^{(min)} \right| \leq 10^{-3} \tag{3.1}$$

$$\epsilon_{C_L} = \left|\left(C_L^{(max)} - C_L^{(min)}\right)/C_L\right| \leq 0.01 \tag{3.2}$$

$$\left|C_D^{(max)} - C_D^{(min)}\right| \leq 10^{-4} \tag{3.3}$$

$$\epsilon_{C_D} = \left|\left(C_D^{(max)} - C_D^{(min)}\right)/C_D\right| \leq 0.01 \tag{3.4}$$

The value of 10 000 iterations is empirical and showed good consistency across all our simulations. The 3 OOM reduction is attained for residuals between 10^{-4} and 10^{-5}. Note that in most cases, conditions (3.2) and (3.4) were attained first, thus resulting in 1% accuracy but with absolute errors on the order of 10^{-2} and 10^{-3} for C_L and C_D respectively. As an example, Figure 3-7 and Figure 3-8 present the convergence values of the 20M BWB mesh at an angle of attack $\alpha = 11°$, which represents stall conditions. The zoom presented on the right-hand side of Figure 3-8 shows a precision of at least 2 decimals on C_L and 3 decimals on C_D, and overall a variation of less than 1% for both coefficients in the range of iterations shown. Note that for this case, the bottleneck for convergence was present in the residuals rather than in the values of the aerodynamic coefficients themselves.
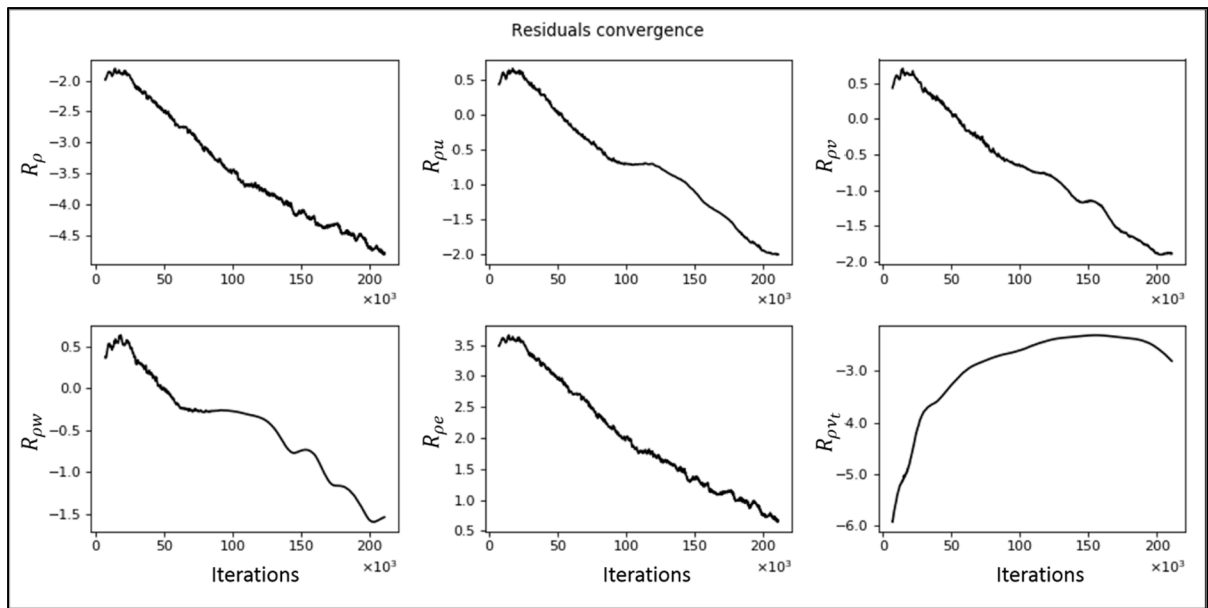
Figure 3-7:   Residuals evolution for the 20M BWB mesh at $\alpha = 11°$
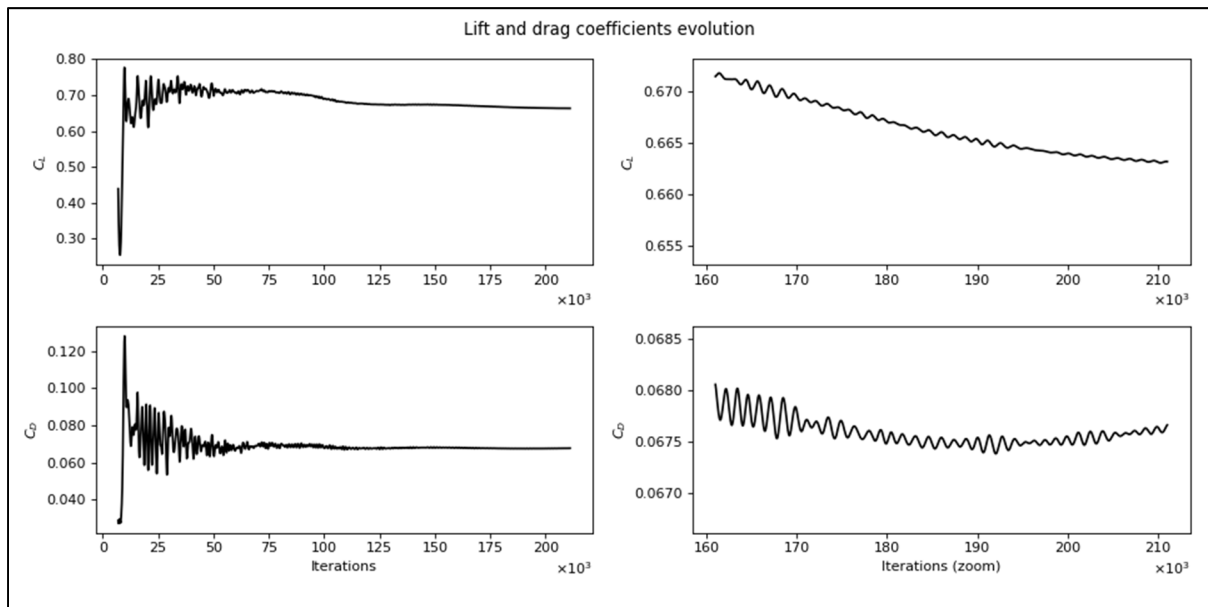
Figure 3-8:   Convergence history of C_L and C_D for the 20M BWB mesh at $\alpha = 11°$: complete (left) and zoomed around the last 50 000 iterations (right).

3.3.1.2   Validation on the NACA0012 airfoil

This verification is done on a NACA 0012 2D airfoil using NASA's finest mesh for this geometry, the $n0012\ 1793 \times 513$ (Rumsey, 2016/06/28). The simulation is run at a temperature $T_k = 300K$, at Mach 0.15 and at a Reynolds number of 6 million for a unitary chord length. The simulations are stopped after attaining residuals of 10^{-9}, according to the convergence criteria established further in section 3.3.1.1. The angle of attack varies as $\alpha \in \{0°, 10°, 15°, 16°, 17°, 18°, 19°, 20°\}$. Proper convergence was attained up to $\alpha = 17°$. Figure 3-9 presents a comparison with the experimental results from Abbott and Von Doenhoff (1959) and Ladson et al. (1987). The CFD predictions show good agreement with experimental results up to the stall. This is particularly true when compared to the tripped results from Ladson et al. While the stall angle varies between both experimental results, the maximum lift coefficient $C_{L_{max}}$ is properly estimated with an error of 0.2% with respect to Ladson et al. (1987). As for C_D, the absolute error up to stall is inferior to 3 decimals with respect to Ladson et al. (1987).
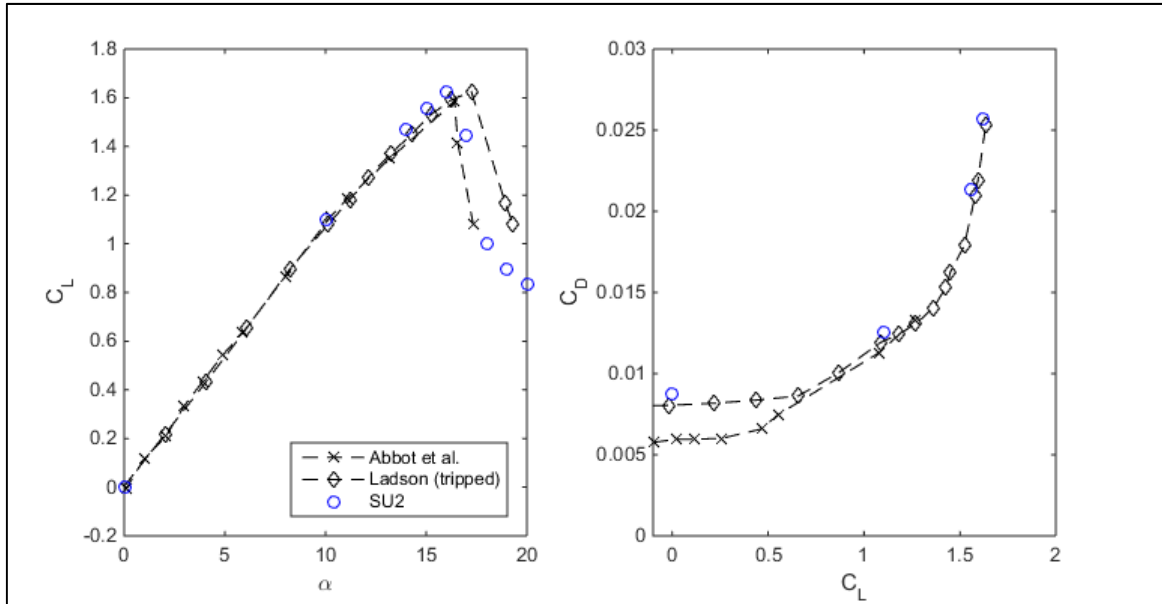
Figure 3-9:   Validation of the aerodynamic coefficients of the NACA 0012 airfoil

Figure 3-10 presents a comparison for the local pressure and friction coefficients, c_p and c_f, against experimental (EXP) and (CFD RANS) data available from (Rumsey, 2016/06/28). While this data is available for the upper surface only, good agreement is found between NASA's results and our NACA 0012 simulations, particularly when close to stall conditions ($\alpha = 15°$). As an example, the most difficult case ($\alpha = 15°$) presents an average error of 5% on c_p, amounting to an average absolute error of $\Delta c_p = 0.1$ where $0 \leq |c_p| \leq 10$. As for c_f, NASA's numerical values and SU2's numerical values on the upper surface are superposed and almost undistinguishable.
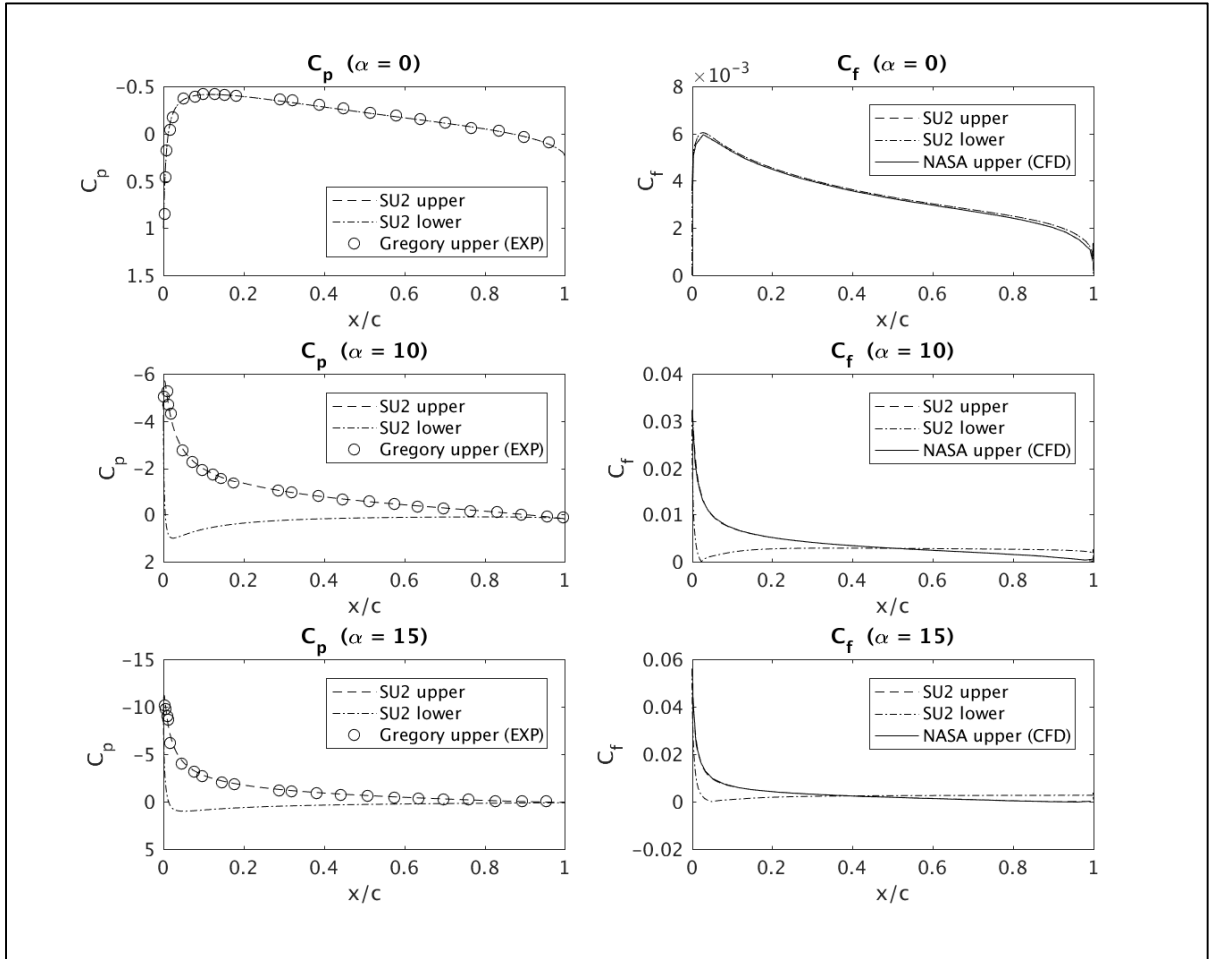
Figure 3-10: NACA 0012 C_p (left) and C_f (right) chordwise distribution at multiple angles of attack.

Finally, it must be noted that, due to resource limitations, 3D simulations are limited in the number of nodes they can allocate to any given section. Thus, the mesh refinement chosen is substantially higher than that of the section of a 3D simulation. However, this approach gives a good idea of the capabilities of the chosen RANS solver when not limited by mesh refinement.

3.3.2 Mesh generation

This section introduces the mesh strategies used to generate the regional BWB fluid domain. First the domain geometry and size are introduced. This is followed by the presentation of the structured block strategy. Then, a brief definition of the boundary conditions is presented.

3.3.2.1 Fluid Domain

Figure 3-11 presents the fluid control volume; represented by an extruded 3D C-shape domain. By assuming symmetry along the centerline, only half of the aircraft is represented. Let $L = 25m$ be the length of the center chord. The farfield is positioned $20L$ away from the aircraft in all 3 directions as presented in Figure 3-11. This is based on reviewed preliminary results from Velazquez, Weiss, and Morency (2017), where analysis of the airflow at $20L$ showed less than 1% deviation from freestream-defined values with respect to pressure P_∞, density ρ_∞, temperature T_∞ and velocity V_∞. For comparison, this is twice the $10L$ distance for non-stalled BWBs proposed by (Blessing et al., 2009).
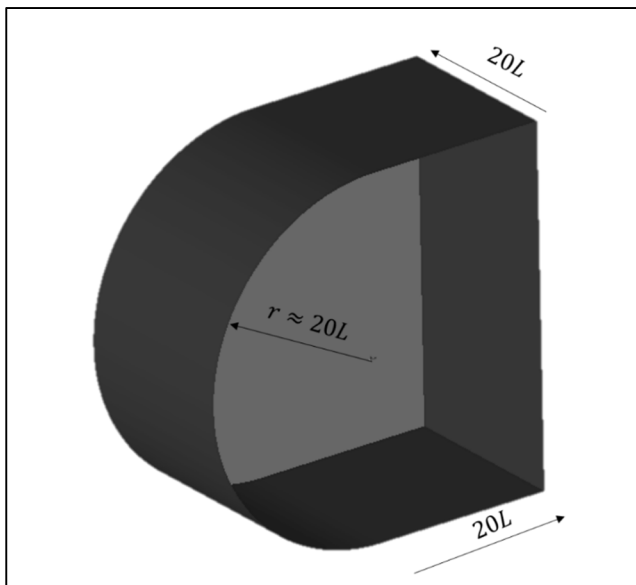
Figure 3-11:   3D Fluid domain of the BWB

3.3.2.2   Structured approach

The fluid domain is meshed using a 3D C-Grid structured block approach under the ICEM CFD environment (ICEM, 2013). Figure 3-12 presents the 64 blocks of the fluid domain. These blocks account for a boundary layer close to the BWB and a refined wake up to $6L$ downstream as well as a vortex development zone after the tip along the wingspan direction.
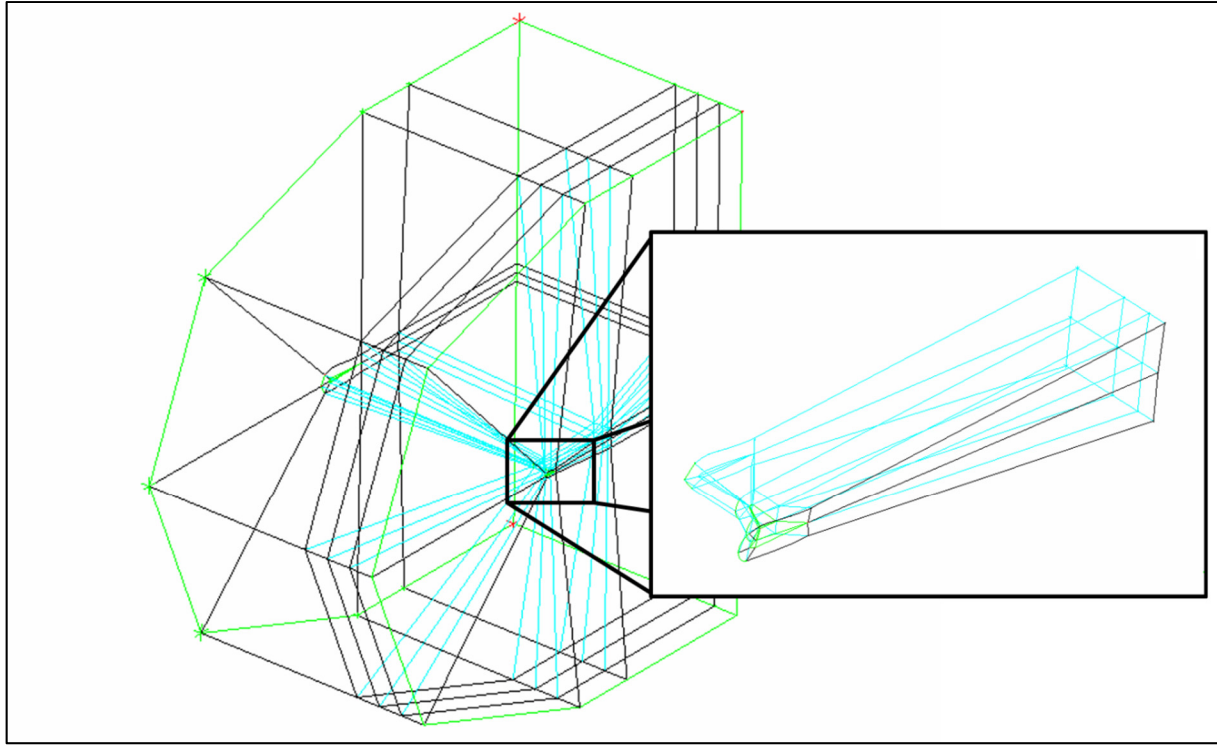
Figure 3-12:   Fluid domain structured blocking for the BWB

Development of in-house tcl scripts for ICEM CFD allowed for the automated generation of 4 different meshes; each one doubling the number of total cells. This is accomplished by multiplying the number of cells in each direction by $2^{1/3}$. Let N be the number of cells; the average cell size is calculated as $h = \left[\frac{1}{N}\sum_{i=1}^{N}(\Delta V_i)\right]^{1/3}$ (Celik et al., 2008). This defines a refinement factor r between two contiguous meshes. Finally, accounting for eventual flow separation, the initial spacing normal to all viscous walls δs is set so that the boundary layer is resolved. Average values of y^+ at an $11°$ angle of attack – close to BWB stall - are given in Table 3-9.

Table 3-9:   BWB mesh size parameters

Mesh	Code	Cells ($\times 10^6$)	h (m)	r	δs (mm)	y^+_{avg}
Coarse	5M	4.64	4.55		10	1.76
Medium	10M	9.59	3.58	1.27	5.0	0.93
Fine	20M	19.5	2.83	1.26	3.8	0.60
XFine	40M	43.0	2.17	1.30	2.5	0.47

3.3.3   Farfield Low-speed conditions

The low-speed conditions are attained at both takeoff and landing. For the current work, the low-speed considers the approach phase of the aircraft at standard sea level conditions. The theoretical approach speed V_{REF} is estimated as a multiple of the stall speed $V_{REF} = 1.3V_s = 1.3\sqrt{\frac{W/S}{\frac{1}{2}\rho C_{L,max}}}$. A simple sensitivity analysis on V_{REF} with respect to W and $C_{L,max}$ shows that, as long as $W_L < 50 \times 10^3 kg$, $V_{REF} < 68m/s$ at sea level. For comparison, Bombardier's regional CRJ-900 has an approach speed between 230 KIAS – with no flap deflection - and 170 KIAS – with full flap deflection - (Transport Canada, 2008); this is equivalent to a speed range between 118 m/s and 87 m/s. Based on these considerations, an approach speed of Mach 0.2 was fixed. With all this into account, Table 3-10 presents the farfield conditions for low speed approach.

Table 3-10:   Approach conditions

Altitude	Temp	Reynolds	$\bar{c}$	Mach	V_{REF}	ρ
0 m	288 K	73.8 $\times 10^6$	16.9 m	0.200	68.0 m/s	1.15 kg/m^3

3.3.4   CFD mesh dependence analysis

According to existing literature (Celik et al., 2008), CFD numerical simulations are prone to mesh dependence. This means that the results vary with respect to the mesh refinement level. To choose an acceptable mesh size, a mesh dependence analysis was carried out to estimate the level of confidence in the predictions based on the number of nodes per mesh. Considering the total number of simulations carried out, both precision and resource efficiency was accounted for.

The mesh dependence analysis is based on the baseline geometry at low speed conditions for each mesh size (5M, 10M, 20M, 40M). An initial full run of the 10M mesh for $\alpha \in \{-4°, 0°, 2°, 3°, 4°, 5°, 6°, 7°, 8°, 9°, 10°, 11°, 12°, 13°, 14°, 15°\}$ allowed to select 4 different angles to analyze mesh independence. The selected angles represent the zero-lift angle of attack $\alpha_{C_L=0} = -4°$, the linear lift zone $\alpha = \{0°, 3°\}$ and the stall zone $\alpha = 11°$. The 16 simulations were run on Compute Canada's Cedar and Niagara cluster (see APPENDIX VI).

Figure 3-13 presents the global aerodynamic coefficients C_L (left) and C_D (right) with respect to $N^{-2/3}$, where N is the number of nodes on each mesh, for each angle of attack $\alpha \in \{-4°, 0°, 3°, 11°\}$. Note that, in each graph, the finer mesh corresponds to the leftmost point available. The figure shows that the absolute error between 20M and 40M stays around 10^{-2} for C_L and 10^{-3} for C_D for all angles. This represents a relative error of 1.7% and 2% with respect to the 40M mesh at $\alpha = 11°$ for C_L and C_D respectively. As such, while the finest mesh is always more desirable, the 20M mesh yields acceptable results for aerodynamic coefficients prediction for less computational resources (7 core-years for the 20M mesh instead of 20 core-years for the 40M mesh). The 20M mesh is chosen for all future BWB predictions in this research.
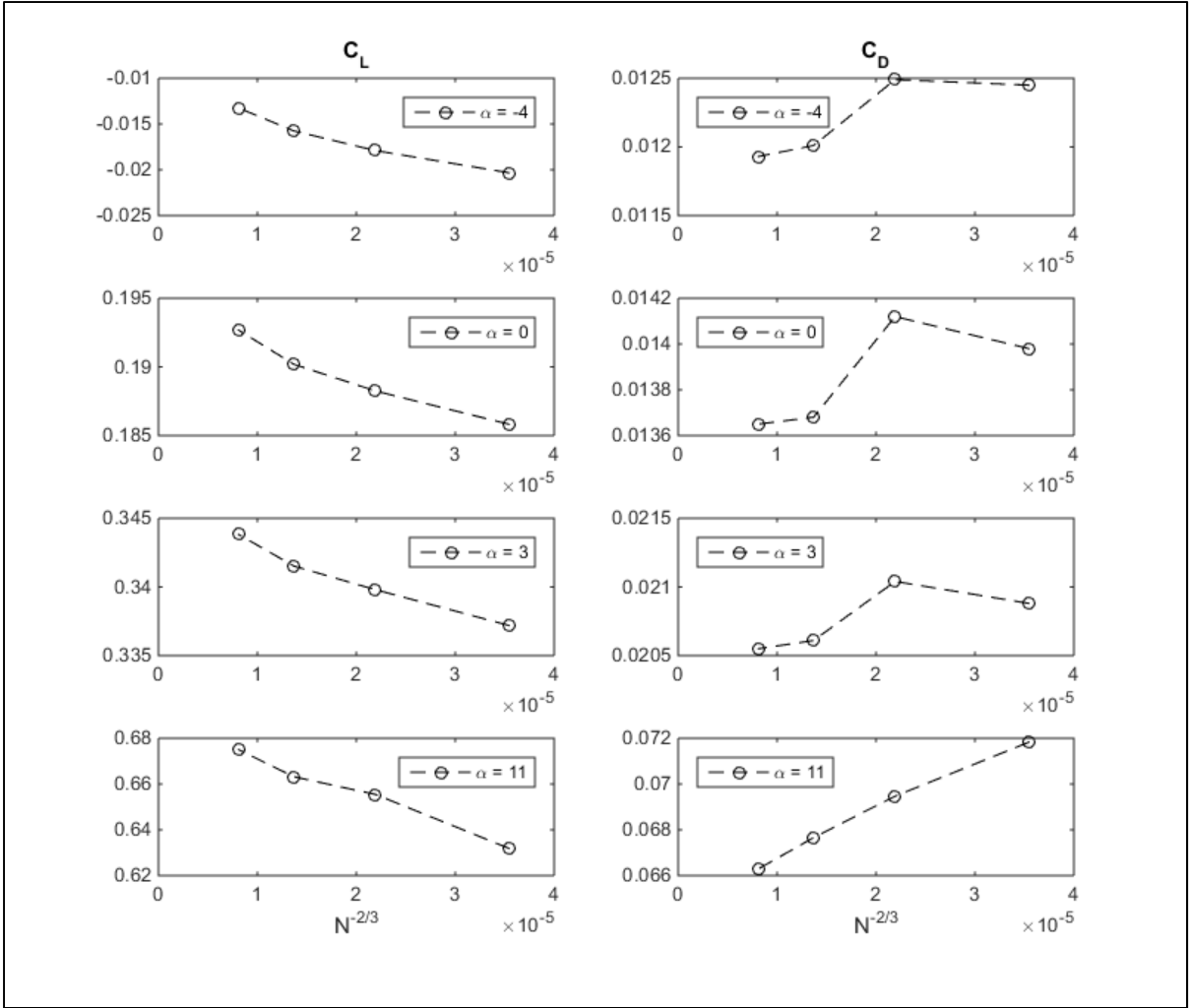
Figure 3-13:   Evolution of the aerodynamic parameters with respect to mesh size

A side note is now made for the C_D variable evolution between 5M (rightmost point) and 10M for $\alpha \in \{-4°, 0°, 3°\}$. These results contrast with the monotonicity between 10M, 20M and 40M. This shows that the 5M mesh is not accurate enough for the precision we're looking for, not only due to its bigger absolute error with respect to 40M, but in particular because it breaks the monotonicity of the variable $C_D(N^{-2/3})$. Fortunately, the finer meshes do not present this problem, all the while maintaining lower relative and absolute errors with respect to the finest mesh.

3.4   Chapter summary

This chapter's objective was to establish the geometrical and numerical framework used to study the low speed phenomena for the BWB. This was done by introducing a regional BWB geometry and by validating the chosen RANS model near stall. Future low speed analysis on the BWB is carried out based on these results.

First, the conceptual design approach was presented based on the mission requirements for the regional BWB. The modifications added to the classic conceptual design approach allowed to integrate the geometric constraints of the regional BWB into the configuration. Iterative design loops using 2.5D low-fidelity prediction models is used. The final characteristics are validated using the RANS-SA models verified in the second part of this same chapter. This allowed to obtain a mission-compliant BWB geometry.

The second part of this chapter focused on the validation of the mathematical model. On one hand, the turbulence model and the spatial discretization scheme were successfully validated against available results from the literature. This, coupled with existing literature on the application of RANS-SA models near stall validate our choice. On the other hand, the fluid domain characteristics and dimensions were presented. Furthermore, a mesh size analysis was carried out to estimate and ascertain the impact of the mesh size on the accuracy of the simulations.

The regional BWB geometry and the numerical framework have been tested and validated. Now, the low speed phenomena can be fully analysed and compared with other aircraft configurations. This will allow us to explore the aerodynamic differences at low speed between the BWB and the TAW configurations.

CHAPTER 4

LOW-SPEED AERODYNAMICS AND STALL EVOLUTION

4.1 Introduction

The previous chapter introduced the BWB geometry and the numerical framework used, in this work, to study the low speed approach. The existing literature review shows extensive research on the advantages of the BWB over the TAW under cruise conditions (Liebeck, 2004). But this literature is not present for low-speed conditions. The objective of this chapter is to identify any aerodynamic differences between these two geometries at low speeds. In particular, it must be analysed how the aerodynamic behaviour of the BWB's airfoil-shaped CB and its blending with the OW's introduces exploitable changes in C_L and C_D behaviour when compared to the aerodynamic behaviour of the cylindrical fuselage of the TAW at low speeds and its interaction – or lack of thereof - with the TAW's wing; particularly near stall. In other words, part of this chapter will focus on how the introduction of aerodynamic shapes in the CB modify the overall low-speed behaviour of the BWB with respect to the TAW aircraft. First the representative TAW geometry is presented. Then, both geometries are simulated using the RANS-SA approach previously validated. Finally, both local and global comparisons are proposed to explain the stall evolution and differences between both configurations. This chapter follows our second research sub-objective; identifying potentially exploitable design differences for low speed application.

4.2 Low-speed simulations settings

This section presents the study cases applied to the BWB and the TAW. These cases are focused around the maximum lift-to-drag ratio for the BWB and around the non-linear stall angles for both the BWB and the TAW. First, the TAW model is introduced, followed by the low-speed test matrix for each configuration.

4.2.1 TAW Model

The TAW model is based on NASA's Common Research Model (CRM) (Vassberg et al., 2008) "wing-body" (WB) version used during Drag Prediction Workshop 5 (DPW5) (Levy et al., 2014). This aircraft geometry presented in Figure 4-1 was selected based on the fact that it was literally developed to serve as a baseline representative of modern TAW geometries; as such, the CRM has been at the center of recent and relevant numerical workshops like AIAA's DPW 4, 5 and 6 and High Lift Prediction Workshop 3. Moreover, this geometry is publicly available and some cases can be compared against experimental data. The WB version was selected for comparative purposes against our BWB. Its geometric characteristics, including its wingspan b and its fuselage length L, are presented in Table 4-1.
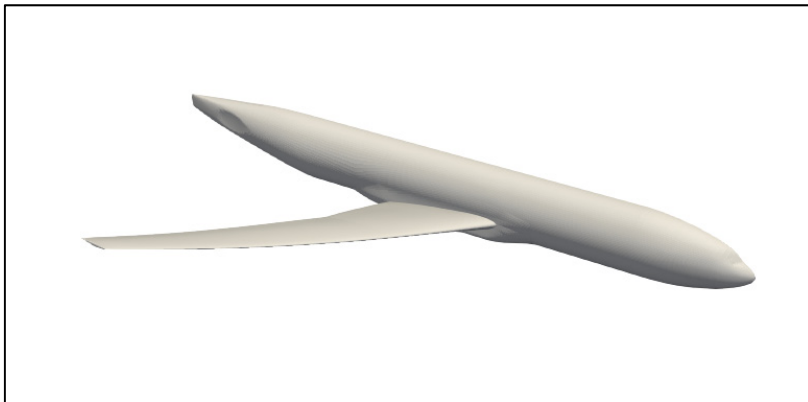
Figure 4-1:   CRM WB geometry

Table 4-1:   Geometric characteristics of the CRM geometry

S_{ref}	$\bar{c}$	AR	b	L
$383.7m^2$	$7.00\ m$	9.00	$58.8m$	62.7

The fluid domain for this geometry is represented by a square frustum. Consider the fuselage length L, then the fluid domain spans $60L$ in the longitudinal direction, $6L$ to $11L$ in the wingspan direction and $8L$ to $17L$ in the transversal direction. These distances are given in fuselage lengths instead of the more conventional mean aerodynamic chord $\bar{c}$ because, for the

BWB, $L_{BWB} \approx \bar{c}_{BWB}$ whereas for the TAW, $L_{TAW} \approx 10\ \bar{c}_{TAW}$. Figure 4-2 presents a scheme of this domain, where the TAW is placed $21L$ away from the front of the domain and $38L$ away from the back of it..
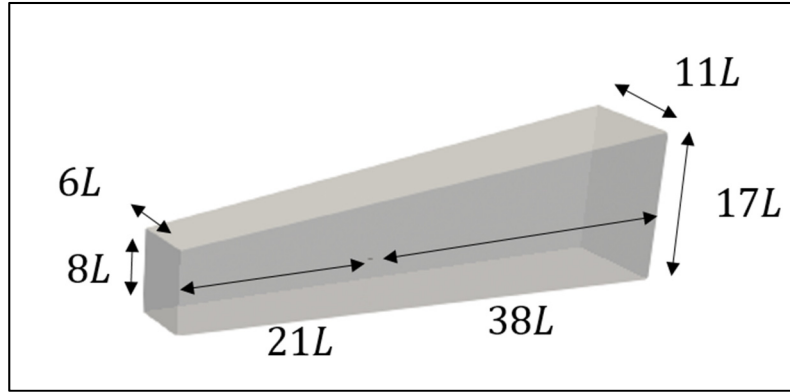
Figure 4-2:   TAW fluid domain scheme

The mesh used for the TAW was originally developed by the IDEA Research Chair at Polytechnique Montreal and presented at NASA's DPW5 (Gariépy, Malouin, Trépanier, & Laurendeau, 2013); it is publicly available through the DPW server (NASA, 2012). The hexa mesh was created with the ICEMCFD software by using a structured H-C blocking approach. Following indications by the DPW5, only the medium mesh size proposed by the DPW5 case 2 was considered. The chosen mesh contains 5.9 million nodes and an average y^+ of 0.23.

4.2.2   Test Matrix

This subsection introduces the multiple simulation cases done for each geometry at low-speed. Particular effort was done for the BWB geometry to obtain a detailed aerodynamic polar, within 1° precision, allowing to estimate the zero-lift drag coefficient C_{D0}, the maximum lift-to-drag ratio $(L/D)_{max}$, and the stall initiation and evolution past the linear lift zone. While $(L/D)_{max}$ varies with Re and $Mach$, it is more sensitive to Re so long as $Mach < M_{cr}$. Furthermore, the Reynolds at sea level and low speed is comparable to the Reynolds at cruise altitude and speed. Thus, $(L/D)_{max}$ can be used as an approximation of $(L/D)_{max}$ at cruise

88

conditions. This use is necessary in order to integrate these values into the mission performance analysis, as was briefly presented in CHAPTER 3. As for the TAW geometry, the simulations were mainly focused around the stall zone. For this study, a total of 19 simulations were considered for a resource usage of 109 core-years (cf. Table 4-2). The chosen angles of attack cover both the zero-lift angle of attack, the linear lift zone, and the stall zone. This zone is unique to each aircraft, thus resulting in different studied angles for each configuration. The BWB simulations took place in the Cedar and Niagara clusters whereas the TAW simulations took place in the Placentia cluster. Refer to APPENDIX VI for cluster details. Finally, the farfield conditions are the same ones specified in Table 3-10 page 81. The reader is referred to section 3.3.3 for the details on their determination.

Table 4-2:   Aircraft test cases (TAW vs BWB)

Geometry	Angle of attack	Total	Nodes
BWB	$\alpha \in \{-4°, 0°, 2°, 3°, 4°, 5°, 9°, 10°, 11°, 12°, 13°, 14°, 15°\}$	11	20M
TAW	$\alpha \in \{3°, 8°, 9°, 10°, 11°, 12°, 13°, 14°\}$	8	6M

We are now ready to compare the results from both geometries. First, a qualitative approach of the airflow as it detaches from the airframe is carried out based on airflow direction and local skin friction measurements. This allows to loosely identify the stalled regions and link them to local pressure (c_p) and skin friction (c_f) coefficients. This is followed by a quantitative analysis of the evolution of the local and global aerodynamic parameters for lift and drag on both geometries.

4.3   Qualitative analysis (3D)

This subsection presents a visual analysis of the airframe state and the airflow around both geometries at pre and post stall angles. To do so, graphic post-processing of the state of the airframe surface is introduced. Concerning the 3D airflow, the reader is advised to consider this qualitative subsection for what it is: a general view on the tendencies of the flow with respect to surface attachment/detachment. The nature of the RANS model used wouldn't allow

to make any precise quantitative analysis of the airflow structures themselves, and it is not the purpose of this work to do so, thus we use the 3D airflow results to find global tendencies only. For this section, first, the recirculation bubbles around the airframes are presented. Then, the $\overrightarrow{c_f}$ surface streaklines present the local boundary layer detachment progression.

4.3.1   Airflow and recirculation bubbles

Let $\overrightarrow{e_{st}}$ be the farfield stream direction vector defined as $\overrightarrow{e_{st}} = \cos(\alpha)\,\overrightarrow{e_x} + \sin(\alpha)\,\overrightarrow{e_z}$. Let $\vec{V}$ be the velocity vector, and $V_{stream} = \vec{V}.\overrightarrow{e_{st}}$ the projection of the velocity vector in the streamwise direction. Figure 4-3 shows the velocity streamlines near the BWB airframe at $\alpha = 13°$. The color scale represents the normalized value $\frac{V_{stream}}{\|\vec{V}\|}$ which corresponds to the portion of the local velocity aligned with the streamwise direction. In the case of Figure 4-3, some of these streamlines show the presence of vortices above the upper wing surface curling around the spanwise axis. These twisting streamlines describe zones of airflow recirculation However, the amount of streamlines needed to visualize the whole recirculation zones characterized by these vortices, is both numerically and visually impractical. To simplify these visuals, the streamlines are replaced by the isosurface $V_{stream} = 0$. This isosurface effectively represents the zone in space where the airflow switches direction with respect to $\overrightarrow{e_{st}}$. We define this isosurface as a recirculation bubble. Figure 4-3 shows how the blue recirculation bubble is effectively equivalent to the vortices generated by the recirculating streamlines.
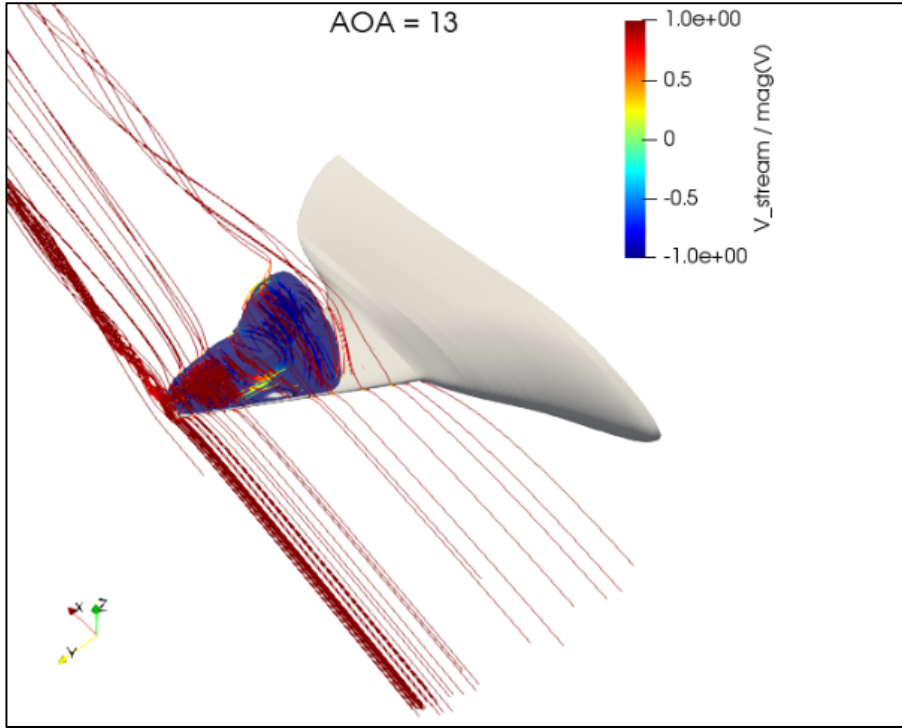
Figure 4-3:   Streamlines and recirculation bubble over the regional BWB at $\alpha = 13°$. Recirculation bubble represented by blue isosurface.

Figure 4-4 and Figure 4-5 present the recirculation bubbles at different angles of attack, as well as the local skin friction coefficient $c_f = \left\| \vec{c_f} \right\|$ in log10 scale. Blue isocontours represent $c_f = 10^{-4}$. c_f can be considered almost negligible below this value. Note that, excluding the trailing edge (TE), the recirculation bubbles seem to appear above surfaces where $c_f < 10^{-3}$. Figure 4-4 shows this evolution for the BWB. The recirculation bubble appears close to the wingtip at $\alpha = 11°$ and progressively spreads towards the centerbody. While the OW is fully covered by recirculation bubbles at $\alpha = 14°$, the CB is barely affected by this recirculation, even at this angle of attack. Note that it takes from $\alpha = 11°$ to $\alpha = 14°$ to fully engulf the OW. Further data will show that this BWB geometry presents a stall at $\alpha_s = 10°$, which is the last angle prior to the apparition of recirculation bubbles. This suggests, as expected, that there is a link between stall and the presence of recirculation bubbles above the upper surface via boundary layer detachment.
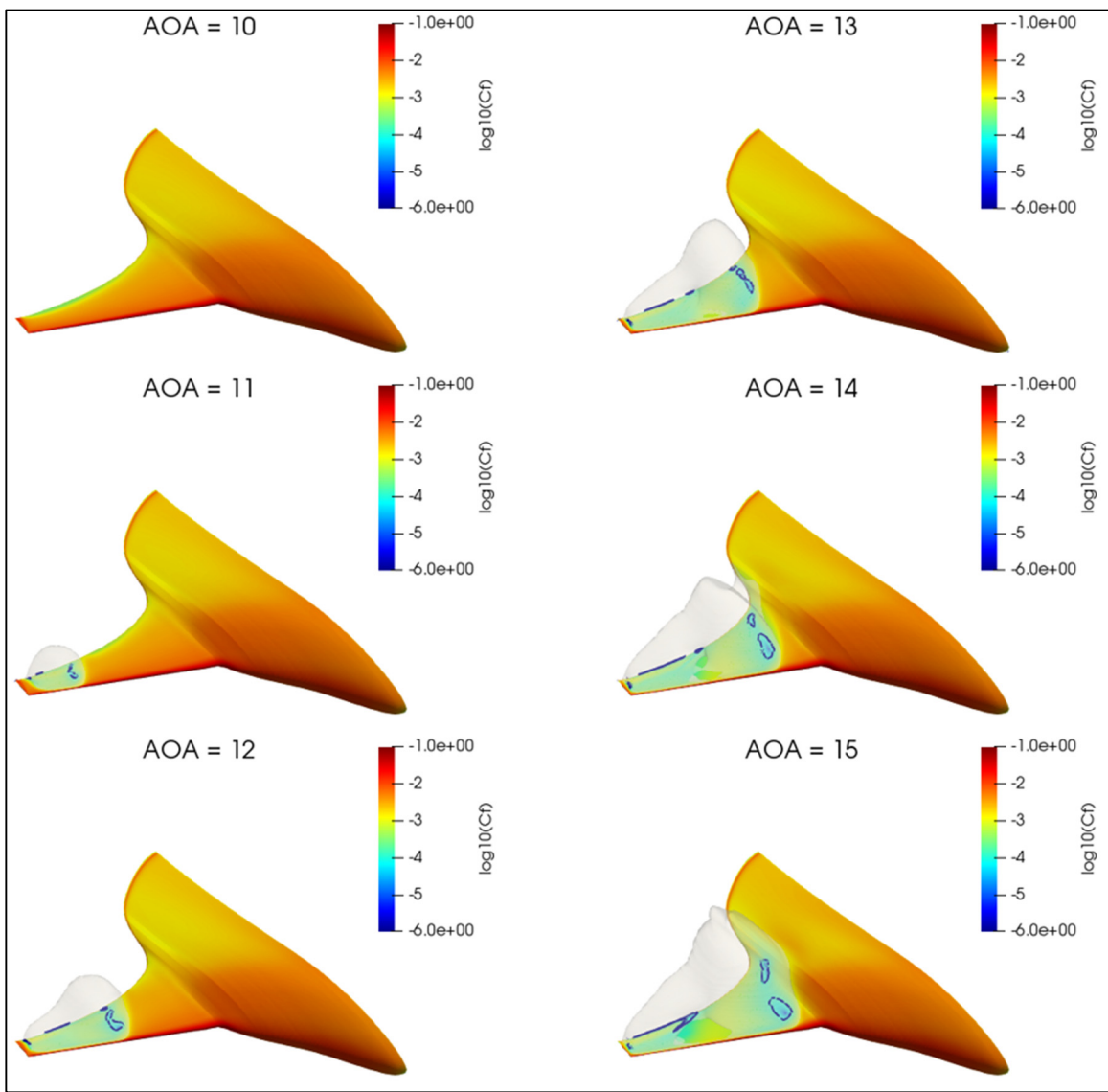
Figure 4-4:   BWB - Evolution of the skin friction coefficient (log10 scale) and recirculation bubbles (grey isosurface).

Figure 4-5 presents the equivalent visuals for the TAW at slightly different angles of attack. In this case, the recirculation bubble appears at $\alpha = 10°$ at the wingtip and slowly spreads towards the fuselage. However, at $\alpha = 12°$, a second recirculation appears above the midwing. The wing is fully covered at $\alpha = 14°$. In this case, the global stall appears at $\alpha_s = 11°$. In this case, this is the last angle right before a critical section of the wing is engulfed by recirculation bubbles ($\alpha = 12°$). Up until this angle, the recirculation bubbles are contained close to the

airframe and near the wing tip whereas after this point they quickly engulf the rest of the wing. Note that while the bubbles appear early, they don't trigger global stall until the midwing is covered by vortexes, which would imply that the TAW's wing is capable of handling a limited amount of local wingtip stall. Note that, just like for the BWB, the fuselage doesn't present any sign of recirculation bubbles or local stall.
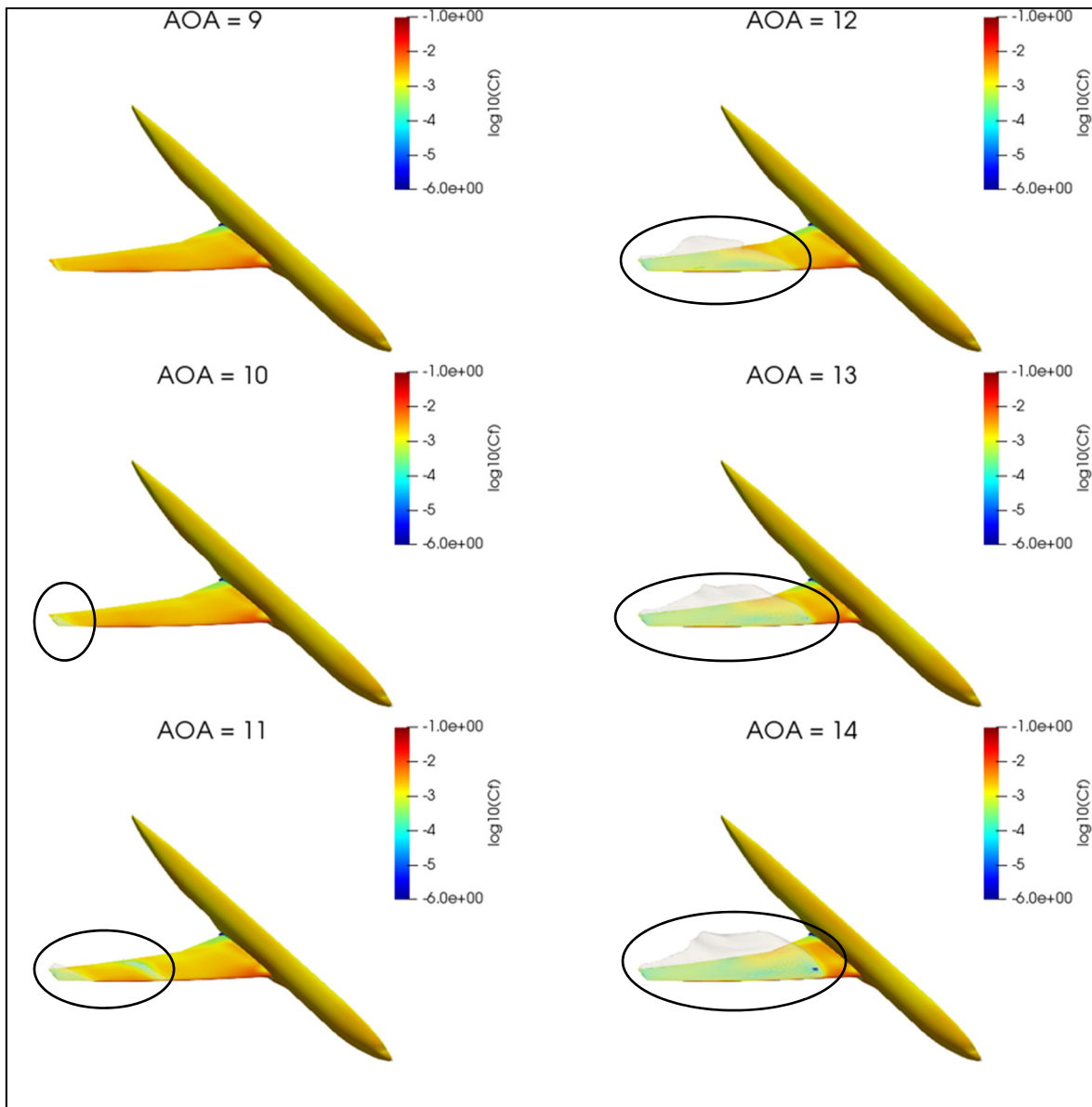

Figure 4-5:   TAW - Evolution of the skin friction coefficient (log10 scale) and recirculation bubbles (grey isosurface).

So far, both geometries act similarly: lift is maintained so long as the wing is not engulfed in recirculation bubbles. Presence of recirculation bubbles is linked to stall as they indicate that either the plane has already stalled (BWB) or that it is very close to stalling (TAW). In both cases, neither the fuselage nor the CB show any recirculation bubble, even at angles known to be higher than the corresponding global stall angle. The difference in bubble evolution seems to be linked more to the specific wing or OW design than to the shape of the fuselage or CB respectively. A closer look at the local surface coefficients will be necessary to find geometric-induced differences between the influence of the fuselage and that of the CB.

4.3.2   Surface detachment

Analysis of the skin friction coefficient $\overrightarrow{c_f}$ along the upper surface of both aircrafts show the detachment evolution on the surfaces above which the recirculation bubbles develop. Each one of the different angles of attack presented in Figure 4-6 (BWB) and Figure 4-7 (TAW) is divided into 2 sides. The right hand side shows a conventional c_p distribution along the upper surface along with some $\overrightarrow{c_f}$ streaklines (in white) which help visualize the path of the particles next to the surface. The left hand side shows an oil flow visualization of the whole surface along with a measure of the boundary layer detachment. For this case, the streamwise detachment indicator $c_{f,x}/c_f$ presented in APPENDIX V is used.

The surface evolution presented in Figure 4-6 and Figure 4-7 confirms the link between presence of recirculation bubbles above the airframe and partial detachment on the airframe surface along $\overrightarrow{e_x}$. The detachment zones indicated by $c_{f,x}/c_f < 0.5$ closely follow the projection of the recirculation bubbles on the airframe. Note however that inside these detachment zones, only the sectors where $c_{f,x}/c_f$ is in light blue to dark blue represent negative airflow.

Consider angles 14° and 15° from Figure 4-6. Positive airflow zones (green to red) appear past the detachment front towards the leading edge of the aircraft. However, Figure 4-4 showed that these sectors are covered by a recirculation bubble, which means that the airflow is trapped

inside the bubble. Thus, even if some airflow zones are locally attached, this local attachment is of no consequence with regards to the global stall state of the aircraft. Moreover, just as for the recirculation bubble, the detachment starts at $\alpha = 11°$ near the wingtip – right after the global stall is attained - and progresses towards the centerbody. In this particular case, the outskirts of the detachment zones present the highest detachment as proved by the presence of dark blue zones.

As for the TAW, Figure 4-7: shows a slightly different pattern. While the detachment zone starts at the wingtip at $\alpha = 9°$, the mid-section of the wing presents detachment at $\alpha = 11°$, which then expands to the rest of the wing. This is a desirable feature since it allows the pilot to react faster in the presence of stall development. This feature is linked to this specific wing design rather than linked to the BWB or the TAW configurations per se. Contrary to the BWB though, the detachment seems to be mostly initiated at the leading edge, although, again, this is likely due to the nature of the wing and its airfoil section rather than the aircraft configuration itself. Note that in this case too, the fuselage doesn't present signs of local detachment.
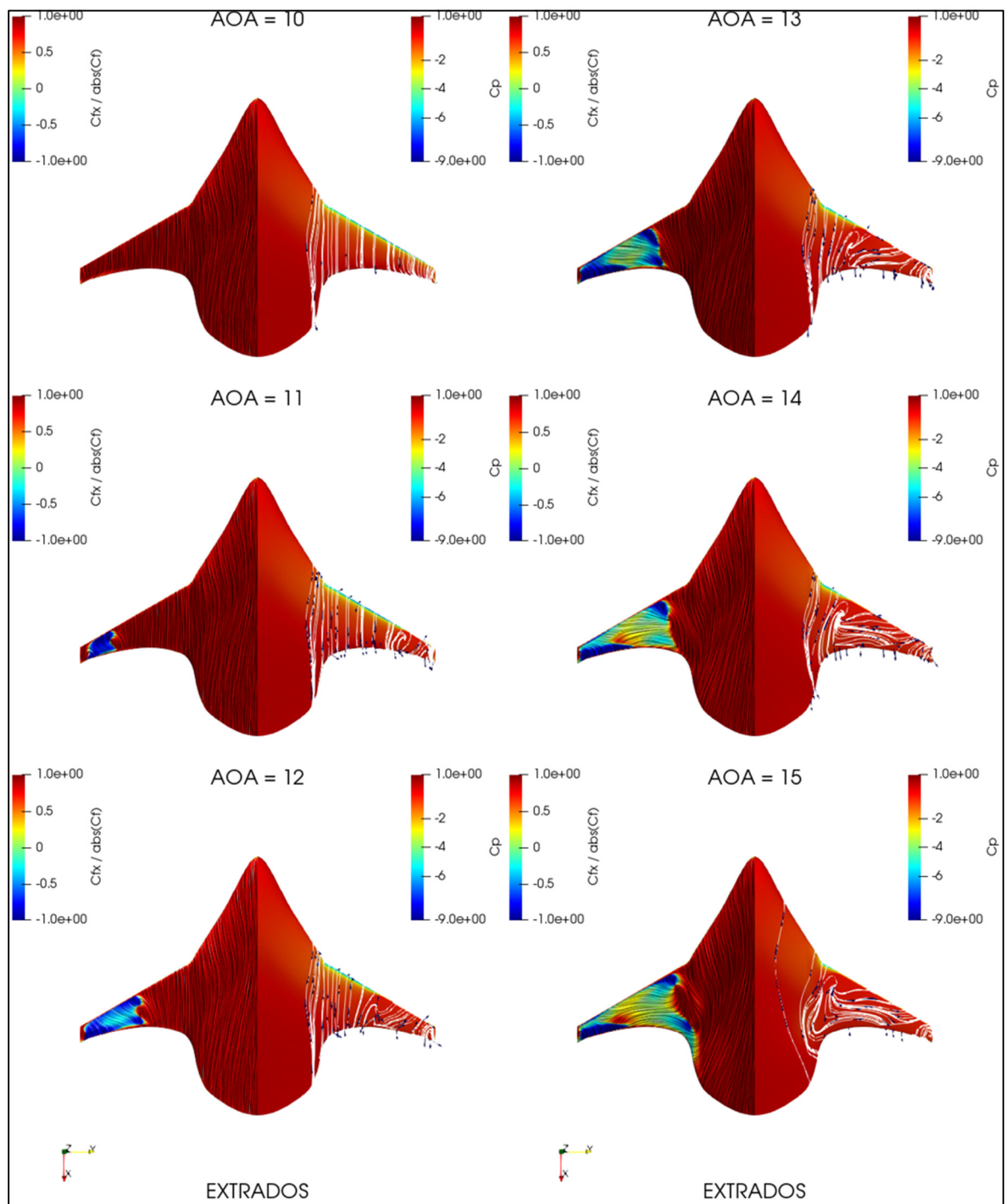
Figure 4-6: BWB upper surface (Extrados) at different angles of attack. Oil flow visualization and skin friction detachment indicator $c_{f,x}/c_f$ (left side wing). Conventional presentation of the pressure coefficient and surface streamlines (right side wing).
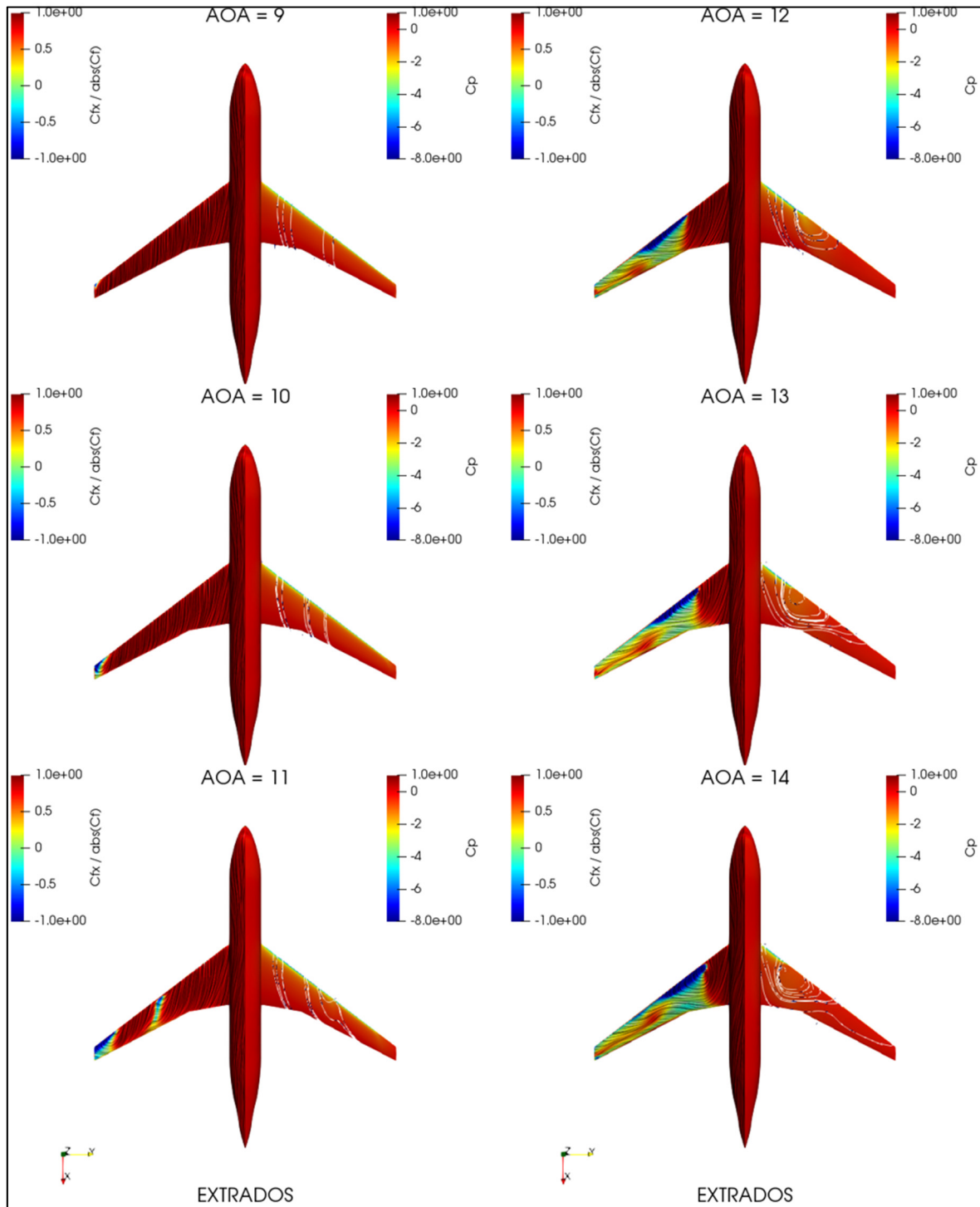
Figure 4-7:   TAW upper surface (Extrados) at different angles of attack. Oil flow visualization and skin friction detachment indicator $c_{f,x}/c_f$ (left side wing). Conventional presentation of the pressure coefficient and surface streamlines (right side wing).

It must be noted that while neither the fuselage of the TAW nor the CB of the BWB present signs of flow detachment – even at high angles of attack -, it is interesting that the BWB's wider CB doesn't present stall even though it is technically part of the whole BWB wing. This is associated with the change in section characteristics between the CB and the OW. In other words, the higher stall angle of the LA-2573A airfoil at the CB over that of the SC(2)-0712 airfoil at the OW, coupled with local geometric and aerodynamic parameters like sweep, twist, chord, Reynolds and Mach result in an outer wing that stalls first and a CB that doesn't stall because its own aerodynamics still allow it to continue generating lift. Note that the stall only grows progressively towards the CB and seems to slow down at the point where the change in sections take place. The presence of a smooth transition between the CB and the OW seems to delay the propagation of stall towards the CB.

A similar thought process can be applied towards the TAW's fuselage: it could be possible that the fuselage doesn't stall because its local aerodynamic characteristics don't allow it, even though the TAW's has already stalled. In this regard it would behave in the same way as the BWB's CB. However, a deeper analysis of the local lift capacity will show, as expected, that the amount of lift generated by the CB is higher than that of the fuselage. Inversely, the amount of drag generated by the fuselage is higher than that generated by the CB.

Do note however that a closer look at the TAW wing shows a similar "stall resistance" phenomenon as that of the BWB. Stall is initiated outboard and seems to stop at the Yehudi break at the point where the TE sweep changes radically. At this point, the local airfoil presents a slight modification – see Figure 4-8 - while the local sweep diminishes radically; thus, generating a non-smooth variation of the local properties. This break point happens to coincide with the limit of the stall propagation. This reinforces the idea that sudden local changes in geometry parameters or airfoil shape have a significant impact in stall propagation – or lack of thereof -. In particular, we retain the basic idea that the different sections of both aircrafts stall at different angles of attack. Based on this qualitative approach, the following sections will explore how these local changes are linked to the global aerodynamic evolution of the aircraft.
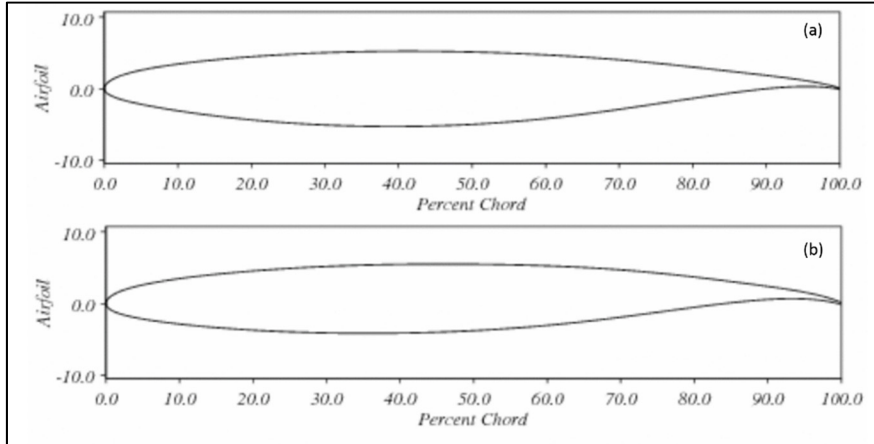
Figure 4-8:   TAW Airfoils at the Jehudi break (a) and at the
outboard station (b).

4.4   Quantitative analysis (2D): section and wingspan distribution

In order to better identify the local aerodynamic behavior and the stall triggers on both geometries, this section presents the local distribution of pressure, skin friction and local aerodynamic coefficients. The classic link between the airflow detachment and the aircraft stall is established for the BWB. More importantly, the different contributions of the multiple wetted surfaces of each aircraft are identified.

4.4.1 c_p and c_f chordwise distribution

Consider the local pressure and skin friction coefficients $(c_p, c_{f,2D})$, where $c_{f,2D} = \left\| c_{f,x}\vec{e_x} + c_{f,z}\vec{e_z} \right\|$. Now consider the normalized spanwise coordinate $\eta = \frac{y}{b/2}$. This section presents a comparative analysis at a reduced number of angles of attack ($\alpha_{BWB} \in \{0°, 9°, 11°, 13°\}$ and $\alpha_{CRM} \in \{3°, 9°, 11°, 13°\}$). This is done for ease of visualisation. The chosen stations are the same stations chosen for the DPW5 plus the center line ($\eta = 0$) and the end of the wing ($\eta = 0.99$).

First, Figure 4-9 presents the c_p of the BWB at both centerbody ($\eta = 0, \eta = 0.13$) and outer wing ($\eta > 0.3$). Note that the normalized chords x/c go from 0 to 1 for each station; in other words, only the local chords are used at each station. This figure shows the double cambered nature of the centerbody airfoil section. This is exactly the reason why the LA2573A airfoil was chosen for the CB. Note that all stations have an increasing pressure differential with α even at high angles of attack. Finally, note that the local pressure differential generated by the CB's upper surface seem to be 10 times weaker than that created around the OW. This is in line with the idea that the OW is responsible for generating most of the lift. While this is true, it must be noted that the CB's pressure distribution still generates lift and it does so over a larger surface than the OW.
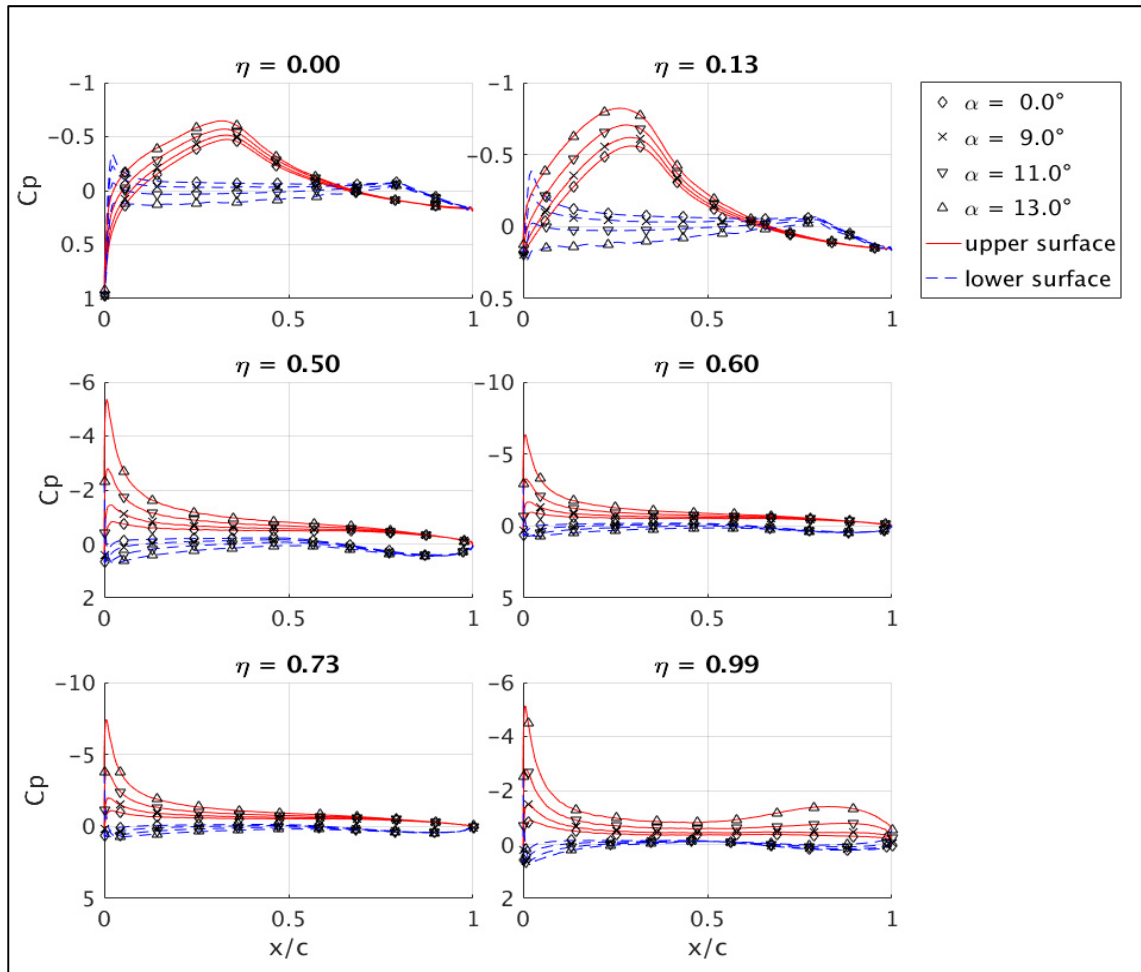
Figure 4-9 :   BWB pressure coefficient chordwise distribution at different sections

Respectively, Figure 4-10 shows a similar evolution but for the TAW: pressure differential keeps increasing with angle of attack. In this case, the fuselage ($\eta = 0$) brings little to no contribution while the wing generates most of the pressure differential. This is in line with classic TAW behaviour. Comparing both geometries, it is clear that while both CB and fuselage avoid stall, the CB acts as a secondary wing while the fuselage doesn't.
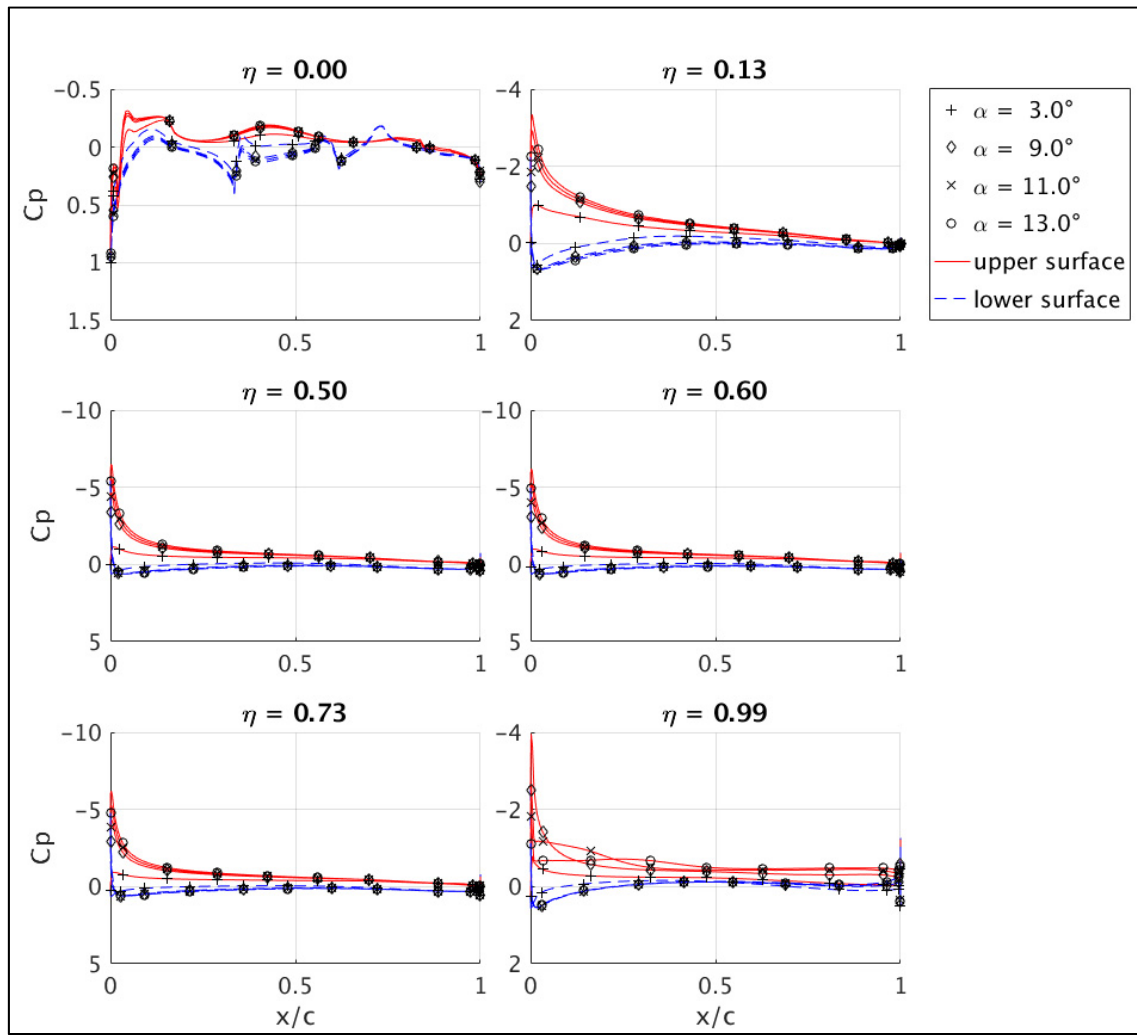
Figure 4-10 : TAW pressure coefficient chordwise distribution at different sections

The analysis of the skin friction coefficient is relevant, for our case, in the context of local stall identification. For this reason, the initial detachment front, inspired from the detachment front

presented in DPW5 (Levy et al., 2014), is drawn in Figure 4-11 and Figure 4-12 . These figures are based on the local 2D friction coefficient vector $\overrightarrow{c_{f,2D}} = c_{f,x}\overrightarrow{e_x} + c_{f,z}\overrightarrow{e_z}$, and they show the points along the wingspan where $c_{f,2D}$ first switches sign ($c_{f,2D} = 0$). On these 2 figures, the y axis represents the local normalized chord from trailing edge (TE) to leading edge (LE), and the x axis represents the normalized wingspan η. These figures allow to follow the progression of the detachment front (if any) along – or close to – the leading edge of the aircraft. The idea behind it is that any portion of the chord located behind the detachment front can be considered as compromised. By extension, once the detachment front has hit the LE, the whole section is considered as compromised. The graphs allow to have a global view of the evolution of compromised wingspan sections as α increases. Figure 4-11 shows that, for the BWB, the detachment front first appears at $\alpha = 11°$ near the wingtip – once global stall has been attained - and slowly expands towards the wingtip and towards the CB; stopping at $\eta \approx 0.33$, which corresponds to a point within the transition wing. Note that this analysis is more precise than the recirculation bubbles: local stall appears initially near – but not at – the wingtip and it spreads towards the CB without reaching it.
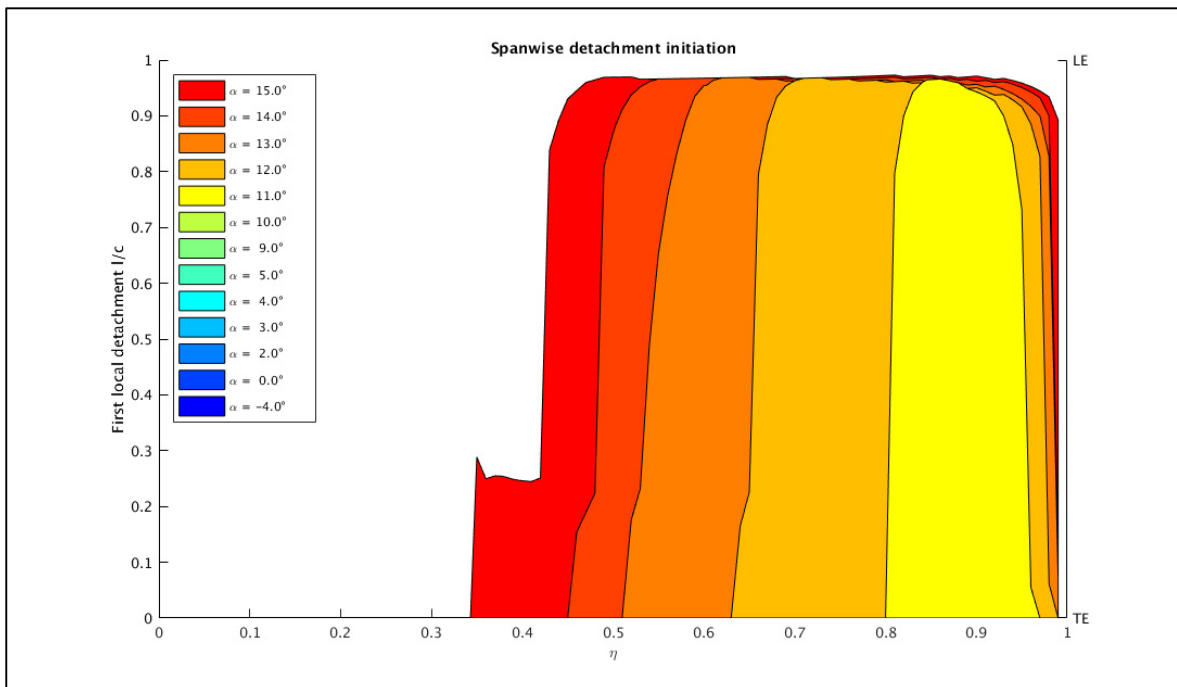
Figure 4-11 :   BWB detachment front

102

In the case of the CRM, Figure 4-12 shows that, the detachment front first appears at the wingtip at $\alpha = 9°$. At $\alpha = 11°$, the detachment front abruptly appears in the middle of the wing, cutting the wing in 2 attached and 2 detached zones. Finally, after $\alpha = 11°$, the detachment front is present almost everywhere on the wing. We observe the presence of the detachment front near $\eta = 0.1$ which corresponds to the fuselage/wing interface of the TAW, and which is always present even at low angles of attack.
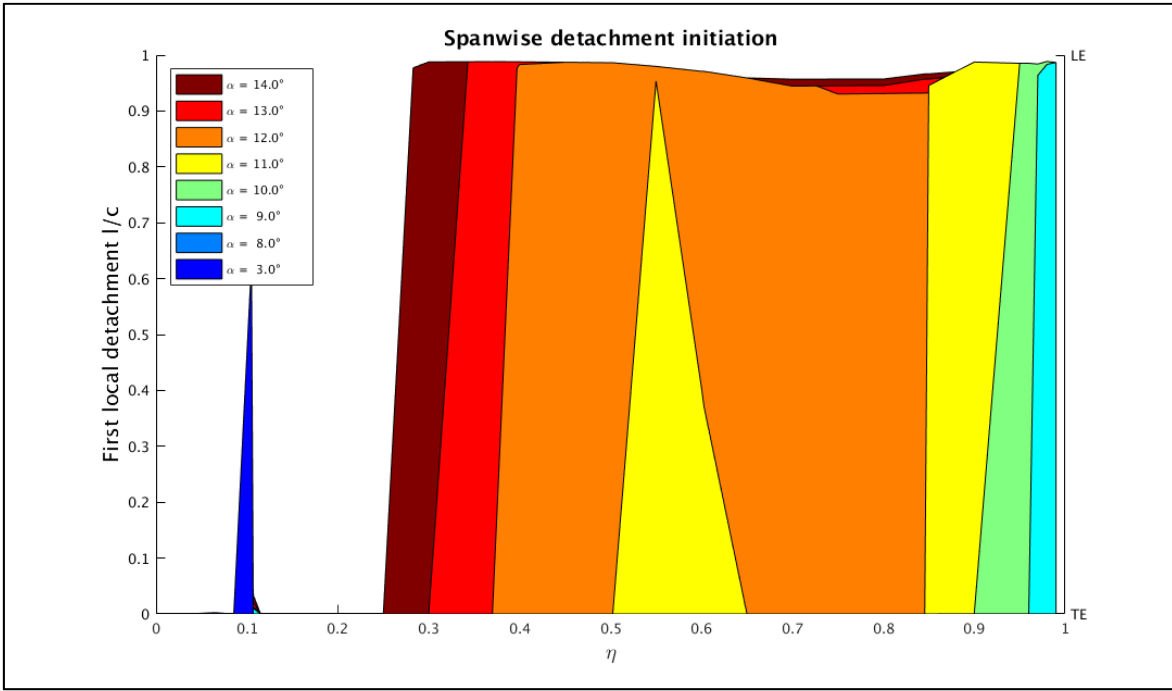
Figure 4-12 :   TAW detachment front

Analysis of Figure 4-9 to Figure 4-12 show that the BWB possesses a critical section near the wingtip that triggers global stall as soon as this section stalls. In the case of the TAW, this critical section is located at the midwing. This relates to the idea proposed by Phillips and Alley (2007) that the global stall for both geometries might be linked and triggered by a reference critical section η_{ref}. On top of this, we retain that the CB keeps providing positive pressure differentials even past the BWB's global stall. This means that only the OW presents local stall. In the particular case of the BWB this is interesting since the CB is designed to also

provide lift; in other words, it would be interesting to play with the geometry in order to delay stall and use this non-stalled CB surface. If this hypothesis is correct, this would imply that there might be a chance to attain higher C_{Lmax} values if the stall of the critical section could be delayed somehow. Further analysis provided below will point us in this same direction.

4.4.2 Local aerodynamic coefficients: spanwise distribution

Let us now integrate c_p and $\overrightarrow{c_{f,2D}}$ into local lift and drag coefficients C_l and C_d along the wingspan. In particular, we will analyse the link between these local coefficients and the contribution of the different lifting surfaces. Let us now introduce the wetted surface ratio $S_{wet}/S_{wet\,tot}$, representing the percentage of the total wetted surface at a given station η, comprised between the centerline and η. The wetted surfaces are introduced so as to compare the TAW performance with an all-wing aircraft like the BWB (Raymer, 2006). Note that for the TAW, the fuselage represents around 50% of the total wetted surface, whereas for the BWB, the CB represents 67% of it. On top of this, the following figures represent normalized values, allowing for further comparisons.

First, Figure 4-13 shows the normalized local lift distribution C_l/C_L for the BWB along the wingspan for multiple angles of attack. This figure shows the magnitude of the local lift coefficient C_l with respect to that of the global lift coefficient C_L. The red and blue vertical dashed lines delimit the centerbody/transition wing interface and the transition wing/outer wing interface respectively. This figure shows that the OW generates C_l values between 1 and 3 times that of C_L at all times, while the CB generates, on average, C_l values between $0.4C_L$ and $0.7C_L$ only. A closer view to the spanwise distribution shows that, up to $\alpha = 15°$ the CB simply doesn't present stalled sections; on the contrary, these sections' C_l keep increasing with α. This, increase, however, is not sufficient to compensate for the loss of lift on the OW present at $\alpha_s^{BWB} = 10°$. This would suggest that by tweaking the BWB design, it might be possible to use some of this centerbody's extra lift available. At this point, this is highly speculative. For this reason, this specific hypothesis will be treated in the next chapter.
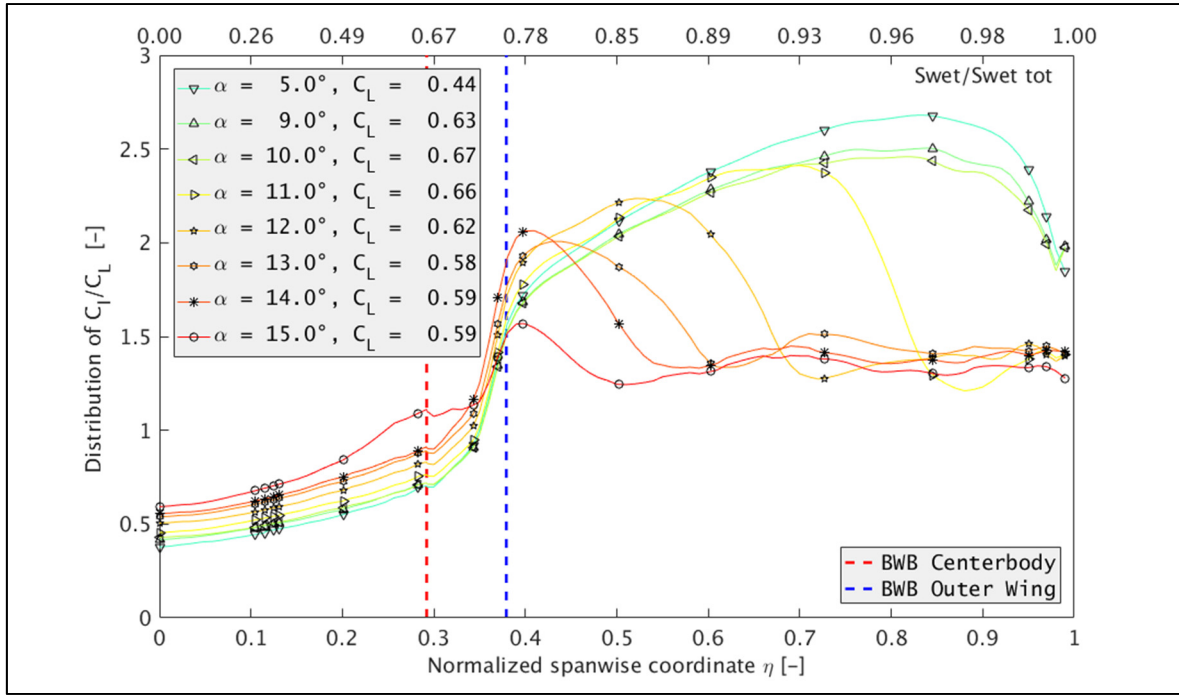
Figure 4-13 :   BWB Section lift coefficient distribution

Figure 4-14 is the equivalent figure for the TAW. In this case, the local lift C_l for the wing presents average wingspan values between 1 and 1.5 times C_L prior to stall and around $0.5 C_L$ past stall. For the fuselage however, C_l is located between $0.12 C_L$ and $0.22 C_L$. As expected, the fuselage generates almost no lift, yet represents almost 50% of the wetted surface. In this case, just as for the BWB, the fuselage doesn't attain stall either. With values of $C_l / C_L \approx 0.17$, it is unrealistic to consider that the fuselage could take over for the loss of lift of the main wing. This is normal, since that is not the function of the fuselage, and this fuselage was not designed to generate lift efficiently.
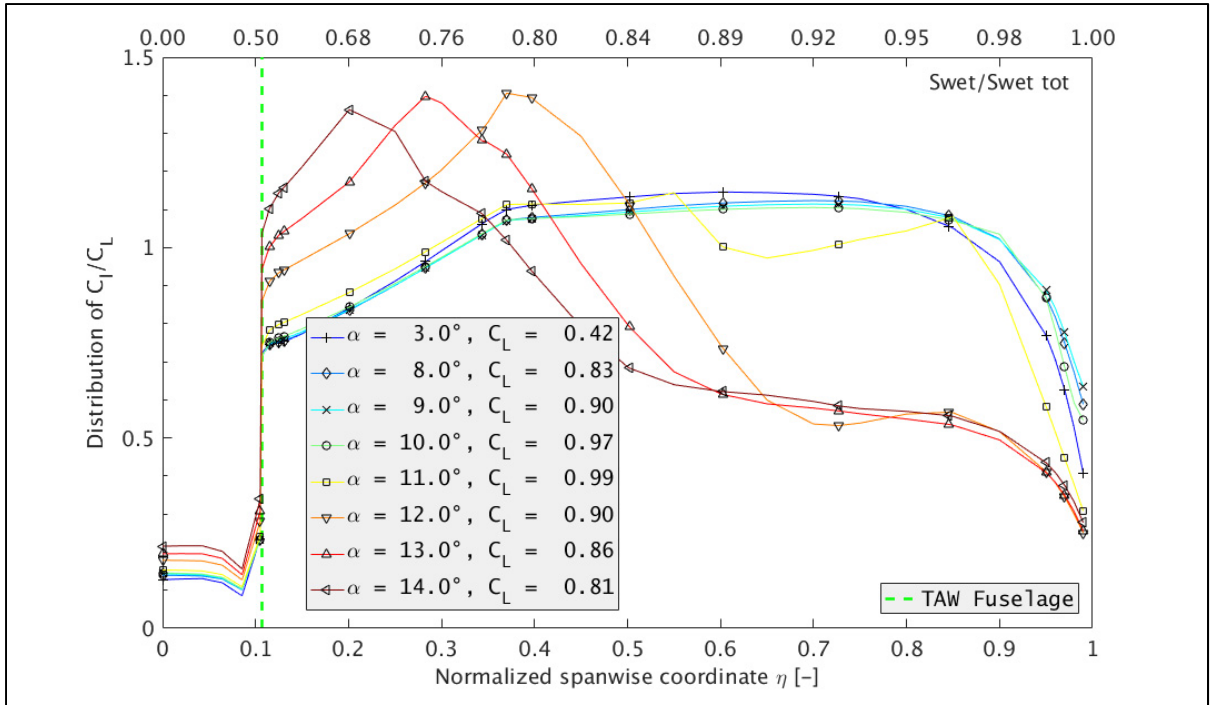
Figure 4-14 :   TAW section lift coefficient distribution

While the lift coefficient distribution is adequate to analyze local stall, it fails to measure local contribution to the global lift force. Therefore, Figure 4-15 shows the local lift distribution l (per unit span) for the BWB normalized by the global lift force L. The results are clearer: as the angle of attack increases, the CB not only increases its lift contribution, but it also becomes the highest source of lift on the aircraft; thus compensating partially for the loss of lift due to outer wing stall. Note that the Transition Wing is characterized by a rugose valley, which represents a missed opportunity for the baseline BWB to better blend the local aerodynamic forces between the CB and the OW as proposed by Figure 1-2. This shows that a smooth surface blending between CB and OW is not enough: blending of the aerodynamic behavior between CB and OW is also required to optimize lift and drag participation. Furthermore, note that the CB provides the steadiest source of lift on the aircraft at all angles. In this case, 65% of the wetted surface corresponds to the CB. Furthermore, as previously stated, the centerbody doesn't present signs of stall, even past the BWB's global stall angle, so it is probable that, past $\alpha_s^{BWB} = 10°$, it just simply can't generate enough lift on its own to compensate for the loss of the outer wing.

Let us note that for $\alpha = 9°$, $L = 52.8 \times 10^4 N$. According to Chapter 3, this lift force is superior than the BWB's takeoff weight W_{TO} $(44.7 \times 10^3 \ kgf)$ and its zero-fuel weight $(35 \times 10^3 kgf)$. With this, one of the initial questions of this research has been answered: this means that this configuration of the BWB doesn't require high lift devices to generate enough lift to sustain its ascent/descent at low speed. This, however, may seem counterintuitive seeing as how the BWB's maximum lift coefficient has a value of 0.66 when compared to conventional aircrafts whose maximum lift coefficients – with high lift devices – are more than 3 times this value. This was explained back in Chapter 3, where it was stated that the reference surface of the BWB is roughly 3 times that of a TAW. Thus, the larger lifting surface of the BWB allows to diminish C_{Lmax} to values naturally attainable by the wing without the need for high lift devices. It must be noted that more than the choice of reference surfaces, this is a consequence of the active wetted surfaces participating in the lift effort: the BWB has 100% of its wetted surfaces generate lift while only 50% of the TAWs wetted surfaces generate lift. In this case, the choice of reference surfaces is merely a transposition of the lift generating surfaces and that's why analysing S_{ref} is equivalent to analysing S_{wet} with respect to lift generation. By extension, regional BWB's should be able to comply with this result. While extrapolation to larger BWB's could be hypothesized, this would require a dedicated analysis for aerodynamic performance and weight estimation at larger scales.
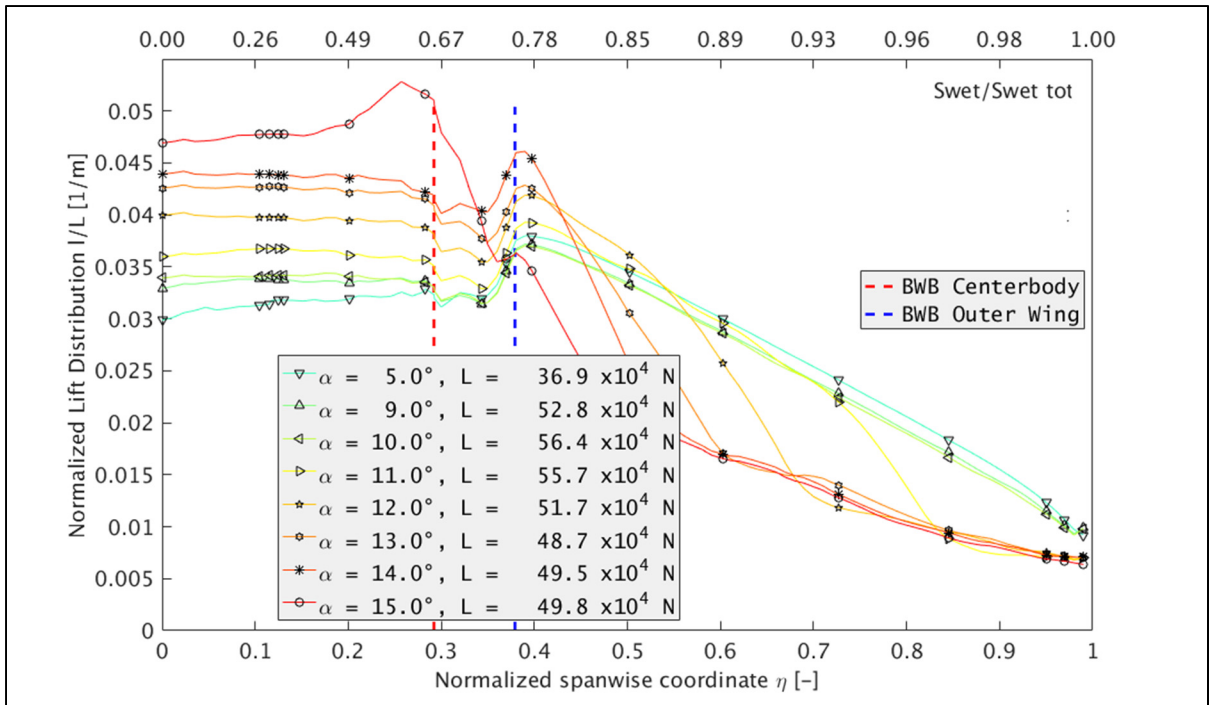
Figure 4-15 :   BWB normalized lift force distribution at different angles of attack

In the case of the TAW, the fuselage also generates lift, but it is mainly concentrated along the centerline ($\eta = 0$) but not nearly as much nor with the same distribution or with a smooth transition with respect to the main wing. Most of the lift is provided by the inner wing, which, while well designed to face progressive boundary layer detachment, results in an abrupt stall.

108
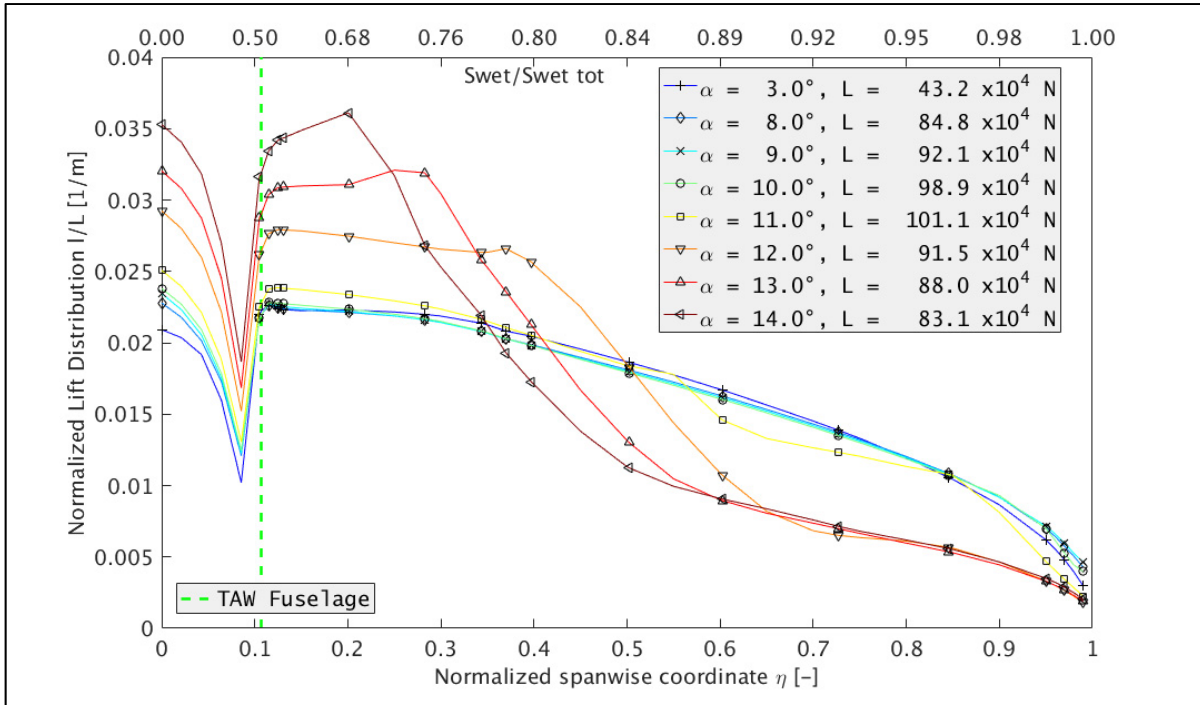
Figure 4-16 :   TAW Lift force distribution at different angles of attack

Overall, the lift distribution is more homogeneous for the BWB, even around global stall conditions. Furthermore, it may not be necessary to use high-lift devices since the BWB should be capable of generating enough lift on its own. Note that this doesn't justify the lack of control surfaces which can be added in the shape of canards, empennages, ailerons or even slats. Control surfaces stay, however, outside the subject of this thesis.

4.5   Quantitative analysis (1D): global aerocynamic coefficients

The previous sections introduced the airflow recirculation, local detachment and lift distribution. Finally, this section presents the global aerodynamic coefficients: lift, drag and pitch moment coefficient (C_L, C_D, C_{My}) for a global aerodynamic comparison. This comparison is based on the global aerodynamic coefficients presented by Figure 4-17 and Figure 4-18.

Figure 4-17 presents the aerodynamic coefficients for the BWB. Concerning the lift coefficient C_L, the lift slope $C_{L,\alpha}$ is smaller for the BWB. We assume that, aside from airfoil geometry,

this is due to the low lift generated by the centerbody which represents almost 65% of the wetted surface. Furthermore, the BWB presents a global stall at $\alpha = 10°$. Note however that $C_L(10°) \approx C_L(11°)$, which means the global stall isn't abrupt. Going further into the post-stall zone, we must remind the reader about the limits of the RANS model: past stall, these results serve as trends and guidelines rather than precise reference values. This being said, past this point, we note that there is a slight increase in C_L between $\alpha = 14°$ and $\alpha = 15°$. This falls in line with previous experimental results obtained by Vicroy (2009) and Gebbie et al. (2007), where different BWB geometries would present multiple or extended stalls along with a lift recovery past the first stall. The hypothesis proposed by Gebbie et al. (2007) with respect to his BWB's multiple stall are linked to a possible delta wing behaviour at very high angles of attack. While interesting, this hypothesis remained outside the scope of this research, but might be worthy of exploration in future works. As for the moment coefficient C_{M_y}, it is calculated at the minimum and maximum center of gravity (CG) position for the BWB. This moment presents a negative-to-neutral slope, which is a favourable attribute. These moment results present similar trends as the ones presented by (Vicroy, 2009) and referenced in Figure 1-4. Finally, the drag coefficient C_D shows the typical quadratic evolution while C_L is linear. It is interesting to note that, while C_D values remain on the same order of magnitude to those of the TAW for the same C_L values at the linear lift zone, the values of C_D past stall are visibly lower than those of the TAW. This could be partially due to the stall resistance brought forth by the CB and its lift-induced drag and partially by the lower interference drag between the CB and the OW.

110
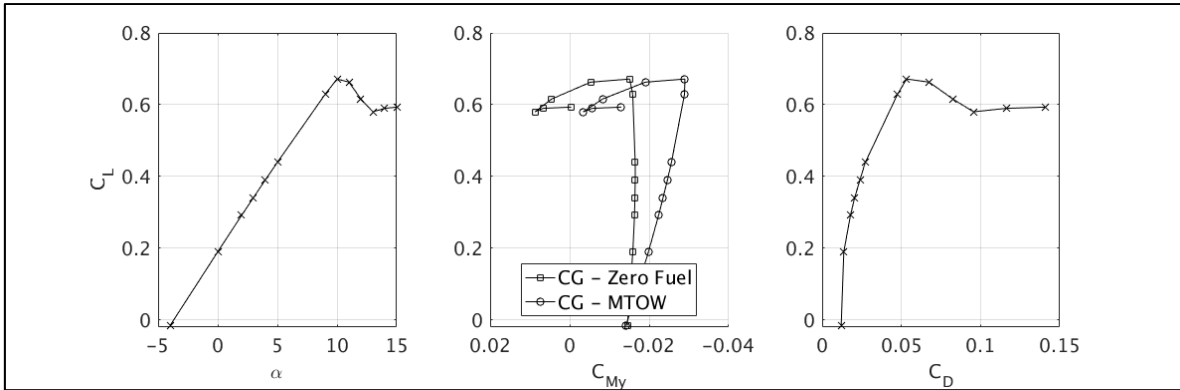
Figure 4-17 :   BWB aerodynamic coefficients

Figure 4-18 presents the equivalent figure for the CRM. For this case, the lift slope $C_{L,\alpha}$ is higher than that of a BWB. Analysis of the CRM's C_L shows an abrupt stall at $\alpha = 11°$. This is curious since it was proven that local stall was present in the outer wing at $\alpha = 9°$. However, it was also proven that most of the lift was generated by the CRM's inner wing. In a parallel thought process as the one used for the BWB, this shows that different wing sections trigger stall differently and that so long as the critical sections remain attached, the whole aircraft can avoid stall. The moment coefficient C_{M_y} is calculated at the point $P(33.6, 0, 4.5)[m]$ in accordance to DPW5 indications. C_{M_y} presents a neutral slope. This is expected since the geometry studied doesn't present horizontal stabilizers. Finally, C_D is also given for comparison purposes. It is noted that this configuration presents a more linear drag evolution at low angles of attack; but still presents higher drag on average.
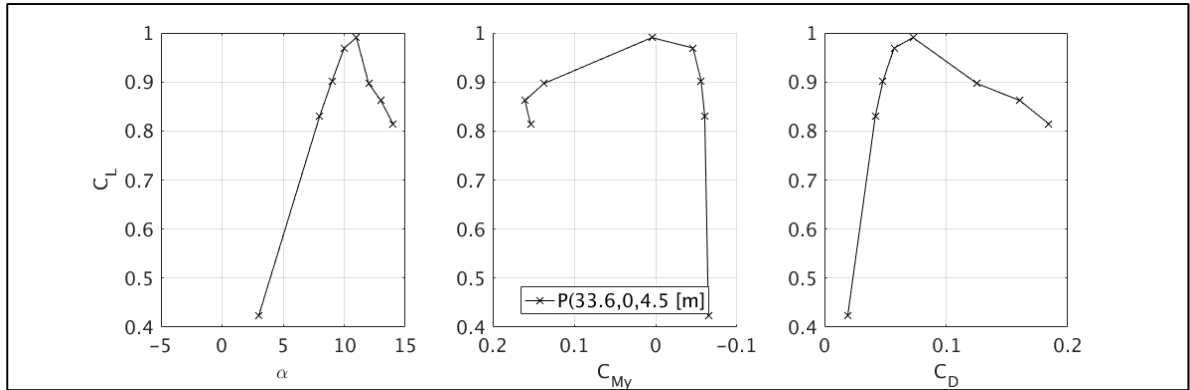
Figure 4-18 : TAW aerodynamic coefficients

Overall, the TAW seems to have the advantage of being able to endure local detachment for a few angles of attack before the wing is fully lost, but then the stall is abrupt and unrecoverable; whereas the regional BWB geometry stalls right as the detachment appears at the wingtip but it does so more smoothly, over a slightly larger range for α; giving some time to recover from stall. Furthermore, both aircrafts show different stalling patterns for each wing section, allowing for some sections to remain active while some other sections have already stalled. In particular the idea of a stall resistance linked to section change due to airfoil shape or local geometry parameters was introduced for both aircrafts.

At this point, it would be tempting to suggest that improving the aerodynamics of the BWB's CB by modifying its airfoil shape would increase the BWB performance. While this sounds interesting, consider that, as stated in chapter 3, the CB is already subject to multiple design constraints concerning, in particular, effective floor space constraints. As such, modification of the CB would require a research on its own, similar to the one carried out by Reist (Reist & Zingg, 2013, 2014, 2015, 2016). For this project, a different approach is conceived. Based on the previous results, the $C_L - \alpha$ curves show that stall for the TAW is abrupt, while stall for the BWB is progressive. Results at higher angles of attack would suggest that, for the BWB, lift starts to increase past $\alpha = 13°$. This is pushing the limit on the RANS model. However this is the exact behaviour seen in previous works by (Gebbie et al., 2007). This trend suggests that the CB progressively takes over the lifting effort of the aircraft as was proven by Figure 4-15. This means that our focus must be on delaying initial stall rather than trying to continue flying

past it. Overall, these coefficients suggest that, under the correct wing coupling of geometrical parameters between the CB and the OW, it could be possible to delay BWB stall while generating less drag than the conventional CRM at all times. This, coupled with the fact that the centerbody doesn't reach stall will be used to propose a design configuration where the CB could attain higher lift generation and compensate, if only a bit, for the loss of lift on the OW. This specific hypothesis will be tested in CHAPTER 5.

4.6   Chapter summary

This chapter's objective was to identify any aerodynamic differences between the TAW and the BWB geometries at low speeds. This chapter presented the aerodynamic evolution of a regional BWB and a TAW representative near stall through the use of the RANS model implemented in SU2. Qualitative analysis of the airflow along with an analysis of the local surface state and the link to the stall propagation phenomena was presented in this chapter.

First, we introduced the concept of recirculation bubbles to avoid visual cluttering when analysing airflow streamlines. The results show that recirculation bubbles are present above the detachment zones on the upper surface. Moreover, these recirculation zones are particularly present right after global stall is reached (near the wingtip for the BWB and on the mid-wing for the TAW). This means, as expected, that recirculation bubbles are indicators of the presence of local and/or global stall. These bubbles, however, show the same results for both aircrafts: global stall is attained when the wing/OW is engulfed by recirculation bubbles and neither the fuselage nor the CB attain local stall within the studied angles of attack.

Second, analysis of the local pressure and skin friction distribution shows the progressive development of detachment fronts on both geometries, and the existence of critical sections which, after local stall, trigger the global stall of the aircraft. A consequence of this result is the fact that sections with different shapes and geometric parameters are allowed to stall locally at different angles of attack: both the fuselage and the CB refuse to stall even after their respective wing/OW has stalled.

Third, on a similar note, when global stall is attained, local stall seems to engulf the wing only up to the point of local geometry break points where either the airfoil, and/or the sweep and/or the twist of the aircraft change suddenly. It is deduced that these local break points result in local lift curves that attain stall at different angles of attack; thus, delaying local stall in the case of the fuselage and the CB.

Fourth, the results showed that the BWB's CB participated in the lift effort more efficiently than a classic fuselage, and by doing so, it allowed the BWB to provide enough lift to support its weight at low speeds without high lift devices. This is linked to the larger reference surface of the BWB which would allow the aircraft to stall at lower lift coefficients C_L, themselves now attainable by the baseline wings without high lift devices. As a result, the existing debate of whether or not high-lift devices are needed is partially resolved: for regional sized BWB and from a lift capability perspective, these devices are unnecessary. However, extrapolation of these results to larger BWBs would require further scale analysis for weight and aerodynamic prediction. Nevertheless, this doesn't compensate for the need of control and stability surfaces in the absence of an empennage: while triple slotted slats may not be needed for lift generation, some designers may still use simple flaps or slats to control and stabilize the aircraft. This result answers to one of the initial questions of this research: no, the regional BWB doesn't need high lift devices to generate sufficient lift at all times.

Finally, it was found out that the BWB presents a smoother stall than the TAW which presents an abrupt stall. Assumptions on the reasons behind this smooth stall are associated with the compound wing nature of the aircraft where the CB evolves differently than the OW. It was noted that the BWB's OW stalls so early that it doesn't allow the CB to attain its maximum lift capability, which means that there is a design margin to enhance the BWB lift generation at low speed. A more conclusive study based on local aerodynamic differences and stall delaying parameters is proposed in Chapter 5.

CHAPTER 5

CENTERBODY-OUTER WING INTERACTION: INFLUENCE OF TWIST ON AERODYNAMIC PERFORMANCE

5.1   Introduction

The previous chapter showed that introducing sections with different local aerodynamic behaviours resulted in a body with different local stall zones, where some zones like the OW would stall first and some others like the CB would refuse to stall within the studied angle range. Furthermore, it was shown that these different aerodynamic behaviours were linked to the local geometric parameters like the airfoil, the sweep Λ, the chord c or the twist ϕ along the wingspan. Particularly, the transition wing was characterized by a stall resistance derived from the abrupt changes in sweep, airfoil and chord parameters. We use this result to explore the opposite effect: we hypothesize the existence of a possible coupling between the CB and the OW that could allow both zones to stall at roughly the same time. This would accomplish two things: it would delay OW stall while allowing for the CB to develop higher lift values. In other words, the maximum lift coefficient could be enhanced by playing with the local geometric parameters between the CB and the OW. Based on this idea, CHAPTER 5 presents a study on the twist influence on the stall of the BWB lift generation at low speeds. Our objective here is to model the maximum lift coefficient C_{Lmax} as a function of the geometrical coupling between the CB and the OW. The idea here is to delay OW stall as long as possible in order to allow the CB to increase its lift contribution as much as possible. The choice was made to limit this study to one parameter: the twist distribution ϕ. While other parameters like the sweep distribution could have been studied, the natural choice of study was the twist distribution since this parameter directly modifies the effective angle of attack of the local section. Furthermore, note that the existing literature shows that twist manipulation allows to conveniently delay local stall and displace the initial stall section towards the inboard of the wings. Based on this, we use twist variation to analyze CB/OW coupling near stall. To do this, this chapter is divided in two main sections: (1) a CFD study on the effect of twist on C_{Lmax}

and (2) the calibration and application of the low-fidelity compound wings LLT model presented in section 2.5.

5.2   CFD analysis of the twisted BWB geometries

This section introduces three different BWB geometries with varying twist values. These geometries are analyzed using the previously introduced RANS-SA model at different angles of attack. Finally, the results are used to extract comparative behaviour between each geometry accounting for the only variating factor: the twist ϕ. Figure 5-1 presents a side view of a positive local twist ϕ at a given wingspan section y, where x is the chordwise coordinate and z is the altitude.
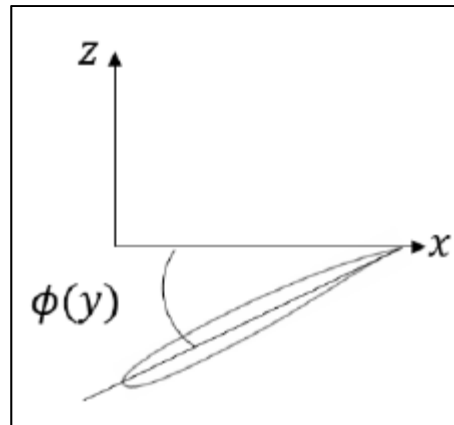

Figure 5-1:   Scheme for twist

Note that only the condensed results directly relevant to our objective are presented in this chapter. The reader may refer to APPENDIX VII for a detailed database concerning the local aerodynamic results (c_p, c_f, C_l, C_d) for the twisted geometries in a similar approach as the one proposed in CHAPTER 4.

5.2.1   BWB Geometries

Three geometries are used to analyze twist effect. We remind that, for the purpose of this research, we consider ϕ as positive when it decreases the local angle of attack and negative otherwise. Note that only the OW is subject to twist. This is a consequence of the CB geometric requirements since the cabin itself cannot be twisted. All three configurations analyzed present a linearly varying twist angle ϕ from the beginning of the outer wing ($y_{OW} = 6.54m$) to the tip ($y_{tip} = 17.2\ m$), as defined in equation (5.1). For this case study, three different geometries were considered: $\phi_{max} \in \{0°, 4°, 8°\}$. These geometries are labeled as V00, V04 and V08 respectively. The fluid domain is the same as the one presented in section 3.3.2.1. All meshes are generated following the same algorithm than mesh 20M presented in section 3.3.2.2, and present the same density and repartition than mesh 20M. Finally, the farfield initial conditions are the same ones specified in Table 3-10 page 81 of this thesis and correspond to the low-speed conditions.

$$\phi = \begin{cases} 0 \ if \ y \le y_{OW} = 6.54m \\ \phi_{max}\left(1 - \dfrac{y_{tip} - y}{y_{tip} - y_{OW}}\right) if \ y \ge y_{OW} \end{cases} \tag{5.1}$$

5.2.2   Test Matrix

This subsection introduces the multiple simulation cases done for each geometry at low-speed. Particular effort was done for each BWB geometry to obtain a detailed aerodynamic polar, within 1° precision. This allowed to estimate multiple design values like the zero-lift drag coefficient C_{D0}, the linear lift slope, and the stall initiation and evolution past the linear lift zone.

For this study, a total of 32 completed simulations were considered for a resource usage of $\sim$160 core-years (cf. Table 5-1). These simulations took place in the Cedar and Niagara clusters. Refer to APPENDIX VI for cluster details.

Table 5-1:   Aircraft test cases (Twist)

BWB Geometry	Angle of attack	Total	Nodes
V00	$\alpha \in \{-4°, 0°, 2°, 3°, 4°, 5°, 9°, 10°, 11°, 12°, 13°, 14°, 15°\}$	13	20M
V04	$\alpha \in \{-4°, 2°, 3°, 4°, 8°, 9°, 10°, 11°, 12°, 13°, 14°, 15°\}$	12	20M
V08	$\alpha \in \{-4°, 3°, 4°, 10°, 11°, 12°, 13°, 14°, 15°\}$	9	20M

5.2.3   Results (1): Local lift evolution

This section presents the results concerning the section lift variation with respect to α for each proposed twist distribution. In this case, a cloud representation is proposed to visually inspect the topology of stall evolution with respect to both ϕ and α. Three particular points are focused: the C_l topology, the $dC_l/d\phi$ topology and the active lifting surface evolution for each geometry.

First, Figure 5-2 presents a map of the value of the local lift C_l with respect to the normalized spanwise coordinate $\eta = \frac{y}{b/2}$ and global angle of attack α. All three twists are presented from left to right. The isolines represent the C_l values and help to localise the local maxima. The value of C_{lmax} at each station is represented by the red dotted line. In turn, the red dotted line represents the stall front. The boundaries between CB, TW and OW are represented by white dashed lines.

The interest of Figure 5-2 consists in the visualization of the C_l values along the wingspan as α evolves between $0°$ and $15°$. Note how every C_{lmax} is directly linked to a local section stall, as proven by the concentration of isolines right behind the red dotted line. Note however that, as shown in Chapter 4, not all sections stall at the same angle of attack. Furthermore, not all sections present abrupt stall. For all geometries, abrupt stall is present mainly around the section of maximum lift coefficient (at a given α) which is represented by the peak of the

topology. At the same time, progressive stall is rather present farther from this peak, all the way to the CB which, in the case of V00 doesn't show signs of stall, even at $\alpha = 15°$.

When comparing the three configurations on Figure 5-2, it is first noted that the section containing the maximum attainable lift $C_{lmax,max} = \max(C_l(\alpha, \eta))$ is progressively displaced inboard of the wing as ϕ_{max} increases: $\eta_{C_{lmax,max}}^{\phi_{max}=0°} \approx 0.82, \eta_{C_{lmax,max}}^{\phi_{max}=4°} \approx 0.76, \eta_{C_{lmax,max}}^{\phi_{max}=8°} \approx 0.66$. In a similar way, the initial stall front, represented by the red dotted line expands inboard with ϕ_{max}: $\eta_{stall}^{\phi_{max}=0°} \in [0.67; 1.00], \eta_{stall}^{\phi_{max}=4°} \in [0.57; 1.00], \eta_{stall}^{\phi_{max}=8°} \in [0.00; 1.00]$. It is noted that the zone occupied by the initial stalling sections widens as ϕ_{max} increases. The expansion of the initially stalled zones along the wingspan, goes in the same direction as the coupling hypothesis; allowing more sections to stall at roughly the same time. It is clear that as ϕ increases, the red line becomes more and more horizontal. This result is extremely positive, as it shows that it is possible to configure the geometry in such a way that it stalls everywhere at the same time. This partially validates the initial hypothesis of this chapter: it is indeed possible to align the CB and the OW stalls through the twist distribution.

Now, note that C_l values at a given α are, on average, smaller as ϕ_{max} increases. This results from the stall delay introduced by ϕ. However, closer inspection of the data used to create Figure 5-2 shows that the maximum achievable local lift coefficient amongst all angles and sections, $C_{lmax,max}$, increases with ϕ_{max}: $C_{lmax,max}^{\phi_{max}=0°} = 1.65, C_{lmax,max}^{\phi_{max}=4°} = 1.69, C_{lmax,max}^{\phi_{max}=0°} = 1.73$. This reinforces another part of our hypothesis where, as stall is delayed from the OW, it allows the inboard sections to attain higher C_l values at higher α, thus more than compensating for the lower C_l values at the same α with respect to the other configurations. This result was predicted by our hypothesis: if α_{stall} increases, then the previously unstalled sections are allowed to attain higher angles of attack and thus higher C_l values. The real question though concerns the impact on the global C_{Lmax}, which is expected to drop in the case of TAW aircrafts.

For now, let us note the increasing C_l values attained by the CB with respect to ϕ_{max}. Closer inspection shows initial development of smooth stall particularly at sections $\eta \in [0.00; 0.29]$ for $\phi_{max} = 8°$. This smoothness is easily identified by the very low isolines density behind the stall front at these sections. Note that, up to $\alpha = 15°$, no stall is present for the CB at $\phi_{max} = 0°$; however, at $\phi_{max} = 8°$, the CB fully stalls at $\alpha = 14°$. This suggests that by delaying the stall of the outer wing, the stall of the CB is accelerated. This is acceptable given that, overall, the global stall angle is increased from $\alpha_s = 10°$ to $\alpha_s = 14°$.

At this point, it must be noted that as the local stall of the OW is delayed, so is the global stall. It is clear that a significant zone of stalled sections appear at $\alpha \approx 10°$ for $\phi_{max} = 0°$, $\alpha \approx 12°$ for $\phi_{max} = 4°$, and $\alpha \approx 14°$ for $\phi_{max} = 8°$. This, in turn, delays the global stall, allowing the BWB to work at higher angles of attack before reaching global stall conditions. Note that, as ϕ_{max} increases, the stall angles become homogeneous along the wingspan, progressively transforming the red dotted line into an horizontal line at $\phi_{max} = 8°$. Again, this result validates the coupling aspect of our hypothesis by proving the existance of one configuration where stall is attained on every section at the same time.

120
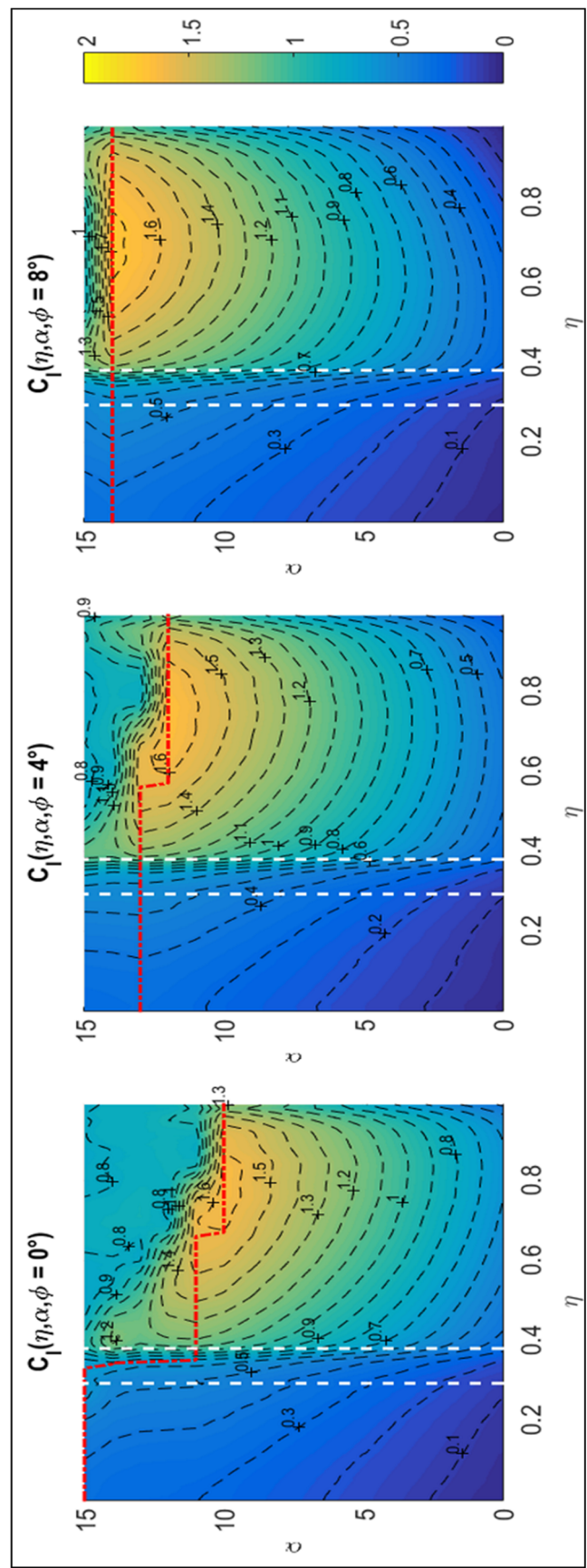
Figure 5-2:   Local lift mapping for each geometry V00, V04, V08 (left to right)

Let us now consider the variation of C_l with respect to ϕ. Consider the relative variation $\Delta C_l(\phi_{max1}, \phi_{max2}) = \frac{C_l(\phi_{max1}) - C_l(\phi_{max2})}{C_l(\phi_{max2})}$, where $(\phi_{max1}, \phi_{max2}) \in \{0°, 4°, 8°\}^2$. This relative variation allows to estimate which zones are the most impacted by the increase in maximum twist. Figure 5-3 presents the topology of ΔC_l for the cases $(4°, 0°)$ (left), $(8°, 4°)$ (center) and $(8°, 0°)$ (right). The horizontal and vertical axes remain the same (η, α). The ΔC_l isolines are used to identify the zones of maximum variation between geometries.

In the case $(\phi_{max1}, \phi_{max2}) = (4°, 0°)$, Figure 5-3 shows ΔC_l values between 0.5 and 1 for sections $\eta > 0.6$. Note that this increase is present even past the global stall angle at $\alpha = 12°$. The increase in C_l past the global stall angle shows a smoothing of the stall abruptness at the considered sections $\eta \in [0.6; 0.7]$. As for the sections $\eta > 0.7$, we remark an "L" shaped cloud near the wingtip. Naturally, the outer sections benefit directly from the twist increase by delaying its stall. Moreover, by delaying stall the slightly more inboard sections are allowed to reach higher maximum lift values than before. Finally, note that the most affected section is actually not the wingtip, but the segment $\eta \in [0.7; 0.8]$.

In the case $(\phi_{max1}, \phi_{max2}) = (8°, 4°)$, Figure 5-3 shows, again, ΔC_l values between 0.5 and 1 for sections $\eta \in [0.6; 0.9]$. Note that this time, the outboard sections don't benefit as much from the twist as in the prior case. The twist influence is now displaced inboard to sections $\eta \in [0.6; 0.9]$. Note, again, the presence of the "L" shaped cloud, with a maximum relative ΔC_l at $\eta \in [0.6; 0.7]$. The sections presenting the highest increase are still the same as in the previous case, with the difference that now the global stall angle is $\alpha = 14°$.

Finally, the case $(\phi_{max1}, \phi_{max2}) = (8°, 0°)$ shows the zones of maximum impact between the lowest twist $\phi_{max2} = 0°$ and the highest twist $\phi_{max1} = 8°$. This figure shows an overall impact focused on sections $\eta \in [0.5; 0.9]$. Note that the maximum ΔC_l is attained at angle $\alpha = 14°$. This suggests that, as hypothesized, the real benefit of this twist distribution is to allow inner sections to attain higher C_l values.

122
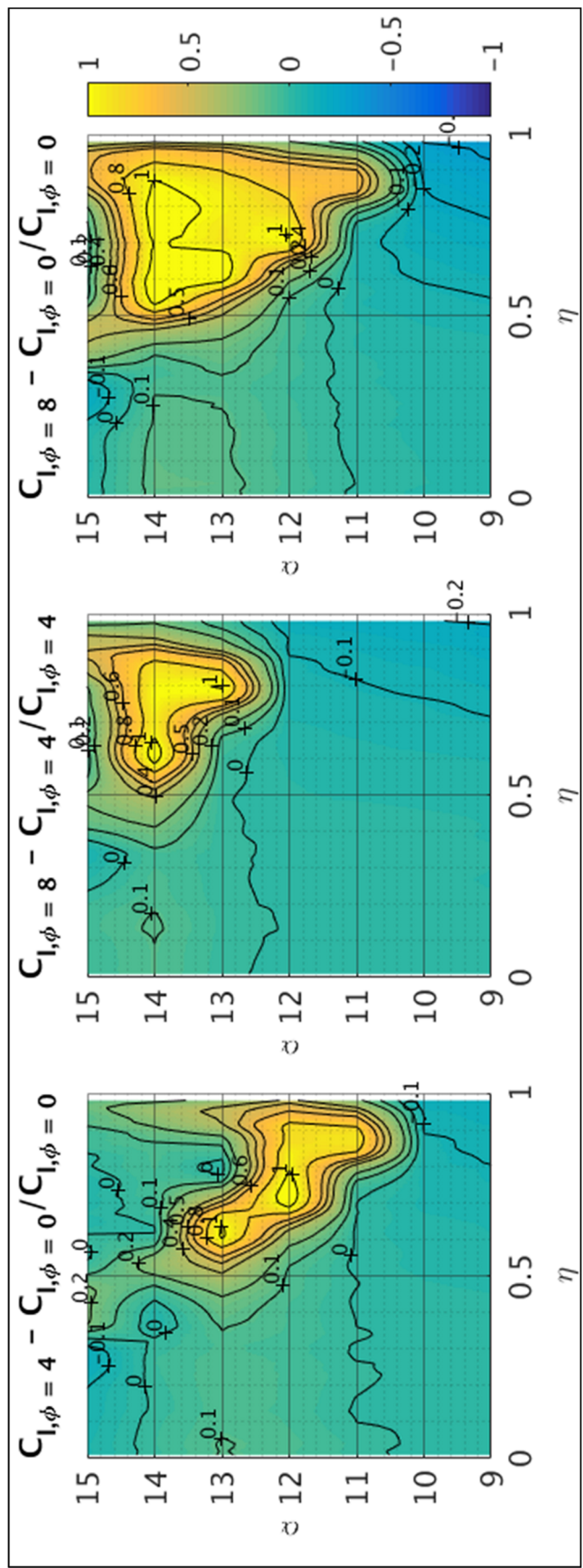
Figure 5-3: Relative variation of local lift between each BWB geometry.

We will now consider the impact of the different wetted surfaces on the stall trigger of each geometry. Figure 5-4 presents how the C_L at each angle is distributed between the CB, the TW and the OW. This is measured as the ratio of the lift force L_i generated at a given wing section (CB, TW, OW) and the total lift L. The horizontal axis represents the global angle of attack α. The vertical axis represents the cumulated fraction of total lift going from 0 at the root to 1 at the tip. Again, the three twist distributions are present from top to bottom. Finally, the stall angles α_{stall} are represented by dashed vertical lines on each block.

This figure is of particular interest because it shows, as hypothesized, the increasing participation of the CB to the global lift generation as ϕ_{max} increases. On average, and prior to stall, the global lift generation is divided as 40% from the CB, 10% from the TW and 50% from the outer wing. Note however that in all 3 geometries, as α increases, the OW participation decreases with respect to the CB while the transition wing participation remains constant. While the variation of the participation of the OW is minimal, this variation is enough to delay stall and attain higher lift values.

Furthermore, the reader may note that as ϕ_{max} increases, the participation of all zones is more constant with respect to α: as ϕ_{max} increases, the load on the OW diminishes ever so slightly. In turn, this results in a higher stall angle α_{stall}. In other words, the twist allows for the CB to generate more lift, thus delaying the global stall.

Finally, a quick comment must be made on the importance of the OW surface. It must be noted that at all times prior to stall, the OW is responsible for roughly 50% of the total lift force. This shows the importance of the CB whose contribution adds up to 40% of the global lift effort. And yet, it remains clear that without an OW, the BWB wouldn't be able to fly.
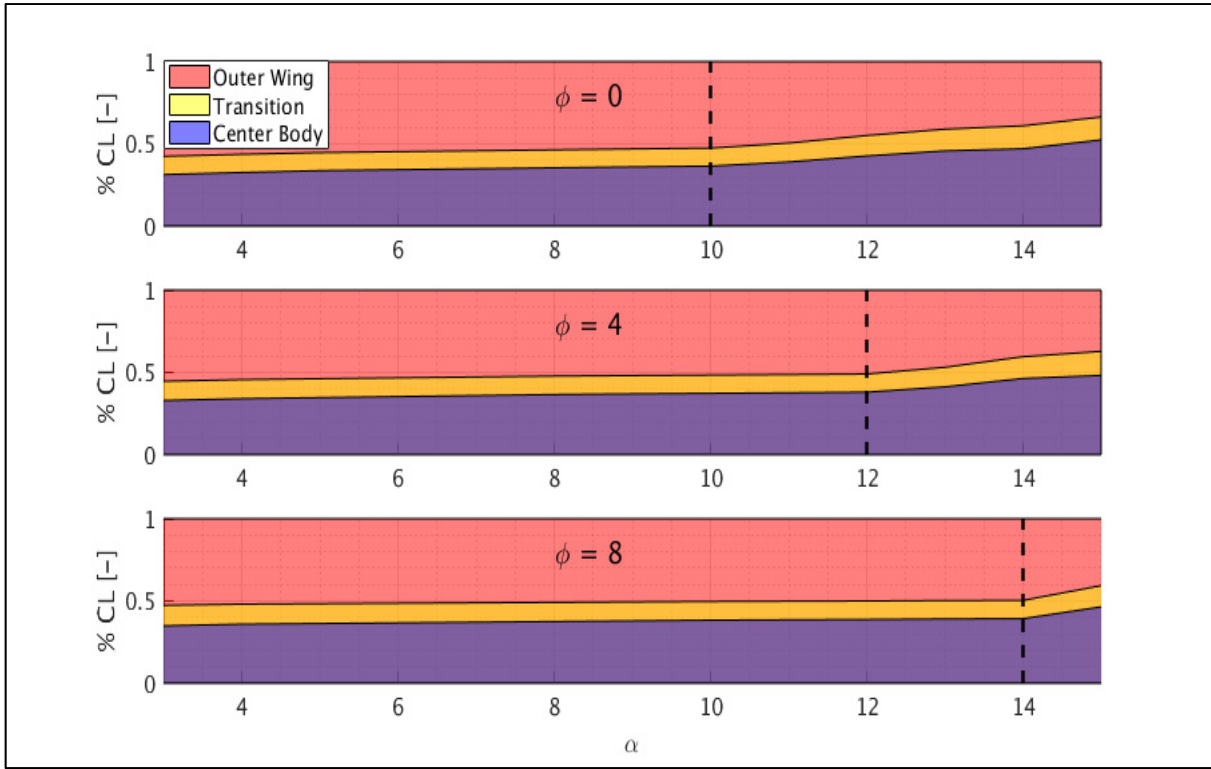
Figure 5-4: Participation to the total C_L by each wetted surface for all 3 twist distributions on the BWB geometry.

To summarize this section, we introduced a local analysis of the aerodynamic lift with respect to twist. Based on this we identified the impact of ϕ on the first stalling section, the impact of ϕ on the section supporting the maximum local lift coefficient, the impact of ϕ on the stall angle α_{stall}, the zones of maximum impact with respect to ϕ, and the increasing participation of the CB as ϕ_{max} increases. It is now time to analyze the global aerodynamic coefficients and their relation with ϕ.

5.2.4 Results (2): Global aerodynamic variables

The previous subsection analyzed the local effects of twist on C_l. This section will now focus on the global effects of twist on two critical parameters: C_L and L/D. The addition of L/D follows the concept of non-optimality where optimization of one parameter may lead to suboptimal performances of other parameters. It is noted that, at this speed, L/D wouldn't be

an influential parameter since it is rather linked to cruise speeds at high altitude. Nevertheless, the tendency can be used to try and predict what the impact of ϕ_{max} will be on L/D at cruise conditions. Again, the objective here is to show how the enhancement of one aspect of the aircraft (BWB) usually results from trade-offs chosen by the designer.

First, lets analyze the influence of twist on L/D. Figure 5-5 shows the evolution of the lift-to-drag ratio L/D with respect to the angle of attack α for the three different twist distributions. Furthermore, the legend includes the value of the maximum L/D for each distribution.

Figure 5-5 shows that the flight angle α corresponding to the maximum L/D increases with ϕ_{max} by up to 1°. While not particularly desirable, these angles remain under 5°. Note that the angles that correspond to $\frac{\sqrt{3}}{2}(L/D)_{max}$ result in values inferior to 3°. This is compliant with the safety cabin angles usually proposed for passenger cabins.

Furthermore, Figure 5-5 shows a decrease in $(L/D)_{max}$ as ϕ_{max} increases. Delaying the global stall ultimately results in an inferior L/D parameter. Note however that this decrease is on the order of 1.2% between $\phi_{max} = 0°$ and $\phi_{max} = 4°$ and on the order of 3.0% between $\phi_{max} = 0°$ and $\phi_{max} = 8°$.

126
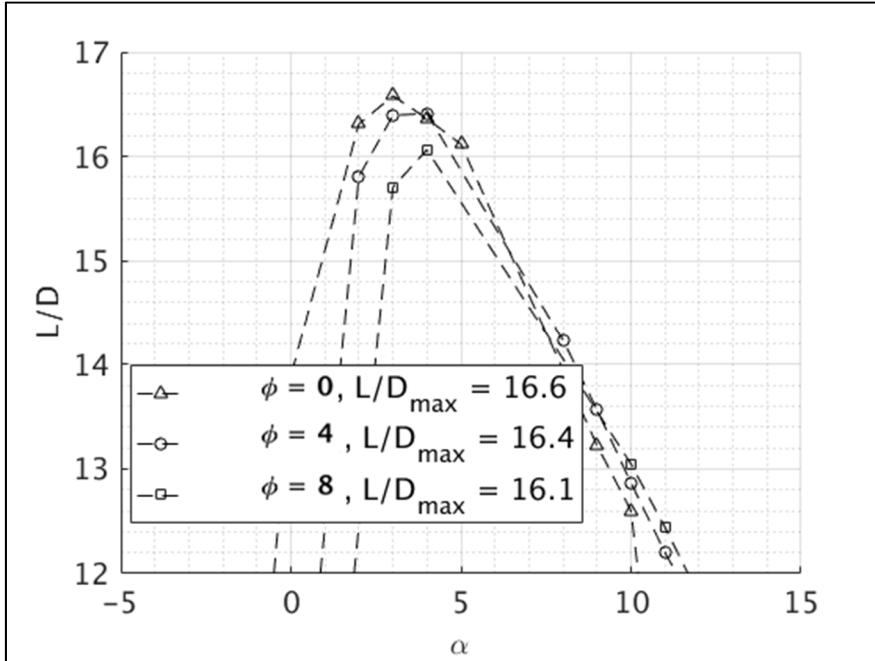
Figure 5-5:   L/D evolution of the BWB for different twist
distributions.

Let us now focus on the global lift coefficient C_L and, particularly, on the maximum lift coefficient C_{Lmax}. Figure 5-6 presents the $C_L - \alpha$ curves for all three BWB geometries. Each marker in this figure corresponds to a CFD simulation. The C_{Lmax} for each configuration is reported in the legend.

First, we analyze the linear lift zone. Note that for all three configurations, the linear zone extends almost all the way to stall. No significant change in lift slope is observed between configurations. As expected though, for a given angle α, C_L decreases as ϕ_{max} increases. In this case, it can be assumed that ϕ displaces the $C_L - \alpha$ curve down at an approximate rate of $dC_L/d\phi_{max} \approx 0.0086\,\text{deg}^{-1}$.

In the case of the stall zone, the stall angle is displaced to the right: α_{stall} increases in ϕ_{max} at a rate of $\frac{d\alpha_{stall}}{d\phi} \approx 2\,°/°$. This means that the aircraft can operate at higher angles before reaching stall. As seen in the previous subsection, this is due to both the OW delayed stall and

the CB increased lift generation at higher angles of attack. Finally, it is obvious that C_{Lmax} increases with ϕ_{max}. The next figure is dedicated to this specific variation.
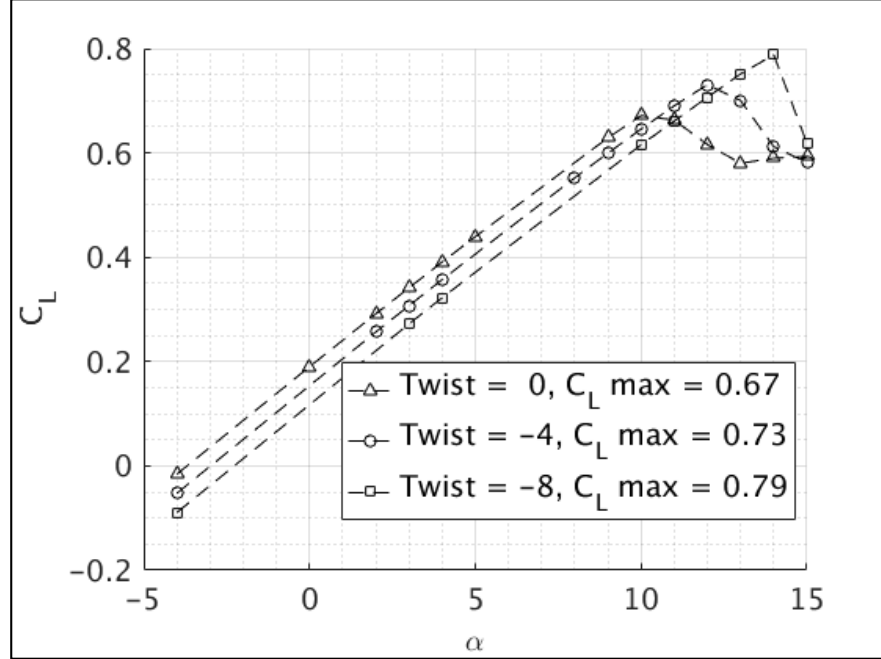
Figure 5-6:   Evolution of the global lift coefficient C_L with respect to angle of attack α for all twist distributions.

Following the results provided by Figure 5-6, Figure 5-7 shows the evolution of C_{Lmax} with respect to ϕ_{max}. Each marker represents 1 of the 3 available C_{Lmax}. On top of this, the linear regression proposed shows good agreement with the available points, with a variation of 0.0146 per ° of twist. This basically means that there is a 8.9% improvement in C_{Lmax} between V00 and V04, and a 18% improvement between V00 and V08. Finally, for BWB design purposes, it can be concluded that, up to $\phi = 8°$, C_{Lmax} increases linearly with ϕ_{max}.
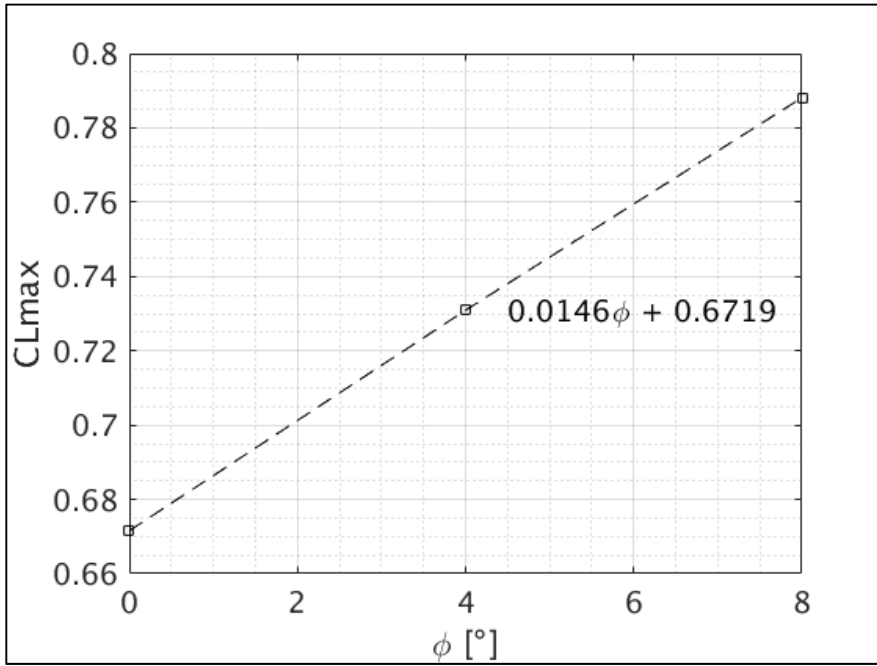
Figure 5-7:   Variation of C_{Lmax} with twist

All in all, this section shows that it is indeed possible to couple OW stall with CB stall to augment lift performance. This derives from the fact that the CB retakes the lift that the OW isn't capable to provide up to a certain extent. We remind the reader that contrary to classic aircrafts, the CB airfoil is very stable and takes longer to stall than the OW airfoil; thus it makes it so that the OW stalls first. While this is not optimal, we note that the critical section $\eta_{Clmax,max}$ is displaced inboard as ϕ increases. Furhtermore, adding twist to the OW allows for the OW to stall at higher angles of attack which in turn allows the CB to generate more lift, resulting in a higher C_{Lmax}. This comes with a negligible trade-off. While ϕ_{max} has a positive impact in C_{Lmax} by up to 2.2% per twist degree – up to 18% -, it decreases $(L/D)_{max}$ by up to 0.4% per twist degree. This adds up to a maximum range loss of 75km (3%) for the V08 configuration due to a decrease of $(L/D)_{max}$. Note that, the 3% variation is within the weight uncertainty. However, the tendency is clear: ϕ_{max} has a relatively negative impact on $(L/D)_{max}$, even though this impact is almost negligible.

5.3   Compound wing C_{Lmax} prediction model

The last section validated our previous hypothesis on the existence of a twist coupling between the CB/OW to optimise C_{Lmax} at low speeds. In order to generalize these findings to any BWB geometry it is necessary to build a predictive model based on the multi-section nature of the aircraft. Particularly, we're interested in the prediction of the maximum global lift coefficient (C_{Lmax}). To do this, the compound wing LLT model is proposed. The development of this model is presented in CHAPTER 2, while the implementation and calibration are presented in this section.

5.3.1   Context

In order to give a reference to compare with, the original Phillips model (Phillips & Alley, 2007) is used to estimate lift coefficient results against the CFD results. This model was never intended to be used on compound wings; it is therefore knowingly applied outside of its original hypotheses. Two different results are analyzed: the prediction capability in the linear lift zone and the C_{Lmax} prediction.

Considering the linear lift zone, Figure 5-8 presents the C_L variation with respect to the global angle of attack α_{3D} for all three BWB geometries for both the original Phillips model (Phillips & Alley, 2007) and the CFD results. To avoid confusion with other angles defined in CHAPTER 2, the subscript "$3D$" is added to the global angle of attack. Values for the maximum lift coefficient for each geometry – as calculated by the CFD model – are presented in the legend.

Figure 5-8 shows a misprediction on the lift slope value $\left(\frac{dC_L}{d\alpha}\right)$ in the linear zone. However, the spacing between C_L curves for each value of ϕ, in the linear zone, is almost identical: $\left(\frac{\partial C_L}{\partial \phi}\right)_{Phillips} \approx \left(\frac{\partial C_L}{\partial \phi}\right)_{CFD}$. Due to the additional hypotheses brought in by the BWB, the

original model manages to properly account for the twist variation, but doesn't predict actual C_L values for the BWB in the linear zone.
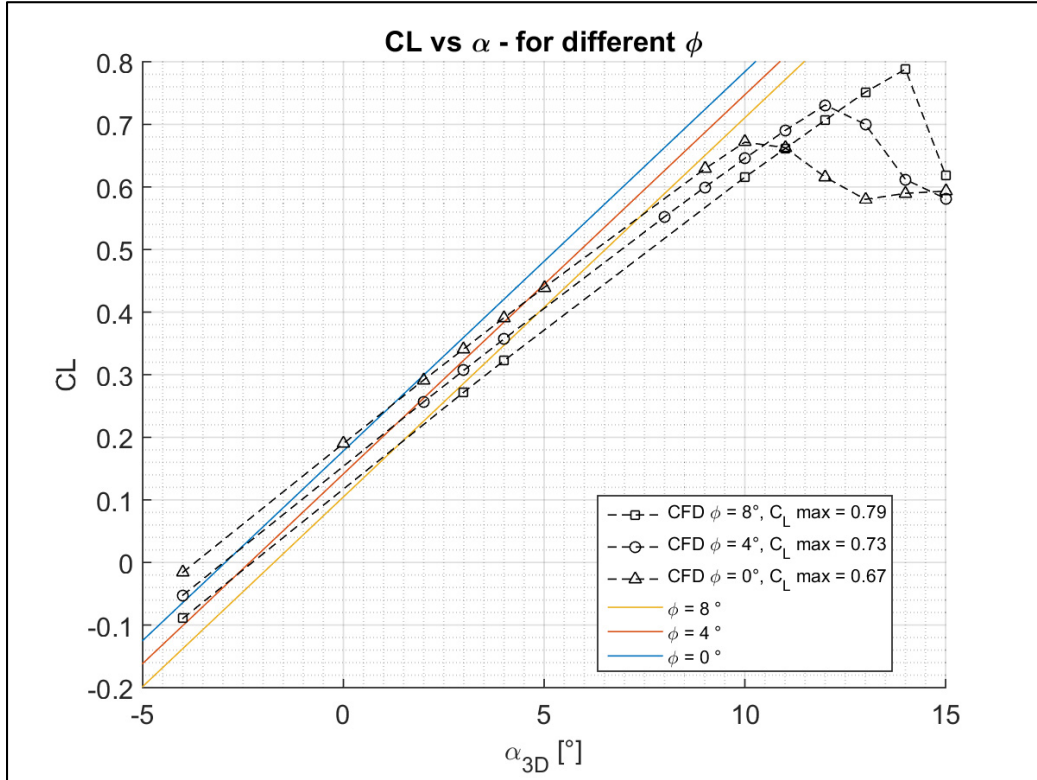
Figure 5-8:   Comparison between Phillips Twisted LLT and CFD results for the BWB

Considering the results at stall, the parameter $\kappa_{L\Lambda}$ is calculated according to Phillips and Alley (2007) by substituting $\Lambda_{0.25c}$ by $\overline{\Lambda}$ as presented in equations (2.89) and (2.90). Furthermore, the stall correction coefficient κ_{Ls} is calculated using equation (2.92) as proposed by Phillips and Alley (2007). It is noted that the CFD procedure for calculating κ_{Ls} depicted by Alley et al. (2007) was also tested, but gave incoherent results with higher C_{Lmax} at lower twist distributions. Table 5-2 presents the values of $\kappa_{L\Lambda}^{phill}$ as well as both values of κ_{Ls}.

Table 5-2: κ_{Ls} values for original LLT model.
(*) Calculated based on Phillips and Alley (2007).
(**) Calculated based on Alley, Phillips, and
Spall (2007)

Configuration	$\kappa_{L\Lambda}^{phill}$ (*)	κ_{Ls} (*)	κ_{Ls} (**)
BWB V00	0.302	0.965	1.815
BWB V04	0.302	0.951	1.556
BWB V08	0.302	0.938	1.573

Following through, by applying the previous corrective coefficients, C_{Lmax} was estimated. Table 5-3 presents the C_{Lmax} values comparison. Here, again, the original model fails to predict C_{Lmax}. In the case of (Phillips & Alley, 2007), the prediction is off by up to 27%. In the case of (Alley et al., 2007), the prediction error is smaller (up to 25%). However, the (Alley et al., 2007) results present grave inconsistencies where C_{Lmax} is higher at lower twist values. For this reason, for the coming compound wing calibration, only the κ_{Ls} model proposed in (Phillips & Alley, 2007) was retained – see equation (2.92) -. Table 5-3 presents a summary of these results.

Table 5-3: C_{Lmax} prediction error for Phillips' Twisted LLT model for the BWB geometries. (*) Parameter calculated based on Phillips and Alley (2007). (**) Parameters calculated based on Alley et al. (2007)

Configuration	CFD	Phillips (*)	Error	Phillips (**)	Error
BWB V00	0.67	0.49	27%	0.60	22%
BWB V04	0.73	0.56	23%	0.56	23%
BWB V08	0.79	0.64	19%	0.59	25%

At this point, it is safe to assume that, there is room for improvement when applying the Phillips and Alley model on this BWB geometry. The model hypotheses don't contemplate the case of

the studied BWB. These results are now used to show the gains in accuracy brought by the compound wing LLT model.

5.3.2 Implementation of the compound wing model

The compound-wing model is now proposed for C_{Lmax} prediction. This model, however, requires calibration of the parameter n_{LLT}. This sub-section calibrates the compound wing LLT model with the CFD data obtained from the BWB geometries.

Note that in the case of a constant sweep and constant airfoil, the proposed model is equivalent to Phillips' model. This means that, in the case of simple-wing geometries, our proposed model benefits from the previous validations established by Phillips et al. for the original Phillips et al. model (Alley et al., 2007). This demonstration is fully developed in APPENDIX VIII.

For the case of multi-sweep geometries, the proposed calibration requires to generate an LLT equivalent geometry of the BWBs. To do this, we use the 29 different airfoils presented in Table 3-3. For each one of these airfoils, the XFOIL method (Drela, 1989) is used to obtain a viscous $C_l - \alpha$ database. Each airfoil is calculated at its respective Reynolds number based on the local chord c, at sea level at an approach speed of $68m/s$ (Mach 0.2), with free transition ($NCrit = 9$) and no tripping. This yields the airfoil's lift evolution $C_l - \alpha$, the local lift slope a_0, the zero lift angle of attack α_{L0}, the airfoil's maximum lift coefficient C_{lstall} and its corresponding stall angle $\alpha_{2Dstall}$. These values are linearly interpolated between the 29 reference sections to generate a continuous function for each airfoil parameter along the wingspan. Figure 5-9 shows the example of the resulting C_{lstall} distribution along the normalized wingspan $\eta = \frac{y}{b/2}$.
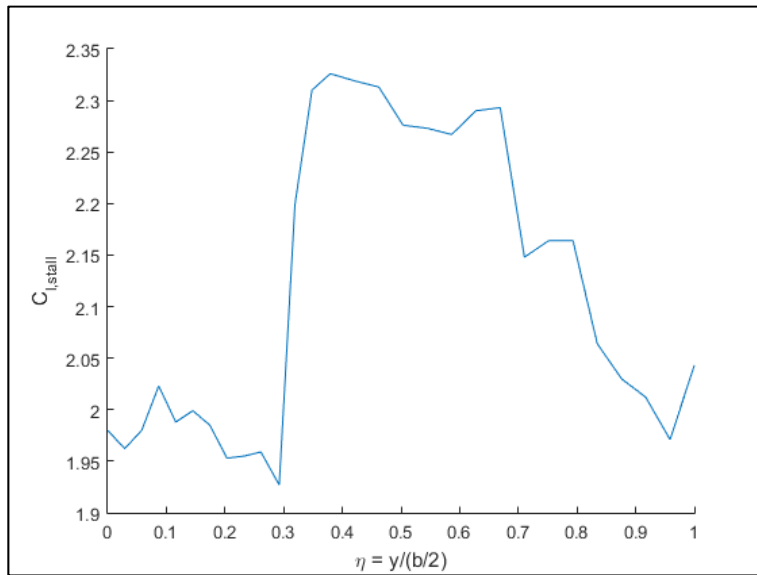
Figure 5-9: C_{lstall} distribution of the BWB along the wingspan

The LLT model implementation is done using Matlab R2015a. Once the common planform database has been created, it is incorporated into the model. Then each twist distribution is added, and the coefficients for each geometry are calculated automatically

5.3.3 Calibration of the compound wing model

Let us start with the linear lift zone. Note that no calibration is needed at this point. Whatever the value of n_{LLT}, the linear lift zone will behave in the same manner independently of n_{LLT}. Figure 5-10 shows both the CFD and the compound wing LLT results. The dashed curves in black correspond to the $C_L - \alpha$ values from the CFD calculations. The lines in color correspond to the compound wing LLT model. We can see a closer agreement with the lift slope $C_{L,\alpha}$ in this model with respect to the $C_{L,\alpha}$ obtained in Figure 5-8. Furthermore, the variation of C_L with respect to ϕ corresponds to $dC_L/d\phi \approx 0.35$ which is the same variation as the one presented by the CFD results. While there is still a notable absolute error on C_L prediction of up to 0.05 at low angles of attack, this model presents better agreement with the CFD results than the previous LLT model in the linear lift zone.
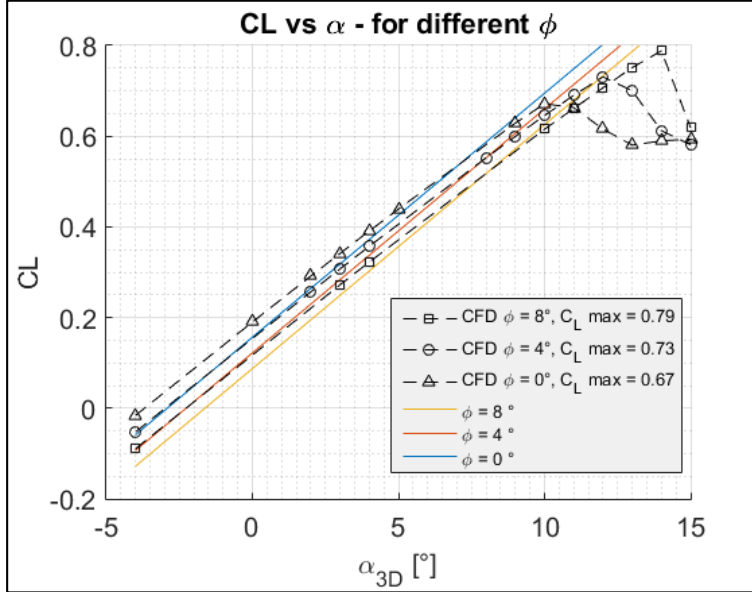
Figure 5-10: C_L prediction for the multisweep correction
model in the linear lift zone

Now, we estimate the values of C_{Lmax} with the compound wing model. In this case, we use the CFD results to calibrate the value of n_{LLT}. The optimal parameter minimizing the error for all 3 geometries is found as $n_{LLT} = 3.7$. Table 5-4 presents the C_{Lmax} obtained for the three geometries with $n_{LLT} = 3.7$. By construction, these results show good agreement with the CFD results with under 3% error. Based on this calibration, it is now possible to use this model to explore the design space of the BWB. As an example, we show how this model allows to find an optimum twist configuration for the BWB.

Table 5-4: C_{Lmax} calibration for compound wing LLT

Configuration	C_{Lmax} (CFD)	C_{Lmax} (Compound wing)	Relative error
BWB V00	0.672	0.676	0.66%
BWB V04	0.731	0.733	0.29%
BWB V08	0.788	0.767	2.68%

5.3.4　　Finding an optimum twist configuration

The compound wing LLT model is now capable of predicting the C_{Lmax} of other BWBs with respect to the twist distribution. We are interested in obtaining the twist distribution that would yield the highest possible maximum lift coefficient under the constraint of a limited maximum twist ϕ_{max}. To do so, an optimization algorithm is generated. At each iteration, this algorithm starts from an initial twist distribution and generates 15 different new distributions where a fixed small twist $d\phi$ has been added independently to each one of the 15 OW sections. After calculating C_{Lmax} for the 15 new different configurations, it chooses the configuration giving the highest C_{Lmax}. The resulting configuration is then taken as the starting configuration and the process is repeated until no possible modifications can be done to increase C_{Lmax}. This process is constrained by the condition that no local twist can surpass a given value ϕ_{max}.

Starting from the configuration without any geometric twist BWB V00, the algorithm was applied 3 times with the conditions $\phi_{max} \in \{2°, 4°, 8°\}$ respectively. Remember that in this case, the distribution of ϕ is not necessarily linear, and it cannot go past ϕ_{max}. For a visual representation, Figure 5-11 presents the twist distribution proposed by configuration BWB V04 while Figure 5-12 presents the twist distribution found with the optimization algorithm for the condition $\phi_{max} = 4°$. These two figures show that for the same $\phi_{max} = 4°$, the optimized twist distribution is capable of generating up to 5.5% more maximum lift than the linear distribution. While seemingly small, this added value can be compounded when compared to the baseline geometry V00, where the original V04 geometry gives only a 7% increase and the optimized V04 offers a 13% increase; almost doubling the increase in maximum lift coefficient with the same constraint of $\phi_{max} = 4°$. Furthermore, the figure shows that it is not necessary to apply twist right from the beginning of the OW ($\eta = 0.38$), but that, under the $\phi_{max} = 4°$ constraint, it is more important to apply a constant twist for $\eta > 0.46$.
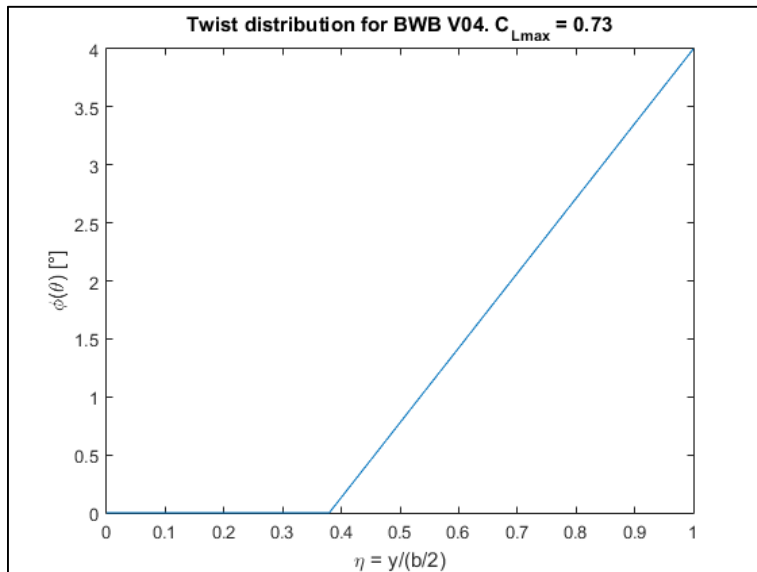
Figure 5-11:   Twist distribution for the BWB V04
geometry
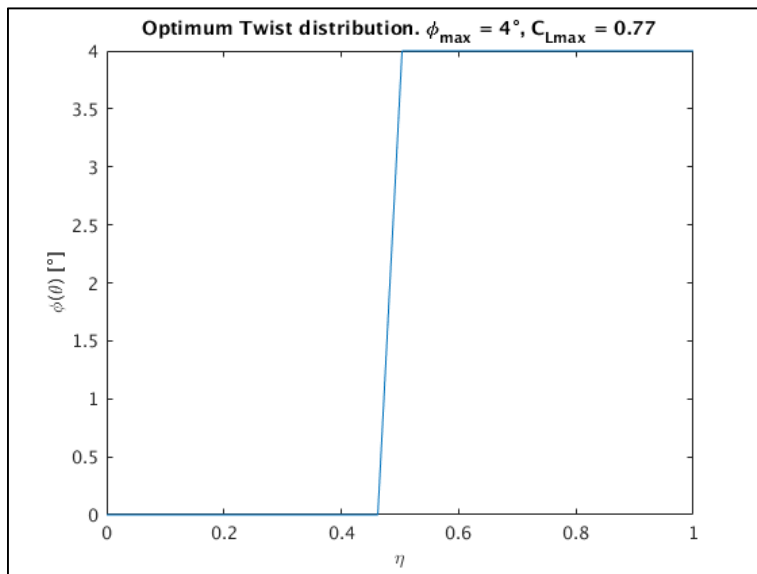
Figure 5-12:   Optimized twist distribution using LLT for
ϕ_{max}=4°

Table 5-5 presents the C_{Lmax} predictions obtained by optimizing the twist distribution compared to the original V00, V04 and V08 results. The optimized distributions (on the right) show better C_{Lmax} at lower twist angles than the linear distributions. In particular, the OW constant distribution seems to be optimal for this aircraft up to $\phi_{max} \approx 8°$. With this, optimal twist distributions have been found without having to run extra CFD simulations by applying the compound wing LLT model. At this point, future works should focus on running the optimum geometry with CFD methods to further confirm these findings.

Table 5-5: C_{Lmax} prediction for optimum twist (compound wing LLT)

Configuration	C_{Lmax} (Compound wing)	Optimized twist	C_{Lmax} (Compound wing)
BWB V00	0.68	$\phi_{max} = 2°$	0.72
BWB V04	0.73	$\phi_{max} = 4°$	0.77
BWB V08	0.77	$\phi_{max} = 8°$	0.85

All in all, this model shows promising results. It is however necessary to expand this validation to more compound wing testcases consisting of other BWB geometries with more twist distribution, different sweep distributions, and different airfoil choices. In any case, this model can be used as a first step to estimate the low speed maximum lift coefficient for the BWB aircraft.

A particular characteristic of this model lays in its non-iterative nature. Introducing a new calibration parameter n_{LLT} and assuming all the other correction factors as true according to the rules proposed by Phillips and Alley, allows to set a model insensitive to terms like "stability" or "convergence". The trade-off here being the requirement of further accuracy and development of design rules for the n_{LTT} term. By comparison, other iterative approaches have seen good results on different non-trapezoidal geometries like the model proposed by (Gallay & Laurendeau, 2015) for elliptic wings.

The LLT model proposed can now be added to the pool of tools available to the aeronautical designer when faced with BWB design. This model is, in fact, not limited to BWB configurations, and it may be applied to other complex geometries sharing similar compound wing qualities – i.e. wings with varying geometric parameters -. Do note that this model doesn't account for vortex lift generation and may not be used accurately for primarily delta geometries.

5.4   Chapter summary

Based on the hypothesis of a compound wing nature of the BWB, this chapter's objective was to verify the existence of a parametrizable coupling between the CB and the OW to predict and enhance C_{Lmax} at low speeds and to propose a low-fidelity model capable of exploiting this interaction. This was achieved by using both a high fidelity CFD approach and a low-fidelity LLT model. This section will summarize these results in the context of the original contributions brought forward by this research work.

First, the CFD RANS approach used 32 simulations to build multiple local-section databases concerning the stall of the BWB geometries. The results were condensed into local topologies showing the impact of twist on both C_l and C_L. These topologies showed, as expected, the delay on local stall due to twist. More than that, the section of maximum lift C_{lmax} and the first stalling section are both displaced inboard. In turn, this increases the CB's contribution to global lift generation by allowing it to operate at higher angles of attack. This explains, the increase of both $\alpha_{3Dstall}$ and C_{Lmax} with ϕ_{max}. Finally, this result shows that it is possible to use the compound wing nature of the BWB to enhance the C_{Lmax} by coupling the OW stall with the CB lift. This validates the initial hypothesis of this chapter.

It is worth noting that this coupling effect was shown to increase C_{Lmax} with minimal effects on $(L/D)_{max}$. Note that the percentage increase in C_{Lmax} is higher than the percentage decrease in $(L/D)_{max}$. The designer may choose the optimal twist distribution depending on the needs of the mission.

Furthermore, the CFD analysis also concluded that there is a linear variation between C_{Lmax} and ϕ_{max}. This new result is limited, so far, to linear twist distributions. It must however be accounted for in future compound wing designs like the BWB.

Concerning the low-fidelity design tool, the modified compound wing LLT model was calibrated based on the three available BWB geometries. The calibration parameter returning the lowest error with respect to the CFD results was fixed at $n_{LLT} = 3.7$. This allows to give an initial maximum lift prediction framework for compound wing geometries.

The original contributions of this chapter concern: (1) the detailed CFD analysis of the twist impact on C_{Lmax}. Previously available studies carried out by Park et al. (2017) proposed basic analyses based on the C_p coefficients. In contrast, this work establishes a topography of the evolution of C_{lmax}; allowing to see and understand the impact of local twist on the global lift behaviour of the aircraft. This impact validates the idea that the stall behaviour of the CB and the OW can be coupled in order to stall together everywhere along the wingspan. This topography can be used as a baseline for predicting local behaviour or the BWB. In particular, it shows how twist can be used to not only delay stall, but enhance C_{Lmax} while doing so. (2) The clear linear relation between C_{Lmax} and ϕ_{max} was established and can now be used as a rule of thumb when estimating C_{Lmax} variations with ϕ_{max} for linear twist distributions. (3) The validation of the initial hypothesis sustaining that the characteristics of the CB and the OW can indeed be coupled to enhance C_{Lmax} was a major contribution. While simple to conceive, there was no previous evidence of this idea actually working on a BWB. This result allows to devise new couplings between the CB and the OW. (4) The low-fidelity prediction tool that is now available for BWB conceptual design will save time and numerical resources when designing compound wings; in particular when designing BWBs.

At this point it must be noted that the compound wing LLT C_{Lmax} prediction model was calibrated based on 3 geometries only. This doesn't account for all possible twist distributions, but it provides a good starting point. Further geometries may be needed for comparison, but

this model can already be used as a stepping stone for BWB and compound wing low-fidelity prediction.

CONCLUSION

The advent of the BWB as an answer to the ever-increasing performance constraints from the international regulatory associations (ICAO, IATA) brought forth multiple challenges and reassessments concerning the applicability of classical aircraft design. The vast number of early research works on BWB between 2004 and 2014 focused, naturally, on extra-large and large BWB aircrafts (450+ passengers), mainly at cruise conditions (see Velazquez et al., 2015). However low speed aerodynamic behaviour was often glossed over. This usually led to authors working with assumptions based on classic TAW tools rather than relying on BWB-specific knowledge when predicting low-speed behaviour (Diedrich et al., 2006; Leifsson et al., 2013). This research was born from the necessity to shed some light into the actual workings of the low speed aerodynamics of this aircraft so as to validate or invalidate these assumptions. To do so, the maximum lift coefficient was chosen as the driving variable for this research. The objective of this thesis was to develop BWB-specific design tools, based on the hypothesis of a stall-delaying CB/OW interaction, that could be used to better predict and design natural lift at low speeds for this aircraft configuration. The thesis objective was attained through the development of three sub-objectives: (1) tailored design of a BWB regional geometry, (2) comparison with representative TAW aircraft at low speed and (3) exploration of the CB/OW coupling hypothesis via the twist distribution. These three sub-objectives resulted in the successful development of a BWB-specific low-fidelity prediction model and general guidelines for low speed. Throughout this thesis, it was possible to characterise the low-speed aerodynamics of the regional BWB aircraft through the use of a CFD RANS approach, in order to extract tendencies and design guidelines for the BWB configuration as a whole. These contributions remain, however, limited to the framework where they were developed and can always be improved upon further iterations. These limitations will be developed in the recommendations. An overview of the main results from this thesis is proposed in the following paragraphs.

The first sub-objective of this thesis consisted on the design of a regional BWB configuration and numerical model. This objective consisted of two parts: (1) the development of a regional

BWB baseline geometry and (2) the verification of the CFD RANS approach for near-stall prediction on the BWB. The proposed approach dives into the geometry constraints that appear only at the regional level, and which limit the effective cabin space. This work proposed a slight modification to the conceptual design loop in order to obtain a geometry that matches both geometrical and mission constraints. This contrasts with classic BWB approaches (Diedrich et al., 2006; Liebeck, 2004) which don't face these geometry constraints inherent to regional BWB sizes. Both low-fidelity VVLM and high-fidelity CFD RANS methods are used in the dimensioning of the BWB baseline geometry, resulting in a BWB geometry model for which we have all the dimensions. In particular, the use of a RANS approach with the SA turbulent model for stall analysis is verified by comparing test cases against existing experimental data with positive results. This is coherent with similar approaches for maximum lift prediction for wings (Alley et al., 2007; Geissler & Haselmeyer, 2006).

The second sub-objective of this research work is focused on the differences in low-speed stall behaviour between a representative TAW geometry and the regional BWB geometry. The two geometries were exposed to low-speed conditions at multiple angles of attack focused around their respective global stall angles. Qualitatively, the data links the skin friction state to the presence of local stall and, eventually, the propagation of said local stall into global stall. Furthermore, this research shows that, for both cases, stall is focused at the wing / outer wing, meaning that neither the fuselage nor the center-body attain local stall conditions. This introduces the hypothesis of CB/OW interaction for the BWB treated later-on on this thesis. Quantitatively, the data reveals that the center-body generates almost twice as much local lift than a classic fuselage, which is relevant considering that it constitutes around 67% of the wetted surface. Furthermore, the global aerodynamic parameters of both aircrafts are provided. These indicate that, the BWB baseline geometry is capable of generating sufficient lift to sustain its own weight during low-speed approach without the need of high-lift devices. This result validates the hypothesis advanced by previous BWB designers who consider that some or all high-lift devices might be unnecessary from a lift generation perspective for the BWB (Hileman, Reynolds, et al., 2007). These results also brought up new concerns: (1) the geometry proposed initiated stall at the wing-tip and (2) the hypothesis of the existence of a

parametric coupling between the CB and the OW allowing to align the stall properties of the CB with those of the OW needed to be confirmed or denied.

The third sub-objective aimed to explore the CB/OW interaction of the BWB and propose solutions to optimize the geometry playing around the hypothesized coupling. To do so 2 more BWB geometries were added with a linearly increasing twist distribution each. The same low speed conditions were considered and multiple angles of attack allowed to analyse the changes between each configuration with respect to maximum lift and stall initiation. The results show that, as expected, the stall delay introduced by the twist on the outer wing section, allowed for a higher participation of the CB into the generation of lift, which in turn resulted in a higher maximum lift coefficient and a higher stall angle of attack. The introduction of twist allowed to attain higher C_{Lmax} by coupling the low-speed behaviour of the CB with that of the OW, thus validating the hypothesis of the existence of an exploitable CB/OW interaction. Even more so, the stall front expands towards the centerline, thus homogenizing stall angles along the wingspan. Furthermore, abrupt stall is displaced from the wingtip to the center of the outer wing. These improvements come with an almost negligible trade-off in $(L/D)_{max}$ for an increase in 18% in C_{Lmax}. Moreover, from a design perspective, the results suggest that the maximum lift coefficient is linearly proportional to the value of maximum twist angle for the linear twist distribution. Based on these results, a low fidelity LLT model was proposed to predict the maximum lift coefficient of a compound wing and calibrated with the BWB results from this chapter. Said model represents a stepstone for low-fidelity compound wing low-speed prediction and can provide future aircraft designers with initial C_{Lmax} values for their BWB designs.

To sum it up, this research, born from the debate of whether or not the BWB needs high-lift devices to generate enough lift at low-speeds – it doesn't - resulted in a deeper research of the design interactions between the CB and the OW at low speeds. More than that, this research provides a new perspective to the compound wing nature of the BWB, allowing for a better understanding of the CB/OW coupling at low-speeds. This research proposes guidelines and rules of thumb to estimate C_{Lmax} variation with twist, as well as a more developed low-fidelity

prediction model so as to save up on computational resources at early design stages. It separates itself from the other BWB low-speed works (Paulus et al., 2013) by analysing the need of high-lift devices rather than delving directly into the design of high-lift devices for the BWB. From a BWB perspective, this research brings evidence to previously stated assumptions when facing BWB low-speed design and offers tools to quickly calculate the important maximum lift. The author hopes that in doing so, the BWB community will be, as a whole, one small step closer to the advent of the BWB as the next-generation transport aircraft. As for the limits of this work, it is obvious that, by its nature, the RANS approach cannot properly deal with turbulent structures or time-sensitive variations; thus its accuracy might lag behind more recent, detailed or expensive numerical models like DDES, LES or even DNS. On top of this, these results were obtained on a baseline geometry lacking control surfaces or engines. A detailed list of future works and recommendations is proposed in the next section as an addendum to the general conclusion with the general idea that richer numerical models will allow to propose better design rules for the BWB. With this being said, the current work will have proposed a satisfactory initial insight into the aerodynamic behaviour of the regional BWB at low speeds.

RECOMMENDATIONS

This research work proposed an insight into the aerodynamic behaviour of the regional BWB at low-speeds. In light of the results and lessons of this project, the following section introduces recommendations that would result either in more accurate results or in a better and more in-depth understanding of this phenomenon. These recommendations show the limits of the current work as well as the opportunities for future research.

One of the main simplifications of this work lie in the use of a baseline geometry without engines or control surfaces. This was consciously decided so as to slightly simplify the geometry and focus specifically on the aerodynamics rather than on the details of specialized surfaces. It is now natural to continue the research with more complex geometries including control surfaces and engines.

This project was based, early on, on the choice of a RANS methodology. This was justified, at the time, by the intense calculation resources needed to converge dozens of low-speed cases at the scale of an actual aircraft – including its fluid domain -. Furthermore, the verifications showed that, for the current purposes, this was enough. However, chapter 4 introduced the limits of this approach. Proposing recirculation bubbles on an averaged field is limiting since the accuracy of said bubbles cannot be verified and it can only be considered, at best, as a tendency under a qualitative approach. In order to analyse turbulent structures linked to stall behaviour it is necessary to tap into more detailed numerical models. Doing so will require far more computational resources than the ones used in this research. This can be offset by limiting the number of simulations to only a few angles. To do so, the current geometry can be used in tandem with the aerodynamic knowledge already available on this geometry.

This thesis applied a conservative static stall approach; always initializing the fluid domain with farfield conditions. However, current high-lift workshops introduced the problem of a possible dependence of C_{Lmax} on initial flow conditions. This suggests that different initializations, like restarting from a preceding angle of attack, would yield different results.

Due to the high variance of results for high-lift simulations for these workshops, it is still not clear if this dependency is the result of the numerical method accuracy or the result of an actual physical phenomenon. This hesitation exists because while initial condition dependence has been found in the literature, dynamic stall is also a known phenomenon, particularly for rotor blades systems. This suggests the two following hints for future research: (1) analysis of initial condition dependency of stall from a numerical method perspective and (2) analysis of dynamic stall effects on BWB configurations.

Finally, in order to limit the extent of this work, a framework had to be fixed. While satisfying, the work done on the twist parameter is limited to a piecewise linear distribution with $\phi_{max} = 8°$. At this point the next natural step would be to explore a larger design space with greater ϕ_{max} and multiple twist distributions. Continuing from this, it would be necessary to test more geometries with different sweep distributions, different airfoil distributions and different aspect ratios in order to continue developing the multi-section LLT model.

APPENDIX I

RANS MODEL

This appendix presents the high-fidelity RANS model used to estimate the aerodynamic coefficients of the TAW and the BWB. Specifically, this appendix presents the Reynolds-Averaged Navier-Stokes equations along with the Spalart-Allmaras turbulence model. For further content, the reader may look into the works of (Currie, 2002) and (Pope, 2000).

I.1 Time averaging

The *RANS* approach is based in the decomposition of a given field ϕ into its time-averaged component $\bar{\phi}(x) = \frac{1}{T} \int_{t_0}^{t_0+T} \phi(x,t)\, dt$ and its instantaneous fluctuation $\phi'(x,t)$. The instantaneous value at a given time is then given by $\phi = \bar{\phi} + \phi'$. In the scope of compressible flow, a new density-weighted time-averaging (Favre averaging) is introduced so that $\phi = \tilde{\phi} + \phi''$, where $\tilde{\phi} = \frac{\overline{\rho\phi}}{\bar{\rho}}$. Applying the original Reynolds time-average filter to equations (2.11) through (2.13) and using the Favre-average notation for the velocity vector, the energy and the stress tensor, yields the compressible RANS equations:

$$\frac{\partial \bar{\rho}}{\partial t} + div(\bar{\rho}\tilde{v}) = 0 \tag{I.1}$$

$$\frac{\partial}{\partial t}(\bar{\rho}\tilde{v}) + div(\bar{\rho}\tilde{v}\otimes\tilde{v} + \bar{p}\underline{I}) - div(\underline{\tilde{\tau}} - \overline{\rho v'' \otimes v''}) = 0 \tag{I.2}$$

$$\frac{\partial}{\partial t}(\bar{\rho}\tilde{e}_0) + div(\bar{\rho}\tilde{v}\tilde{e}_0 + \bar{p}\tilde{v}) - div\left(\left(\underline{\tilde{\tau}} - \overline{\rho v'' \otimes v''}\right).\tilde{v} - \overline{q}\right)$$
$$+ div\left(\overline{\rho e_0'' v''} + \overline{p v''} - \overline{\underline{\tau}.v''}\right) = 0 \tag{I.3}$$

where $e_0 = e + \frac{1}{2}v.v$ is the total specific energy and $\tilde{e}_0 \equiv \tilde{e} + \frac{1}{2}\tilde{v}.\tilde{v} + \frac{1}{2}\widetilde{v''.v''}$ is the Favre-averaged total specific energy. Multiple non-zero terms have appeared due to the correlation of the non-average residuals in the forms $\overline{\phi''} \neq 0$ and $\overline{\psi''\phi''} \neq 0$. Special attention is brought

to the term $\boldsymbol{\tau_{rey}} = -\overline{\rho \boldsymbol{v''} \otimes \boldsymbol{v''}}$ representing the Reynolds-stress tensor. In order to close these equations, an eddy viscosity model is introduced. By reintroducing Fourier's law of thermal conductivity, the compressible time-averaged equations become:

$$\frac{\partial \overline{\rho}}{\partial t} + div(\overline{\rho} \widetilde{\boldsymbol{v}}) = 0 \tag{I.4}$$

$$\frac{\partial}{\partial t}(\overline{\rho} \widetilde{\boldsymbol{v}}) + div(\overline{\rho} \widetilde{\boldsymbol{v}} \otimes \widetilde{\boldsymbol{v}} + \overline{p}\underline{\boldsymbol{I}}) - div(\underline{\boldsymbol{\tau_{tot}}}) = 0 \tag{I.5}$$

$$\frac{\partial}{\partial t}(\overline{\rho} \widetilde{e}_0) + div(\overline{\rho} \widetilde{e}_0 \widetilde{\boldsymbol{v}} + \overline{p} \widetilde{\boldsymbol{v}}) - div\left(\left(\underline{\boldsymbol{\tau_{tot}}}\right).\widetilde{\boldsymbol{v}} + \lambda_{tot} \boldsymbol{grad}(\widetilde{T})\right) = 0 \tag{I.6}$$

where

$$\underline{\boldsymbol{\tau_{tot}}} = \underline{\boldsymbol{\tau_{dyn}}} + \underline{\boldsymbol{\tau_{rey}}} \tag{I.7}$$

$$\underline{\boldsymbol{\tau_{dyn}}} = \mu_{dyn}\left(\underline{\boldsymbol{grad}}(\widetilde{v}) + \underline{\boldsymbol{grad}}(\widetilde{v})^T\right) - \frac{2}{3}\mu_{dyn} div(\widetilde{v})\underline{\boldsymbol{I}} \tag{I.8}$$

$$\underline{\boldsymbol{\tau_{rey}}} = \mu_{tur}\left(\underline{\boldsymbol{grad}}(\widetilde{v}) + \underline{\boldsymbol{grad}}(\widetilde{v})^T\right) - \frac{2}{3}(\mu_{tur} div(\widetilde{v}) + \overline{\rho}k)\underline{\boldsymbol{I}} \tag{I.9}$$

$$k = \frac{1}{2}\widetilde{\boldsymbol{v''}.\boldsymbol{v''}} \tag{I.10}$$

$$\lambda_{tot} = \mu_{tot}^* c_p \tag{I.11}$$

$$\mu_{tot}^* = \frac{\mu_{dyn}}{Pr_{dyn}} + \frac{\mu_{tur}}{Pr_{tur}} \tag{I.12}$$

where $Pr_{dyn} = 0.72$ is the laminar Prandtl number, μ_{tur} represents the turbulent viscosity, k is the specific turbulent kinetic energy, and $Pr_{tur} = 0.9$ is the turbulent Prandtl number. The following sub-section explains the particular turbulence model used to represent μ_{tur} and k.

I.2   Spalart-Allmaras turbulence modeling

As previously stated, a model for the turbulent viscosity μ_{tur} and the turbulent kinetic energy k is needed. The Spalart-Allmaras (SA) turbulence model was chosen based on its large presence in aeronautical works for both drag and lift prediction workshops (Rumsey &

Slotnick, 2014; Rumsey et al., 2018; Vassberg et al., 2010) as well as its relative success to follow the airflow even through boundary layer separation (Grosvenor, 2007). The specific SA model used in this project corresponds to the one implemented by Palacios et al. (2013). In this one-equation model, only the turbulent viscosity μ_{tur} is calculated via a unique transport equation. In this context, the Reynolds stress looses the dependence on the kinetic energy $\underline{\boldsymbol{\tau_{rey}}} = \mu_{tur}\left(\boldsymbol{grad}(\tilde{v}) + \boldsymbol{grad}(\tilde{v})^T\right) - \frac{2}{3}\left(\mu_{tur}div(\tilde{v})\right)\underline{\boldsymbol{I}},$ and equation (I.7) becomes equation (I.13):

$$\underline{\boldsymbol{\tau_{tot}}} = \mu_{tot}\left(\boldsymbol{grad}(\tilde{v}) + \boldsymbol{grad}(\tilde{v})^T - \frac{2}{3}div(\tilde{v})\underline{\boldsymbol{I}}\right) \tag{I.13}$$

where $\mu_{tot} = \mu_{dyn} + \mu_{tur}$. In this model, the turbulent viscosity is computed as follows:

$$\mu_{tur} = \overline{\rho}\hat{v}f_{v1}, \qquad f_{v1} = \frac{\chi^3}{\chi^3 + c_{v1}^3}, \qquad \chi = \frac{\hat{v}}{v}, \quad v = \frac{\mu_{dyn}}{\overline{\rho}} \tag{I.14}$$

where the variable $\hat{v}$ is obtained by solving the following transport equation:

$$\frac{\partial}{\partial t}(\hat{v}) + div(\hat{v}\tilde{v}) - div(\frac{v + \hat{v}}{\sigma}\boldsymbol{grad}(\hat{v})) \tag{I.15}$$

$$= c_{b1}\hat{S}\hat{v} - c_{\omega1}f_{\omega}\left(\frac{\hat{v}}{d_S}\right)^2 + \frac{c_{b2}}{\sigma}|\boldsymbol{grad}(\hat{v})|^2$$

where $\hat{S} = |\boldsymbol{\omega}| + \frac{\check{v}}{\kappa^2 d_S^2}f_{v2}$, $\boldsymbol{\omega} = \boldsymbol{curl}(\tilde{v})$, d_S is the distance to the nearest wall, and $f_{v2} = 1 - \frac{\chi}{1+\chi f_{v1}}$. The function f_{ω} is computed as $f_{\omega} = g\left[\frac{1+c_{\omega3}^6}{g^6+c_{\omega3}^6}\right]^{1/6}$, where $g = r + c_{\omega2}(r^6 - r)$ and $r = \frac{\hat{v}}{\hat{S}\kappa^2 d_S^2}$. Finally, the model constants are given as $\sigma = 2/3$, $c_{b1} = 0.1355$, $c_{b2} = 0.622$, $\kappa = 0.41$, $c_{\omega1} = \frac{c_{b1}}{\kappa^2} + \frac{1+c_{b2}}{\sigma}$, $c_{\omega2} = 0.3$, $c_{\omega3} = 2$, $c_{v1} = 7.1$.

As for the initial boundary conditions, the far-field boundary condition on the turbulent viscosity imposes a fraction of the laminar viscosity at the far-field $\hat{v} = 0.1v$. For viscous walls, $\hat{v}$ is set to zero to model the absence of turbulent eddies close to the wall. For more detail on this model and this particular implementation, the reader is referred to the works of Spalart and Allmaras (1992) and Palacios et al. (2014).

APPENDIX II

FINITE VOLUME METHOD

This appendix presents the finite volume method as implemented by (Palacios et al., 2013). A general description of the method is proposed before delving into the space and time schemes and the boundary conditions. The equations (I.2), (I.3), (I.14) and (I.15) are solved numerically using the open source software "Stanford University Unstructured" (SU2) v5.0.0 developed by Palacios et al. (2013). This software uses a finite volume method (FV) to discretize the RANS equations and return a discretized version of the solution field. For more details, the reader may refer to the works of Ferziger and Peric (2012), Blazek (2015) and (Palacios et al., 2013), from which this section was inspired.

II.1   The Finite Volume Method

The finite volume method is based upon the spatial discretization of the fluid domain into a finite number of cells or control volumes (CV). **Erreur ! Source du renvoi introuvable.** presents a one-dimensional grid with nodes $(i - 1, i, i + 1)$, the control volume CV around node i and the interfaces of this control volume with the neighboring CVs denoted as S_i and S_{i+1}. The one-dimensional velocity is given as $\boldsymbol{v} = u\boldsymbol{e_x}$.
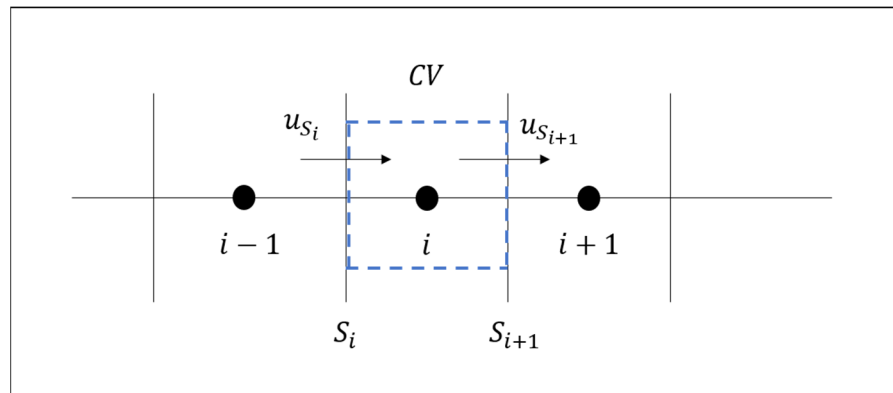

Figure A II-1: Representation of a discretized control volume for 1-dimensionnal problems

Let φ be a scalar field evolving in time and space. Then a continuous generic transport equation for this field is presented as:

$$\frac{\partial}{\partial t}(\rho\varphi) + div(\rho\boldsymbol{v}\varphi) - div(\gamma\boldsymbol{grad}(\varphi)) = Q \tag{II.1}$$

Where the first term represents the temporal variation of φ, the second term corresponds to the convective transport, the third term corresponds to the diffusive transport and the last term Q corresponds to the source terms. In this case $\boldsymbol{v} = (u, v, w)^T$ is the convective velocity, ρ is the density of the fluid, and γ is the diffusivity coefficient for φ. An integral form for this equation around a control volume Ω is as follows:

$$\frac{d}{dt}\int_\Omega \rho\varphi d\Omega + \int_{\partial\Omega} (\rho\varphi)\boldsymbol{v}.\boldsymbol{n}dS - \int_{\partial\Omega} \gamma\boldsymbol{grad}(\varphi).\boldsymbol{n}dS = \int_\Omega Qd\Omega \tag{II.2}$$

where $\boldsymbol{n}$ denotes the outward normal vector at the local surface. Applying this conservative form to a control volume Ω of boundaries $\partial\Omega = \sum_k S_k$, where k is the number of interfaces with the neighbouring CVs, yields equation (II.3).

$$\frac{d}{dt}I_\Omega(\rho\varphi) + \sum_k \int_{S_k} (\boldsymbol{v}.\boldsymbol{n})\rho\varphi dS_k - \sum_k \int_{S_k} \gamma(\boldsymbol{grad}(\varphi).\boldsymbol{n})dS_k \tag{II.3}$$
$$= I_\Omega(Q)$$

Let U be the integrand of any of the 4 terms in eq. (II.2). Then the volume integral $I_\Omega(U) = \int_\Omega U d\Omega$ can be defined as a function of U in the current and neighboring nodes. It is very common to assume that the volume integral at node i depends only on the values of U inside its control volume. Most usually, for each node i, the integral inside its associated CV is given as $I_{\Omega_i}(U) = U_i|\Omega_i|$ (Palacios et al., 2013). At this point it is necessary to introduce interface values U_{S_k} so that the surface integrals from equation (II.3) may be calculated:

$$\int_{S_k} \boldsymbol{U}.\boldsymbol{n}dS_k = I_{S_k}(\boldsymbol{U}) \qquad \text{(II.4)}$$

Equation (II.4) indicates that the value of the surface integral can be discretized as a function of the values of U in both the local and the surrounding nodes. While not as straightforward as the volume integral, it is possible to find a linear relation between $I_{S_k}(\boldsymbol{U})$ and $(\boldsymbol{U_k})$.

At this point, if all the variables but ϕ are considered known at each node, equation (II.3) can be solved by using discretization schemes and interpolations to obtain the values of the unknown derivatives and variables at each node as well as at the interfaces. As such, after some algebraic manipulations, the transport equation for node i takes the following form:

$$\sum_{n=1}^{N} a_{in}\varphi_n = b_i \qquad \text{(II.5)}$$

Where $(a_{in})_{(i,n)\in[1,N]^2}$ and $(b_i)_{i\in[1,N]}$ depend on the values of the known variables at neighboring nodes. This simplifies the convection problem into a linear algebra problem. The FV method can be summarized as follows: the conservative transport equation consisting of temporal, convective, diffusive and source terms is discretized and transformed into a linear algebra problem in the form $A\Phi = B$ where $A = (a_{ik})_{(i,k)\in[1,N]^2}$ must be inverted in order to solve for $\Phi = (\varphi_k)_{k\in[1,N]}$. The following subsections present the specific temporal and spatial discretization schemes used to solve the RANS equations (I.4), (I.5) and (I.6) as well as the turbulent transport equation (I.15).

II.2 Discretization schemes

The previous subsection presented the general approach of the FV method. However, an approximation method for time and space derivatives as well as interface integrals is needed. The choice of a specific discretization scheme will determine the precision, the speed and the stability of the calculations. SU2 (Palacios et al., 2013) proposes multiple schemes for the

different terms of the transport equation: a discretization set for the convective and diffusive terms, another set for the temporal discretization and yet a different one for the turbulent equation. This section presents the discretization schemes used in this study.

II.2.1   Time discretization

Let $\varphi(x,t)$ be a scalar field of interest. Let i denote the center of the control volume and n denote the time iteration, so that, for a given node i, $\varphi_i^{(n)} = \varphi(x_i, t_n)$. Now let φ be described by partial differential equation (II.6). Applying a 1st order approximation for the derivative on the left hand side, this equation can become implicit (eq. (II.7)) or explicit (eq.(II.8)). In other words, the derivative can depend on current values of the right-hand side (implicit) or past values of the right-hand side (explicit).

$$\frac{d\varphi}{dt} = f(\varphi) \tag{II.6}$$

$$\frac{\varphi_i^{(n)} - \varphi_i^{(n-1)}}{t^n - t^{n-1}} = f(\varphi^{(n)}) \tag{II.7}$$

$$\frac{\varphi_i^{(n)} - \varphi_i^{(n-1)}}{t^n - t^{n-1}} = f(\varphi^{(n-1)}) \tag{II.8}$$

In this case, the Euler-implicit 1st order scheme described in eq. (II.7) was chosen. This temporal scheme is more robust than explicit schemes (Ferziger & Peric, 2012). However, each temporal iteration takes longer to process since a new algebraic matrix must be solved to account for the presence of variables at time t^n in both sides of the equation.

According to Palacios et al. (2013) "despite implicit schemes being unconditionally stable in theory, a specific value for the time step [at the volume i at time n] $\Delta t_i^{(n)}$ is still required to relax the problem". SU2 uses local time stepping, which means that each CV is allowed to advance at different local time steps. The local time step for the i-th CV is calculated as:

$$\Delta t_i = N_{CFL} \min\left(\frac{|\Omega_i|}{\lambda_i^{conv}}, \frac{|\Omega_i|}{\lambda_i^{visc}}\right) \tag{II.9}$$

where N_{CFL} is the Courant-Friedrichs-Lewy (CFL) number, $|\Omega_i|$ is the volume of the i-th control volume and λ_i^{conv} is defined as the integrated convective spectral radius:

$$\lambda_i^{conv} = \sum_{j \in \text{neighbours}(i)} \left(|\overrightarrow{v_{ij}} \cdot \overrightarrow{n_{ij}}| + c_{ij}^s\right)\Delta S \tag{II.10}$$

where $\overrightarrow{v_{ij}} = \frac{1}{2}\left(\overrightarrow{v_i} + \overrightarrow{v_j}\right)$ is the velocity at the interface between i and j, $c_{ij}^s = \frac{1}{2}\left(c_i^s + c_j^s\right)$ is the speed of sound at the interface, $\overrightarrow{n_{ij}}$ is the normal direction of the control surface and ΔS, its area. Furthermore, λ_i^{visc} represents the viscous spectral radius:

$$\lambda_i^{visc} = \sum_{j \in \text{neighbours}(i)} C\frac{\mu_{ij}}{\rho_{ij}}S_{ij}^2 \tag{II.11}$$

where C is a constant, μ_{ij} is the total viscosity at the interface and ρ_{ij} is the density evaluated at the midpoint of the edge ij.

For implicit calculations, N_{CFL} is selected by the user. N_{CFL} represents the amount of times that the information φ would traverse the representative CV in a time-step. One mathematical definition for N_{CFL} can be given as:

$$N_{CFL}^{(n)} = \Delta t^{(n)}\frac{u^{(n)}}{\delta x} \tag{II.12}$$

where $u^{(n)}$ is a representative scalar measure of the velocity at time n, and δx is a pertinent length of the representative CV. Again, these representative measures are not defined by SU2, but rather $\Delta t_i^{(n)}$ is calculated using equation (II.9) based on the N_{CFL} values provided by the user. On this regard, N_{CFL} was allowed to "adapt" between iterations based on equation (II.13):

$$N_{CFL}^{(n+1)} = N_{CFL}^{(n)} \left(\left(\max\left(\left(\frac{R_\rho^{(n-1)}}{R_\rho^{(n)}} \right) - 1{,}0 \right) + 1 \right)^{k_u} \right.$$

$$\left. + \left(\min\left(\left(\frac{R_\rho^{(n-1)}}{R_\rho^{(n)}} \right) - 1{,}0 \right) + 1 \right)^{k_d} - 1 \right)$$

(II.13)

where $R_\rho^{(n)}$ is the global density residual for the n-th time step, $k_u = 0.8$ is the "factor up" coefficient and $k_d = 1.2$ is the "factor down" coefficient. N_{CFL} is initialized at 5, with a minimum allowed value of 0.5 and a maximum allowed value of 100. Posteriori analysis showed that, for the studied cases, N_{CFL} would automatically seek the smallest possible value, resulting in an effective average N_{CFL} of 0.5 over the domain.

II.2.2   Spatial discretization of the convective terms

Let's now generalize $\boldsymbol{\varphi}$ to be a vectorial function. If we define the state variable $\boldsymbol{U} = \rho\boldsymbol{\varphi}$ and the convective flux $\underline{\boldsymbol{F^c}}(\boldsymbol{U}) = \boldsymbol{U} \otimes \boldsymbol{v}$, then the convective terms in equations (II.1) to (II.3) can be given as:

$$\int_{\Omega_i} div(\rho\boldsymbol{\varphi}\otimes\boldsymbol{v})d\Omega = \int_{\Omega_i} div\left(\underline{\boldsymbol{F^c}}(\boldsymbol{U}) \right)d\Omega$$

$$= \sum_{j\in neighbours(i)} \int_{S_{ij}} \left(\underline{\boldsymbol{F^c}} . \boldsymbol{n_{ij}} \right)dS_{ij}$$

(II.14)

$$\approx \sum_{j\in neighbours(i)} F_{ij}^C(U)\Delta S_{ij}$$

where S_{ij} represents the interface between neighbour CVs i and j, ΔS_{ij} represents its surface, $\boldsymbol{n_{ij}}$ its normal vector, and $\boldsymbol{F_{ij}^c}$ represents the equivalent surface flux at the interface S_{ij}. In SU2, the evaluation of $\boldsymbol{F_{ij}^c}(\boldsymbol{U})$ can be done using either central or upwind methods.

For this work, the Jameson-Schmidt-Turkel (JST) scheme implemented by Palacios et al. (2013) in SU2 was used. This scheme is considered a central scheme, based on the idea of obtaining the values at the interface by averaging the conservative variables from the values on both sides of the interface. In this case, F_{ij}^c is given as:

$$F_{ij}^c = \underline{F^c}\left(\frac{U_i + U_j}{2}\right).n_{ij} - d_{ij} \qquad (II.15)$$

where d_{ij} is an artificial dissipation using "a blend of 2nd and 4th order differences" (Blazek, 2015). For this reason, the JST scheme is considered of 2nd order in space. The reader may refer to the work of Palacios et al. (2013) for a detailed description the JST scheme and its implementation.

II.2.3   Spatial discretization of the gradient terms

The viscous terms $\int_{\partial \Omega} \gamma \underline{grad}(\varphi).n dS = \sum_k \int_{S_k} \gamma \left(\underline{grad}(\varphi).n\right) dS_k$ imply the need to approximate the values of the gradients at the interfaces S_k. A Green-Gauss method is applied. Calculation of the gradients at the interfaces is done by first obtaining the gradients at the cell center $\underline{grad}(\varphi)_i$ and then interpolating for the interfaces. This value can be approximated as the average value of the gradient over the cell and transformed into a surface integral by the Green-Gauss theorem. Finally, this surface integral is approximated by the values at the center of the interface:

$$\underline{grad}(\varphi)_i \approx \frac{\int_{\Omega_i} \underline{grad}(\varphi) d\Omega}{|\Omega|} = \frac{1}{|\Omega|} \sum_{j \in neighbours(i)} \int_{\partial S_{ij}} \varphi \otimes n dS$$
$$\approx \frac{1}{|\Omega_i|} \sum_{j \in neighbours(i)} \varphi_{ij} \otimes n_{ij} \Delta S_{ij} \qquad (II.16)$$

From here, the values of $\boldsymbol{\varphi_{ij}}$ at the interface are calculated as an average between the values of the 2 contiguous cells.

II.3   Boundary conditions

To close the problem, boundary conditions at the domain limits are needed. Three types of boundary conditions are used: symmetry, viscous wall and far-field boundary conditions. These are briefly presented here. The reader may refer to Hirsch (2007) for more details.

II.3.1   Symmetry condition

The symmetry condition is described as an inviscid wall with no normal fluxes. Let P be a point at the boundary and b the final boundary condition. Let $\boldsymbol{n}$ be the local normal vector. Then this condition becomes.

$$\boldsymbol{v_b} = \boldsymbol{v_P} - (\boldsymbol{v_P}.\,\boldsymbol{n})\boldsymbol{n} \tag{II.17}$$

In turn, $\boldsymbol{v_b}$ is used to correct the total energy

$$e_b = e - \frac{1}{2}v_p^2 + \frac{1}{2}v_b^2 \tag{II.18}$$

And the final pressure p_b is calculated based on the state equations of the fluid.

II.3.2   Aircraft airframe

The aircraft airframe is modeled by a viscous wall with zero heat flux in order to obtain an adiabatic wall. The viscous wall is defined by a no-slip condition ($\boldsymbol{v_b} = \boldsymbol{0}$). The heat flux in the normal direction is simply set to zero ($\boldsymbol{q_b} = -\lambda \boldsymbol{grad}(T).\,\boldsymbol{n} = 0$).

II.3.3   Farfield

The farfield is calculated differently depending on if it behaves as an inlet or an outlet. For a compressible, subsonic flow, the Riemman invariants are computed as $R_+ = v_{n,b} + \frac{2a}{\gamma-1}$ at the inlet and $R_- = v_{n,\infty} + \frac{2a}{\gamma-1}$ at the outlet, where $v_{n,b}$ is the normal velocity inside the domain boundary and $v_{n,\infty}$ is the fixed normal freestream velocity. Then, the normal velocity at the boundary is given as $v_n = \frac{1}{2}(R_+ + R_-)$ and the speed of sound is given as $a = \frac{1}{4}(R_+ - R_-)(\gamma - 1)$. From there, if s is the entropy of the system, the velocity is given by:

$$\begin{cases} \boldsymbol{v} = \boldsymbol{v}_\infty - (v_n - v_{n,\infty})\boldsymbol{n} \; if \; inlet \\ \qquad\qquad s = s_\infty \\ \boldsymbol{v} = \boldsymbol{v}_b - (v_n - v_{n,b})\boldsymbol{n} \; if \; outlet \\ \qquad\qquad s = s_b \end{cases} \tag{II.19}$$

And the reconstructed primitive variables are:

$$\rho = \left(\frac{sa^2}{\gamma}\right)^{\frac{1}{\gamma-1}} \tag{II.20}$$

$$p = \frac{\rho a^2}{\gamma} \tag{II.21}$$

$$e_0 = \frac{p}{(\gamma-1)\rho} + \frac{1}{2}v^2 \tag{II.22}$$

With this, the description of the physical and numerical approach used for RANS simulations is finished.

# APPENDIX III

CLASSIC CONCEPTUAL DESIGN APPROACH
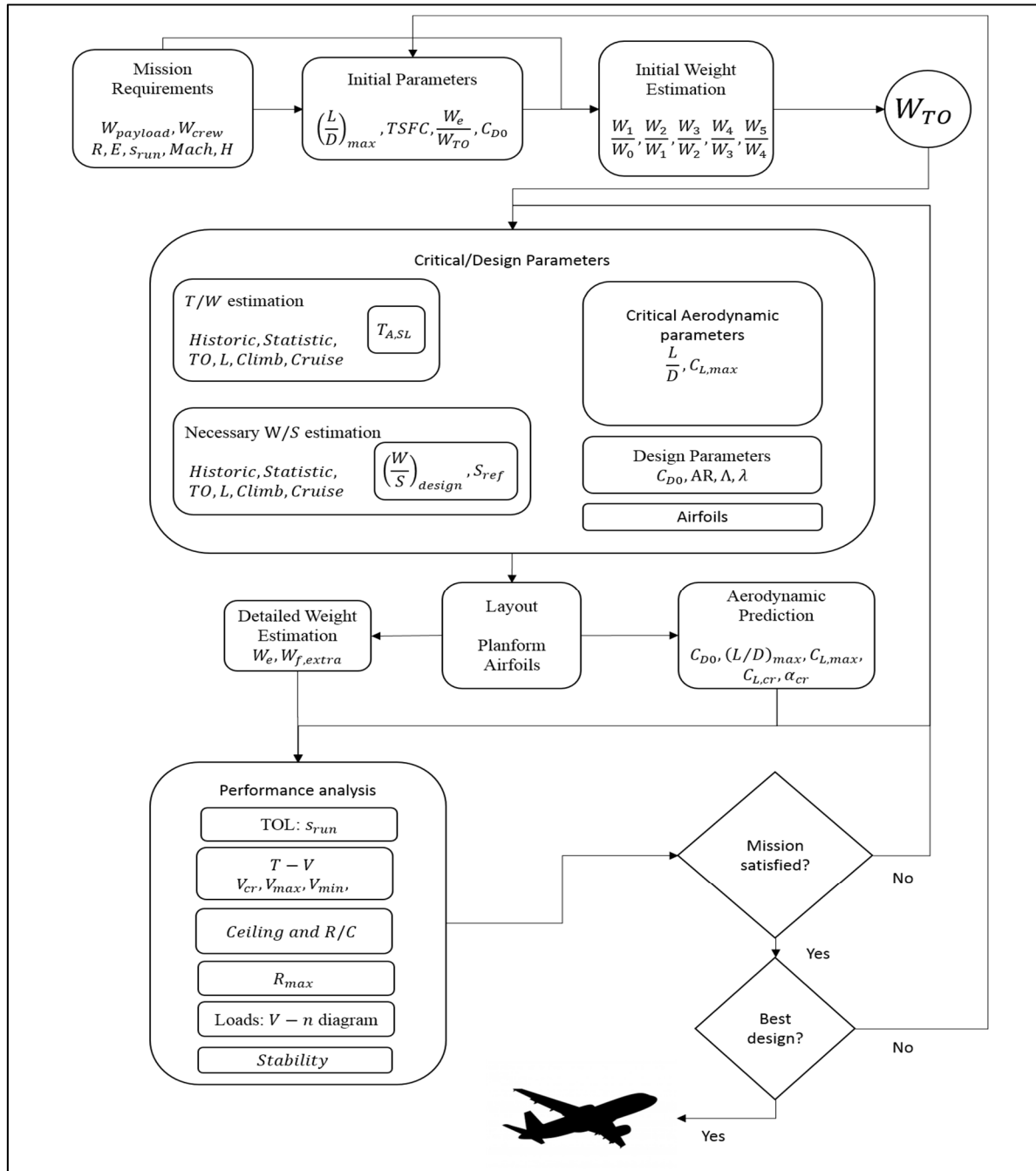
Figure A III-1: Scheme for the classical conceptual design approach. Based on works by Anderson (2001) and Raymer (2006)

LOW FIDELITY VISCOUS VORTEX LATTICE METHOD

This appendix introduces original work developed during the conceptual design phase concerning the low fidelity prediction model. This model is based on Drela's AVL code (Drela & Youngren, 2008) and introduces the concept of viscosity in an otherwise potential, non-viscous model.

IV.1 Low fidelity aerodynamic prediction model

The aircraft aerodynamic characteristics are estimated by using a viscous-vortex-lattice method (VVLM). This is a modified vortex lattice method based on original AVL code by Drela and Youngren (2008) and the strip method proposed by Cosyn and Vierendeels (2006): the BWB is divided in n strips along the wingspan working as semi-infinite wings. For each strip, viscous drag effects are added by extracting the original AVL induced angle of attack α_i and calculating an effective angle of attack α_{eff} as seen by the strip. This effective angle is used to find the aerodynamic parameters of the strip's airfoil obtained from a viscous airfoil database. This viscous data is reinjected into the VLM model and added along the strips to find the global lift and drag coefficients. This is detailed in the following paragraph.

Figure A IV-1 presents the various forces resulting from this approach. Let α_{BWB} be the aircraft's angle of attack and ϕ be the local twist. Then, the local 3D angle of attack for a given strip is $\alpha_{3D} = \alpha_{BWB} + \phi$. Now let α_i be the induced angle of attack created by the 3D downwash effect and let $\alpha_{eff} = \alpha_{3D} - \alpha_i$ be the effective angle of attack seen by the local strip. Let (L'_{VLM}, D'_{VLM}) be the original non-viscous lift and drag forces at a given strip computed by the original VLM code, let (l', d') be the viscous aerodynamic forces associated with the viscous database and let (L', D') be the viscous aerodynamic forces for a given strip corresponding to the projections of (l', d') into the global reference frame. D'_{VLM} corresponds

directly to the washout induced drag D_{ind}, but it doesn't account for the viscous part of the drag D_{visc}. Furthermore L'_{VLM} corresponds to a slightly overestimated lift. To add viscous effects, the lift and drag (L'_{VLM}, D'_{VLM}) have to be replaced by (L', D'). The difficulty lays in the determination of the effective angle of attack α_{eff} from the original VLM data since the potential lift L'_{VLM} cannot be directly used to calculate the effective angle of attack. To overcome this obstacle, an iterative loop based on the induced angle of attack α_i is generated until the aerodynamic characteristics between the airfoil drag and lift database and the model match. This represents steps 1 to 5 from the viscous algorithm.
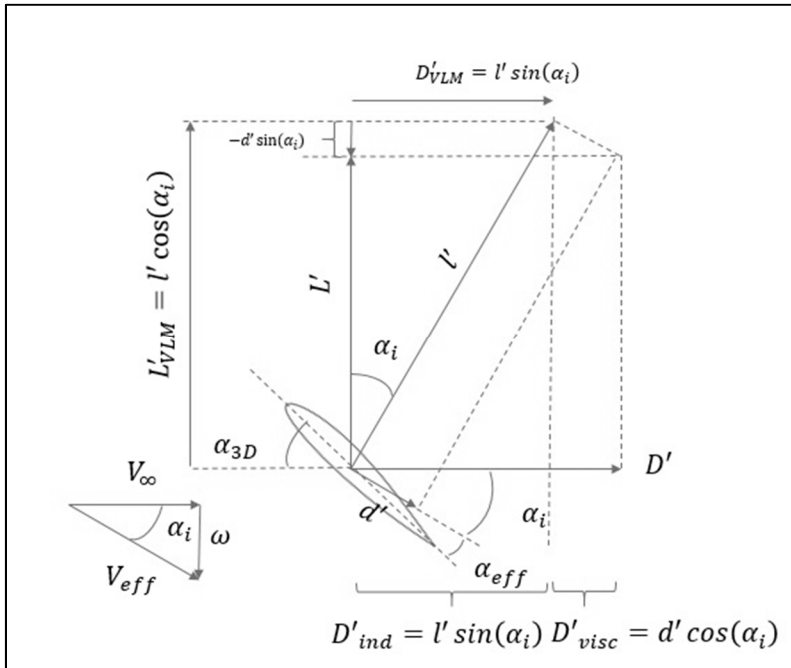

Figure A IV-1:   Non-viscous and viscous forces and transformations

For each strip, the aerodynamic forces are transformed into aerodynamic coefficients. The remaining step is to find the induced angle of attack for each strip. For a given strip with a corresponding airfoil and viscous database values, let $\left(\frac{dC_l}{d\alpha}\right)_{db}$ be the rate of change of lift coefficient with respect to angle of attack in the linear lift zone as read in the viscous database. Let $\alpha_{l=0,db}$ be the zero-lift angle of attack of the given airfoil as read in the database. Then,

according to (Anderson, 2001), the effective angle of attack corresponding to a given lift C_l' can be found from the equation: $C_l' = \frac{dC_l}{d\alpha}(\alpha_{eff} - \alpha_{l=0})$. The procedure to obtain and integrate the induced angles is summarized in the following algorithm:

1. Set $\alpha_i = 0$, $\alpha_{eff} = \alpha_{3D}$;
2. Determine the viscous lift coefficient $C_l = C_{L,VLM}'\cos(\alpha_i)$;
3. Determine the local velocity $V_{eff} = V_\infty / \cos(\alpha_i)$;
4. Determine the effective angle of attack $\alpha_{eff} = \frac{C_l}{\left(\frac{dC_l}{d\alpha}\right)_{db}} + \alpha_{l=0,db}$;
5. Estimate a new induced angle $\alpha_i = \alpha_{3D} - \alpha_{eff}$;
6. Repeat steps 2 through 5 until convergence on α_i;
7. Determine C_d' from the viscous database at angle α_{eff};
8. From the estimated (C_l', C_d'), project the viscous values into the global axis: $C_L' = C_l'/\cos(\alpha_i) - C_d'\sin(\alpha_i)/\cos(\alpha_i)^2$, $\quad C_{D,visc}' = C_d'/\cos(\alpha_i)$, $C_{D,ind}' = C_l'\sin(\alpha_i)/\cos(\alpha_i)^2$;
9. Estimate the global lift coefficient C_L: $C_L = \sum_{strips} C_L'\left(\frac{S_{strip}}{S_{ref}}\right)\left(\frac{V_{eff}^2}{V_\infty^2}\right)$;
10. Estimate the global drag coefficient C_D: $C_D = \sum_{strips} C_D'\left(\frac{S_{strip}}{S_{ref}}\right)\left(\frac{V_{eff}^2}{V_\infty^2}\right)$, where $C_D' = C_{D,visc}' + C_{D,ind}'$.

Finally, the viscous database used is generated using the Drela's panel method (Drela, 1989) for cruise conditions: Mach 0.78 and a Reynolds number between 77×10^6 and 166×10^6 depending on the section chord, at initial cruise altitude of $12500\ m$.

IV.2 Low fidelity model validation and verification

The VVLM model is verified using Trips' 243085 wing (Trips, 2010) and a NACA 4424 wing (Neely, Bollech, & Westrick, 1947). These 3D wings correspond to wind tunnel experimental tests. The results on aerodynamic prediction for this model are presented in the following lines.

Trips' wing is comprised of a NACA2415 airfoil at the root and a NACA2409 airfoil at the tip. Table-A IV-1 presents the wing's main geometric characteristics. The wing experimental data is extracted from (Trips, 2010). Test conditions comprise a local speed of 272m/s and a

Reynolds number of 3.2×10^6 at the root chord. The viscous database is generated using XFOIL values (Drela, 1989) with fully turbulent boundary layer on the NACA2415 and NACA2409 airfoils. The comparison for lift and drag coefficients between experimental, VLM and VVLM methods is presented in Figure A IV-2. Results on lift show that both VLM and VVLM methods present a relative error inferior to 5% in all angles above 5° and between 5% and 20% on angles between −5° and 5° with the exception of angles around the zero-lift angle of attack (0° and 1°). Results on drag show that VVLM presents a better estimation of drag than VLM. VVLM shows errors inferior to 5% for angles of 5° and above, between 5% and 10% error for angles between 2° and 5° and below 20% error for angles between −4° and 2° with a maximum absolute error of 33 drag counts at −4°.

Table-A IV-1: Trip's 243085 wing geometric parameters

| Wing	b	S_{ref}	AR	$\Lambda_{0.25x/c}$	C_r	MAC	ϕ	λ
Trips' 243085	$0.762m$	$0.0968m^2$	6	$30°$	$0.1693m$	$0.132m$	$8.5°$	0.5
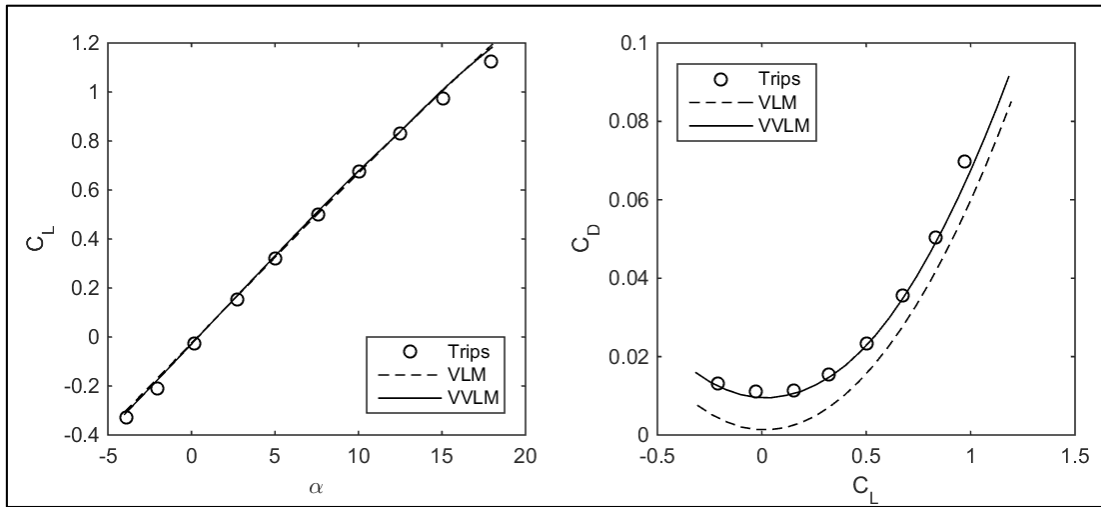
Figure A IV-2: VVLM Validation for Trips' 243085 wing.

The NACA 4424 wing (Neely et al., 1947) has a NACA 4424 airfoil at the root and a NACA 4412 airfoil at the tip. Table-A IV-2 shows the geometric characteristics of this wing. To test

the dependency on the viscous database, the airfoil viscous database was generated twice for the 2 concerned airfoils at a Reynolds number of 3×10^6: (1) from experimental airfoil data (Abbott & Von Doenhoff, 1959) and (2) from XFOIL fully turbulent boundary layer simulations. For the VVLM 3D analysis, a Reynolds number of 4.32×10^6 and a speed of $77m/s$ are considered to encompass the same conditions as the ones from (Neely et al., 1947). The results presented in Figure A IV-3 show similar results for the lift coefficient C_L for both VLM and VVLM methods with an average absolute error of $\Delta C_L = 0.1$ with respect to experimental results. With respect to drag however, the VVLM shows a better performance than VLM with both databases, showing absolute errors between 25 and 117 drag counts for the experimental airfoil database and between 14 and 91 drag counts for the XFOIL database for an average error of 72 and 57 drag counts respectively. For a relative comparison, the VLM approach presents an average drag relative error of 40% while the VVLM presents an average drag relative error of 11% for both databases with respect to the $C_D(C_L)$ curve.

Table-A IV-2: NACA 4424 wing characteristics.

| Wing	b	S_{ref}	AR	$\Lambda_{0.25x/c}$	C_r	MAC	ϕ	λ
NACA 4424	$4.572m$	$2.6m^2$	8.04	0°	$0.812m$	$0.607m$	2.4°	0.4
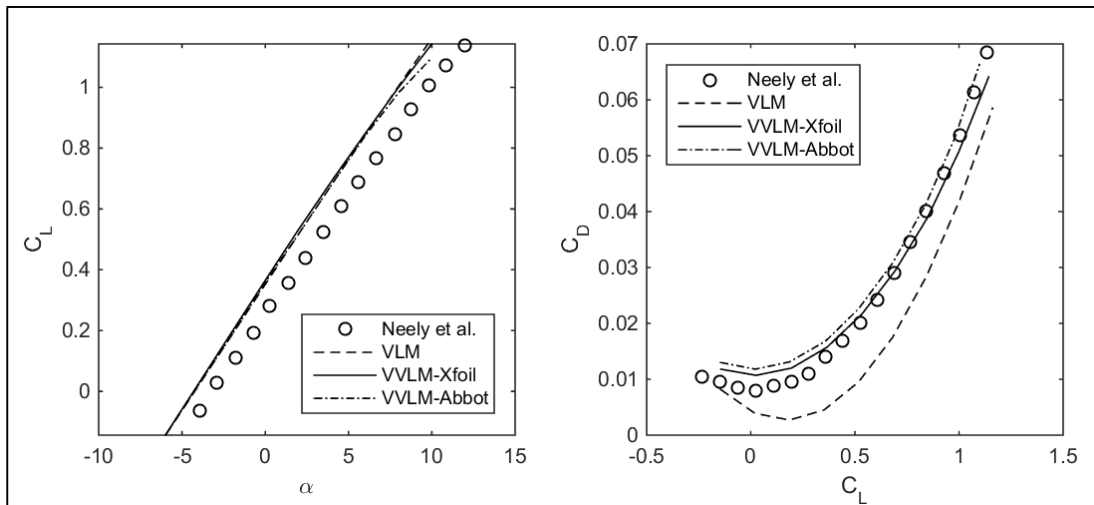
Figure A IV-3: VVLM Validation for the NACA25-8-44,24 wing

We conclude that this viscous inclusion approach gives better drag results for the VVLM: between 5% and 11% error with respect to experimental results on average. As a reference, common low-fidelity models prediction error ranges between 5% and 20% (Huang, Gao, & Zhang, 2013).

APPENDIX V

VALIDATION OF THE CRM BUFFET STUDY

The DPW5 case 2 buffet study is used as a reference to analyse the capability of the numerical solver to predict boundary layer detachment, which is itself linked to loss of lift, and stall. This case was chosen since it presents boundary layer detachment on a geometry without high lift devices - just like the proposed BWB geometry -, and there are available comparisons against both experimental and numerical data from participants of the DPW5 (Levy et al., 2014). Moreover, the CRM is used as the TAW representative for low speed comparisons against the BWB; these results serve to verify the numerical model and the TAW geometry used on CHAPTER 4. The CRM aircraft and numerical domain are properly presented on CHAPTER 4 and only briefly presented here for the purposes of the numerical verification.

Note that while the buffet separation mechanism is not the same as trailing edge or leading edge separation mechanism, this study allows us to consider the aerodynamic behaviour in the presence of boundary layer separation, under the assumption that if the physical model and the numerical method allow to reasonably predict separation due to pressure drops at high speeds, it may be acceptable to consider that it can also predict separation due to pressure drops at low speed and high-angles. This is necessary since low speed stall data on the specific CRM geometry without high-lift devices is not available.

This case study is done using a 6 million cells "medium" mesh of the CRM as advised by the DPW5 organisers (Levy et al., 2014). This mesh was developed by the IDEA Research Chair at Polytechnique Montreal (Gariépy et al., 2013) for the DPW5; The original mesh is publicly available through the DPW server (NASA, 2012). The test conditions correspond to a temperature $T_k = 311K$, at Mach 0.85 and at a Reynolds number of 5 million for a chord length of $7\ m$. The angle of attack varies as $\alpha \in \{2.5°, 3.0°, 3.5°\}$.

Figure A V-1 shows the development of flow detachment as α increases from 2.5° to 3.5°. This figure presents the oil flow visualization based on the skin friction vector $\overrightarrow{c_f} = c_{fx}\overrightarrow{e_x} +$

$c_{fy}\overrightarrow{e_y} + c_{fz}\overrightarrow{e_z}$, showing the local direction of the flow next to the airframe . Row (a) introduces a streamwise detachment indicator, which is the skin friction coefficient in the x direction $c_{f,x}$ divided by $c_f = \|\overrightarrow{c_f}\|$. This indicator varies between -1 and 1, and shows if the friction force is applied in the same $(c_{f,x}/c_f \rightarrow 1)$, opposite $(c_{f,x}/c_f \rightarrow -1)$, or different $(c_{f,x}/c_f \rightarrow 0)$ direction than x, which itself is equivalent to the local section curvilinear abscise due to the convex nature of each section geometry. This indicator, complemented with the oil flow pattern show the position of detachment zones, if any, along the upper surface of the CRM. For reference purposes, row (b) presents the more conventional pressure coefficient along the upper surface which shows the presence of shockwaves, which in turn create the local detachment as the angle of attack increases.
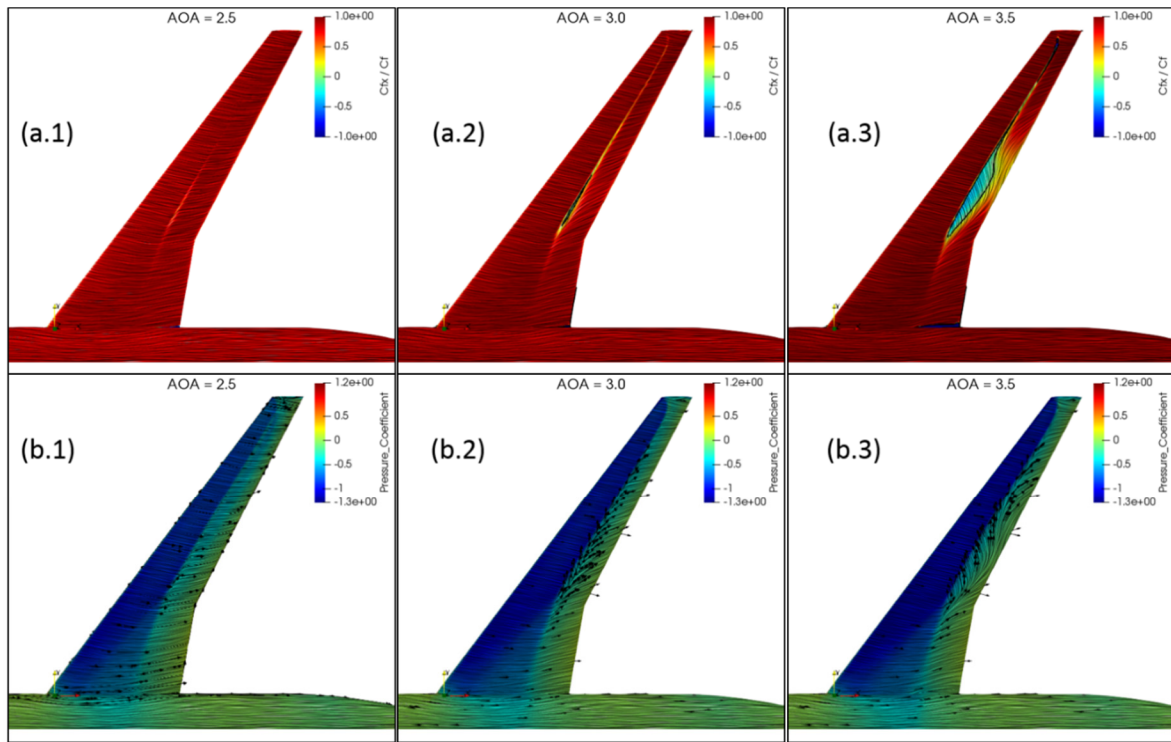
Figure A V-1: Oil flow visualization on the CRM at different angles of attack. Row (a.X) presents the ratio between the skin friction coefficient in the x direction $c_{f,x}$ divided by the magnitude of the total 3D skin friction $\|\overrightarrow{c_f}\|$; negative values show streamwise detachment; isocontour represents $c_{f,x} = 0$. Row (b.X) shows a typical streakline and c_p representation of the flow.

Figure A V-2 presents the pressure coefficient distribution at the normalized wingspan coordinate $\eta = 0.5024$, where $\eta = \frac{y}{b/2}$, for all 3 angles of attack. The dashed lines represent our results, the markers show the experimental data from NASA's National Transonic Facility (NTF) and the blue shaded areas represent the DPW5 participants data envelope; all available from the summary of data from DPW5 (Levy et al., 2014). It can be noted that while there is no perfect agreement with experimental data, the current simulations remain within the envelope of the DPW5 participants. As for the global aerodynamic parameters, Figure A V-3 presents our results (blue marker), the presudo-test data from NASA (black squares) and the DPW5 participants using SA turbulence models (blue cloud). The figure shows that this numerical method is able to predict, with reasonable accuracy (under 2 decimals) the evolution of these coefficients under buffet conditions, which reflects the ability of our numerical method to properly estimate aerodynamic coefficients in the presence of boundary layer detachment with reasonable confidence and precision: with an estimated absolute error with respect to NASA's pseudo-test data of $\Delta C_L \approx 0.01$ and $.\Delta\left(C_D - \frac{C_L^2}{\pi AR}\right) \approx 0.003$.
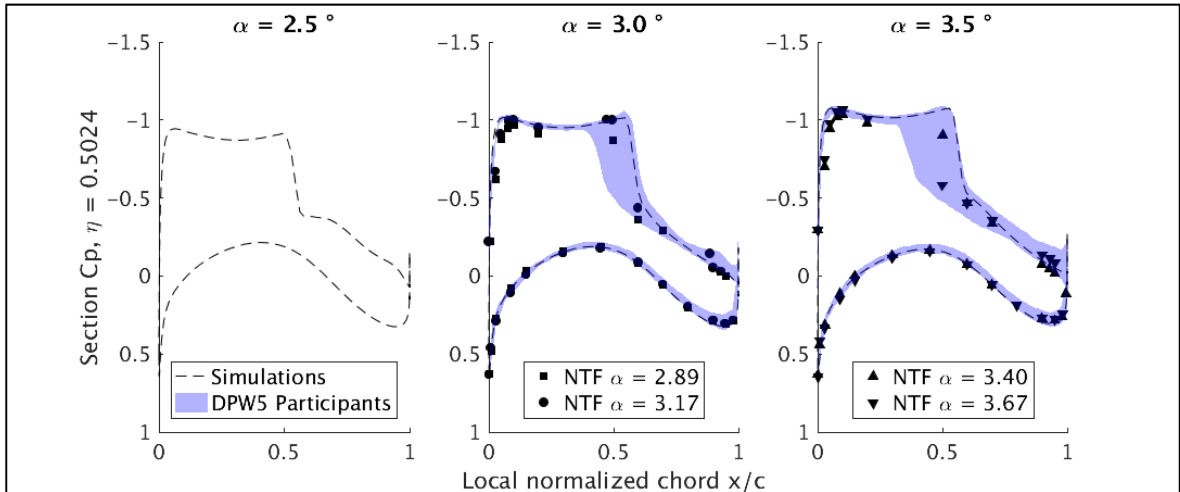

Figure A V-2: DPW5 - case 2: Pressure coefficients at section $\eta = 0.5$.
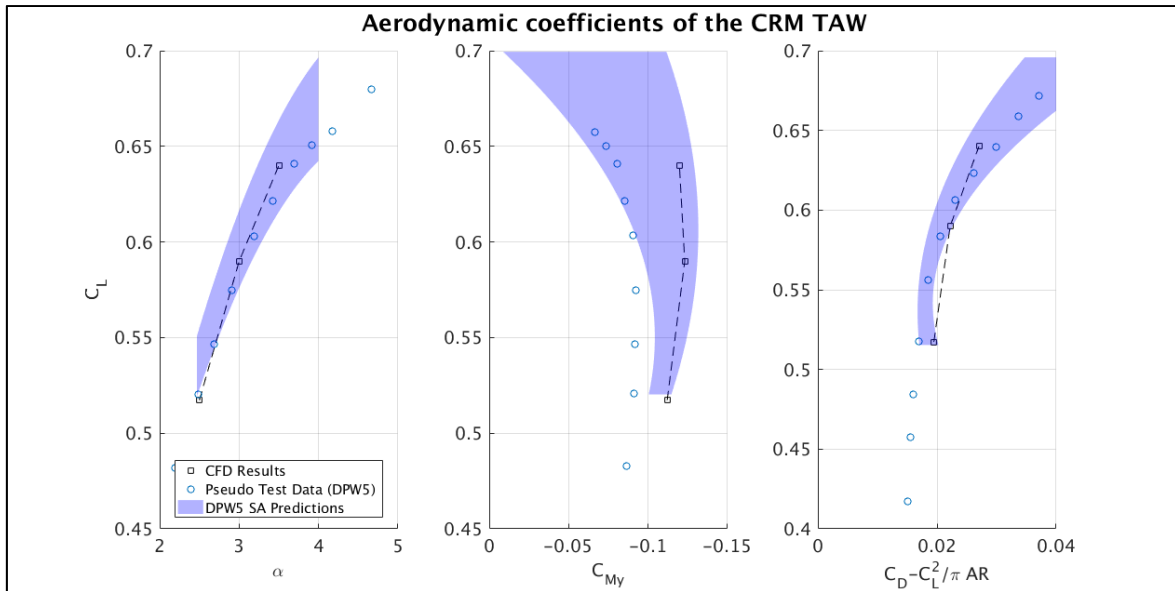
Figure A V-3: DPW5 - case 2: Global aerodynamic parameters

Based on the existing validations on the SA turbulence model at high angles of attack (Grosvenor, 2007; Rumsey et al., 2018; Tagawa et al., 2018) and on our own verification, we conclude that the chosen models were adequate to predict stall initiation within 1°, and with acceptable error (around 0.01 for C_L and 0.001 for C_D) for our validation cases.

APPENDIX VI

COMPUTE CANADA CLUSTERS

The numerical work done in this thesis was made possible by the gracious collaboration of Compute Canada who provided access to its high-performance Clusters through the Ressource Allocation Competition. The 3 different clusters used in this research work are presented in the following paragraphs. For any more details, please refer to (Compute Canada, 2019).

VI.1   Cedar

According to Compute Canada, "Cedar is a heterogeneous cluster suitable for a variety of workloads; it is located at Simon Fraser University. It is named for the Western Red Cedar, B.C.'s official tree, which is of great spiritual significance to the region's First Nations people. Cedar is sold and supported by Scalar Decisions, Inc. The node manufacturer is Dell, the high performance temporary storage /scratch filesystem is from DDN, and the interconnect is from Intel". The cluster characteristics are summarized in

Table-A VI-1: Cedar cluster specs.

Cluster	Cpu Description	Nodes	Cores	RAM/core	Interconnect
Cedar	Intel E5-2683 v4 "Broadwell", 2.1 GHz Intel E7-4809 v4 "Broadwell", 2.1 GHz Intel E5-2650 v4 "Broadwell", 2.2 GHz Intel Platinum 8160F "Skylake", 2.1 GHz	32 cores/node (Broadwell) 24 cores/node (Broadwell + GPU) 48 cores/node (Skylake)	58416	4 Gb – 96 Gb	Intel OmniPath Interconnect (100 Gbps)

VI.2   Niagara

Niagara is a homogeneous cluster, owned by the University of Toronto and operated by SciNet, intended to enable large parallel jobs of 1040 cores and more. It was designed to optimize throughput of a range of scientific codes running at scale, energy efficiency, and network and storage performance and capacity.

Table-A VI-2: Niagara cluster specs

Cluster	Cpu Description	Nodes	Cores	RAM/core	Interconnect
Niagara	Intel "Skylake" 2.4 GHz	Lenovo SD530 (× 1548). 40 cores/node	61920	5 Gb	EDR InfiniBand "Dragonfly+"(100 Gbps)

VI.3   Placentia

Placentia was a Compute Canada cluster, operated by ACENET. Placentia was decommissioned in may 2019.

Table-A VI-3: Placentia cluster specs

Cluster	Cpu Description	Nodes	Cores	RAM/core	Interconnect
Placentia	Dual-Core AMD Opteron 2.6 GHz Dual-Core AMD Opteron 2.8 GHz Dual-Core AMD Opteron 3.0 GHz Quad-Core AMD Opteron 2.4 GHz Quad-Core AMD Opteron 2.7 GHz	SunFire X4600 SunFire X2200M2 SunBlade X6240 SunBlade X4140 4, 8, 16 cores/node	3756	2-16 Gb	InfiniBand (20 Gbps)

APPENDIX VII

STALL DATABASE OF THE TWISTED BWB GEOMETRIES

This appendix shows the numerical postprocessing used in Chapter 4, but applied to the simulations of Chapter 5. These figures constitute a database of the V00, V04 and V08 simulations. These figures were let out of the main text to avoid visual cluster. While nice to have, the following figures are not necessary to understand the results of Chapter 5 since the relevant results are still presented in a concise manner in said chapter.

Figures A IV-1 to A IV-3 present the recirculation bubbles introduced in Chapter 4 for all three geometries. It is noted that these appear at higher angles of attack than the V00 configuration and that they appear closer to the midwing as opposed to the tip of the wing in V00. The next three figures (4 to 6) present the detachment figures for the upper surface (Extrados) for the V00, V04 and V08 configurations respectively. These images contain an oilflow visualization on the left side, colored by a streamwise detachment indicator, and a classic c_p and streamline visualization on the right side. Figures A IV-7 to A IV-12 present the section c_p and the section c_f evolution for each geometry. Furthermore, figures A IV-13 to A IV-15 show the spanwise c_l distribution while .figures A IV-16 to A IV-18 show the local lift spanwise distribution and evolution. Finally, figures A IV-19 to A IV-21 show the global aerodynamic coefficients for each configuration.
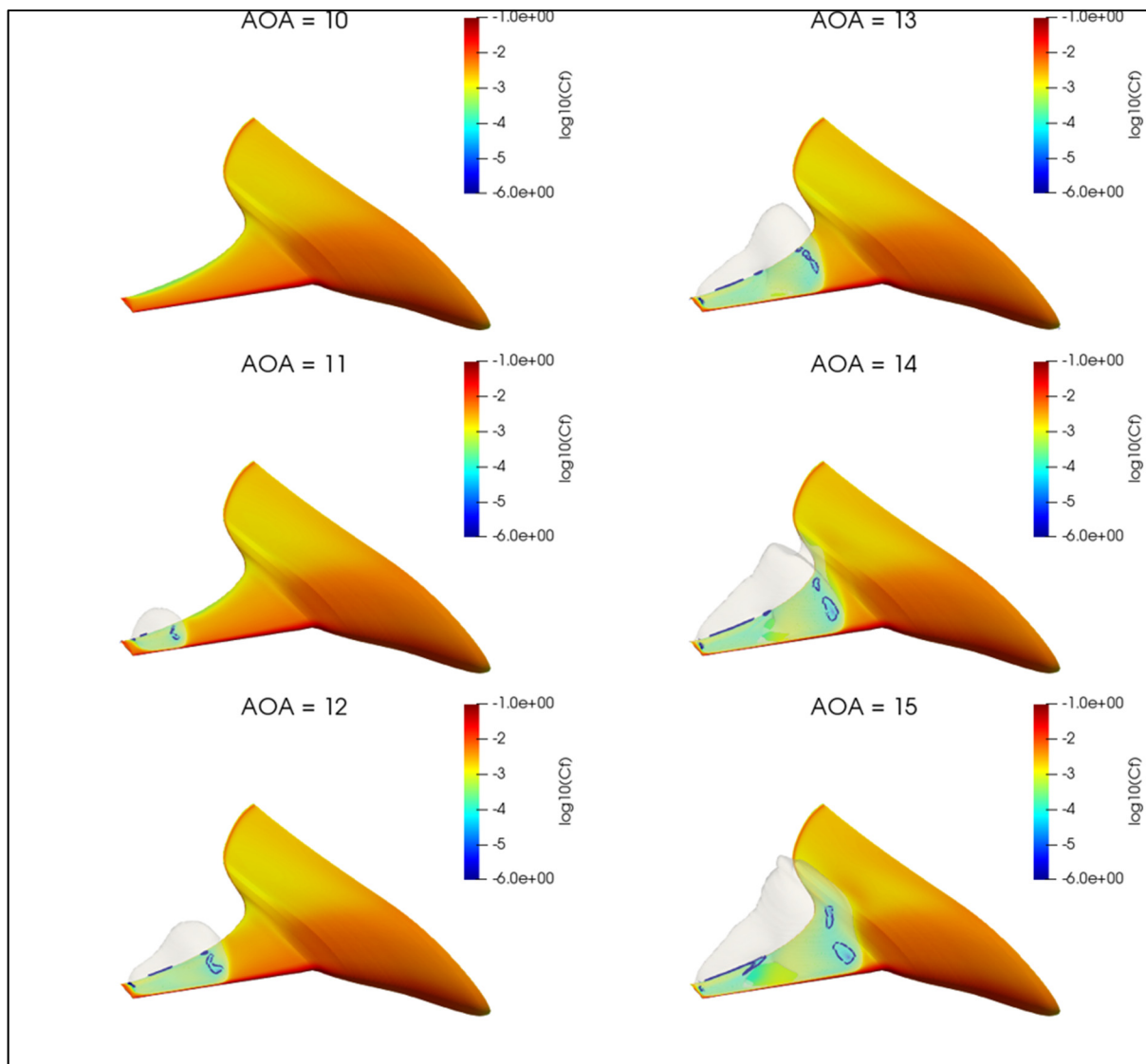
Figure A VII-1:   Recirculation bubble - BWB V00
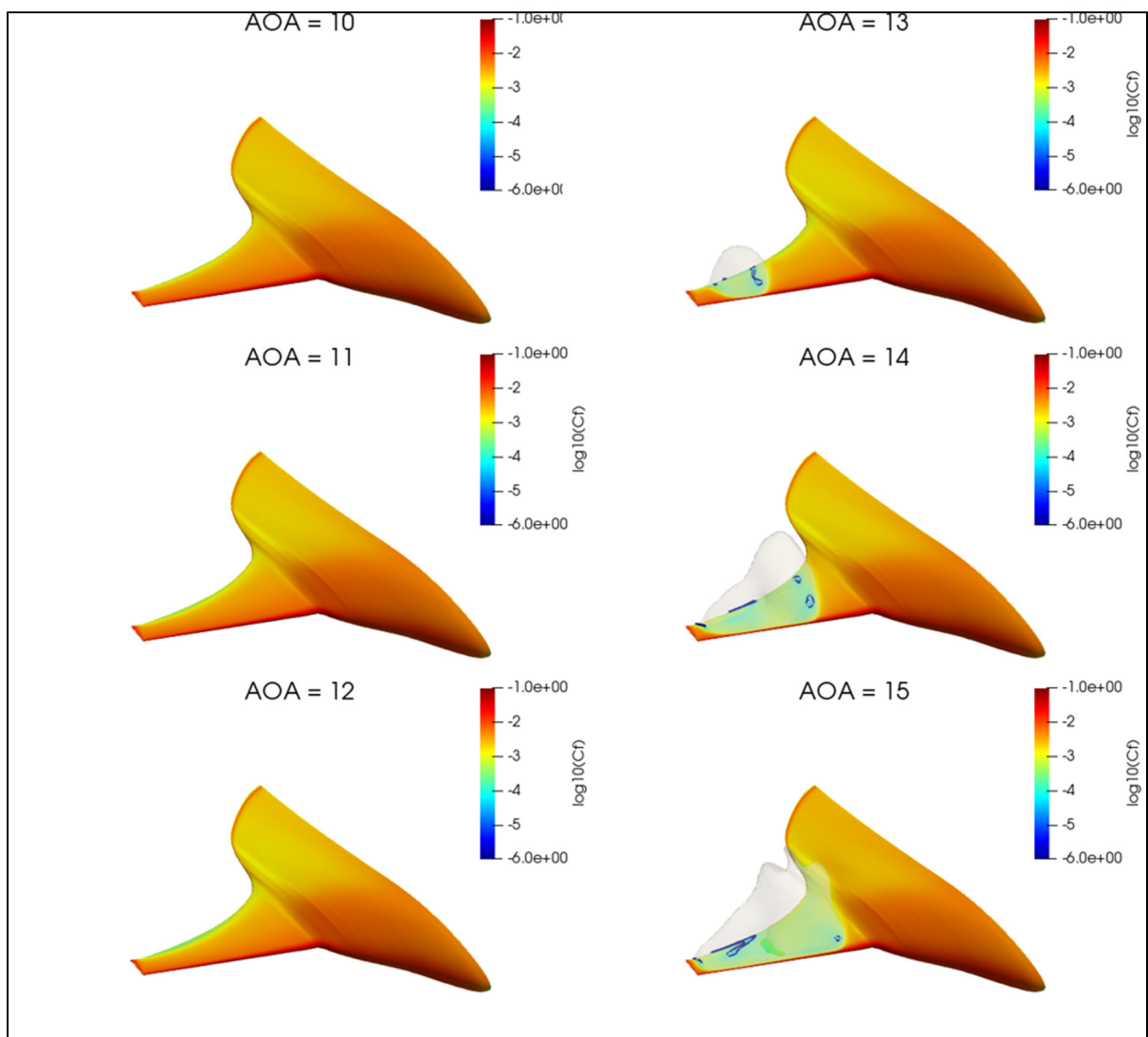
Figure A VII-2:   Recirculation bubble - BWB V04
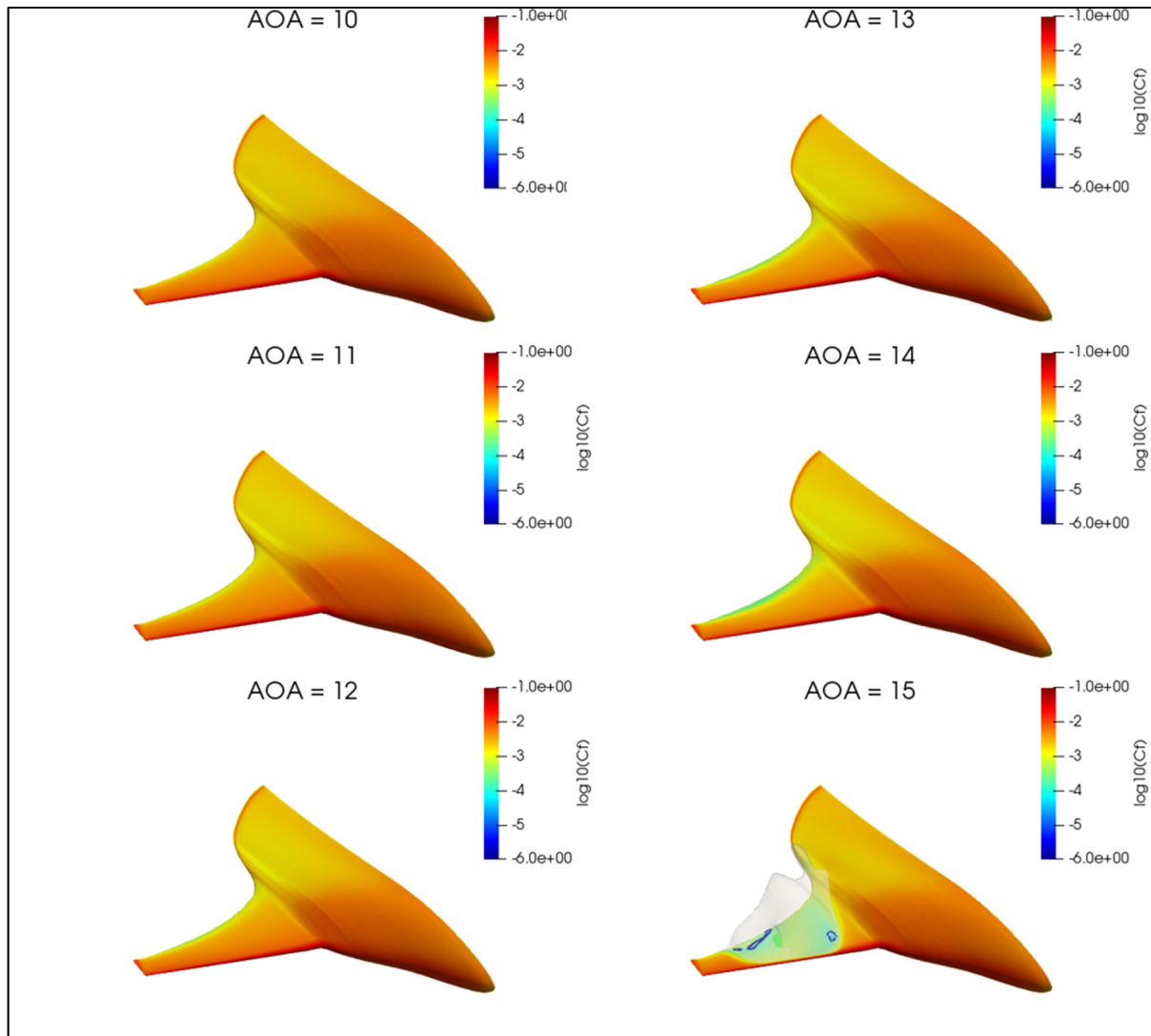
Figure A VII-3:   Recirculation bubble - BWB V08
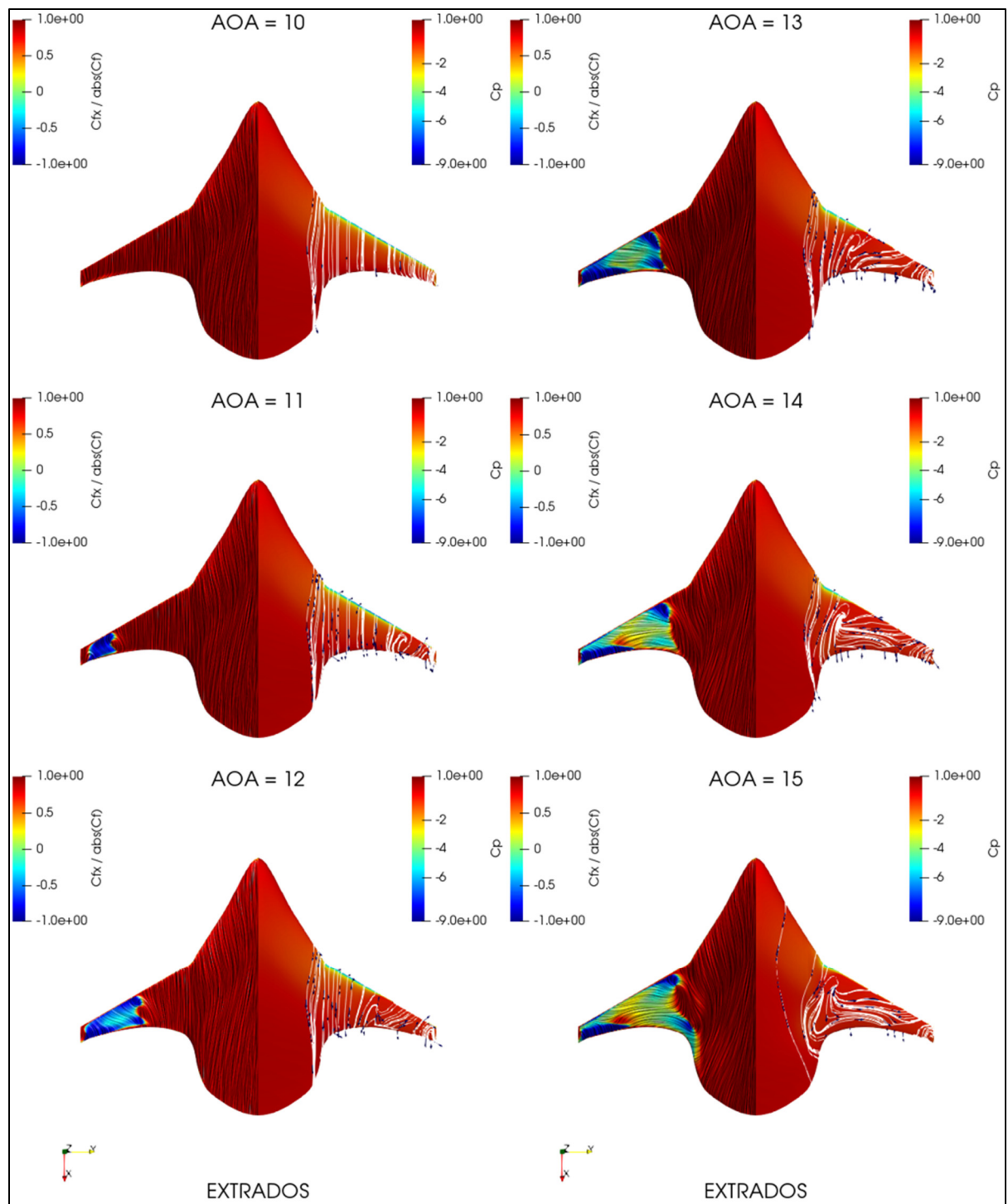
Figure A VII-4:   Surface detachment evolution - BWB V00
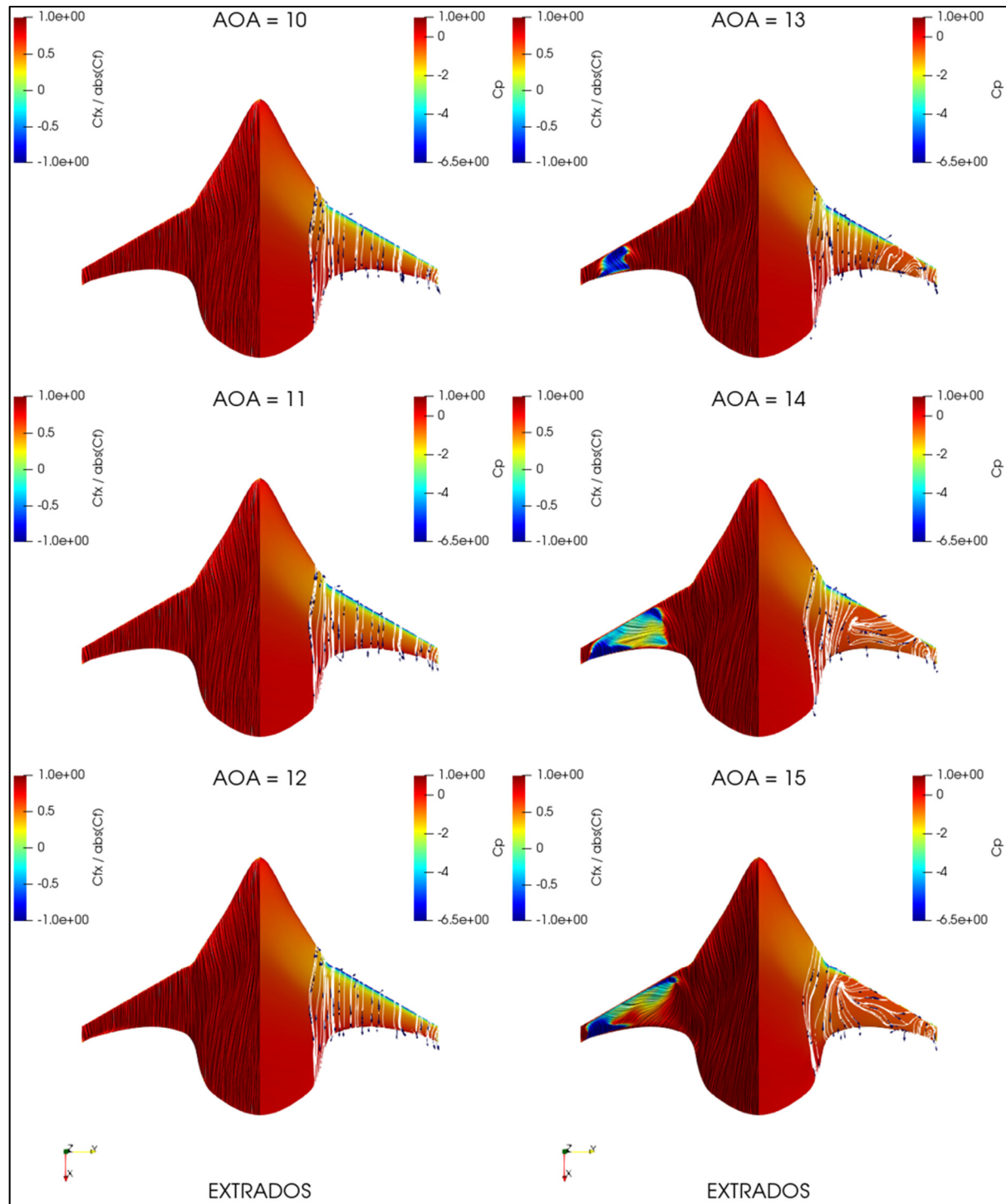
Figure A VII-5:   Surface detachment evolution - BWB V04
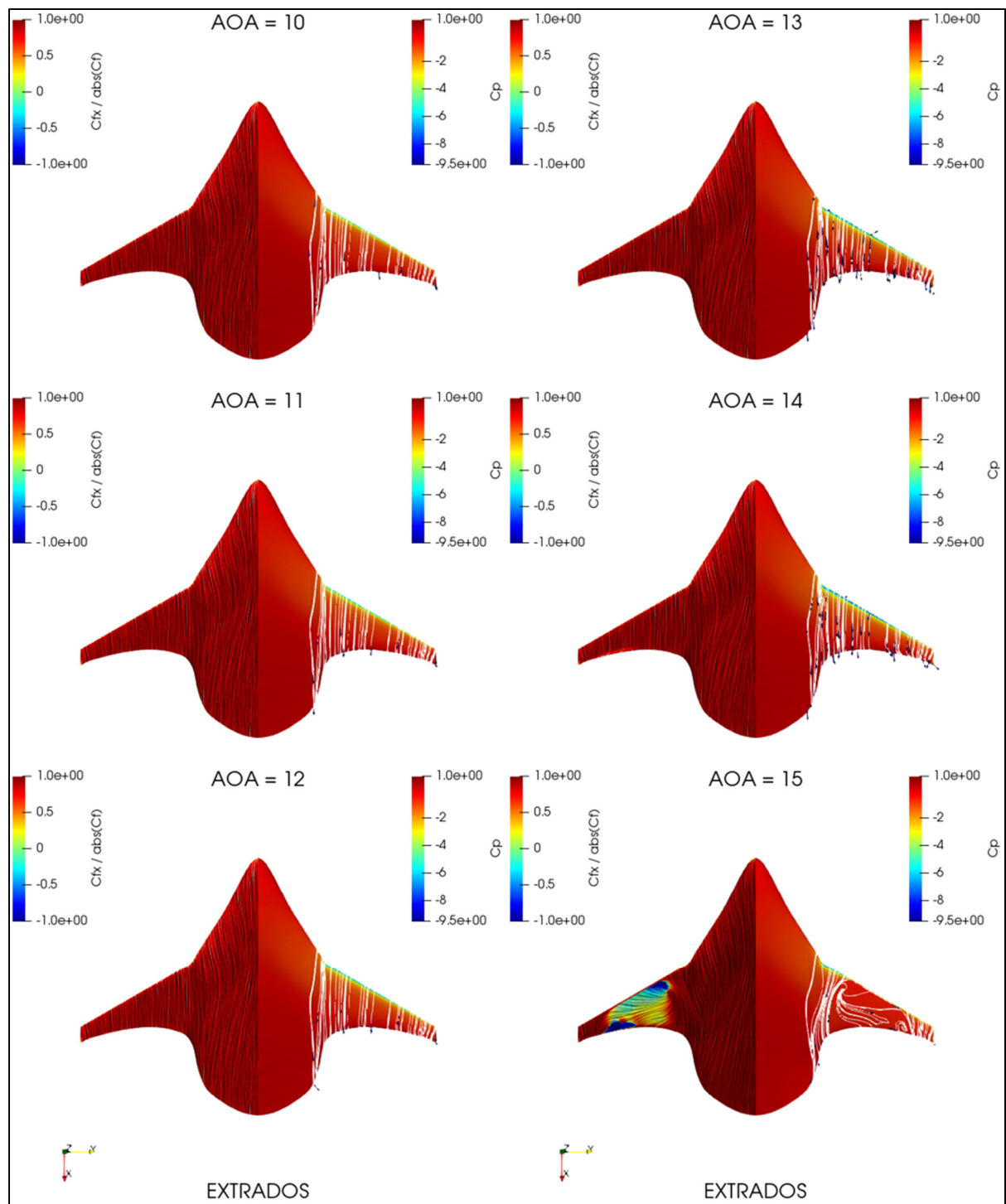
Figure A VII-6:   Surface detachment evolution - BWB V08
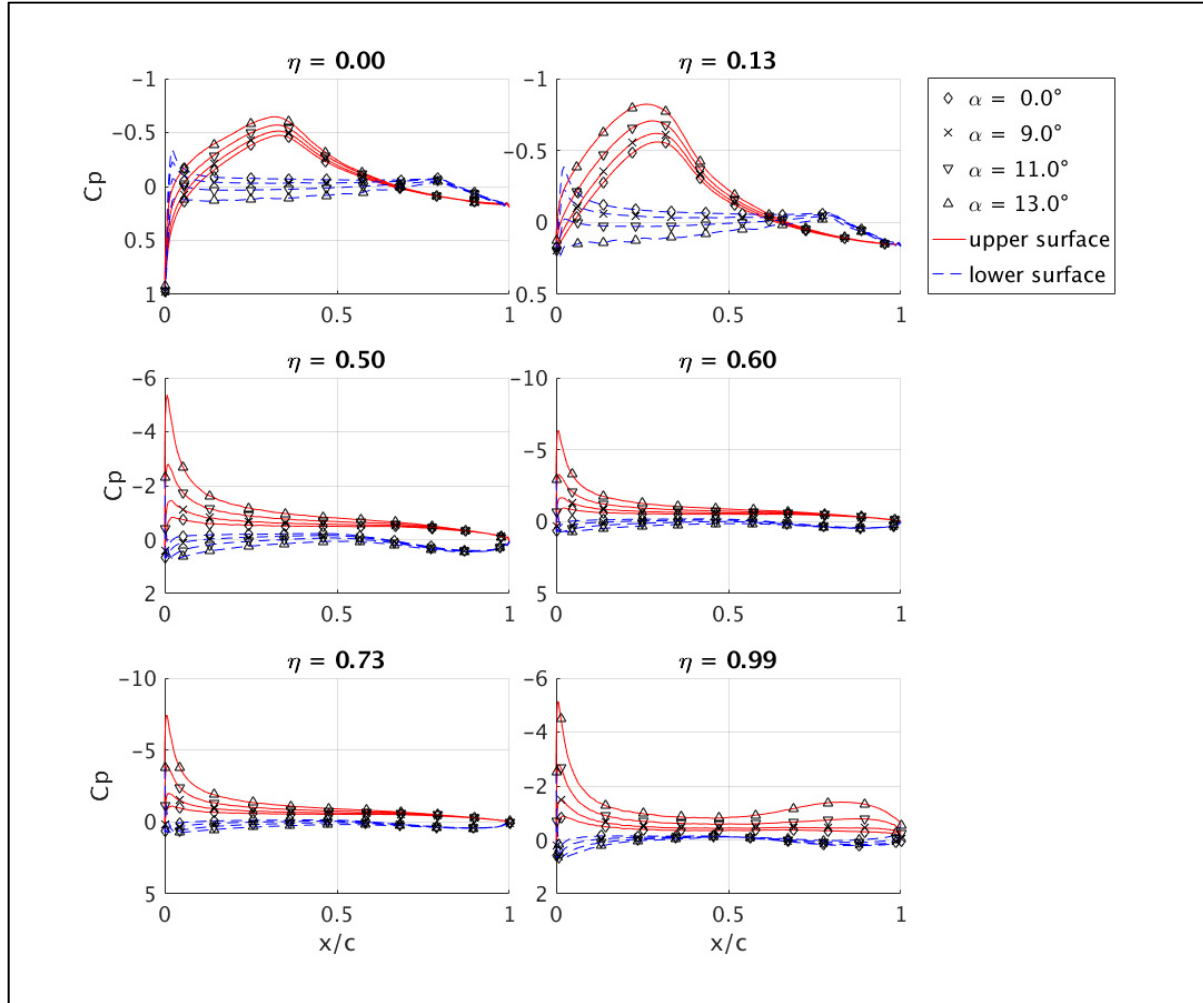
Figure A VII-7: C_p distribution at different angles of attack. - BWB V00
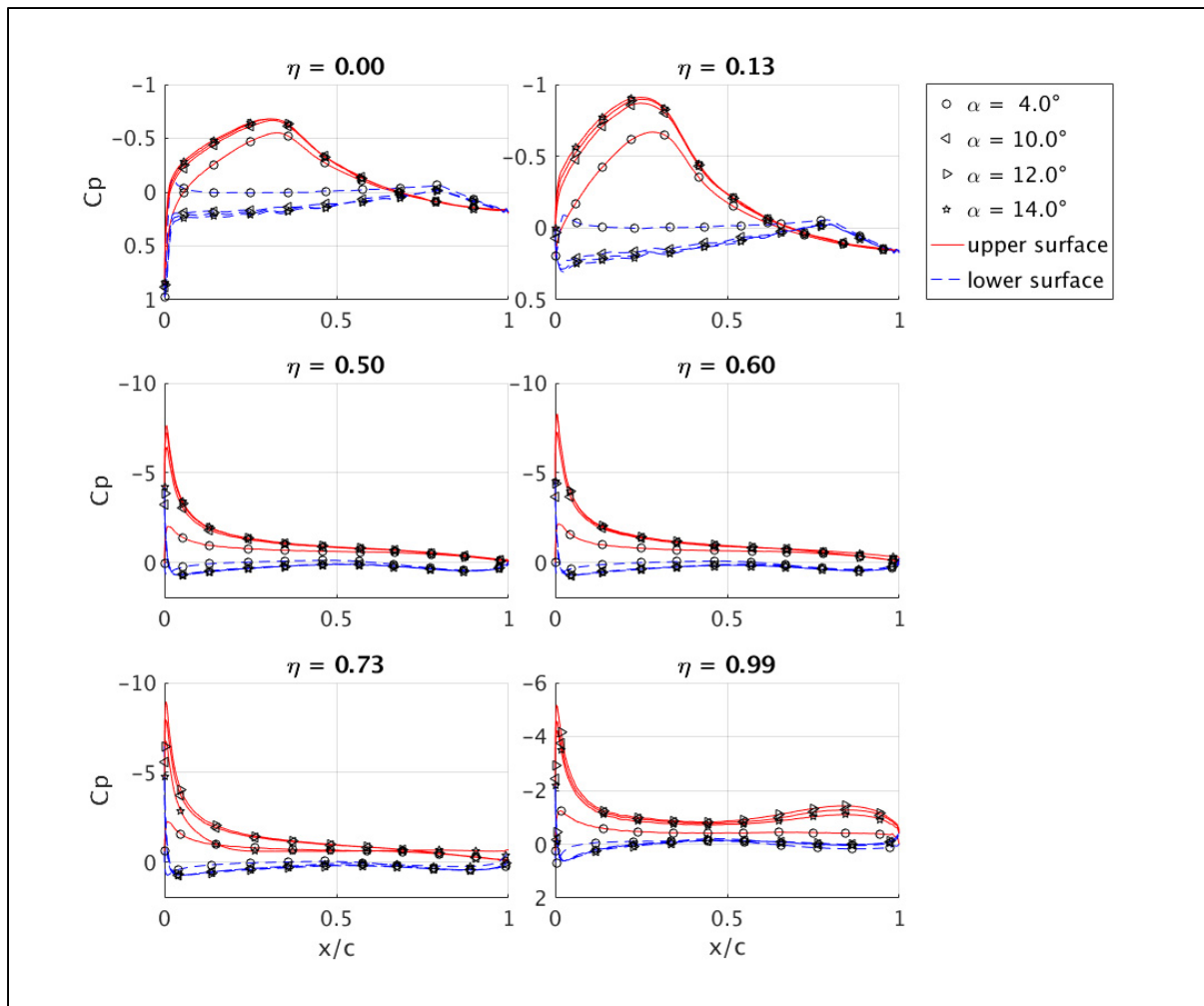
Figure A VII-8: C_p distribution at different angles of attack. - BWB V04

184
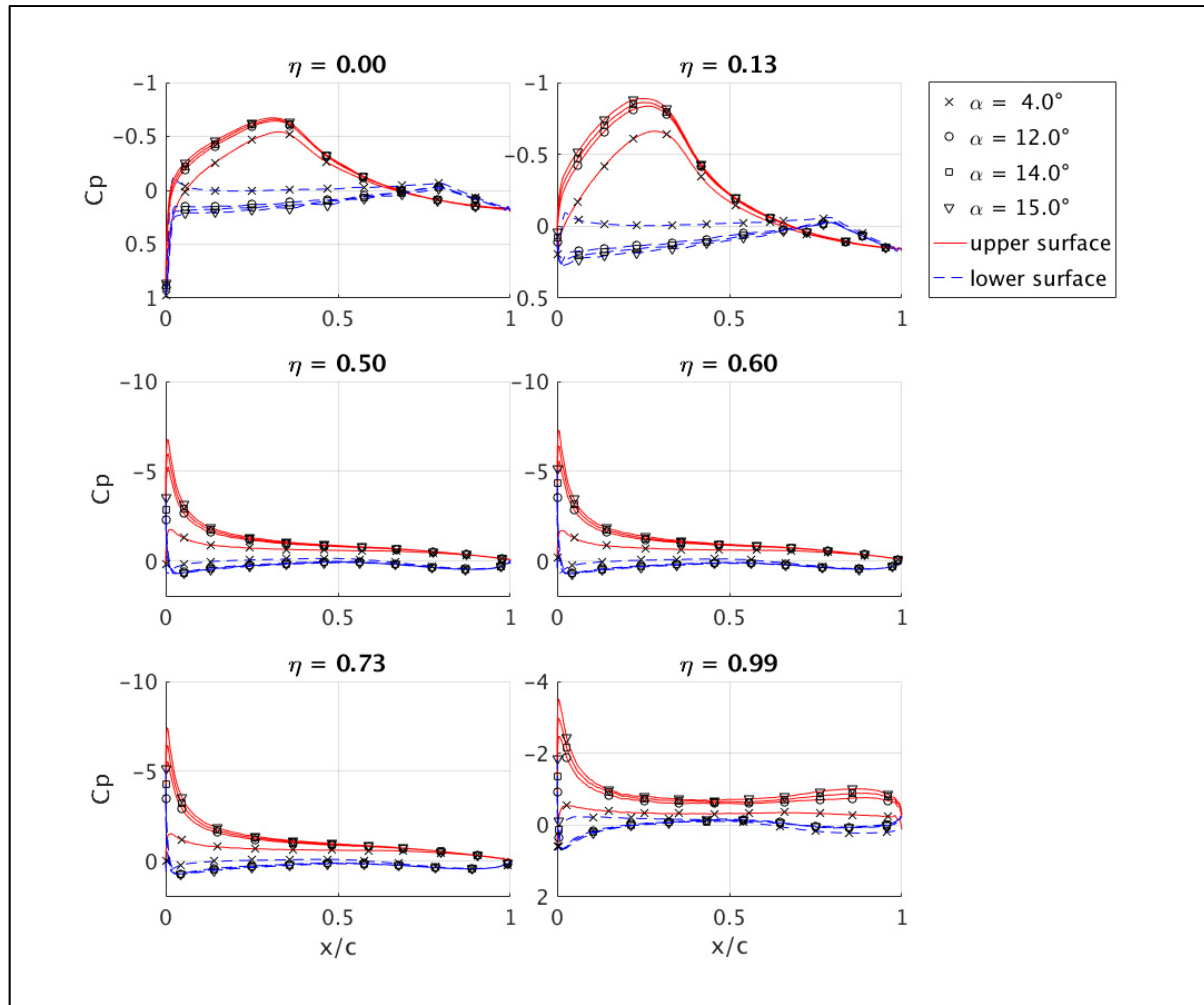
Figure A VII-9: C_p distribution at different angles of attack. - BWB V08
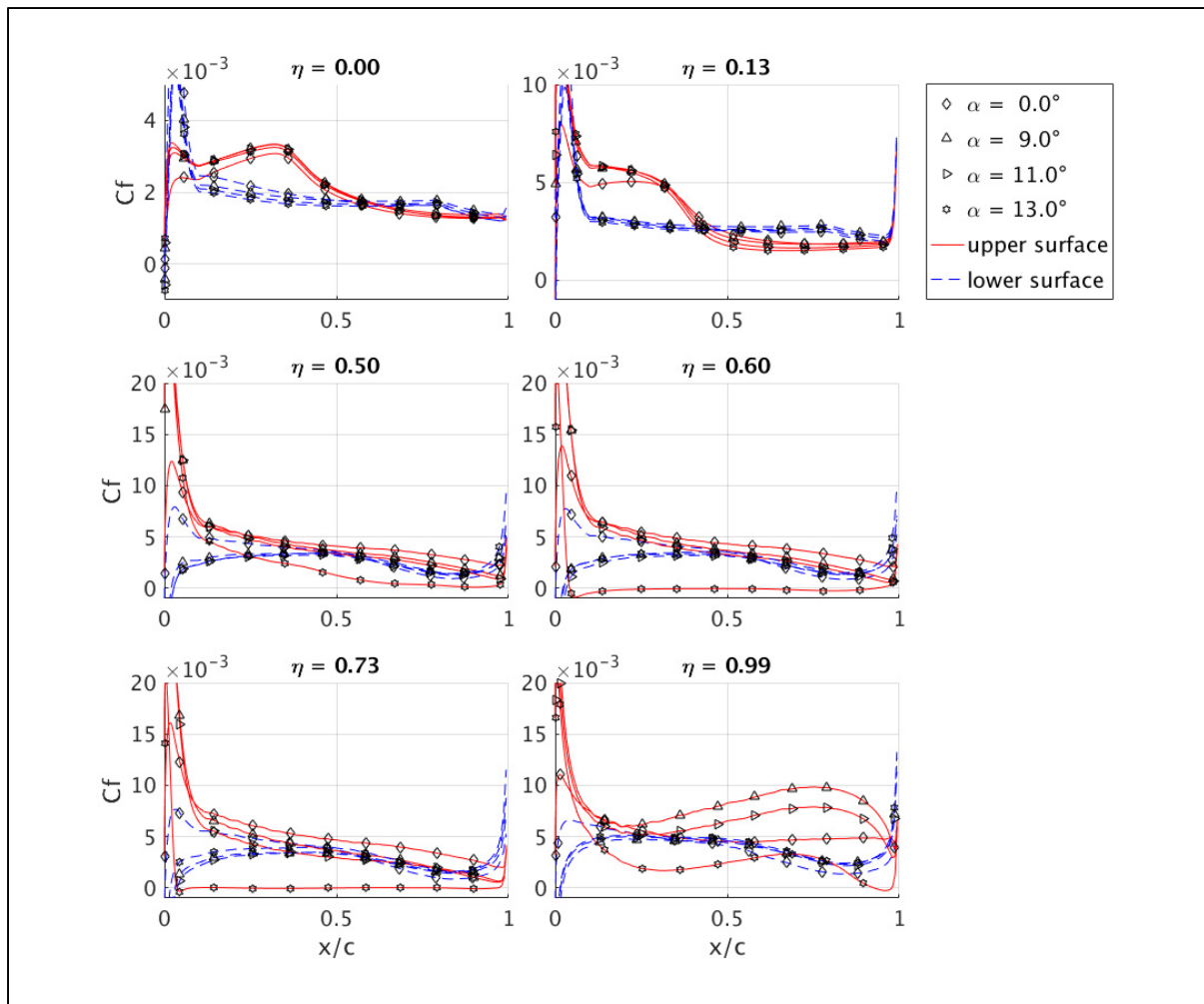
Figure A VII-10: C_f distribution at different angles of attack. - BWB V00
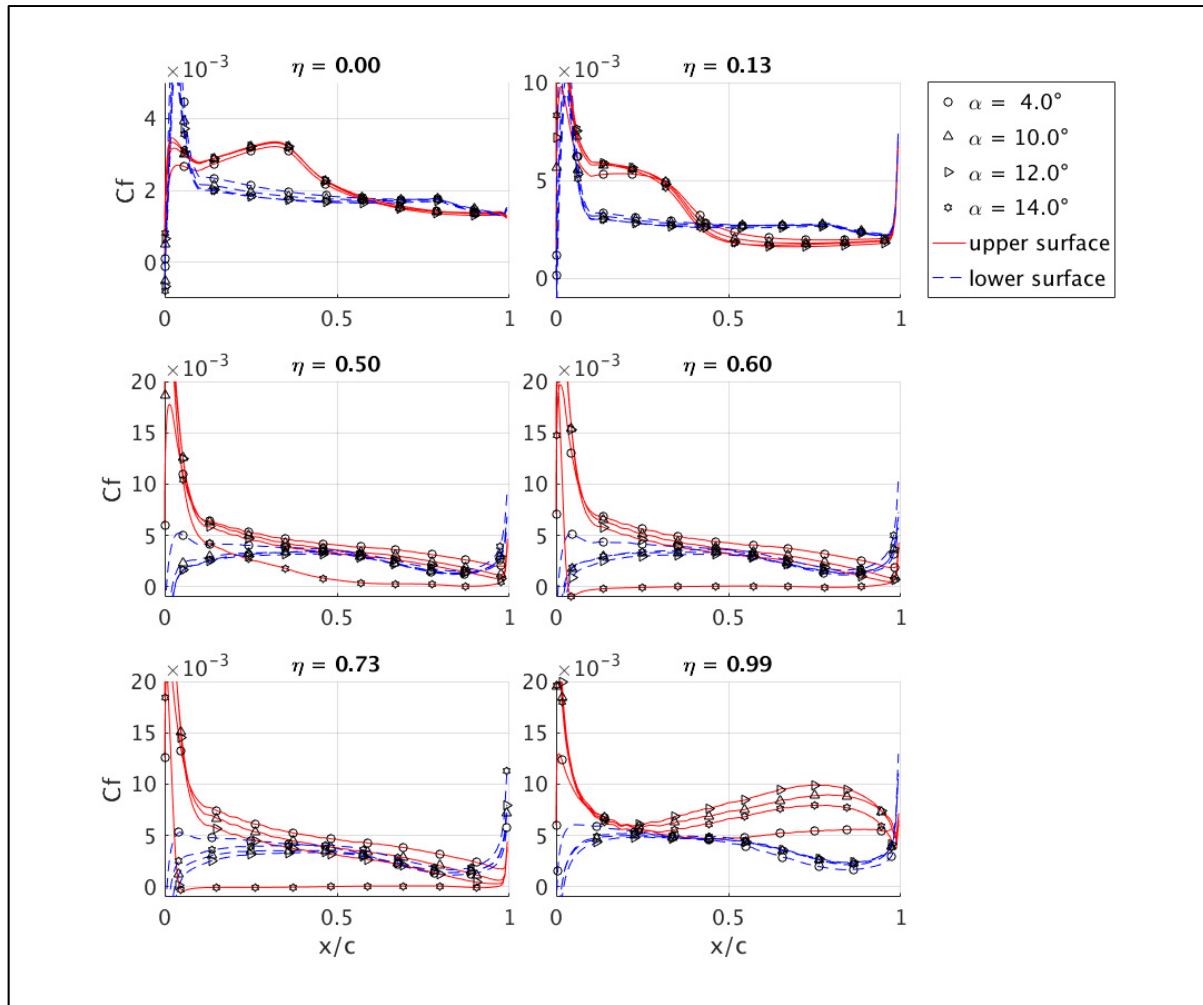
Figure A VII-11: C_f distribution at different angles of attack. - BWB V04
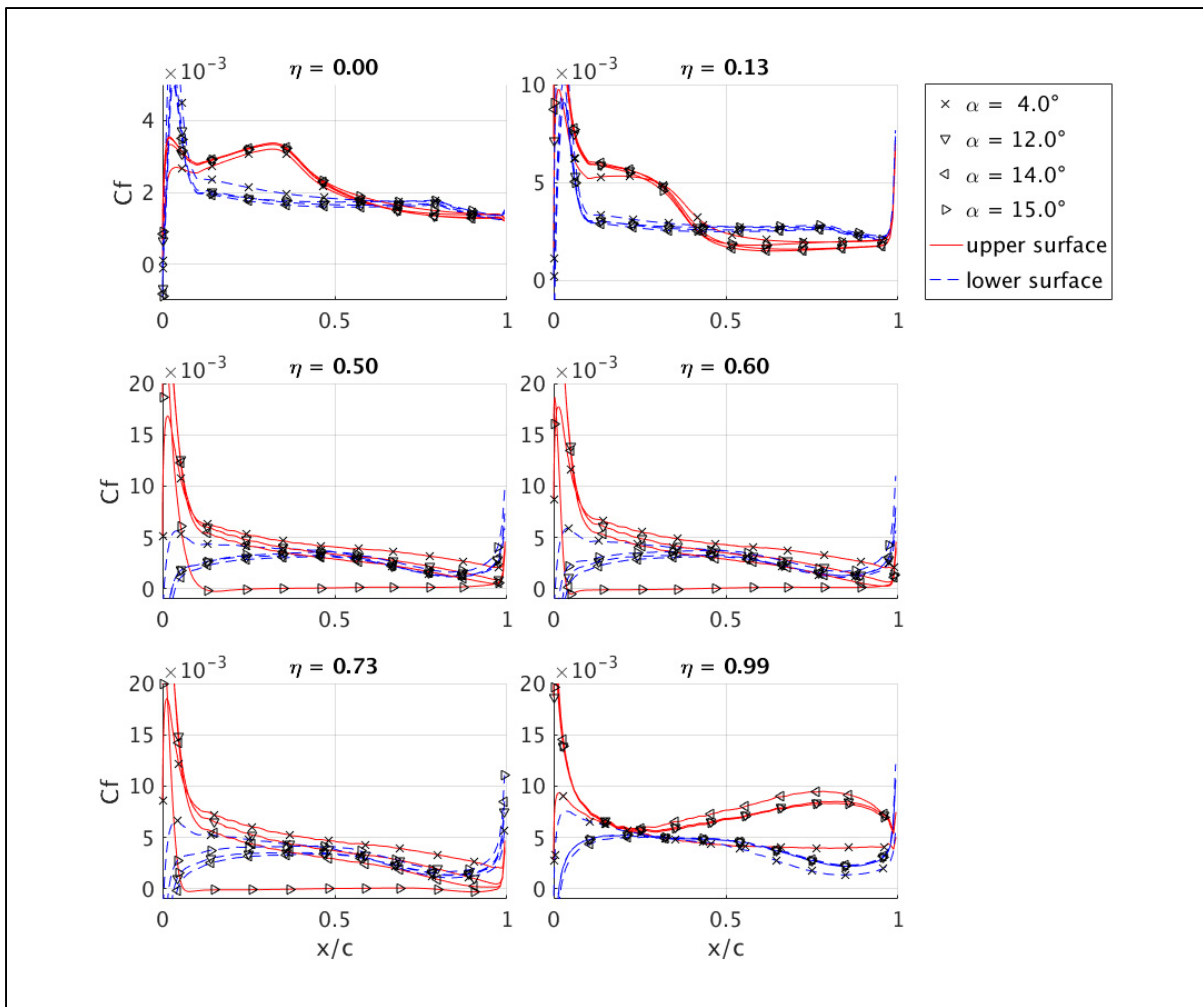
Figure A VII-12: C_f distribution at different angles of attack. - BWB V08
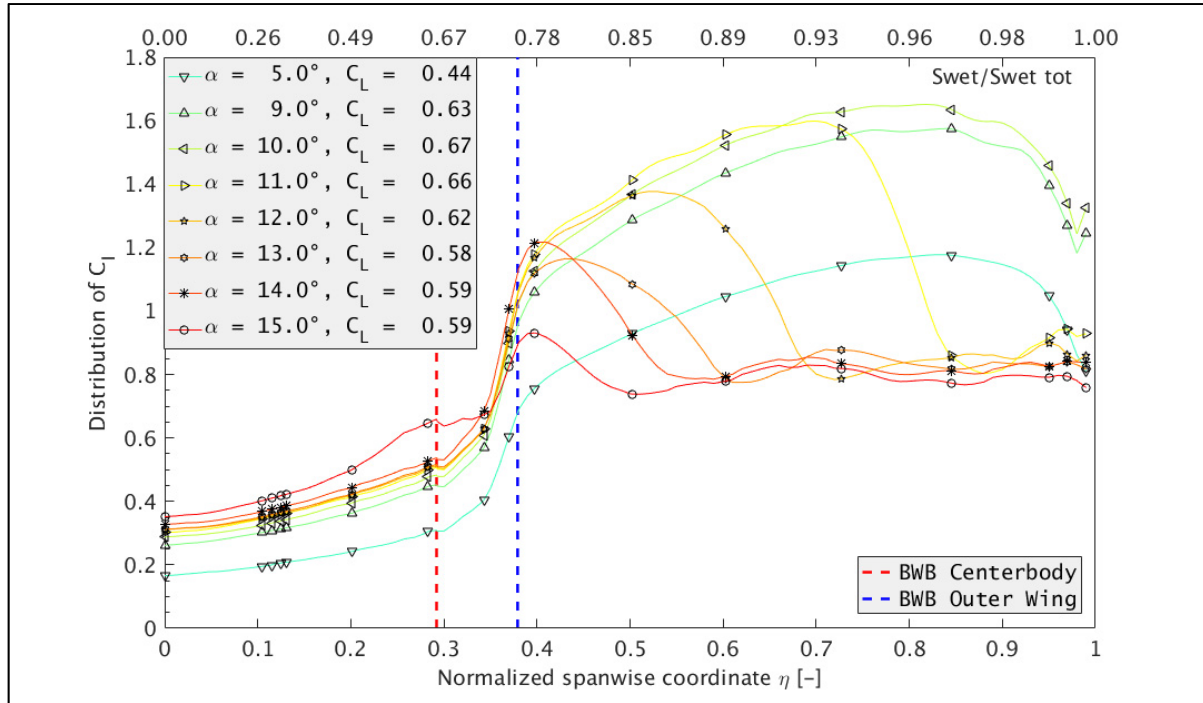
Figure A VII-13:   Spanwise C_l distribution. BWB V00
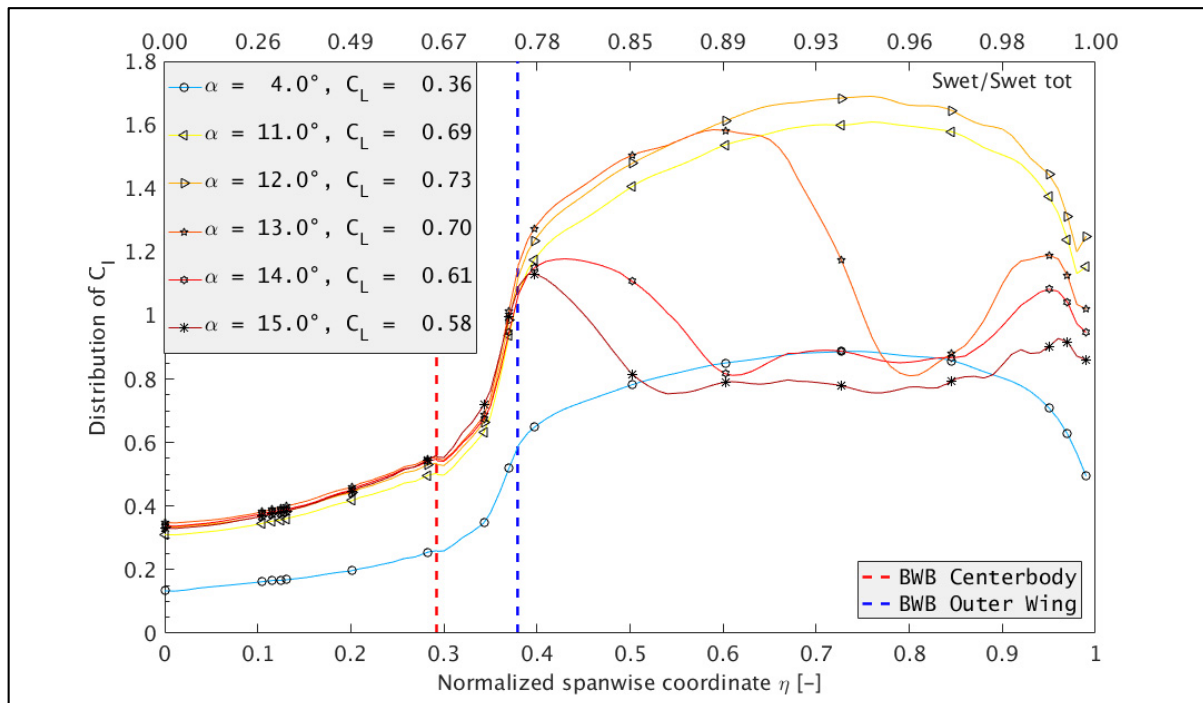
Figure A VII-14:   Spanwise C_l distribution. BWB V04
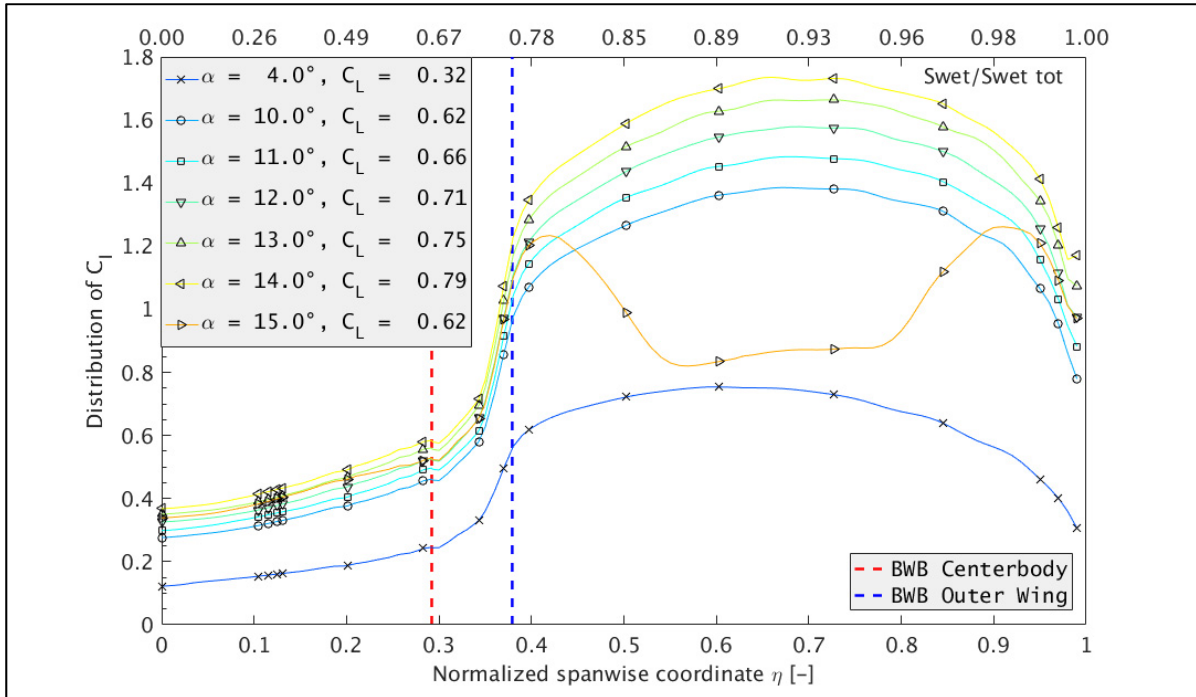
Figure A VII-15:   Spanwise C_l distribution. BWB V08
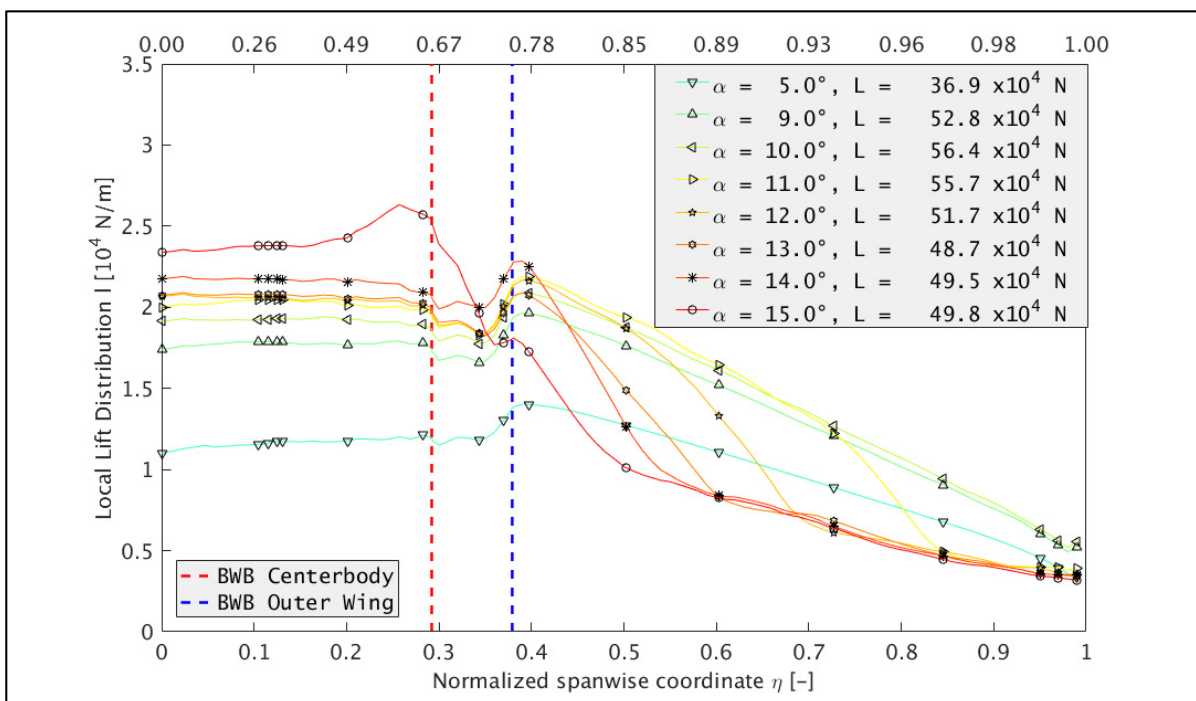

Figure A VII-16:   Spanwise local lift distribution. BWB V00
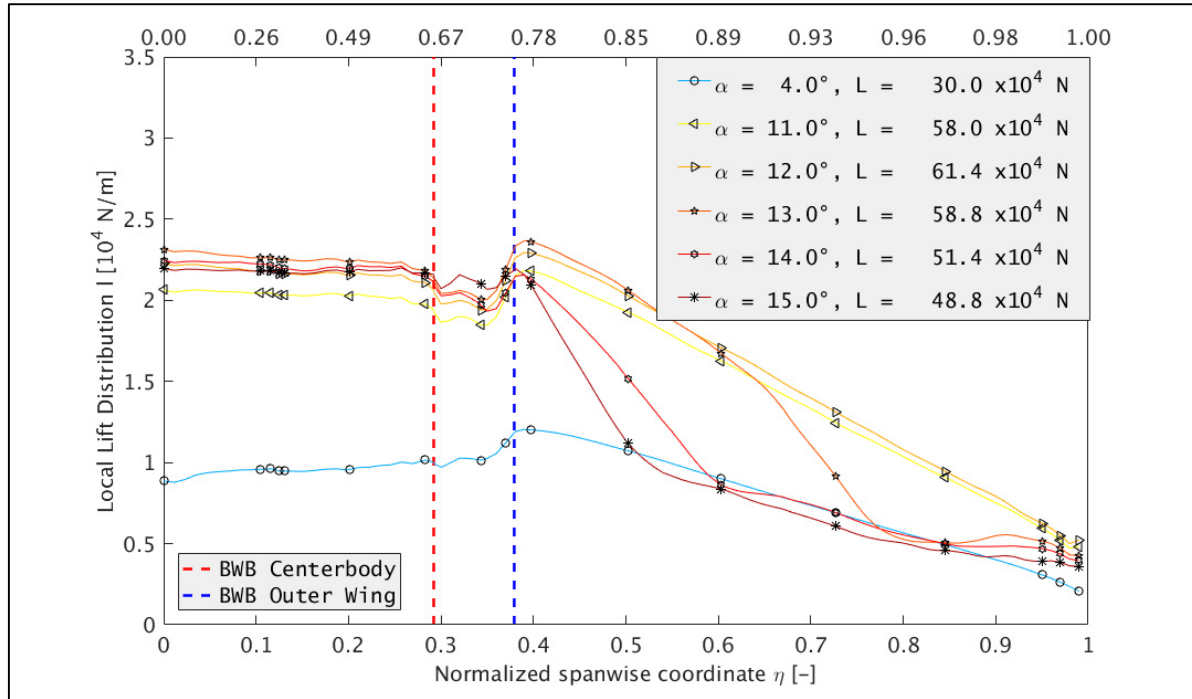
Figure A VII-17:   Spanwise local lift distribution. BWB V04
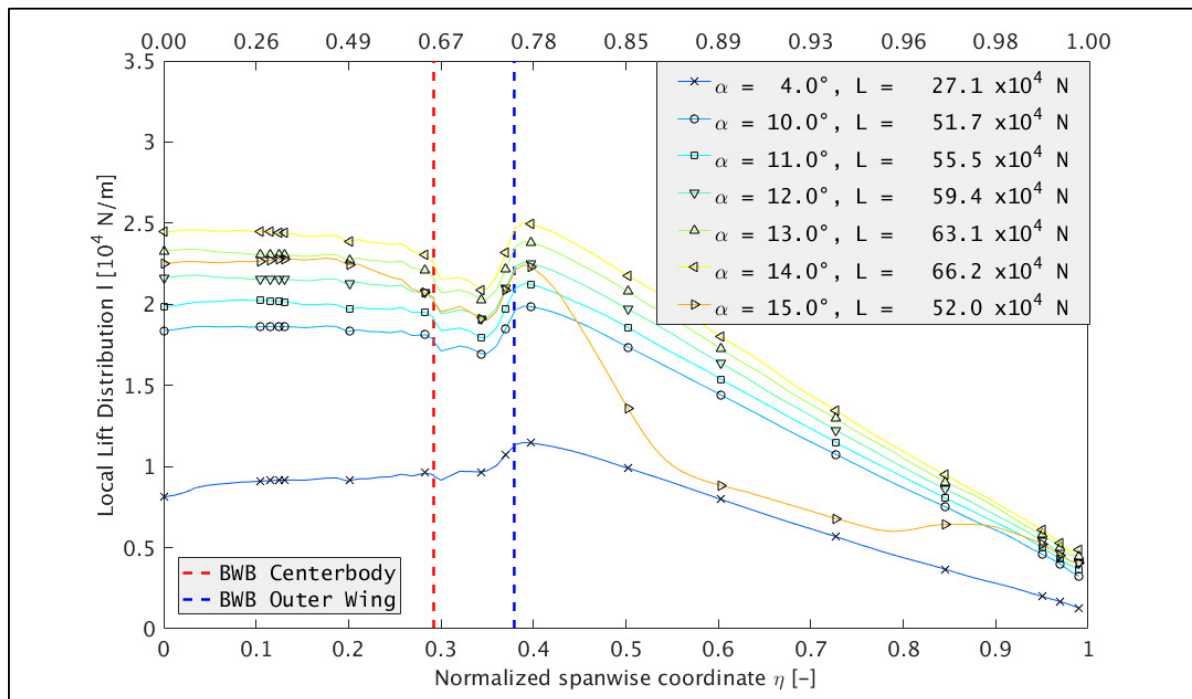
Figure A VII-18:   Spanwise local lift distribution. BWB V08
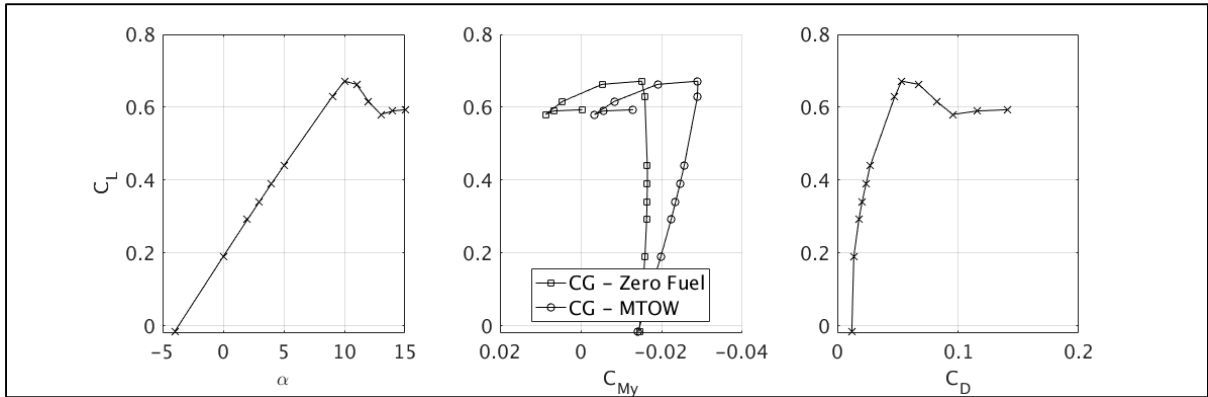
Figure A VII-19:   Aerodynamic coefficients - BWB V00
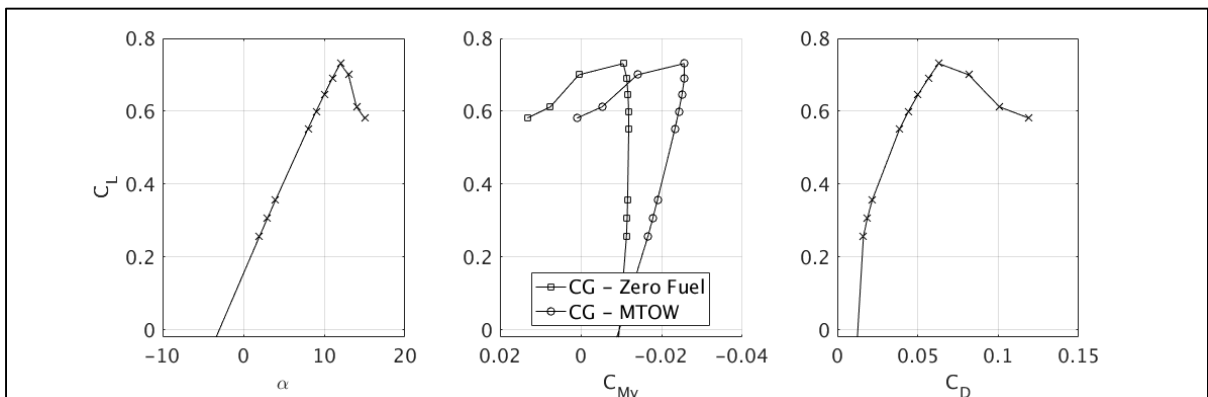
Figure A VII-20:   Aerodynamic coefficients - BWB V04
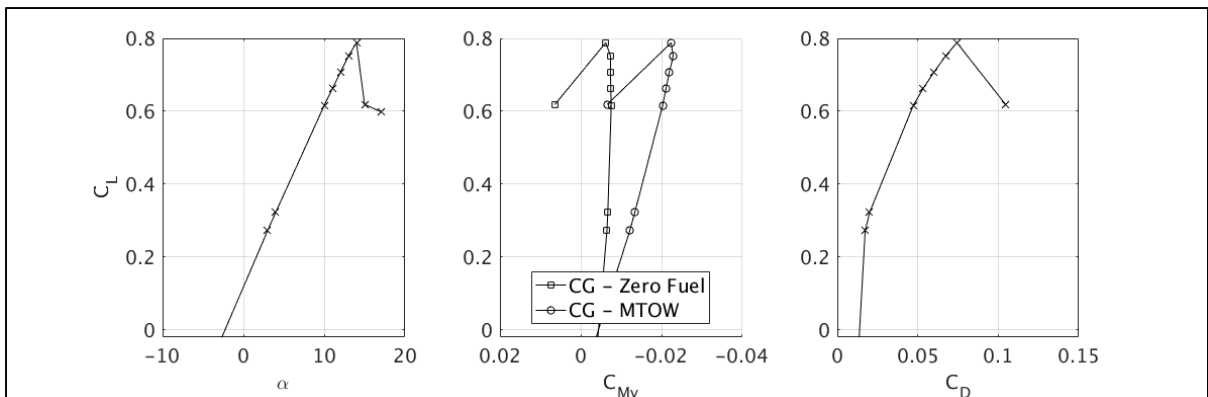
Figure A VII-21:   Aerodynamic coefficients - BWB V08

APPENDIX VIII

MULTI-SECTION, MULTI-SWEEP TWISTED LLT FOR CONSTANT SWEEP WINGS

Chapters 2 and 5 introduced an LLT model capable of predicting maximum lift for complex sweep, twist and section geometries. This appendix will focus on analysing the case of monotonically increasing twist, constant airfoil section and constant sweep Λ, and compare this to the model proposed by Phillips et al. (Phillips & Alley, 2007).

If Λ is constant, then the following simplifications apply:

$$f(\Lambda) = cst \Leftrightarrow \frac{df(\Lambda)}{d\theta} = 0 \qquad \text{(VIII.1)}$$

If, on top of that, the airfoil is constant along the wingspan, the following simplifications apply

$$\frac{d\alpha_{L0}}{d\theta} = 0 \qquad \text{(VIII.2)}$$

$$\frac{da_0}{d\theta} = 0 \qquad \text{(VIII.3)}$$

$$\frac{d\alpha_{2Dstall}}{d\theta} = 0 \qquad \text{(VIII.4)}$$

With these simplifications we will compare our variables and results from the ones proposed by Phillips et al. First, a reminder of the Phillips model is presented. Followings this, the constant-sweep, constant-airfoil simplifications are applied to our proposed model and linked to the original Phillips model.

VIII.1   Phillips model

Let us define the original Phillips' circulation $\tilde{\Gamma}$ as presented in equation (VIII.5). Note that the only difference consists in the absence of $f(\Lambda)$. From now on, we use "$\widetilde{}$" for the variables associated with this circulation.

$$\tilde{\Gamma}(\theta) = 2bV_\infty \sum_{n=1}^{N} \widetilde{A_n} \sin(n\theta) \qquad \text{(VIII.5)}$$

From this circulation, the resulting fundamental LLT equation is presented in equation (VIII.6). The reader is referred to (Phillips & Alley, 2007) for the derivation of this expression.

$$\alpha_{3D} - \phi(y_0) - \alpha_{L0}(y_0) = \sum_{n=1}^{N} \left(\widetilde{A_n} \left(\frac{4b}{a_0(\theta)c(\theta)} + \frac{n}{\sin(\theta)} \right) \sin(n\theta) \right) \qquad \text{(VIII.6)}$$

We are now introducing $\Delta\alpha$ and Ω. In the case of the Phillips et al. model, the original definition of $\Delta\alpha$ still applies: $\Delta\alpha(\alpha_{3D}, \theta) = \alpha_{3D} - \phi(\theta) - \alpha_{L0}(\theta)$. If we define $\Delta\alpha_{root} = \Delta\alpha\left(\alpha_{3D}, \frac{\pi}{2}\right)$ and $\Delta\alpha_{tip} = \Delta\alpha(\alpha_{3D}, 0)$, then we obtain

$$\tilde{\Omega} = \Delta\alpha_{root}(0) - \Delta\alpha_{tip}(0) \qquad \text{(VIII.7)}$$

$$\tilde{\omega}(\theta) = \frac{\Delta\alpha_{root}(\alpha_{3D}) - \Delta\alpha(\alpha_{3D}, \theta)}{\tilde{\Omega}} \qquad \text{(VIII.8)}$$

$$\Delta\alpha(\alpha_{3D}, \theta) = \Delta\alpha_{root}(\alpha_{3D}) - \tilde{\Omega}\tilde{\omega}(\theta) \qquad \text{(VIII.9)}$$

We are now going back to the fundamental equation. Let us define $g_n(\theta) = \left(\frac{4b}{a_0(\theta)c(\theta)} + \frac{n}{\sin(\theta)} \right) \sin(n\theta)$. This expression allows us to simplify the fundamental equation as follows:

$$\Delta\alpha(\alpha_{3D}, \theta) = \sum_{n=1}^{N} \widetilde{A_n} g_n(\theta) \tag{VIII.10}$$

From here, we can define the Phillips' Fourier series $\widetilde{a_n}$ and $\widetilde{b_n}$ as follows:

$$\sum_{n=1}^{N} \widetilde{a_n} g_n(\theta) = 1 \tag{VIII.11}$$

$$\sum_{n=1}^{N} \widetilde{b_n} g_n(\theta) = \widetilde{\omega}(\theta) \tag{VIII.12}$$

This section has introduced the original Phillips model variables. These variables are identified by the " ~ " marker. The following sections will apply the hypothesis of constant sweep, constant airfoil and linear twist for the multi-sweep multi-section model to compare against the original Phillips et al. model.

VIII.2   Total twist

The prior section introduces the original Fourrier series for the Phillips model. From this section onwards, we will consider our own model under the assumptions of constant-sweep constant-airfoil and monotonically increasing twist. We start with the calculation of the total twist. Our model proposes a definition of the total twist as follows:

$$\Omega = \Delta\alpha_{rmax} - \Delta\alpha_{rmin} \tag{VIII.13}$$

Remember that $\Delta\alpha_{rmax} = \Delta\alpha(\alpha_{3D}, y_{rmax})$ where y_{rmax} correspond to the sections that maximize $\Delta\alpha$. Similarly, y_{rmin} minimizes $\Delta\alpha$. For a constant-airfoil, monotonically increasing twist – as hypothesised by Phillips et al. -, $\Delta\alpha$ is maximum at the root (where no twist applies)

and is minimum at the tip (where twist is maximum). Thus, $\Delta\alpha_{rmax} = \Delta\alpha_{root}$ and $\Delta\alpha_{rmin} = \Delta\alpha_{tip}$. This implies that, for a constant-airfoil, monotonically increasing twist,

$$\Omega = \tilde{\Omega} \tag{VIII.14}$$

$$\omega(\theta) = \tilde{\omega}(\theta) \tag{VIII.15}$$

$$\Delta\alpha(\alpha_{3D}, \theta) = \Delta\alpha_{root} - \tilde{\Omega}\tilde{\omega}(\theta) \tag{VIII.16}$$

We conclude that for this case scenario, the total twist and the total twist distribution are the same for both models.

VIII.3   Fourrier series a_n, b_n for constant sweep and section.

The prior section introduces the total twist in the case of constant-airfoil and monotonically increasing twist. Lets now focus on the Fourier series. In this case, the term $\delta_n^{\alpha_i}$ from equation (2.44) becomes

$$\delta_n^{\alpha_i}(\Lambda = cst) = \sum_{j=0}^{M-1} f_j q_{nj} = f(\Lambda) \tag{VIII.17}$$

And the induced angle becomes:

$$\alpha_i(\theta_0) = \frac{1}{\pi}\sum_{n=1}^{N} nA_n\delta_n^{\alpha_i}\frac{\sin(n\theta_0)}{\sin(\theta_0)} = \frac{f(\Lambda)}{\pi}\sum_{n=1}^{N} nA_n\frac{\sin(n\theta_0)}{\sin(\theta_0)} \tag{VIII.18}$$

Thus, equations (2.59) and (2.60) become:

$$
\begin{cases}
\displaystyle\sum_{n=1}^{N} a_n g_n(\theta) = \frac{1}{f(\Lambda)} \\[2em]
\displaystyle\sum_{n=1}^{N} b_n g_n(\theta) = \frac{\omega(\theta)}{f(\Lambda)}
\end{cases}
\tag{VIII.19}
$$

As a result, the series (a_n, b_n) are multiples of $(\widetilde{a_n}, \widetilde{b_n})$:

$$
\begin{cases}
a_n = \dfrac{\widetilde{a_n}}{f(\Lambda)} \\[1.5em]
b_n = \dfrac{\widetilde{b_n}}{f(\Lambda)}
\end{cases}
\tag{VIII.20}
$$

VIII.4   Global lift coefficient for constant sweep and section

If Λ is constant, the term δ_n^{CL} becomes $f(\Lambda)$ if $n = 1$ and 0 otherwise. Thus, the base and twist lift corrections for C_L become:

$$
\begin{cases}
\delta_\alpha^{CL} = \displaystyle\sum_{n=1}^{N} a_n \delta_n^{CL} = a_1 f(\Lambda) = \widetilde{a_1} \\[2em]
\delta_\Omega^{CL} = \displaystyle\sum_{n=1}^{N} b_n \delta_n^{CL} = b_1 f(\Lambda) = \widetilde{b_1}
\end{cases}
\tag{VIII.21}
$$

And the global lift coefficient is given as:

$$
C_L = \pi AR \delta_\alpha^{CL} \left(\Delta\alpha_{root} - \frac{\delta_\Omega^{CL}}{\delta_\alpha^{CL}} \Omega \right) = \pi AR \widetilde{a_1} \left(\Delta\alpha_{root} - \frac{\widetilde{b_1}}{\widetilde{a_1}} \Omega \right) = \widetilde{C_L}
\tag{VIII.22}
$$

Furthermore, the global lift coefficient slope becomes:

$$
C_{L,\alpha} = \pi AR \widetilde{a_1} = \widetilde{C_{L,\alpha}}
\tag{VIII.23}
$$

VIII.5 Circulation Γ

If Λ is constant, then the circulation Γ is linked to $\widetilde{a_n}$ and $\widetilde{b_n}$. By definition, the circulation is given as

$$\Gamma = 2bV_\infty f(\Lambda) \sum_{n=1}^{N} (a_n \Delta\alpha_{rmax} - b_n\Omega) \sin(n\theta) \tag{VIII.24}$$

Note now that for this case scenario, $\Delta\alpha_{rmax} = \Delta\alpha_{root}$, $\Omega = \widetilde{\Omega}$, $f(\Lambda)a_n = \widetilde{a_n}$ and $f(\Lambda)b_n = \widetilde{b_n}$. After injecting this into the above equation, we obtain the same circulation as the one proposed by Phillips et al.

$$\Gamma(\theta) = 2bV_\infty \sum_{n=1}^{N} \left(\widetilde{a_n}\Delta\alpha_{root} - \widetilde{b_n}\Omega\right) \sin(n\theta) = \tilde{\Gamma}(\theta) \tag{VIII.25}$$

This implies that, for this specific case, the local lift coefficients are the same: $C_l = \tilde{C}_l$. Furthermore, for this case, the derivative of the circulation gives the same as the Phillips' model.

$$\frac{d\Gamma}{d\theta} = 2bV_\infty \sum_{n=1}^{N} \left(\widetilde{a_n}\Delta\alpha_{root} - \widetilde{b_n}\Omega\right)n \cos(n\theta) = \frac{d\tilde{\Gamma}}{d\theta} \tag{VIII.26}$$

VIII.6 Lift ratio

We recall here equation defining the lift coefficient ratio:

$$\frac{C_L}{C_l} = \frac{K}{\sum_{n=1}^{\infty} a_n \sin(n\theta)} \left(1 - \chi \sum_{n=1}^{\infty} \frac{1}{K}\left(\frac{b_1}{a_1}a_n - b_n\right) \sin(n\theta)\right) \tag{VIII.27}$$

Remember that $K = \frac{C_{L,\alpha}c}{4b}\frac{1}{f(\Lambda)}, \chi = \frac{C_{L,\alpha}\Omega}{C_l}$. If we now introduce the variable changes with respect to the Phillips series, we obtain:

$$\frac{C_L}{C_l} = \frac{\widetilde{C_{L,\alpha}}c}{4b}\frac{1}{\sum_{n=1}^{\infty}\widetilde{a_n}\sin(n\theta)}\left(1\right.$$

$$\left.-\frac{\widetilde{C_{L,\alpha}}\widetilde{\Omega}}{\widetilde{C_l}}\sum_{n=1}^{\infty}\frac{\widetilde{C_{L,\alpha}}c}{4b}\left(\frac{\widetilde{b_1}}{\widetilde{a_1}}\widetilde{a_n}-\widetilde{b_n}\right)\sin(n\theta)\right)$$

(VIII.28)

This means that, for the constant-sweep, constant airfoil case scenario, the lift coefficient ratios are the same as Phillips' non-corrected model in the linear zone.

VIII.7 Reference section

One of the biggest differences between the two models lies in the definition of the reference section. Phillips chooses the reference section as the section that carries the maximum lift coefficient:

$$\widetilde{\theta_{ref}} = \left\{\theta \in \left[0,\frac{\pi}{2}\right] \text{ so that } \widetilde{C_l}(\theta_{ref},\alpha_{3D}) \text{ is maximum}\right\}$$

(VIII.29)

Based on Phillips, this is equivalent to finding the section θ that solves the following equation:

$$\sum_{n=1}^{N}\left(\widetilde{a_n}+\left(\widetilde{a_n}\frac{\widetilde{b_1}}{\widetilde{a_1}}-\widetilde{b_n}\right)\left(\frac{\widetilde{C_{L,\alpha}}\Omega}{\widetilde{C_L}}\right)\right)\left(n\cos(n\theta)c(\theta)-\sin(n\theta)\frac{dc}{d\theta}\right)$$
$$= 0$$

(VIII.30)

Now, in the case of our model, our reference section is given as

$$\theta_{ref} = \left\{ \theta \in \left[0, \frac{\pi}{2}\right] \; so \; that \; r_\alpha = \frac{\alpha_{eff}}{\alpha_{2Dstall}} \; is \; maximum \right\} \tag{VIII.31}$$

From chapter 2, we recall the equivalent condition for maximizing r_α:

$$\left(\frac{2 \frac{d\Gamma}{d\theta} a_0 V_\infty c - 2 \Gamma V_\infty (\frac{da_0}{d\theta} c + a_0 \frac{dc}{d\theta})}{(a_0 V_\infty c)^2} + \frac{d\alpha_{L0}}{d\theta} \right) \alpha_{2Dstall}(\theta)$$

$$- \left(\frac{2\Gamma}{a_0 V_\infty c} + \alpha_{L0} \right) \frac{d\alpha_{2Dstall}}{d\theta} = 0 \tag{VIII.32}$$

In the case of a constant section airfoil, $\frac{d\alpha_{2Dstall}}{d\theta} = 0$. Furthermore, a_0 becomes constant along the wingspan and $\frac{da_0}{d\theta} = 0$. Thus, if we recall that, for this scenario, $\Gamma = \tilde{\Gamma}$, the reference condition is equivalent to:

$$\frac{dr_\alpha}{d\theta} = 0 \Leftrightarrow \left(\frac{d\tilde{\Gamma}}{d\theta} c - \tilde{\Gamma}(\frac{dc}{d\theta}) \right) = 0 \tag{VIII.33}$$

This expression is readily developed into

$$\sum_{n=1}^{N} \left(\widetilde{a_n} + \left(\frac{\widetilde{b_1}}{\widetilde{a_1}} \widetilde{a_n} - \widetilde{b_n} \right) \frac{\widetilde{C_{L,\alpha}\Omega}}{\widetilde{C_L}} \right) \left(n \cos(n\theta) c(\theta) - \sin(n\theta) \frac{dc}{d\theta} \right) = 0 \tag{VIII.34}$$

This is the exact same condition as the one proposed in the original model. This basically means that our reference section corresponds to the section of maximum local lift coefficient in the case of a simple geometry, whereas it differs for the case of more complex geometries.

VIII.8   Reference lift ratio and maximum lift

From the previous sections it has been deduced that, in the constant sweep and airfoil case study, the circulation Γ, the total lift coefficient C_L, the reference section θ_{ref} and the linear lift coefficient ratio $\frac{C_L}{C_l}$ are the same as the ones proposed by Phillips et al. The only part left to analyze is the case $C_l = C_{lstall}(\theta_{ref})$. The multi-sweep model proposes:

$$\frac{C_L}{C_{lstall}} = \left(\frac{C_L}{C_l}\right)_{\Omega=0} \kappa_{L\Lambda}\kappa_{Ls}(1 - \chi\kappa_{L\Omega}) \tag{VIII.35}$$

Where

$$\kappa_{L\Lambda} = \left(\frac{\delta_{L\Lambda}}{f(\Lambda)}\right)^{3.7} \kappa_{L\Lambda}^{phill}\left(\Lambda_{0.25c}(\theta_{ref})\right) \tag{VIII.36}$$

$$\kappa_{Ls} = \kappa_{Ls}^{phill} \tag{VIII.37}$$

For a constant sweep and airfoil wing, $\delta_{L\Lambda} = f(\Lambda)$. Thus, since $\Lambda_{0.25c}$ is also constant, $\kappa_{L\Lambda} = \kappa_{L\Lambda}^{phill}$. Furthermore, after applying some simplifications, it is found that $\left(\frac{C_L}{C_l}\right)_{\Omega=0} = \left(\widetilde{\frac{C_L}{C_l}}\right)_{\Omega=0,\Lambda=0}$. Finally, since $\chi = \tilde{\chi}$. Note that, by definition $\kappa_{L\Lambda}^{phill} = \widetilde{\kappa_{L\Lambda}}$ and $\kappa_{Ls}^{phill} = \widetilde{\kappa_{Ls}}$. Eventually, this means that for a constant sweep and constant airfoil section, our model is equivalent to Phillips' when calculating maximum lift:

$$\frac{C_L}{C_{lstall}} = \left(\widetilde{\frac{C_L}{C_l}}\right)_{\Omega=0,\Lambda=0} \widetilde{\kappa_{L\Lambda}}\widetilde{\kappa_{Ls}}(1 - \tilde{\chi}\widetilde{\kappa_{L\Omega}}) = \left(\widetilde{\frac{C_L}{C_{lstall}}}\right) \tag{VIII.38}$$

Based on the validation work proposed by Phillips et al. our model is valid for simple geometries. Based on the multi-section, multi-sweep data available, our model complies with the CFD obtained for the BWB. This model should give a reasonable prediction (within 5%

accuracy) of the maximum global lift coefficient for multi-section, multi-sweep wings like the BWB, double deltas, all-wing aircraft and others.

LIST OF BIBLIOGRAPHICAL REFERENCES

Abbott, I. H., & Von Doenhoff, A. E. (1959). *Theory of wing sections, including a summary of airfoil data*: Courier Corporation.

Alley, N. R., Phillips, W. F., & Spall, R. E. (2007). Predicting Maximum Lift Coefficient for Twisted Wings Using Computational Fluid Dynamics. *Journal of Aircraft, 44*(3), 911-917. doi:https://doi.org/10.2514/1.25643

Anderson, J. D. (1999). *Aircraft performance and design*. Boston, Massachussets: McGraw-Hill.

Anderson, J. D. (2001). *Fundamentals of aerodynamics* (3rd ed. ed.). New York, N.Y.: McGraw-Hill.

Anderson, J. D. (2005). *Introduction to flight* (5th ed. ed.). Boston: McGraw-Hill Higher Education.

Blazek, J. (2015). *Computational fluid dynamics: principles and applications*: Butterworth-Heinemann.

Blessing, B. H., Pham, J., & Marshall, D. D. (2009). *Using CFD as a design tool on new innovative airliner configurations.* Paper presented at the 47th AIAA Aerospace Sciences Meeting including the New Horizons Forum and Aerospace Exposition, January 5, 2009 - January 8, 2009, Orlando, FL, United states.

Bolsunovsky, A. L., Buzoverya, N. P., Gurevich, B. I., Denisov, V. E., Dunaevsky, A. I., Shkadov, L. M., . . . Zhurihin, J. P. (2001). Flying wing—problems and decisions. *Aircraft Design, 4*(4), 193-219. doi:http://dx.doi.org/10.1016/S1369-8869(01)00005-2

Bombardier. (2015). *Fiche Technique CRJ1000*. Retrieved from

Bombardier. (2017). *Bombardier Commercial Aircraft Market Forecast 2017-2036*. Retrieved from https://ir.bombardier.com/var/data/gallery/document/01/87/55/05/15/BCA-2017-2036-Market-Forecast-EN.pdf

Bradley, K. R. (2004). A sizing methodology for the conceptual design of blended-wing-body transports. *NASA CR, 213016*, 2004.

Cai, C. F., Wu, J. H., & Liang, B. (2014). *The effect of gust on blended-wing-body civil aircraft.* Paper presented at the 5th International Conference on Mechanical and Aerospace Engineering, ICMAE 2014, July 18, 2014 - July 19, 2014, Madrid, Spain.

Carter, M. B., Campbell, R. L., Pendergraft Jr, O. C., Friedman, D. M., & Serrano, L. (2006). Designing and testing a blended wing body with boundary-layer ingestion nacelles. *Journal of Aircraft, 43*(5), 1479-1489. doi:10.2514/1.22765

Carter, M. B., Vicroy, D. D., & Patel, D. (2009). *Blended-Wing-Body Transonic aerodynamics: Summary of ground tests and sample results (Invited).* Paper presented at the 47th AIAA Aerospace Sciences Meeting including the New Horizons Forum and Aerospace Exposition, January 5, 2009 - January 8, 2009, Orlando, FL, United states.

Celik, I., Ghia, U., Roache, P., Freitas, C., Coleman, H., & Raad, P. (2008). Procedure for Estimation and Reporting of Uncertainty Due to Discretization in CFD Applications. *Journal of Fluids Engineering, 130*(7), 078001-078001. doi:10.1115/1.2960953

Cheng, H., Chow, R., & Melnik, R. E. (1981). Lifting-line theory of swept wings based on the full potential theory. *Zeitschrift für angewandte Mathematik und Physik ZAMP, 32*(5), 481-496.

Collier, F., Thomas, R., Burley, C., Nickol, C., Lee, C.-M., & Tong, M. (2010). *Environmentally responsible aviation-real solutions for environmental challenges facing aviation*. Paper presented at the 27th International Congress of the Aeronautical Sciences (ICAS), Nice, France.

Compute Canada. (2019). Compute Canada Documentation. Retrieved from https://docs.computecanada.ca/wiki/Compute_Canada_Documentation

Corke, T. C. (2003). *Design of aircraft*: Pearson College Division.

Cosyn, P., & Vierendeels, J. (2006). Numerical investigation of low-aspect-ratio wings at low Reynolds numbers. *Journal of Aircraft, 43*(3), 713-722. doi:https://doi.org/10.2514/1.16991

Currie, I. G. (2002). *Fundamental mechanics of fluids*: Crc Press.

Deloitte. (2010). *AIAC - Global Aerospace Market Outlook and Forecast*. Retrieved from

Deperrois, A. (2009a). XFLR5 - WRONG CITATION. *Guidelines for XFLR5*.

Deperrois, A. (2009b). XFLR5 Analysis of foils and wings operating at low reynolds numbers. Retrieved from xflr5.com

Diedrich, A., Hileman, J., Tan, D., Willcox, K., & Spakovszky, Z. (2006). *Multidisciplinary design and optimization of the silent aircraft.* Paper presented at the 44th AIAA Aerospace Sciences Meeting 2006, January 9, 2006 - January 12, 2006, Reno, NV, United states.

Dobrzynski, W. (2010). Almost 40 Years of Airframe Noise Research: What Did We Achieve? *Journal of Aircraft, 47*(2), 353-367. doi:10.2514/1.44457

Drela, M. (1989). *XFOIL: An Analysis and Design System for Low Reynolds Number Airfoils*, Berlin, Heidelberg.

Drela, M., & Youngren, H. (2008). Athena vortex lattice (AVL).

Ferziger, J. H., & Peric, M. (2012). *Computational methods for fluid dynamics*: Springer Science & Business Media.

Frawley, G. (2003). *The International Directory of Civil Aircraft 2003/2004*: MBI Publishing Company.

Gallay, S., & Laurendeau, E. (2015). Nonlinear Generalized Lifting-Line Coupling Algorithms for Pre/Poststall Flows. *AIAA Journal, 53*(7), 1784-1792. doi:https://doi.org/10.2514/1.J053530

Gariépy, M., Malouin, B., Trépanier, J.-Y., & Laurendeau, É. (2013). Far-Field Drag Decomposition Applied to the Drag Prediction Workshop 5 Cases. *Journal of Aircraft, 50*(6), 1822-1831. doi:10.2514/1.C032204

Gebbie, D. A., Reeder, M. F., Tyler, C., Fonov, V., & Crafton, J. (2007). Lift and Drag Characteristics of a Blended-Wing Body Aircraft. *Journal of Aircraft, 44*(5), 1409-1421. doi:https://doi.org/10.2514/1.22356

Geissler, W., & Haselmeyer, H. (2006). Investigation of dynamic stall onset. *Aerospace Science and Technology, 10*(7), 590-600. doi:https://doi.org/10.1016/j.ast.2006.05.001

General Electric. (2015). *CF34-8C Datasheet.* Retrieved from http://www.geaviation.com/engines/docs/commercial/datasheet-CF34-8C.pdf

Geuskens, F. J. J. M. M., Bergsma, O. K., Koussios, S., & Beukers, A. (2009). *Pressure vessels pressure cabins for blended wing bodies.* Paper presented at the 17th International Conference on Composite Materials, ICCM-17, July 27, 2009 - July 31, 2009, Edinburgh, United kingdom.

Greener by Design. (2003). *The Technology Challenge 2003*. Retrieved from http://aerosociety.com/Assets/Docs/About_Us/Greener%20By%20Design/GbD%20-%202003%20The%20Tech%20Challenge.pdf

Grosvenor, A. D. (2007). RANS Prediction of Transonic Compressive Rotor Performance Near Stall. (47950), 279-293. doi:https://doi.org/10.1115/GT2007-27691

Guermond, J.-L. (1990). A generalized lifting-line theory for curved and swept wings. *Journal of Fluid Mechanics, 211*, 497-513. doi:10.1017/S0022112090001665

Hileman, J. I., Reynolds, T. G., De La Rosa Blanco, E., Law, T. R., & Thomas, S. (2007). *Development of approach procedures for Silent Aircraft.* Paper presented at the 45th

206

AIAA Aerospace Sciences Meeting 2007, January 8, 2007 - January 11, 2007, Reno, NV, United states.

Hileman, J. I., Spakovszky, Z. S., Drela, M., & Sargeant, M. A. (2007). *Airframe design for "Silent Aircraft".* Paper presented at the 45th AIAA Aerospace Sciences Meeting 2007, January 8, 2007 - January 11, 2007, Reno, NV, United states.

Hirsch, C. (2007). *Numerical computation of internal and external flows: The fundamentals of computational fluid dynamics*: Elsevier.

Hodson, J., Hunsaker, D. F., & Spall, R. (2017). *Wing Optimization using Dual Number Automatic Differentiation in MachUp.* Paper presented at the 55th AIAA Aerospace Sciences Meeting.

Howe, D. (2001). *Blended wing body airframe mass prediction*.

Huang, L., Gao, Z., & Zhang, D. (2013). Research on multi-fidelity aerodynamic optimization methods. *Chinese Journal of Aeronautics, 26*(2), 279-286. doi:https://doi.org/10.1016/j.cja.2013.02.004

IATA. (2013). *IATA Technology Roadmap 2013*. Retrieved from http://www.iata.org/whatwedo/environment/Documents/technology-roadmap-2013.pdf

ICAO. (2018). *The world of air transport in 2018*. Retrieved from https://www.icao.int/annual-report-2018/Pages/the-world-of-air-transport-in-2018.aspx

ICEM, C. (2013). ver. 15.0. *ANSYS Inc., Southpointe, 275*.

Jamei, S., Maimun, A., Mansor, S., Azwadi, N., & Priyanto, A. (2016). Design Parametric Study of a Compound Wing-in-Ground Effect. I: Aerodynamics Performance. *Journal of Aerospace Engineering, 29*(1), 04015022. doi:https://doi.org/10.1061/(ASCE)AS.1943-5525.0000380

Jameson, A., & Fatica, M. (2006). Using computational fluid dynamics for aerodynamics. In: Stanford University, Stanford, California.

Kanazaki, M., Hanida, R., Nara, T., Shibata, M., Nomura, T., Murayama, M., & Yamamoto, K. (2013). Challenge of design exploration for small blended wing body using unstructured flow solver. *Computers & Fluids, 85*(0), 71-77. doi:http://dx.doi.org/10.1016/j.compfluid.2012.09.023

Ladson, C. L., Hill, A. S., & Johnson Jr, W. G. (1987). Pressure distributions from high Reynolds number transonic tests of an NACA 0012 airfoil in the Langley 0.3-meter transonic cryogenic tunnel.

Leifsson, L., Ko, A., Mason, W. H., Schetz, J. A., Grossman, B., & Haftka, R. T. (2013). Multidisciplinary design optimization of blended-wing-body transport aircraft with distributed propulsion. *Aerospace Science and Technology, 25*(1), 16-28. doi:10.1016/j.ast.2011.12.004

Levy, D. W., Laflin, K. R., Tinoco, E. N., Vassberg, J. C., Mani, M., Rider, B., . . . Brodersen, O. P. (2014). Summary of data from the fifth computational fluid dynamics drag prediction workshop. *Journal of Aircraft, 51*(4), 1194-1213. doi:https://doi.org/10.2514/1.C032389

Liebeck, R. H. (1989). *Low Reynolds number airfoil design for subsonic compressible flow.* Paper presented at the Low Reynolds Number Aerodynamics.

Liebeck, R. H. (2004). Design of the Blended Wing Body Subsonic Transport. *Journal of Aircraft, 41*(1), 10-25. doi:https://doi.org/10.2514/1.9084

Lyu, Z., & Martins, J. R. R. A. (2013). *RANS-based aerodynamic shape optimization of a blended-wing-body aircraft.* Paper presented at the 21st AIAA Computational Fluid Dynamics Conference, June 24, 2013 - June 27, 2013, San Diego, CA, United states.

Maier, R. (2011). *ACFA 2020 Summary of Achievements*. Retrieved from http://cordis.europa.eu/documents/documentlibrary/134654261EN8.zip

Mohr, B., Paulus, D., Baier, H., & Hornung, M. (2012). Design of a 450-passenger blended wing body aircraft for active control investigations. *Proceedings of the Institution of Mechanical Engineers, Part G: Journal of Aerospace Engineering, 226*(12), 1513-1522. doi:10.1177/0954410011426031

Morgado, J., Vizinho, R., Silvestre, M. A. R., & Páscoa, J. C. (2016). XFOIL vs CFD performance predictions for high lift low Reynolds number airfoils. *Aerospace Science and Technology, 52*, 207-214. doi:https://doi.org/10.1016/j.ast.2016.02.031

Mukhopadhyay, V., Sobieszczanski-Sobieski, J., Kosaka, I., Quinn, G., & Vanderpaats, G. N. (2004). Analysis, Design, and Optimization of Noncylindrical Fuselage for Blended-Wing-Body Vehicle. *Journal of Aircraft, 41*(4), 925-930. doi:10.2514/1.417

Nangia, R. K., & Palmer, M. E. (2002). *Flying wings (blended wing bodies) with aft- forward-sweep relating design camber twist to longitudinal control.* Paper presented at the AIAA Atmospheric Flight Mechanics Conference and Exhibit 2002, August 5, 2002 - August 8, 2002, Monterey, CA, United states.

Nara, T., & Kanazaki, M. (2010). *Initial design and evaluation of a novel concept regional aircraft.* Paper presented at the 2010 Asia-Pacific International Symposium on Aerospace Technology, APISAT 2010, September 13, 2010 - September 15, 2010, Xi'an, China.

NASA. (2012). Drag Prediction Workshop 5: Ecole Polytechnique IDEA Grids. Retrieved from https://dpw.larc.nasa.gov/DPW5/contrib/POLY_IDEA_GRIDS/

Neely, R. H., Bollech, T. V., & Westrick, G. C. (1947). Experimental and calculated characteristics of several NACA 44-series wings with aspect ratios of 8, 10, and 12 and taper ratios of 2.5 and 3.5.

Nickol, C. L. (2012). *Hybrid Wing Body Configuration Scaling Study.* Paper presented at the 50th AIAA Aerospace Sciences Meeting including the New Horizons Forum and Aerospace Exposition.

Osterheld, C., Heinze, W., & Horst, P. (2001). Preliminary design of a blended wing body configuration using the design tool PrADO. *DGLR BERICHT*(5), 119-128.

Palacios, F., Colonno, M. R., Aranake, A. C., Campos, A., Copeland, S. R., Economon, T. D., . . . Alonso, J. J. (2013). Stanford University Unstructured (SU2): An open-source integrated computational environment for multi-physics simulation and design. *AIAA Paper, 287*, 2013. doi:https://doi.org/10.2514/6.2013-287

Palacios, F., Economon, T. D., Aranake, A. C., Copeland, S. R., Lonkar, A. K., Lukaczyk, T. W., . . . Tracey, B. (2014). Stanford University Unstructured (SU2): Open-source analysis and design technology for turbulent flows. *AIAA Paper, 243*, 13-17.

Panagiotou, P., Fotiadis-Karras, S., & Yakinthos, K. (2018). Conceptual design of a Blended Wing Body MALE UAV. *Aerospace Science and Technology, 73*, 32-47. doi:10.1016/j.ast.2017.11.032

Parenteau, M., Sermeus, K., & Laurendeau, E. (2018). VLM Coupled with 2.5D RANS Sectional Data for High-Lift Design. In *2018 AIAA Aerospace Sciences Meeting*.

Park, S., Chang, K., & Ko, A. (2017). Numerical simulation of the low speed aerodynamic characteristics for BWB type UCAV configuration with -5 degree twisted angle. In *35th AIAA Applied Aerodynamics Conference*: American Institute of Aeronautics and Astronautics.

Paulus, D., Wirth, C., & Hornung, M. (2013). *Blended Wing Body Aircraft - Recommendations from High Lift and Control Surface Design and Optimization.* Paper presented at the 31st AIAA Applied Aerodynamics Conference, 24 June 2013, Reston, VA, USA.

Phillips, W. F. (2004). Lifting-Line Analysis for Twisted Wings and Washout-Optimized Wings. *Journal of Aircraft, 41*(1), 128-136. doi:https://doi.org/10.2514/1.262

Phillips, W. F., & Alley, N. R. (2007). Predicting Maximum Lift Coefficient for Twisted Wings Using Lifting-Line Theory. *Journal of Aircraft, 44*(3), 898-910. doi:https://doi.org/10.2514/1.25640

Phillips, W. F., & Hunsaker, D. F. (2019). Designing Wing Twist or Planform Distributions for Specified Lift Distributions. *Journal of Aircraft, 56*(2), 847-849. doi:https://doi.org/10.2514/1.C035206

Phillips, W. F., Hunsaker, D. F., & Joo, J. J. (2019). Minimizing Induced Drag with Lift Distribution and Wingspan. *Journal of Aircraft, 56*(2), 431-441. doi:https://doi.org/10.2514/1.C035027

Phillips, W. F., & Snyder, D. O. (2000). Modern Adaptation of Prandtl's Classic Lifting-Line Theory. *Journal of Aircraft, 37*(4), 662-670. doi:https://doi.org/10.2514/2.2649

Pope, S. B. (2000). *Turbulent flows*: Cambridge university press.

Qin, N., Vavalle, A., Le Moigne, A., Laban, M., Hackett, K., & Weinerfelt, P. (2004). Aerodynamic considerations of blended wing body aircraft. *Progress in Aerospace Sciences, 40*(6), 321-343. doi:http://dx.doi.org/10.1016/j.paerosci.2004.08.001

Qin, N., Vavalle, A., & Moigne, A. L. (2005). Spanwise Lift Distribution for Blended Wing Body Aircraft. *Journal of Aircraft, 42*(2), 356-365. doi:https://doi.org/10.2514/1.4229

Raymer, D. P. (2006). *Aircraft Design: A Conceptual Approach and Rds-student, Software for Aircraft Design, Sizing, and Performance Set (AIAA Education)*: AIAA (American Institute of Aeronautics & Ast.

Regan, C. D. (2008). *In-flight stability analysis of the X-48B aircraft.* Paper presented at the AIAA Atmospheric Flight Mechanics Conference and Exhibit, August 18, 2008 - August 21, 2008, Honolulu, HI, United states.

Reid, J. T., & Hunsaker, D. F. A General Approach to Lifting-Line Theory, Applied to Wings with Sweep. In *AIAA Scitech 2020 Forum*.

Reist, T. A., & Zingg, D. W. (2013). *Aerodynamic Shape Optimization of a Blended-Wing-Body Regional Transport for a Short Range Mission.* Paper presented at the 31st AIAA Applied Aerodynamics Conference, 24 June 2013, Reston, VA, USA.

Reist, T. A., & Zingg, D. W. (2014). *Aerodynamically optimal regional aircraft concepts: Conventional and blended wing-body designs.* Paper presented at the 52nd AIAA Aerospace Sciences Meeting - AIAA Science and Technology Forum and Exposition, SciTech 2014, January 13, 2014 - January 17, 2014, National Harbor, MD, United states.

Reist, T. A., & Zingg, D. W. (2015). *Optimization of the Aerodynamic Performance of Regional and Wide-Body-Class Blended Wing-Body Aircraft.* Paper presented at the 33rd AIAA Applied Aerodynamics Conference.

210

Reist, T. A., & Zingg, D. W. (2016). *Aerodynamic design of blended wing-body and lifting-fuselage aircraft.* Paper presented at the 34th AIAA Applied Aerodynamics Conference, 2016, June 13, 2016 - June 17, 2016, Washington, DC, United states.

Roskam, J. (1985). *Airplane design*: DARcorporation.

Rumsey, C. L. (2016/06/28, 2016/06/28). 2D NACA 0012 Airfoil Validation Case. *Turbulence Modeling Resource.* Retrieved from https://turbmodels.larc.nasa.gov/naca0012_val.html

Rumsey, C. L., & Slotnick, J. P. (2014). Overview and Summary of the Second AIAA High-Lift Prediction Workshop. *Journal of Aircraft, 52*(4), 1006-1025. doi:10.2514/1.C032864

Rumsey, C. L., Slotnick, J. P., Long, M., Stuever, R. A., & Wayman, T. R. (2011). Summary of the First AIAA CFD High-Lift Prediction Workshop. *Journal of Aircraft, 48*(6), 2068-2079. doi:10.2514/1.C031447

Rumsey, C. L., Slotnick, J. P., & Sclafani, A. J. (2018). *Overview and summary of the third AIAA High Lift Prediction Workshop.* Paper presented at the 2018 AIAA Aerospace Sciences Meeting.

Spalart, P., & Allmaras, S. (1992). A one-equation turbulence model for aerodynamic flows. In *30th Aerospace Sciences Meeting and Exhibit*: American Institute of Aeronautics and Astronautics.

Suder, K. (2012). *Overview of the NASA Environmentally Responsible Aviation Project's propulsion technology portfolio.* Paper presented at the 48th AIAA/ASME/SAE/ASEE Joint Propulsion Conference & Exhibit.

Sugar-Gabor, O. (2018). A general numerical unsteady non-linear lifting line model for engineering aerodynamics studies. *The Aeronautical Journal, 122*(1254), 1199-1228. doi:https://doi.org/10.1017/aer.2018.57

Tagawa, G. d., Morency, F., & Beaugendre, H. (2018). CFD study of airfoil lift reduction caused by ice roughness. In *2018 Applied Aerodynamics Conference*.

The Cambridge-MIT Institute. (2003). Silent Aircraft Initiative. Retrieved from http://silentaircraft.org/

Torenbeek, E. (2013a). *Advanced aircraft design : conceptual design, analysis and optimization of subsonic civil airplanes*. Chichester, West Sussex, United Kingdom: John Wiley & Sons.

Torenbeek, E. (2013b). Aerodynamic Drag and Its Reduction. In *Advanced Aircraft Design* (pp. 81-120): John Wiley & Sons, Ltd.

Transport Canada. (2008). *Operational Evaluation Board (OEB) Reports: Bombardier CRJ Series*. Canada: Government of Canada Retrieved from https://www.tc.gc.ca/eng/civilaviation/standards/commerce-4059.htm#_Toc324504216

Trips, D. (2010). Aerodynamic Design and Optimisation of a Long Range Mini-UAV. *Delft University of Technology, Holland.*

van der Voet, Z., Geuskens, F. J. J. M. M., Ahmed, T. J., van Eyben, B. N., & Beukers, A. (2012). Configuration of the Multibubble Pressure Cabin in Blended Wing Body Aircraft. *Journal of Aircraft, 49*(4), 991-1007. doi:10.2514/1.0031442

van Dommelen, J., & Vos, R. (2014). Conceptual design and analysis of blended-wing-body aircraft. *Proceedings of the Institution of Mechanical Engineers, Part G: Journal of Aerospace Engineering, 228*(13), 2452-2474. doi:10.1177/0954410013518696

Vassberg, J., Dehaan, M., Rivers, M., & Wahls, R. (2008). *Development of a common research model for applied CFD validation studies.* Paper presented at the 26th AIAA Applied Aerodynamics Conference.

Vassberg, J., Tinoco, E. N., Mani, M., Rider, B., Zickuhr, T., Levy, D. W., . . . Wahls, R. A. (2010). Summary of the Fourth AIAA CFD Drag Prediction Workshop.

Velazquez, O., Weiss, J., & Morency, F. (2015). *Development of blended wing body aircraft design*. Paper presented at the CASI 62nd Aeronautics Conference and AGM, Montréal. https://aero2015.exordo.com/files/papers/216/final_draft/216_Velazquezsalazar_etal_AERO2015.pdf

Velazquez, O., Weiss, J., & Morency, F. (2017). Preliminary investigation on stall characteristics of a Regional BWB for low speed approach. In *35th AIAA Applied Aerodynamics Conference*: American Institute of Aeronautics and Astronautics.

Velicki, A., & Thrash, P. (2010). Blended wing body structural concept development. *The Aeronautical Journal, 114*(1158), 513-519.

Vicroy, D. D. (2009). *Blended-Wing-Body low-speed flight dynamics: Summary of ground tests and sample results (Invited).* Paper presented at the 47th AIAA Aerospace Sciences Meeting including the New Horizons Forum and Aerospace Exposition, January 5, 2009 - January 8, 2009, Orlando, FL, United states.

Vos, R., & Van Dommelen, J. (2012). *A conceptual design and optimization method for blended-wing-body aircraft.* Paper presented at the 53rd AIAA/ASME/ASCE/AHS/ASC Structures, Structural Dynamics and Materials Conference, April 23, 2012 - April 26, 2012, Honolulu, HI, United states.

212

Wan, T., & Chen, Y.-S. (2014). *On the optimization of blended wing body aircraft configuration via the surrogate modeling method.* Paper presented at the 29th Congress of the International Council of the Aeronautical Sciences, ICAS 2014, September 7, 2014 - September 12, 2014, St. Petersburg, Russia.

Wisnoe, W., Nasir, R. E. M., Kuntjoro, W., & Mamat, A. M. I. (2009). *Wind tunnel experiments and cfd analysis of blended wing body (bwb) unmanned aerial vehicle (uav) at mach 0.1 and mach 0.3.* Paper presented at the 13th International Conference on Aerospace Sciences & Aviation Technology, ASAT-13.

Witherden, F. D., & Jameson, A. (2017). Future Directions in Computational Fluid Dynamics. In *23rd AIAA Computational Fluid Dynamics Conference*: American Institute of Aeronautics and Astronautics.